UNIVERSITY of CALIFORNIA
Santa Barbara

Heteroepitaxy and defect characterization in infrared III-V and IV-VI semiconductors

A dissertation submitted in partial satisfaction
of the requirements for the degree

Doctor of Philosophy
in
Materials
by
Brian B. Haidet

Committee in charge:
Professor Kunal Mukherjee, co-chair
Professor Chris Palmstrøm, co-chair
Professor Umesh Mishra
Professor James Speck

June, 2021

The dissertation of Brian Haidet is approved.

Professor Umesh Mishra

Professor James Speck

Professor Chris Palmstrøm, committee co-chair

Professor Kunal Mukherjee, committee co-chair

Acknowledgements

Getting a PhD turned out to be quite the journey, and I've had an enormous amount of help and encouragement along the way. Most of all, I have to thank my parents, Jeff and Victoria Haidet, for their unwavering support and love over the last 27 years. I think I've always been a curious person, which drew me towards science from a young age, and they nurtured this mindset with even more questions, projects, and exploration. My mom, never wanting my curiosity limited, was my unofficial math teacher for many years, and I cherish the great many hours we spent building entertaining contraptions and soldering electronics together in the basement. My dad, the astronomer, instilled me with his phenomenal appreciation for the beauty of physics and nature – I have his enthusiasm to thank for the awe I feel when I look up at the night sky, or now, appreciate the symmetry of a crystalline lattice.

After an upbringing of many questions and sometimes fewer answers, I started to understand what science really was. At some point, we need to find *new* answers, because sometimes nobody knows. In high school in Blythe Tipping's Science Research class, for the first time, I got to answer some "new" questions of my own. Working with Dr. Dean Giolando from the University of Toledo, I embarked on a project that exposed me to real scientific equipment, characterization, and materials synthesis. It left such an impression that only a few months after learning what materials science was, I would apply to the Materials Science and Engineering department at NC State.

As an undergraduate at NC State, I had the amazing opportunity to work for Dr. Ramón Collazo and Dr. Zlatko Sitar. The research team was large, with many brilliant students and post-docs – I began to appreciate just how difficult science is – how many disparate skillsets working together are required to advance the boundaries of human understanding in a useful direction. I got to learn about semiconductors, solid state physics, was first exposed to crystal growth, and had my first full-time job. During this time, I worked very closely with then-graduate-students Isaac Bryan and Zachary Bryan, who guided me through this new world and taught me what scientific research was really all about. I think their support pretty directly formed me into the scientist I hope I am today.

UCSB has an amazingly collaborative campus, and once I was a grad student myself, I got to learn about crystal growth and characterization from so many helpful people – my advisor Dr. Kunal Mukherjee at the top of that list. I like to say that I beat Kunal to campus – he started at UCSB as a professor in the middle of my first quarter, so he was a new professor while I was a new grad student – we sort of got to figure out how everything worked together. Throughout my grad school career, we communicated nearly daily about fresh results, old data interpretations, and new ideas. Without that close collaboration, we would not have come anywhere near achieving the results discussed in this dissertation. On the IV-VI project, I also worked very closely with groupmate Eamon Hughes – we spent a lot of fun and frustrating hours in the MBE lab together, celebrating the slight steps forward that seem to constitute academic research. Although we didn't work on the same projects directly, I learned a lot from groupmates Jenny Selvidge and Lillian Hughes, and thoroughly enjoyed working with the team.

In a small group, Eamonn and I didn't have too much freedom to specialize, but thankfully we had fantastic mentors and support at every turn. Kurt Olsson from the MBE Lab deserves special gratitude for getting us on our feet in the world of crystal growth, and Dr. Gareth Seward and Dr. Aidan Taylor were vital in our learning to characterize the samples we'd grown. Our collaborations with other research teams, especially Dr. Justin Norman and Dr. Daehwan Jung from Bowers Group and Dr. Mihir Pendharkar and Dr. Anthony McFadden from Palmstrøm Group were also instrumental. Throughout my grad school career, other members of my committees, Dr. Ram Seshadri, Dr. Chis Palmstrøm, Dr. Umesh Mishra, and Dr. Jim Speck, have offered great advice and helped to keep me on this track to graduation.

Typing this paragraph and finishing this document is pretty surreal – after five years, it doesn't seem like grad school can be over; memories with the friends I've made and the colleagues I've worked with will stay with me forever. I am so excited to have completed this stage of my life and my education, and I am extremely grateful for all the help I've had along the way. Now, I am looking forward to the future, hopefully continuing to learn even more about this fascinating world we live in.

Curriculum Vitæ

Brian Haidet

Education

University of California, Santa Barbara
PhD, Materials, 2021

North Carolina State University
B.S. Magna Cum Laude, Physics, 2016
B.S. Magna Cum Laude, Materials Science and Engineering, 2016

Honors

2020 – UCSB Quantum Foundry Associate
2018 – Best Student Paper at the 60th Electronic Materials Conference
2018 – NSF Graduate Research Fellowship
2015 – NCSU Provost's Program for MSE Undergraduate Research

First-Author Publications

Interface structure and luminescence properties of epitaxial PbSe films on InAs(111)A B.B. Haidet, L. Nordin, A. Muhowski, K.D. Vallejo, E.T. Hughes, J. Meyer, P.J. Simmonds, D. Wasserman, K. Mukherjee (2021) *JVST A* 39(2), 023404

Nucleation Control and Interface Structure of Rocksalt PbSe on (001) Zincblende III-V Surfaces B.B. Haidet, E.T. Hughes, K. Mukherjee (2020) *Physical Review Materials* 4 (3), 033402

Direct observation of recombination-enhanced dislocation glide in heteroepitaxial GaAs on silicon P.G. Callahan, B.B. Haidet, D. Jung, G.G.E. Seward, K. Mukherjee (2018) *Physical Review Materials* 2 (8), 081601

Nonlinear analysis of vanadium-and titanium-based contacts to Al-rich n-AlGaN B.B. Haidet, B. Sarkar, P. Reddy, I. Bryan, Z. Bryan, R. Kirste, R. Collazo, Z. Sitar (2017) *Japanese Journal of Applied Physics* 56 (10), 100302

A conduction model for contacts to Si-doped AlGaN grown on sapphire and single-crystalline AlN B.B. Haidet, I. Bryan, P. Reddy, Z. Bryan, R. Collazo, Z. Sitar (2016) *Journal of Applied Physics* 117(24), 245702

Abstract

Heteroepitaxy and defect characterization in infrared III-V and IV-VI semiconductors

by

Brian Haidet

While IV-VI materials were some of the first semiconductors ever studied, they have yet to reach widespread commercial application in optoelectronics. Unfortunately, the peculiar bonding and structure of the IV-VI rocksalts that provides them with unique electrical characteristics also makes them very difficult to incorporate on foreign substrates. The rocksalt IV-VIs, PbSe, PbTe, and SnTe, have a mixed-character bonding, which contributes to a curious band structure with a direct L-valley bandgap, low auger recombination, and high dielectric constant, all beneficial features for defect-tolerant optoelectronics, however achieving high structural quality has always been a problem. While the first PbSe and PbTe lasers were demonstrated almost 60 years ago, research on infrared materials has slowly shifted towards II-VIs, III-Vs, HgCdTe, and quantum cascade lasers, with many fundamental materials problems in the IV-VI family left unsolved. In this dissertation, I hope to address some of these questions, specifically related to material growth, and lay groundwork for further exploration of PbSe bonding, optical, and electronic properties on a more robust growth platform.

As the field of epitaxial crystal growth inexorably advances, materials scientists are forced to tackle ever more challenging heteroepitaxial combinations. Beyond direct device applications, PbSe growth on III-V substrates is a compelling model system for understanding high energy interfaces incorporating changes in valency, interface charge, coordination, and lattice mismatch. This dissertation focuses on molecular beam epitaxy of PbSe on zincblende GaSb, InAs, and GaAs substrates. We find that on arsenic-terminated surfaces in both the (001) and (111) orientations,

nucleation is controllable. By exposing a III-V surface to PbSe flux at a temperature above the PbSe re-evaporation temperature, the surface is converted to a better template for growth: subsequent low-temperature initiation of PbSe flux results in single-orientation films. The resulting heterovalent and heterocrystalline interfaces are mapped using high resolution scanning transmission electron microscopy, and possible mechanisms of interface formation are discussed, with emphasis on interfacial symmetry.

As interfacial energetics have not yet allowed for layer-by-layer growth of PbSe on any foreign substrate, understanding and controlling island coalescence is the key to synthesizing high-quality PbSe films. By systematically varying lattice mismatch and comparing films grown in different orientations, different relaxation mechanisms can be activated and studied. We find PbSe island shape and coalescence behavior is a function of surface mismatch, chemistry, and local strain from extended defects. Extensive defect characterization using electron channeling contrast imaging and transmission techniques has allowed for direct characterization of these complex dislocation structures. Through these studies, we present multiple avenues towards high-quality PbSe film growth on III-V substrates. Fascinatingly, even in structurally defective PbSe and PbSnSe films, strong photoluminescence can be observed, speaking to the future of these materials as defect-tolerant infrared emitters and detectors.

Contents

Table of Figures

1.Introduction to IV-VI materials

I. INTRODUCTION TO INORGANIC CRYSTAL GROWTH

Study of crystalline materials dates back to Johannes Kepler's 1611 booklet *On the six-cornered snowflake*, which marked the first connection between the nanoscale structure of a material and it's macroscopic shape and properties. Although Kepler's publication predates atomic theory by almost 200 years, and x-ray crystallography by 300 years, he proposed that snowflakes formed with hexagonal symmetry because "…*vapor coagulates into globules of a definite size*… [and] *These balls of vapor will have a certain pattern of contact: for instance square in a plane, cube in a solid*". Kepler specified that a hexagonal packing in 3D (what we now refer to as face-centered-cubic) would be the most efficient way to arrange these fundamental "globules of vapor".

Today, we have a great many more tools and technologies at our disposal for design, synthesis, and characterization of crystal structures. We live in a world where it is now possible to mathematically calculate the relevant properties of any hypothetical arrangement of atoms, but in our mission to create those arrangements, to grow ever-more-perfect crystalline materials with desired electrical, optical, and mechanical properties, we are still at the mercy of atoms, bonding, thermodynamics, and kinetics – not every structure can be synthesized. Even if we could place atoms one-by-one in a desired configuration, thermal vibration and diffusion would create crystalline defects and incorporate impurities. The field of inorganic crystal growth seeks to gain control over these atomic-scale processes to make crystals with the desired properties as efficiently as possible.

When a crystal terminates in a free surface, a periodic array of partially-bonded atoms is left behind, creating a patchwork of electric fields – electrons and nuclei – that create an "energetic landscape" for charged species to navigate. When new species of atoms or molecules are exposed

to this free surface, they have their own electrons and nuclei – charges which interact with the crystal surface. They traverse this periodic template, eventually finding a stable place to settle, where they dissipate their energy and become part of the structure. As this process repeats many Avogadro's Number of times, a crystal is built up. A periodic pattern of atoms in 3 dimensions is constructed using only random jostling of molecules and local electrostatic interactions between the crystal free surface and free atoms seeking a stable bonding site.

The crystal growth I will focus on in this document is *heteroepitaxial* growth – meaning that two different crystalline materials are coupled at an interface. In this case, the atoms being provided to extend the crystal are not the same as the atoms in the existing crystal. In some cases, like lead selenide growth on gallium arsenide, the equilibrium crystal structures of the two materials may not even be the same, so although the free crystalline surface is periodic and informs the symmetry of the new crystal, the new crystal is distinct. The new atoms stabilize into a 3D structure which is related to, but different than the original template.

Heteroepitaxy can be used to create electrically-active heterojunctions, where the electronic structure of an interface between two different materials is integral to the device's function, or heteroepitaxy may be necessary to grow crystalline materials for which native substrates do not exist. In the present work, we want to investigate the properties of PbSe films, but PbSe substrates are rare, expensive, and low-quality, so we grow PbSe films on crystalline substrates of other materials.

II. LEAD SELENIDE AND THE IV-VI SEMICONDUCTORS

History of PbSe research and devices

The IV-VI rocksalts were some of the earliest semiconductors investigated, with lead sulfide finding application as one of the earliest photodetectors in the 1930s[1,2]. The IV-VI

materials have relatively small bandgaps, meaning that characteristic electronic transitions will have low energies, corresponding to long wavelengths of light in the near and mid-infrared.

The first IV-VI diode lasers using PbTe and PbSe were demonstrated by Butler and co-authors in two papers in 1964[3,4], fabricating so called "diffusion junctions" between Pb-rich and VI-rich rocksalt crystals. PbSe, PbTe, and PbS can all support significant nonstoichiometries – ie. they can form a stable rocksalt structure without a perfect 50:50 ratio of group IV and group VI atoms. The vacancy point defects that manifest such structures are themselves electrically active, with group-IV vacancies acting as electron acceptors, and group-VI vacancies acting as electron donors. In practice, this means that one could anneal a perfectly stoichiometric sample of PbSe in a sealed chamber with excess selenium and it would become p-type by incorporating lead vacancies. Early devices were then simply fabricated as "diffused junctions" where two bulk crystals with differing compositions could be pressed together and annealed. As excess selenium diffused out of a selenium-rich crystal into an n-type selenium deficient crystal, it created a p-type layer near the surface of the formerly n-type crystal, and necessarily a p-n junction[5]. While using stoichiometric doping to create junctions in bulk crystals was a creative method for fabricating electronics without significant process control, it could only create the simplest possible electronic structure, and was quickly replaced.

In a 1979 review of IV-VI lasers by Preier[6], the epitaxial methods: liquid phase epitaxy (LPE), vapor phase epitaxy (VPE), molecular beam epitaxy (MBE) and hot wall epitaxy (HWE), had largely superseded diffusion junctions due to the enhanced control epitaxy grants over device design. By growing a crystalline film on an existing crystalline substrate, adding material in discrete controlled layers, more complex devices like double-heterostructures could be synthesized. Where a diffusion junction consisted of a single blurry interface, a double heterostructure requires at least two reasonably sharp interfaces between disparate materials. For example, by sandwiching a

narrow-bandgap PbSnSe active layer between two higher-bandgap PbSe layers, electrons and holes in the active layer are prevented from escaping prior to recombination, enhancing radiative efficiency.

Such structures (and the closely associated quantum well structures) are most efficient when the surrounding layers have a much higher bandgap than the active region, and in 1993, Springholz and Bauer[7] began exploring MBE growth of europium-containing rocksalts, fabricating superlattices of PbTe/EuTe. As EuTe and EuSe are high-bandgap rocksalts, chemically and structurally compatible with the narrow-bandgap IV-IVs, they made effective reflectors[8] and high-bandgap cladding layers for lasers, allowing for a 3.1 μm laser operating at room temperature in 2001[9,10].

The vast majority of MBE growth of the IV-VI materials, including the aforementioned lasers, has been performed on the fluorite substrates BaF_2 and CaF_2 or buffer layers of fluorite material on silicon(111). This class of substrates was selected in 1974 by Hohnke and Kaiser[11] who noted that BaF_2 was both lattice matched and thermally matched to PbSe. They deposited PbSe and $Pb_{0.94}Sn_{0.06}Se$ on cleaved and baked BaF_2 and SrF_2 substrates via MBE with compound effusion cell sources for PbSe and SnSe. These substrates allowed for high-quality crystal growth, and became a standard substrate for IV-VI epitaxy despite a lack of mechanical strength, a low thermal conductivity, and water solubility.

11 years later, when Zogg and Hüppi[12] were attempting to grow IV-VI layers on more robust Si(111) substrates, they decided to leverage the existing knowledge of growth on fluorite surfaces, and designed CaF_2 and BaF_2 buffer layers that could be grown directly on silicon surfaces via MBE to prepare the surface for PbSe deposition, later noting[13] that the ionic fluorites appeared to bridge a bonding incompatibility between the covalent silicon and the IV-VIs. Zogg's group did a significant amount of work characterizing the relaxation and defect behavior of IV-

VI films[14–16] and the IV-VI/Fluorite/Si buffering technique allowed them to achieve such sophisticated devices as a PbSnSe-based infrared pixel array for thermal imaging[17,18]. Indeed as the IV-VI materials began as photodetectors, infrared sensing is the lone modern commercial application for PbSe and PbS, with companies such as trinamiX, NIT, and Infrared Materials fabricating devices from polycrystalline IV-VI films which have been "sensitized" with a thermal treatment under iodine atmosphere[19].

While polycrystalline materials can make useful detectors, the desire for high-quality PbSe films for infrared lasers never fully vanished, and in 1998, Shi[20] proposed the GaSb/PbSe/GaSb double-heterostructure laser using a III-V semiconductor as both the substrate and cladding for a laser with a IV-VI active region. Although a study on liquid phase epitaxy growth of PbSe quantum dots on GaSb was published in 2002[21], there is almost no literature regarding IV-VI growth on III-V surfaces[21–23]. In this dissertation, I hope to push this knowledge forward, presenting our results growing PbSe not only on GaSb, but also on GaAs, InAs, and InAsSb substrates, and exploring both the (001) and (111) orientations.

Structure of PbSe and the IV-VI family

PbSe in equilibrium, along with the related PbS, PbTe, and SnTe, form the rocksalt crystal structure, best imagined as a 3D checkerboard of lead and selenium atoms, where each atom is bonded to six others, or octahedrally coordinated (Figure 1.1). Bonding in the IV-VI materials appears ionic at first glance, because the rocksalt structure is typically formed by ionic solids like its namesake NaCl, however the electronegativity difference between lead (2.23) and selenium(2.55) isn't significant enough to justify a charge transfer on the scale of ionic bonding to create Pb^{2+} and Se^{2-} ions. Indeed the 10 valence electrons per formula unit contained by the IV-VI materials cause quite a problem for standard polar-covalent models that work excellently for the group IV semiconductors and the III-V semiconductors, each of which conveniently have

four valence electrons and four bonds per atom. In 1973, Lucovsky and White[24] posited that bonding in rocksalt PbSe was based on resonant p-orbitals, similar to bonding in aromatic rings where the number of electrons is insufficient to simultaneously populate every bond, but continuous exchange between two different structures results in a stable intermediate. They highlight an ionic structure where lead donates two electrons to selenium, and a fully-metallic structure where selenium donates one electron to lead. The actual bonding is intermediate, with bonding p-orbitals emerging from each atom at 90° angles resulting in the 3D checkerboard of the rocksalt structure. Excess electrons during this resonance are held by s-orbitals localized on one species.

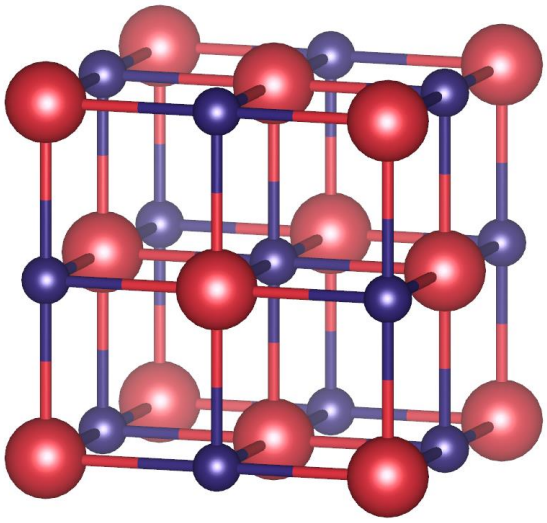

Figure 1.1 – **Rocksalt structure of PbSe.** (Pb: red, Se: blue)

More modern interpretations [25–28] this structure have coined the term "metavalent bonding" to describe materials like PbSe. For nonpolar covalent bonding and metallic bonding, electrons are exclusively and evenly shared between species, while for ionic bonding, electrons are almost exclusively transferred from one species to the other. Bonding in PbSe is a unique intermediary of ionic, covalent, and metallic bonding with a combination of charge transfer and charge sharing that doesn't match well with any of the classic three paradigms. Determining whether metavalent bonding stands on its own as a new class of bonding, should be considered "mixed bonding", or exists as a variant of covalent bonding[29] is an outstanding question.

While PbSe and its rocksalt contemporaries possess this peculiar bonding and structure, it's worth noting that the IV-VI semiconductor family includes a rich variety of related

structures[30]. GeTe assumes a rhombohedral (distorted rocksalt) structure under ambient conditions, and GeSe, SnSe, SnS, and GeS form an orthorhombic layered structure. All of these phases are structurally similar, and at higher temperatures or under increased pressure many of these materials undergo phase transformations[31]. The alloy PbSnSe is cubic rocksalt up to a composition of 45% Sn, beyond which it is orthorhombic Pnma. While the vast majority of the present work relates to cubic phases, later chapters in this dissertation will discuss this layered Pnma structure and illustrate how its symmetry allows it to play host to some unique crystalline defects.

Defect tolerance

The promise of defect tolerance has encouraged much of the research in the IV-VI rocksalts. Defects in the crystal lattice (substitutionals, interstitials, vacancies, extended defects) disrupt the electronic structure of the host crystal, creating extra states within the bandgap and allowing free electrons in the conduction band to recombine with holes in the valence band, using the defect state as an interim stepping stone. This process is called Shockley Reed Hall (SRH) recombination and is deleterious to a wide range of electronic materials.

The fact that materials like PbSe exist very near to a phase transformation (in configuration-space) makes the structure stably deformable and polarizable. This polarizability gives the rocksalt IV-VIs extremely large dielectric constants (ϵ_{PbSe} = 210 at RT, 280 at 4K), allowing them to effectively screen charged defects in their interior[30], and maintaining high mobilities even with significant doping[32] (Figure 1.2). Essentially, the lattice will distort in response to a nearby charged point defect, canceling the electrostatic field emitted by the defect, and reducing the interaction cross section of the defect, and making it less likely to affect the motion of a free electron or hole.

Aside from this more classical view which depends on geometric structure, a great deal of

theoretical work has sought to understand defect-tolerant materials based on their bonding and defect electronic structure[27–29,33,34]. Most of the work in this direction has come not from the IV-VI field, but the realm of lead-halide perovskites[29,33,34], promising photovoltaics with long carrier lifetimes despite extremely high defect densities and polycrystalline synthesis. Rakita et al.[29] observe that bonding in the halide perovskites (as well as PbSe) has significant antibonding covalent character, implying that the valence band maximum is made from repulsive antibonding states instead of attractive bonding states, explaining phenomena such as PbSe's reversed temperature-bandgap relationship. Such a model also places the relevant bands at a different absolute energy range, meaning that previously-midgap-trap defect states may now be shallow traps or even within a band. Granted, because lead selenide has a narrower bandgap than the halide perovskites, thermal excitation can help to depopulate trap states, so the absolute position of traps is not as important.

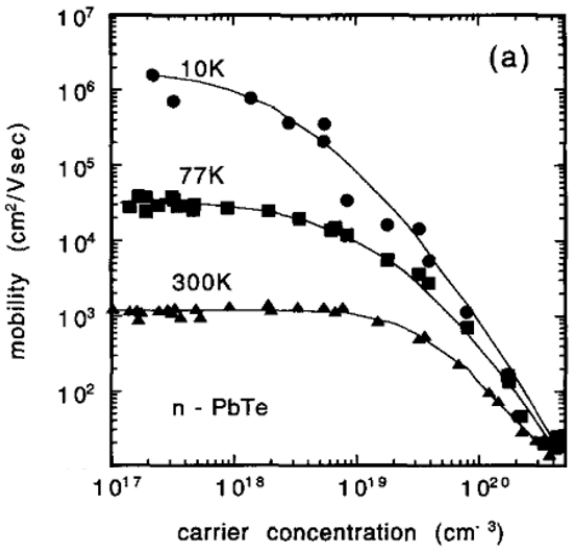

Figure 1.2 – **Hall mobility of n-type PbTe as a function of temperature and doping.**
Reproduced from [32].

Zhang et al.[34], in their 2020 analysis of defect tolerance in halide perovskites, emphasize that mid-gap-traps *can still exist* in these materials, but are largely inactive due to significant energetic barriers to carrier capture. They credit the anharmonicity of bonding in the halide perovskites for providing their defect tolerance. For a trap to capture a free electron or hole, it must traverse a very high saddlepoint in configuration space, distorting in an unfavorable way, granted the anharmonic bonding. We are hoping that the IV-VI rocksalts with their peculiar

bonding also benefit from this effect.

Quantum materials

In the last 10 years, there has been an additional academic momentum towards understanding the IV-VI materials and their growth due to hypothesized application in the realm of quantum materials, spintronics, and quantum computing, with certain phases of IV-VI materials identified as topological crystalline insulators[30,35–41]. Specifically SnTe, and Sn-rich compositions of PbSnSe ([Sn]>22%) possess inverted bandgaps, and play host to topologically nontrivial transport. Even in trivial IV-VI insulators, topological states are predicted to exist for certain orientations of monolayers[42], and have been observed at heterovalent interfaces[43].

This dissertation will not focus on these applications in any detail, but it is important to remember the needs of this still-emerging field. The opportunity to leverage existing materials science MBE techniques in fabrication of these layers opens the design space for topological devices, extending the concept of topological surface states to topological *interface* states, which can be grown with high structural fidelity and buried inside a semiconductor stack, remining pristine and controllable.

III. LEAD SELENIDE GROWTH

Substrates and growth techniques

Where the IV-VI materials show promise, native IV-VI substrates and the conventional cleaved fluorite bulk substrates have many drawbacks. First of all, they are extremely soft, to the point where it is common practice to always move a given PbSe substrate by picking it up from the same sacrificial corner, because simply handling it with tweezers can induce dislocations. The fluorite substrates require fresh cleaving and are water-soluble, so surfaces rapidly degrade in atmosphere before loading into the MBE. Generally, IV-VI growth on fluorite substrates is

characterized by weak bonding, and minimal substrate-film interaction, leading to low sticking coefficients, large islands, and slow coalescence[11,44–46]. Additionally, both of these materials have low thermal conductivity, limiting device performance.

These troubles have prompted research into IV-VI growth on silicon[13,15,47] and III-V substrates like GaAs or InSb[21–23], sometimes with II-VI buffer layers[43,48–50]. We opted to explore the III-V family of semiconductors as substrates for IV-VI growth, but despite favorable strength, thermal and mechanical properties, cost, and availability, the IV-VI/III-V combination brings with it new challenges. These two materials systems have different bonding character, making bonds across the interface a rather uncertain quantity. These materials also have a different crystal structure, meaning that the symmetry and coordination around any given species in each crystal will be different, and at least one layer of interfacial atoms will have an atypical asymmetric coordination. Unless two nonpolar surfaces are involved in the interface, there will also be trapped charge at such a heterovalent boundary, causing additional problems during nucleation. All of these factors contribute to extremely high interfacial energies and result in a difficult-to-control and defect-prone 3D island growth mode in the early stages. Success in developing epitaxial tools to prepare sharp IV-VI/III-V interfaces will enable harnessing of these material dissimilarities for new means to access the unique mid-infrared optical properties of IV-VI materials as well as for the creation and control of novel interfacial electronic phenomena.

As these materials are grown at relatively low temperatures, control over these heterointerfaces may even allow for back end of line integration on top of existing processes. This work will discuss IV-VI/III-V heterointerfaces, and many others are working to grow high quality III-V/Si heterointerfaces, so it is conceivable that IV-VI active layers could exist in a PbSe/III-V or PbSe/III-V/Si stack, added after fab without overtaxing the thermal budget.

Goals of this work

The technological progress of new growth and characterization techniques advances research superlinearly – having more tools in the metaphorical research toolbox changes how one approaches a problem by enabling new experiments. In growth of IV-VI materials, significant progress has been made, but the bulk of the fundamental research in the field was completed more than 30 years ago. Since then, entire new fields of materials science have been explored – the zincblende III-Vs and the nitrides grew from almost nothing to fully fledged commercial technology platforms. There now exists orders of magnitude more institutional knowledge to leverage, taking a new look at an old material.

For this research, I had the privilege to utilize a brand new state of the art molecular beam epitaxy system with high purity sources, cryogenic pumping, and significant recipe automation for growth repeatability. For materials characterization, I make extensive use of electron channeling contrast imaging (ECCI) and atomic-resolution scanning transmission electron microscopy to characterize defects within these materials. ECCI in particular is a technique that is still in its infancy in terms of application, and a technique we have actively pushed forward through the present work.

We sought to understand how PbSe/III-V interfaces would form, especially how materials with mixed bonding interact with conventional (non-ionic) substrates to overcome the need for these problematic fluorite buffers. In our early experiments, we showed that interfacial chemistry plays a critical role, with interfacial reactions preventing high quality interfaces from being synthesized on GaSb substrates, but identified a route towards single-orientation nucleation on the III-As substrates via a novel surface treatment, later expanding these results to alternate crystalline orientations, successfully growing PbSe on InAs(111)A.

Unfortunately, in our experience, PbSe nucleation and growth always proceeds via an

island/coalescence growth mode, and so we have put significant effort into understanding the defects created during said island coalescence, and how these defects behave in a grown film. In the (111) orientation, these dislocations are quite mobile, but in the (001) orientation, the peculiar slip geometry of the IV-VI rocksalts prevents removal of defects, so we have instead focused on reducing the number of defects initially formed within the film. Leveraging existing III-V growth techniques to design metamorphic buffers that act as better templates for PbSe coalescence, we identify a path towards coherent PbSe growth on III-As(001) substrates.

Working with collaborators to explore the optical properties of our materials, we have also found these IV-VI films to have long carrier lifetimes and emit light at mid-IR wavelengths. Despite extremely high defect densities, PbSe films at room temperature can emit 4 μm radiation at intensities to rival dislocated III-V films of similar bandgap. It appears that SRH recombination in our PbSe films is significantly suppressed.

These preliminary structural and optical results lay the groundwork for future study of PbSe and PbSnSe materials and devices on a robust III-V growth platform, leveraging the existing body of knowledge regarding high quality crystal growth, and applying it to a materials system which shows great promise.

2.Experimental methods

I. INTRODUCTION

In this section, I intend to communicate a working knowledge of the synthesis and structural characterization equipment used for MBE crystal growth. I won't go into much of the math or deeper theory, because when performing these experiments, that theory usually isn't top of mind. Instead, focusing on visualizable models (sometimes simplifications) like adatom dangling bond counting at surface steps instead of full kinetics, interpreting diffraction as an image of mosaic-smeared reciprocal space rather than a full mathematical workup with Fourier transforms, or scanning electron micrographs as a sum of multiple superimposed images formed with different "filters" rather than a simulation of each contrast-forming interaction in the material.

When learning these topics and techniques, I normally needed to see the information from a variety of perspectives before it made sense, and my hope is that this section can be either a loose introduction or functional second-pass over the relevant techniques for new students. Especially with the group moving universities during COVID restrictions, and the negligible opportunity for standard knowledge transfer between veterans and new students, I wanted to record the "way it makes sense to me" in a more conversational tone for many of these topics. Hopefully it is helpful!

II. MOLECULAR BEAM EPITAXY

Introduction

Molecular Beam Epitaxy (MBE) is an ultra high vacuum crystal growth technique that provides excellent control over interfaces and surfaces. While sometimes (increasingly) used in industry, historically, MBE has been a research tool, used to gain a better understanding of a

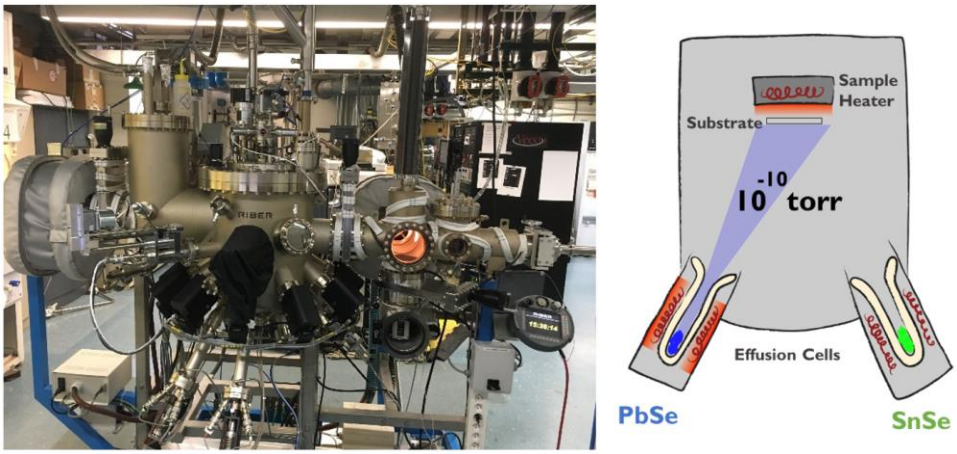

Figure 2.1 – **The Riber C21 MBE System for IV-VI deposition.**
(left, photograph) The central cylinder is the growth chamber, with the effusion cells at the bottom and the sample rotation equipment on top. (right) Schematic view of the growth chamber, with two effusion cells pictured, evaporating precursor material for deposition on the upside-down substrate above.

materials system before transitioning to a more scalable technique for high precision epitaxy like metal-organic chemical vapor deposition (MOCVD), however in the case of the IV-VI materials, MOCVD is not an option. The MBE system used to grow IV-VI films in this work is pictured in Figure 2.1.

In MBE, precursor material is thermally evaporated into a vacuum with a mean free path on the order of kilometers. These evaporated atoms and molecules travel ballistically to the target, a crystalline substrate held at a specific temperature. By controlling the incident molecular flux and the temperature of the substrate, a crystalline film can be epitaxially grown, inheriting symmetry from the single-crystal substrate. In some cases, especially homoepitaxy, the windows for acceptable growth are large, where a wide variety of fluxes and substrate temperatures result in the growth of high quality crystals, but in some cases, notably heteroepitaxy of dissimilar materials, the relevant thermodynamics and kinetics can produce extremely narrow parameter-space windows for high quality growth. Epitaxy of the rocksalt IV-VI materials family on III-V substrates is one of these narrow-window cases.

MBE operation and service is primarily focused on maintaining the ultra-high vacuum conditions necessary for clean, controllable growth. Samples are inserted through a load lock and buffer chamber so the growth chamber is typically separated from atmosphere by a minimum of two UHV gate valves. When source materials need to be refilled, or parts of the system need to be fixed or maintained, the entire system must be vented to atmospheric pressure. Such an "opening" should ideally only be necessary every 6-12 months. This section will discuss MBE operation, maintenance, and vacuum technology.

Generation of molecular flux

MBE is set apart from other methods like MOCVD because the crystal growth process is simple vapor-solid deposition, with few extraneous chemical reactions. Growth of a III-V material like GaAs may involve the use of elemental gallium flux and molecular arsenic flux, where cracking of the molecular arsenic is the only reaction that need occur before epitaxy can proceed. These fluxes need not be supplied in stoichiometric ratio – in fact, V:III ratios for growth of zincblende III-Vs may range from 2-10. By providing many times the necessary arsenic, gallium flux is turned into the growth-rate-limiting parameter, and the immense overpressure of arsenic ensures that the surface always has a similar structure. This means that most of the arsenic that hits the sample surface evaporates without incorporating, but it serves a purpose for control, and it's important to note that any given atom of arsenic *could* be incorporated into the film. This is very different from MOCVD growth, where more complex chemical reactions occur in the vapor and on the film surface, cracking metal ions off of their organic carrier groups, which become waste that does not incorporate on the growing film's surface. For example, when trimethyl gallium is impingent on a heated surface, the methyl groups do not become part of the crystal.

Although effusion cells can operate with only one heating element, a more common design is to have a "base" and a "tip" heater holding a thermal gradient across the crucible in order to

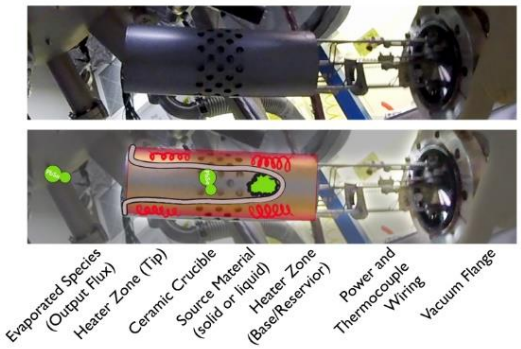

Figure 2.2 – **Thermal effusion cell.**
A DZMM cell from Riber (picture, and annotated picture). This typical effusion cell has a conical crucible with two heated zones, and fits on a standard conflat flange.

control the charge of source material. These heater zones each have an independent power and thermocouple connection for feedback. Because every cell design and thermocouple placement is slightly different, and source material can redistribute within a cell over the course of a growth campaign, constant recalibration of sources is necessary, equating cell thermocouple temperatures with flux rates (measured via ion vacuum gauge) and actual growth rate (measured as grown calibration sample thickness via x-ray diffraction). For the vast majority of materials, the tip is held hotter to prevent deposition of material near the mouth of the cell where the aperture could become partially obscured or completely clogged. In the case of PbSe in these DZMM cells (Figure 2.2), we observe that the initial powder/chunk/flake charge sitting in the bottom of the cell is, over time, fully evaporated and redeposited in the "middle" of the crucible, where the walls are coldest. During service, if the PbSe charge was not completely depleted before opening, a hollow cylinder of solidified polycrystalline PbSe can be found stuck inside the crucible, but can be removed to make room for a fresh charge. In the case of certain source materials, notably aluminum, the tip is actually held colder than the base to prevent liquid metal from wetting the inside of the crucible and creeping up and out of the crucible, where it could freeze and cause cracking or short electrical contacts to the cell. Even a single growth day with the aluminum temperature inverted can ruin a crucible, necessitating an opening to replace and repair.

In usage, compound effusion cells like PbSe are slightly different in that the output flux is not guaranteed to be a constant composition. With separate gallium and arsenic cells, the V:III

ratio while growing GaAs is easy to tune, but with a single compound PbSe cell, the VI:IV ratio is subject to the specific species evaporated from the cell. Solid PbSe, when heated, can be a source of PbSe molecules, elemental Pb, Se, single component molecules like Se_2, or multi-component molecules like $PbSe_2$. All of these evaporated molecules can reach the substrate in equal proportion, but the evaporation rate for any given molecule is dependent on many factors. Figure 2.3 shows the vapor pressure of various molecular species that can be evaporated from a solid PbTe source. In this case, Pb_1Te_1 is the primary evaporant by nearly two orders of magnitude at relevant temperatures. Although overwhelming from a structural perspective, this ~1% level of Pb, Te, and Te_2 species is woefully imprecise from the perspective of doping, as vacancies are electrically active dopants in the IV-VI materials - so controlling precise stoichiometry is synonymous with controlling carrier density.

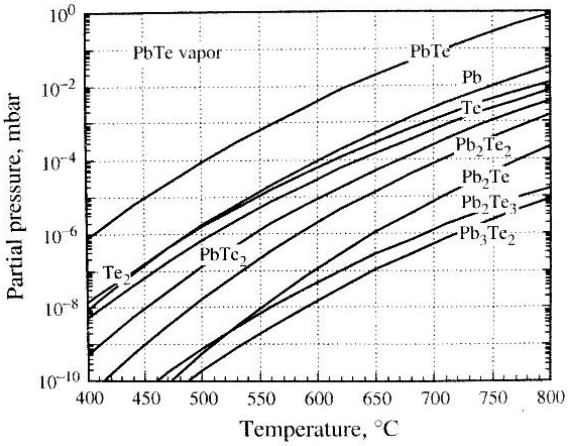

Figure 2.3 – **Flux species evaporated from a PbTe compound effusion cell**. An elemental cell may emit only single-component flux, but a compound cell has many options for molecules which could evaporate from the source, making the total stoichiometry of the flux temperature-dependent. In the case of the IV-VI rocksalts, IV_1VI_1 is the most common molecule by more than an order of magnitude at the relevant temperatures. Reproduced from [44].

These trace biases in flux stoichiometry also eventually result in off-stoichiometry source charges. IV-VI materials have been grown via MBE using both elemental and molecular flux, but for this research, we utilized solid compound PbSe and SnSe sources. PbSe sources are known to become Pb-rich over time, as trace amounts of extra selenium are evaporated early in the growth campaign. The cell starts with a stoichiometric charge producing a selenium-rich flux, and transitions over time to a selenium-depleted charge producing a

lead-rich flux. With very careful control, such an off-stoichiometry cell can be supplemented with an elemental lead or selenium cell to grow a stoichiometric film.

Introduction to epitaxial growth

Epitaxy is the process of organizing atoms into a crystal structure, based on symmetry inherited from a crystalline substrate. In MBE, the effusion cells deliver precursor molecules to the growing surface, but the placement of those atoms in the solid structure is a function of the thermodynamics and kinetics of the free surface. The conceptually simplest crystal growth, where an existing crystal structure is simply extended in space by adding atoms, is known as homoepitaxy – growing a gallium arsenide film on a gallium arsenide substrate is a common example in MBE. The Fm-3m symmetry and basis of the GaAs crystal is applied to the incident gallium and arsenic atoms via interatomic forces: nearest and next-nearest neighbor interactions. Each atom landing on a growing GaAs surface is guided into place by the atoms of the previous layer, then its dangling bonds attract more adatoms for the next layer, and so-on. In general, once source atoms land on the free surface, they can migrate reasonably long distances before finding a stable resting place and becoming part of the solid crystal. Figure 2.4 shows a common simplification of a growing crystal surface, with cubic atoms arranging themselves into smooth steps and terraces. One could imagine that with octahedrally coordinated cubic atoms, a lone adatom would have only a single bond to the substrate and would be relatively easy to dislodge. An atom stuck to a step ledge

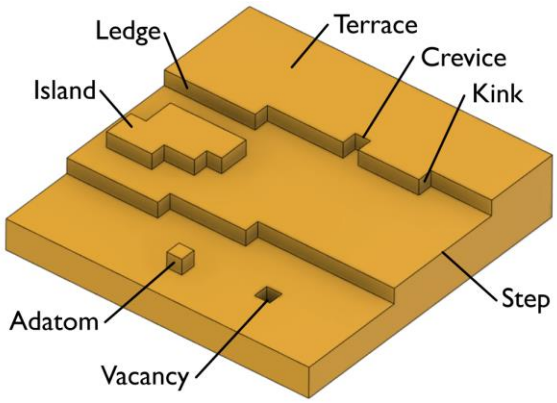

Figure 2.4 – **Classic diagram of epitaxy.** Octahedrally coordinated "cubic" atoms, with 6 bonding "surfaces" each, demonstrate preferential adatom incorporation at step edges and kinks. The number of "dangling bonds" on each adatom is inversely proportional to its stability on the crystalline surface.

would have 2/6 bonds filled, and be roughly twice as stable as a lone adatom. An atom stuck on the inside of a crevice could have 3-4 bonds fulfilled, and be extremely hard to free. At higher temperatures, where bonds are easier to break and individual adatoms can't bind to a free surface easily, so-called step-flow growth is common, where atoms migrate long distance to step edges where they can make multiple bonds to the substrate before becoming part of the crystal.

When adatom mobility is lower, due to properties of the surface or surface temperature, growth can instead occur via a "layer-by-layer" growth mode, where roving adatoms on the crystal's surface collide, stochastically forming stable nuclei that become their own terrace, growing outwards via limited step-flow in all directions. In these cases, it's possible for one complete monolayer of atoms to be deposited and filled in before the next layer starts.

Surface reconstructions and RHEED analysis

Although mathematically, a crystal continues periodically in all dimensions indefinitely, during growth of a real crystal, surfaces need to be considered, and the energetically favorable conformation for atoms near the surface of a crystal need not be the same as the bulk unit cell. Dangling bonds can link together, creating a dimerized surface, atomic rearrangements may take place 2-3 ML beneath the surface, and lone adatoms that are weakly bonded can find a new position or desorb from the crystal entirely; these are all examples of surface *reconstructions*, where the nominal structure of the crystal is different at the surface. Additionally, surface *relaxation* is the process by which atoms without full coordination at the surface may move slightly, shifting within the unit cell to extend some bonds and shorten others without altering the nominal structure of the crystal. Surface relaxation only involves straining of a unit cell, while surface reconstructions require entirely different surface atomic arrangements (bonding).

From a thermodynamics perspective, surface reconstructions decrease the energetic cost for truncating a crystal. Free surfaces, and their associated dangling bonds, are energetically

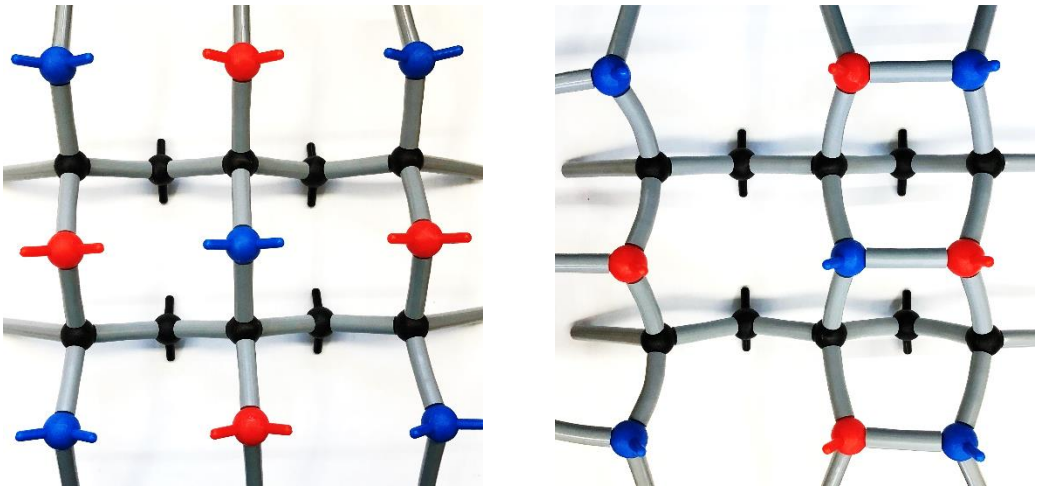

Figure 2.5 – **Model of a simple 1×2 dimer structure.**
(left) a perfectly truncated (001) surface, with a rectangular unit cell and two dangling bonds per surface atom. The red and blue atoms outline the top face of the conventional FCC unit cell (red: corners, blue: face center). (right) the dimerized structure, with only one dangling bond per surface atom, but a larger surface unit cell: a rectangle as wide as the original unit cell and twice as long.

expensive, and therefore unstable. The silicon diamond cubic structure, perfectly truncated on an (001) plane (Figure 2.5), has 2 atoms per conventional unit cell exposed, forming a square grid rotated 45° to the conventional cell. Each of these surface atoms naturally has two dangling bonds upwards to the next layer of Si, but in the case of a truncated crystal, they fold in and bind to each other, each pair forming a surface dimer. This is probably the simplest example of a crystalline surface reconstruction. Although these dimerized atoms have unfavorable bond lengths and angles, and need to rearrange for the crystal to grow, this configuration eliminates one dangling bond per surface atom, a significant energy savings. The surface unit cell also gets larger during this process. The formerly square surface unit cell is now a rectangle, as wide as the original periodic cell, but twice as long. Because periodicity is simple to characterize using in-situ techniques like RHEED, surface reconstructions are frequently referred to by the decrease in symmetry they induce (the size of the unit cell). This simple dimer structure is then a 1×2 reconstruction. Not all reconstructions with the same periodicity necessarily have the same atomic

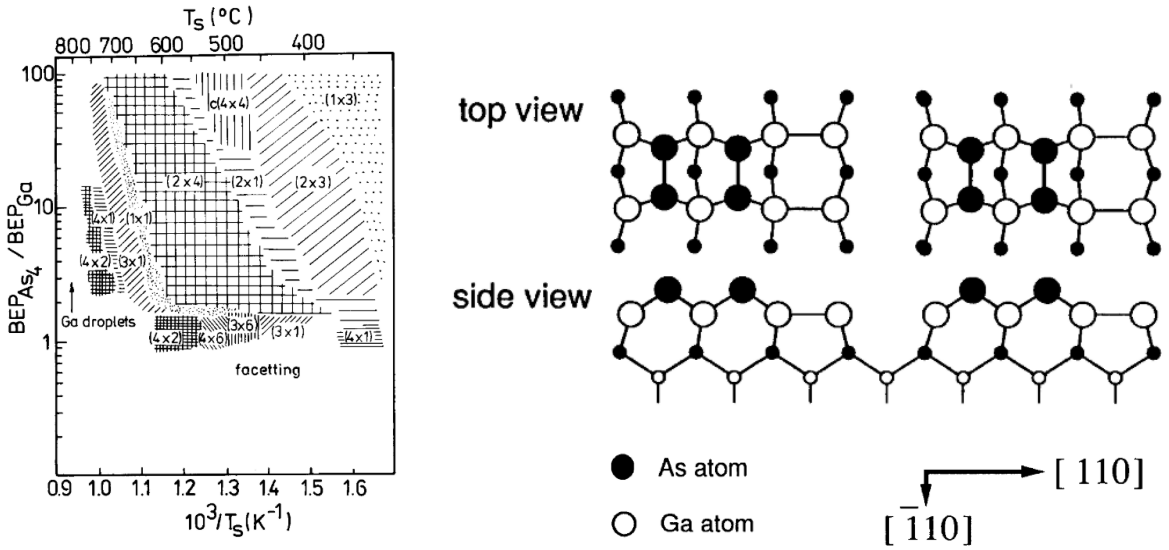

Figure 2.6 – **Reconstruction mapping in GaAs.**
(left) periodicy-based phase diagram of changing GaAs reconstructions with respect to substrate temperature and incident flux[192] (right) α2×4 reconstruction on GaAs (001) determined by kinematic RHEED[193] and STM[194]. Reproduced from [192] and [194].

arrangement, but for most materials systems, the phase space of possible surface reconstructions has been mapped, and periodicity, along with chamber conditions and sample history, are sufficient to determine the reconstruction precisely.

Most surface reconstructions are determined using simulation and high resolution STM, and the III-V zincblende materials have some of the most well-characterized surface reconstruction phase spaces of any materials system. At a particular temperature and particular incident flux (typically group V flux for the III-V materials), the equilibrium surface reconstruction changes based on the kinetic freedom for individual bonds and dimers to break, and the availability of certain species. Figure 2.6 shows a phase diagram for an offcut GaAs (001) surface, and an example of the actual atomic structure of one particular phase. In the example shown, there is not enough arsenic to complete the surface, and the free atoms on the surface dimerize to produce a more stable bonding arrangement.

As a high vacuum technique, MBE has access to *in-situ* electron diffractometry to analyze surfaces during growth. RHEED, or Reflection High Energy Electron Diffraction, is the primary method for examining surface reconstructions, and is an important tool in MBE growth used to determine sample quality, diagnose specific defects as they form, and calibrate certain growth procedures like temperature and growth rate. During growth, an electron beam, typically 10-15 kV, is directed towards the sample at an extremely glancing angle, less than 10° incidence. This beam diffracts from the surface at a similarly shallow angle and produces a pattern on a phosphor screen opposite the electron gun (Figure 2.7). Reciprocal space will be discussed in more detail in the next section on x-ray diffraction, but essentially, using the construction from Figure 2.16, everywhere that the Ewald Sphere intersects with a reciprocal space point will cause a visible spot to be projected on the screen. Because of the extremely shallow incidence angle, the electron beam only interacts with the first few monolayers of atoms, and because the crystal causing diffraction

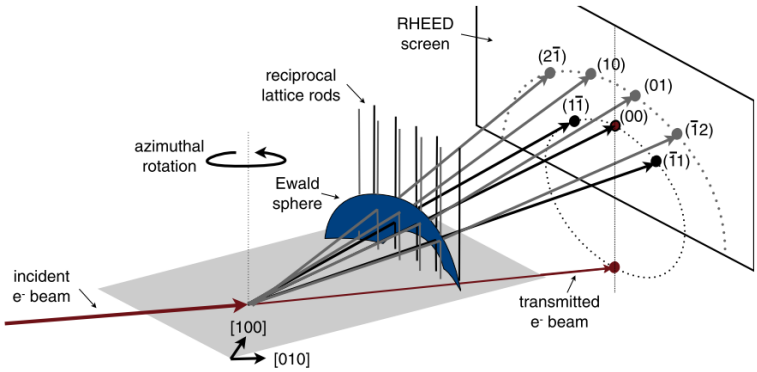

Figure 2.7 – **Mechanism of RHEED image formation.**
An incident electron beam diffracts from the sample and produces a spot pattern on a distant screen. This construction relies on the intersection between the reciprocal space points that represent the crystal and the Ewald sphere, which represents the imaging condition. Neither of these features is an idealized mathematical object, so realistically, the pattern observed is the intersection between a thick-shelled sphere and reciprocal space points or reciprocal space rods of finite radius. The thinner the interaction volume of the beam with the crystal, the more reciprocal space points elongate into reciprocal space rods, "relrods". Reproduced from [195].

is then effectively extremely thin, reciprocal space points are stretched out vertically, forming reciprocal space rods, or "relrods". These relrods intersect with the Ewald sphere over a wide area and produce streaks on the phosphor screen.

First and foremost, RHEED patterns are a diffractive technique, so they provide information about the periodicity of the lattice. Surface reconstructions are referred to by their periodicity (See Figure 2.6), because this parameter is so easy to measure. Figure 2.8a shows a series of RHEED images exhibiting different periodicity. In each of these cases, the lattice parameter of the underlying FCC crystal is similar, but the periodicity of the reconstruction is different. The 4× reconstruction has a much closer fringe spacing then the unreconstructed 1× surface. All of these images also show extremely flat surfaces (the 4× is smoothest and the 2× is roughest, but only slightly). Figure 2.8b provides examples of RHEED patterns from surfaces with widely varying morphology and roughness. On the left, two populations of grains exist on the surface, resulting in two superimposed RHEED patterns: one population of grains is smooth, resulting in 2D diffraction, 2D relrods, and a streaky pattern projected onto the screen. The other population of grains is rough, and as the electron beam interacts with multiple layers of atoms, the 2D array of reciprocal space rods becomes a 3D array of reciprocal space points, and a set of crystallographic spots is projected onto the screen. In this case, the pattern projected is a portion of the [110] zone axis of rocksalt. Figure 2.8c shows schematically how multiple layers of atoms are involved when a glancing incidence electron beam interacts with a very rough surface. The rightmost image of Figure 2.8b shows a more complicated case, where a rough surface actually exhibits flat, crystallographic faceting. In this situation, the 3D diffraction spots formed by these features have angled streaks emanating from them, perpendicular to the angle of the facets, formed by a similar construction as the original relrods, except now there are multiple flat surfaces pointing in different directions. These are coined "chevroned" RHEED patterns, and typically indicate a

severely defective growth. Faceted rough surfaces are very difficult to recover with continued deposition.

Because RHEED can differentiate between rough and smooth surfaces, minute variation in RHEED intensity can be used to calibrate the growth rate of a material in MBE. At high

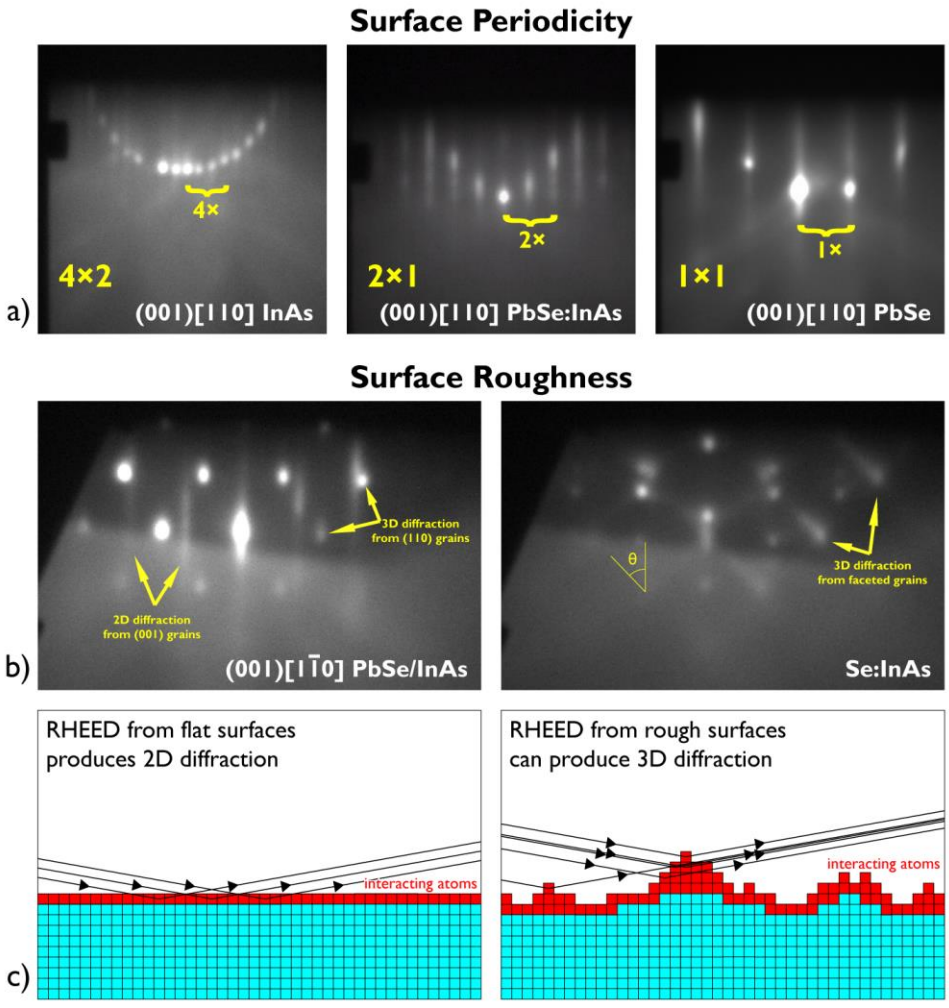

Figure 2.8 – **Example RHEED patterns with structural interpretations.** (a) series of images showing a change in periodicity among surfaces with similar lattice constants, but different reconstruction periodicity. The largest surface unit cell (4×) has the most closely spaced fringes. All of these surfaces are very smooth, exhibiting the "streaks" or "arc of spots" typical of smooth or extremely smooth surfaces. (b) RHEED patterns generated by rough surfaces, smooth surfaces, and faceted surfaces exhibit differently shaped diffraction spots. (c) Schematic demonstration of the mechanism for 3D diffraction. Rough surfaces allow a glancing electron beam to interact with multiple layers of atoms.

temperatures on an on-axis substrate with a low density of surface steps, materials which grow by the Frank-Van der Merwe growth mode can actually grow in discrete steps, where one entire 2D layer of atoms is deposited and coalesces into a smooth surface before the next layer begins forming. This growth mode depends on high adatom mobility and a significant preference for adatoms bonding to island edges and filling surface vacancies. During this process, the surface becomes alternately smooth (complete layer of atoms) and rough (partial layer of atoms). Although there is some nuance to interpreting these results, especially when considering miscut-induced surface steps and stochastic roughening, in general the (000) specular spot in RHEED will oscillate in brightness with the periodicity of layer deposition. This means that at a given cell temperature, the flux leaving the effusion cell, measured as beam-equivalent pressure by an ion gauge, can be calibrated to a known growth rate, measured in monolayers per second. If this calibration is repeated weekly or bi-weekly during a growth campaign, very accurate layer thicknesses can be achieved, important for optical or dislocation-filtering superlattices and devices such as lasers which require many precise layers. In our growth on the Riber system, we only recorded RHEED oscillations once, growing GaSb, to compare our temperature/flux/growth rate ratios vs. other systems at UCSB. In practice, RHEED oscillations have been observed on (111) IV-VI films[51,52], but we have not needed this level of precision, and have not attempted the measurement in the (001) or (111) orientation. As a technical note, On the Riber system, vibration from the cryopump compressor will vibrate the RHEED system and alter the signal, so to measure RHEED oscillations accurately, the compressor should be momentarily unplugged (20-30 seconds), and the cryopump temperature should be monitored to avoid a rise that would trigger the cryo gate interlock.

It is important to not rely on RHEED to produce a high quality surface. RHEED is an extremely valuable tool for determining how a surface has failed – characterizing relative

roughness, facet angle, the orientation of unwanted grains, etc., but RHEED can never confirm that a surface is high quality. When we began growing PbSe on InAs, the RHEED signal showed a 1x1 streaky pattern immediately after the onset of growth, implying a smooth surface with a layer-by layer Van der Merwe growth mode. However, halting growth at this moment and analyzing these truncated (10, 30, 60, 90, 120 second) growths in AFM and SEM showed that the surface was dominated by flat-topped islands – the streaky diffraction was from the island tops, and the relatively small area fraction that fell between the islands was hidden from the grower, although adding a significant number of defects to the samples. RHEED should always be used in conjunction with microscopy and x-ray diffraction experiments. It is most useful to confirm transitions between known states rather than characterize new states.

Temperature measurement

Temperature measurement in an MBE is extremely difficult. The UHV conditions mean that no convective heat transfer is possible, so we rely exclusively on conduction and radiation to heat and cool our materials. Also due to the load-lock vacuum requirements, samples need to be mounted to removable holders which rotate in the system, preventing solid mounting of a thermocouple probe to a sample, the most reliable way of measuring temperature outside of an MBE. This non-contact criterion points towards optical methods like pyrometry, but even optical methods come with distinct challenges. The following will be a cursory overview of temperature measurement in the Riber system. Fortunately, although nucleation of PbSe on III-V substrates does have a growth window, the range of temperatures for good growth appears to be 20-25 °C wide, so ultra-precise methods (or combinations of methods) that can achieve sub 5 °C error are not needed.

The stock Riber C21 system comes with a thermocouple to regulate the sample heater. Unfortunately, this thermocouple temperature does not adequately represent the sample

temperature, especially at relatively low temperatures. Figure 2.9 shows the layout of the sample heating system. The thermocouple is above the heater, which warms the back of the sample platen via radiative heating. This thermocouple is then, at best, measuring the temperature of the heater, not the sample. The back of the platen may be coated in a material that absorbs or reflects more heat, the quality of the indium bond between the sample and platen can vary significantly (20-30 °C) from growth to growth, and the sample itself has thickness, and the front may be heated rapidly from exposure to radiative heat from effusion cells. In order to know the temperature of the sample surface with precision and repeatability, if not accuracy, more complex techniques are required.

Figure 2.9 – **Heater and sample manipulator assembly**.
(J) main shutter, (H) Sample platen, sample facing down, (F) sample heater, (G) thermocouple. The thermocouple that measures sample temperature is actually above the heater, and measures a temperature related to the back of the sample platen, although physically far away. This is not an ideal temperature probe. Reproduced from the Riber C21 User Guide.

When first growing on the system, we used exclusively GaSb substrates, and used RHEED to calibrate the temperature of each growth. GaSb transforms from an antimony-poor 1×3 reconstruction (at high temperature and low antimony overpressure), to an antimony-rich 2×5 reconstruction (at low temperature and high antimony overpressure). For a given antimony flux, this transition occurs at an extremely

consistent temperature, so it was possible to expose the sample to a fixed amount of antimony and vary the sample temperature to observe a change from 3× to 5× reconstruction in RHEED. By repeating this process for multiple iterations, a highly repeatable sample temperature could be obtained. We then assumed local linearity with the thermocouple temperature and measured sample temperature as a thermocouple offset from the 3×/5× transition temperature. This technique was effective, but was not extensible to other substrates, and linearity of substrate temperature with thermocouple temperature did not hold far from calibration.

When we started working with InAs and GaAs substrates, we migrated to pyrometry. Optical pyrometry relies on blackbody radiation, and measures one or two specific wavelengths of infrared light. From the intensity of these wavelengths, a crude fit to a blackbody emission spectrum can be drawn, and a temperature can be determined. Pyrometry suffers from parasitic sources of infrared radiation and inconsistent sample emissivity. In some cases, even sample transparency to the relevant wavelengths. First and foremost, pyrometers should not be positioned such that specular reflection from the sample allows the pyrometer to receive infrared light from a hot effusion cell. Most pyrometers are mounted normal to the sample for this reason, but for ease of access, we have mounted our pyrometer at an angle, looking through an unused source flange. Critically, the opposing flange is also empty, so there is no cell positioned to shine infrared radiation directly into the pyrometer. The other important source of confounding infrared radiation in our system is a heated window. There is a heated glass pane inside vacuum in front of the pyrometer window to prevent deposition and gradual coating of said window. Less than an hour of antimony use within the system can turn an unheated window into an opaque mirror, so this modification is necessary. At low temperatures, however, the temperature measured by the pyrometer is likely influenced by the temperature of the heated window.

For consistency, we always measure the temperature of the substrate before deposition of

IV-VI material. Due to the infrared-transparency of III-V substrates, the actual pyrometer measurement is likely the temperature of the indium between the sample and the platen, but as soon as a narrow-gap IV-VI material is deposited, the measured sample temperature appears to drop. Likely because the IV-VI material absorbs infrared radiation before it exits the sample and reaches the pyrometer. For *accurate* temperature measurement, the pyrometer needs to be programmed with the real sample emissivity. In reality, a useful value of emissivity would account for sample composition, roughness, and reflectivity, and the infrared absorption of the UHV window(s) between the sample and the pyrometer. For *precise and repeatable* temperature measurement, all of these factors must be maintained identical from growth to growth. The extreme difficulty of measuring absolute temperature within an MBE system means that most reported temperatures in MBE literature are wrong, but relative temperatures from one growth to the next can be extremely precise.

Ultra high vacuum

MBE is an ultra-high vacuum (UHV) technique, meaning that the growth takes place below approximately 10^{-9} torr background pressure. In practice, our pressures were much lower, and a well-conditioned system can idle approaching 10^{-11} torr when not growing. The necessity of UHV for MBE comes in the problem of source material delivery and layer purity.

Vaporized species in UHV do not behave intuitively as a typical gas or fluid, but instead as isolated billiard-like particles whose behavior is dominated by collisions with solid surfaces. The mean free path of a particle in air at atmospheric pressure is less than 100 nm, so at ambient pressure, evaporated species can only travel tens of nanometers before scattering off of another gas molecule in the air and relying on diffusion for long distance transport rather than ballistic flight. In clean UHV systems, though, the mean free path can be on the order of kilometers, meaning that interactions between gaseous particles do not occur. Individual particles fly in nearly-

straight line ballistic trajectories from one surface to the next, parts of the internal equipment or chamber walls. With each collision, these particles interact with a surface, sometimes bouncing, and sometimes adsorbing. If the particle loses sufficient energy or lands on a chemically receptive surface, it can even become permanently trapped, and this is the foundation for many pumping systems.

Ballistic transport of species within a vacuum chamber makes precise material delivery possible. An effusion cell can be heated and the material within will evaporate at an inconsistent rate as the cell heats up, but because the evaporated material must travel in straight line trajectories, all of the cell's output can easily be blocked with a mechanical shutter. Without diffusion, there is no way for evaporated species to avoid impacting the shutter, and because the shutter will be at room temperature or below where the evaporated species is hundreds of °C, evaporated atoms are more likely to adhere to the back of the shutter than rebound towards the effusion cell.

A pressure of 1×10^{-6} torr corresponds to a growth rate of approximately one monolayer of atoms every second, assuming that every atom to collide with the surface adheres (known as a sticking coefficient of 1.0). This means that even with a low sticking coefficient, for high pressures, there will be many collisions of vapor molecules with solid surfaces, and many opportunities for foreign species to incorporate into the growing film, becoming point defect substitutionals or interstitials, more than likely degrading the electrical capabilities of the grown material. Crystalline purity depends on chamber cleanliness.

Achieving low pressures

Pumping of UHV systems requires a variety of techniques and technologies. There is no single pump that can remove the atmosphere from an MBE chamber and lower its pressure to UHV range. The requirements to pump large quantities of gas at high pressures are distinct from methods that excel at removing every trace of gas in a ballistic transport regime. In practice, two

or three stages of pumping are common, with many auxiliary pumps and procedures to remove certain contaminants like water.

Removal of large volumes of gas is done by a "rough pump" like a scroll, rotary vane, or diaphragm pump. The most prototypical mechanical displacement fluid pump is probably a cylindrical piston with input and output check valves at its base. On the instroke, fluid from one side is drawn into the piston, and on the outstroke, the same fluid is expelled through a different valve to the outlet. In achieving negative pressures, mechanical pumps are limited by the minimum volume of the pumping chamber during the expelling stroke. If a piston can expand from 1 mL to 1000 mL of volume, then it can, at most, achieve a vacuum of 1/1000 of an atmosphere. To expel gas during the outstroke, a pump must have an internal pressure of one atmosphere or more, so if the pump contains 1 mL of gas at one atmosphere and then expands by 1000×, the internal pressure will equivalently drop by a factor of 1000. Because the pump cannot draw in new gas from the vacuum chamber without an internal pressure *lower* than that of the chamber, the minimum achievable pressure is $1/1000^{th}$ of an atmosphere.

Diaphragm pumps like the one on our Riber system achieve low pressures through mechanical displacement, replacing the prototypical piston with a flexible diaphragm that can be pressed against the internal chamber walls until the internal volume of the chamber becomes vanishingly small. Rotary vane pumps and scroll pumps also achieve extreme ratios, but by pressing carefully machined components against each other, in both cases, metal parts tipped with elastomer seals which occasionally need to be cleaned and replaced. These pumps can rapidly ingest gasses at atmospheric pressure and expel those gasses into atmospheric pressure. Although they can typically only achieve minimum pressures in the millitorr range after long periods, they are the first line of defense necessary for maintaining a UHV system.

Rough pumps are frequently used as "backing pumps" for other high-vacuum pumps which cannot expel gas at atmospheric pressure. In Figure 2.10a, the scroll pump and diaphragm pump are connected to the chamber only through a turbomolecular pump – a mechanical pump will evacuate the chamber through the intermediary turbopump, simultaneously reducing the outlet pressure of the turbopump until it can be spun up without air resistance.

Turbomolecular pumps, known simply as turbopumps, are capable of achieving high vacuum, but do not exhaust at atmospheric pressure. They rely on many layers of turbine blades which spin at tens of thousands of RPM, with linear speeds roughly equal to the speed of the particles of gas it is pumping. Unlike a turbine or centrifugal pump at atmospheric pressure that relies on fluid mechanics, a turbomolecular pump catches individual molecules of gas as they enter the turbine, and by repeatedly impacting those molecules with tilted blades, imparts momentum that pushes them from one end of the pump to the other. If the exhaust of this pump reaches high pressures (order of 1-10 torr), the pump begins to feel a load from air resistance, and prolonged run at high pressures can put excessive wear on the pump bearings and lead to

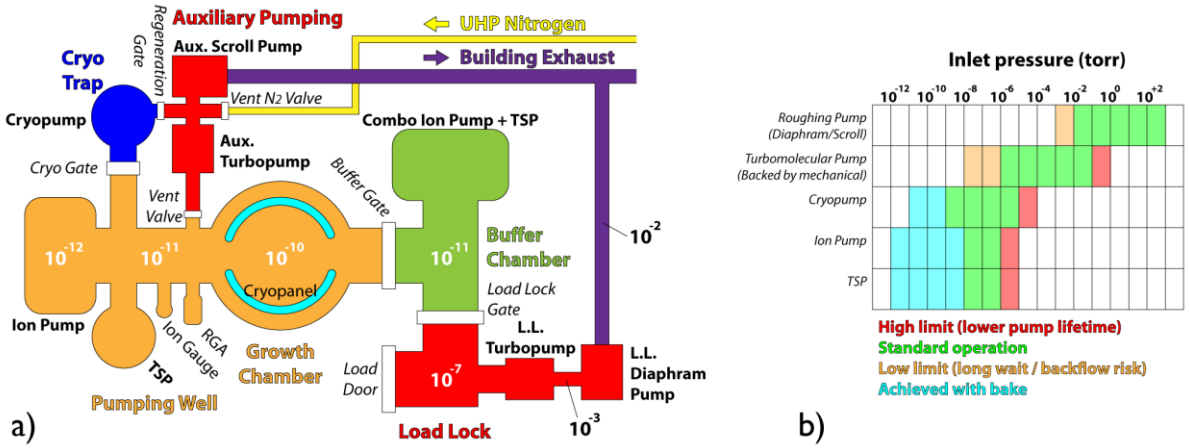

Figure 2.10 – **Pumping diagram for the Riber MBE.**
(a) map of the MBE pumping circuits with the auxiliary pumping station connected as if for a system opening. Gauges in the buffer and load lock have been omitted. (b) Chart of pumping limits for various pumps. Taking a system from atmosphere to deep UHV requires at least three pumps and a gate valve.

premature pump failure. Turbomolecular pumps are designed to operate at 20-30 krpm continuously for years, so engineering limits are important. Because turbomolecular pumps exhaust to a higher pressure, they are susceptible to small amounts of backflow, so for achieving deep vacuum, a chamber will be evacuated with a turbopump and then that turbopump will be gated off and the chamber will be sealed at low pressure before one or more trap pumps are turned on to finish the pumping process.

Trap pumps have no exhaust – they trap all pumped gasses within surfaces and porous materials inside the vacuum chamber, away from sensitive equipment. The simplest example of a trap pump is a TSP, titanium sublimation pump, or "getter pump", which holds a small ingot of titanium inside a heated filament. When the filament turns on, the titanium heats up and is evaporated, depositing a thin layer of pure titanium on the interior of the chamber. This effectively turns the walls of the chamber into a single large pump, as O_2 and N_2 species that impact this fresh surface are likely to bind to the metal, forming TiO_2 and TiN, which have extremely low vapor pressures. Although no nitrogen or oxygen has actually been *removed* from the chamber after this reaction, it has been *trapped* in a non-volatile chemical, reducing the total amount of free gas species. This is an important limitation of trap pumps – if asked to pump too large a volume of gas, they can become saturated, and stop pumping. For this reason, trap pumps are only used when the pressure in a chamber is already very low, once there is very little gas left to capture (Figure 2.10b).

In UHV conditions where diffusion and gas-gas interactions are nonexistent, the area and capture fraction of a pump are important metrics. For example, if every molecule of oxygen was captured by a titanium sublimation pump, the rate of oxygen capture increases linearly with the *area* coated by fresh titanium. This rule also holds for exhausting UHV pumps like turbomolecular pumps – the pumping rate scales linearly with the area of the front orifice. Systems with extreme

pumping requirements like MBEs which use gas sources, require very large tubopumps.

An ion pump is another form of trap pump, effectively an active version of the TSP. It uses an electromagnetic ion trap to charge incoming gas molecules, then accelerates them into a titanium target. The accelerated impact is more likely to trap gasses mechanically (by encasing them in metal) than a passive free titanium surface which only can trap chemically reactive gasses. The high energy impacts in the ion pump also have the side effect of occasionally sputtering titanium from the target, creating additional free titanium surface elsewhere in the pump that can trap chemically reactive species, reducing the load for accelerated mechanical trapping.

Cryopumps are the last type of trap pump we operate in the Riber MBE – they trap gaseous species by freezing them to a cold surface. Cryopumps absorb energy from free species, reducing their vapor pressure and accumulating molecules in a highly porous material like charcoal below 20 Kelvin. Unlike TSPs and ion pumps, cryopumps have very porous capture surfaces, meaning they can pump relatively large quantities of gas, allowing them to be turned on at higher pressures than most trap pumps. They can also be exhausted, although this is a cycling of the entire pump, so it can't be exhausted and continue to pump simultaneously. Exhausting a cryopump is known as "regeneration", and involves allowing a saturated cryopump to warm to ambient temperature while vaporized species are removed with a rough pump. In some cases, a cryopump can actually be heated during this process to vaporize as much adsorbed material as possible. The large pumping volume of a cryopump allows this process to be facilitated entirely with a rough pump like a scroll or diaphragm pump. When the roughing pump has fully evacuated the cryopump below 10^{-3} torr, the cryopump can be isolated and the cryopump temperature can be lowered from room temperature to 8-20 Kelvin using a compressed helium cryostat. Once the pump is cold, the gate separating it from the vacuum chamber can be opened, and it will begin capturing gas from the chamber in its cold porous getter material. Because any rise in temperature

of this pump results the release of gasses into the chamber, it is good practice to have the cryopump gate valve on an interlock – if the temperature of the pump rises above a specific threshold, the gate will close, preventing the warming pump from polluting the chamber with evaporating species.

One common vacuum pump that we don't use on the Riber MBE is a diffusion pump. The diffusion pump is based on a stream of hot low-vapor-pressure oil catching gas molecules in its flow. (The "diffusion" in "diffusion pump" implies that gas *cannot* diffuse against this oil flow. There is actually a continuous film of flowing oil separating ultra high vacuum from ~1mbar pressure. If this flow ever stops, or the sheet of oil is interrupted, then gas can backflow into the vacuum chamber. The same way that the blades in a turbopump impart momentum to individual molecules of gas via impact, any gasses from the vacuum chamber which impact the high-speed sheet of flowing oil will become ensnared, and flow to the oil reservoir at the base of the pump, where the captured air is removed by a rough pump and the oil is recycled to maintain the necessary continuous flow. Unlike turbopumps, diffusion pumps, backed only by a mechanical rough pump, can reach down to 10^{-10} torr. This phenomenal range of operation makes diffusion pumps unique. However, the necessity of maintaining the oil is a significant downside. Oil itself can backflow and contaminate the interior of the vacuum chamber, and the oil cannot be exposed to air without rapidly degrading, so a rough pump failure can simultaneously cause a diffusion pump failure and a dirty system vent.

Despite these challenges, diffusion pumps are able to maintain very high vacuum using mechanical force alone (no chemical reactions necessary) and so pumps all gaseous species effectively, meaning that certain contaminants difficult for other pumps to capture can be removed by a diffusion pump. In the extreme cases where such a system would be necessary (ie. high mobility growth), the diffusion pump can actually be situated behind some type of cryo trap to

eliminate backflowing oil into the main chamber.

Riber pumping sequence

To achieve a quality ultra high vacuum in our MBE, starting from atmospheric pressure, a weeks-long procedure is necessary. This section will refer to components in the vacuum plumbing map and pump sequence chart from Figure 2.10. Although the pumping configuration after the move may be different, for the past years, a portable auxiliary pumping station has been used to assist with system openings. In an ideal case, the system was vented with ultra high purity nitrogen, and that nitrogen flow was maintained to keep positive pressure in the chamber during service. This discourages inflow through open flanges and reduces the amount of water and other gasses that enter the chamber through removed cells, viewports, or other mechanisms. The auxiliary pumping system included a roughing scroll pump and a small turbopump, and could be connected to the system using flexible stainless steel line through the vent port.

When the chamber needs to be evacuated, the scroll pump removes the vast majority of the air in the system, and once the system pressure has dropped into the millibar range, the turbopump can be turned on to begin heading towards UHV. This should drop the system pressure into the 10^{-7}-10^{-8} torr range, but the gate to the cryopump can be safely opened once below 10^{-4} torr. The significant pumping volume of the cryopump will rapidly decrease the chamber pressure by an order of magnitude, and at this point, backflow through the turbopump becomes a factor, so the vent valve can be closed, isolating the system with its three trap pumps. We typically turn on the ion pump once the system reaches 10^{-6} torr, and the TSP is not re-sublimated until much later in the process.

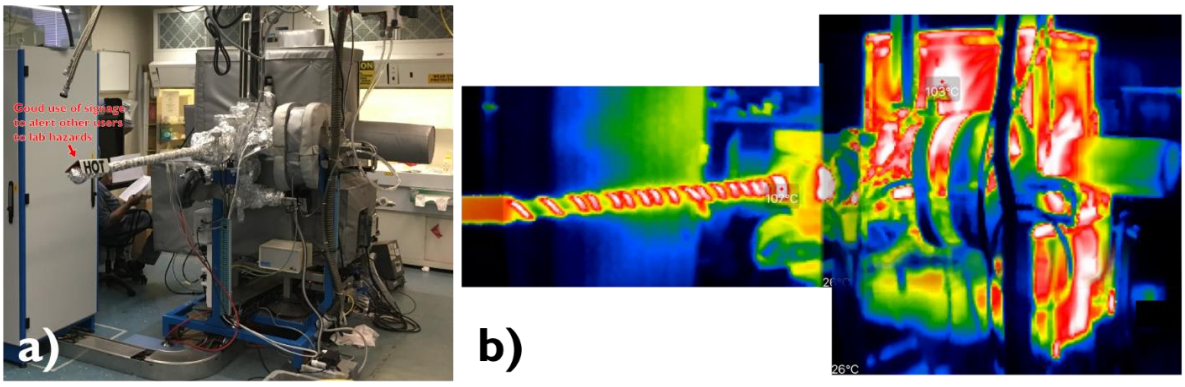

Figure 2.11 – **MBE System "on bake".**
(a), optical, and (b), thermal. These pictures were taken after the initial installation of the system, so both the buffer chamber and the main chamber are being baked – normally only the main chamber is vented so only the main chamber needs to be baked. This bakeout was also before the installation of the cryopump, so ion pumps were doing the bulk of pumpdown.

One of the most significant hindrances to achieving ultra high vacuum is adsorbed water vapor. Water in a chamber can be identified as a series of isotopic peaks, with the most prominent at 18, for H_2O^{16}. If a chamber is ever exposed to wet air, all of the interior stainless steel surfaces become coated with adsorbed water. After the system is pumped down to high vacuum, this water very slowly desorbs and is pumped away, but this process takes an extremely long time at ambient temperatures, and most systems contain a not-insignificant amount of water, even after careful management of open flanges during service. To remove this water, the entire system must be baked at a high temperature (Figure 2.11). All heat-sensitive components (magnets, motors, plastic, etc.) are removed, and a box of thermal insulation is assembled around the chamber with built-in heaters. Portions of the system outside this box are wrapped with heater tape and aluminum foil for insulation. In addition to external heating, Sample manipulators and effusion cells are ramped up inside the system within uncooled limits. During a bake, the goal is to remove adsorbed species, but these species will re-accumulate in the coldest part of the system, so keeping the effusion cells hot (and the source material contaminant free) is critical to a successful bake.

After the system has been pumped down at high temperature for 4-10 days, the system

can be cooled down and the pressure drops rapidly. Water that would have taken months or years to pump from the system can be eliminated by a 1-2 week bake, and with those high-vapor-pressure species gone, the chamber is much cleaner. All of the pumps can be enabled; the TSP can be re-sublimated, and the cryopanel can have liquid nitrogen flow through it, which acts as a sort of cryopump inside the main chamber, enhancing the capture of species evaporated from effusion cells and the sample surface.

III. X-ray DIFFRACTION

Introduction

X-ray diffraction is an extremely valuable technique allowing for cheap and rapid evaluation of the crystalline quality of a sample with no sample preparation. In x-ray diffraction, an x-ray source (typically a high power electron beam incident on a water-cooled copper target) is fed through a monochromator to isolate a particular wavelength (Typically $Cu_{k\alpha}$ at 1.54 Å), and then this monochromated beam is incident on the sample in question. These x-rays are reflected from the sample at angles dependent on the material's crystallinity and detected by a scintillator or solid state x-ray detector. The x-ray source, sample, and detector are all held at exact angles to each other by a sophisticated goniometer with typical angular precision on the order of 0.001°.

Individual atoms within a material act as scattering centers for the x-ray photons, but atoms arranged into ordered planes, like those found in a crystalline material, can collectively reflect x-rays – every planar array of atoms can act as a mirror for x-rays given the right condition. The variety of planes found in any given crystal structure produce many simultaneous diffracted beams based on Bragg's law. By examining the position, shape, and size of these diffraction spots with a mobile detector, the material's mosaicity, orientation, defect density, thickness, and strain state, can be determined.

Bragg's Law

Bragg's law is the foundation of x-ray diffraction, predicting the angles where diffraction spots will appear in angle-space so they can be detected and measured. Figure 2.12 shows the geometry of Bragg's law. A beam of monochromatic x-rays are incident on a crystalline sample, reflecting from a particular crystal plane at an angle θ. Because the incident beam is collimated, and the crystal planes are parallel, the outgoing x-ray photons are always parallel, having turned by an angle 2θ. However, the crystal is a 3D material, and separate parallel planes of atoms occur at regular intervals, so there are many planes any given x-ray photon could reflect from. In this case, two parallel planes of atoms are separated by a distance d. In order to produce a strong reflection, the reflected x-rays from all layers of the crystal must constructively interfere as they leave the sample, so we need to compute the additional path length traversed by the x-rays reaching every subsequent layer, 2d*sin(θ), and ensure that that additional path length is an integer multiple of the x-ray wavelength, nλ.

The full statement of Bragg's law, 2d*sin(θ)=nλ, is actually quite a simple expression. d is the interplanar spacing between the crystal planes producing the reflection; θ is the angle of incidence of the beam on the crystal planes – it's worth noting that these crystal planes are rarely aligned with the surface of a sample, and physical sample tilt is described with a different angle ω in the next section. The full scattering angle 2θ is unambiguously measured in practice via

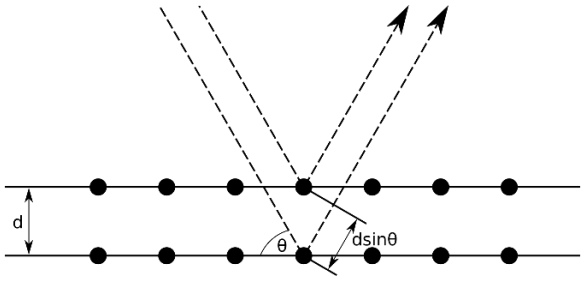

Figure 2.12 – **Bragg's Law geometry.** Two crystalline planes are shown, with incident x-rays reflecting from them both. The extra path length for the x-rays to reflect from the lower plane is 2d*sin(θ). For constructive interference, this extra path length must be an integer number of wavelengths. It's worth noting that real crystals are many layers thick, so even a close match in path length, spread over a large number of planes, will wash out to zero. The Bragg conditions for high quality 3D crystals are extremely narrow.

positioning of the source, sample, and detector; λ is the wavelength of the incident x-rays, typically 1.54 Å; and n is an integer – the order of the reflection, effectively the number of full wavelengths that separate the path lengths of photons reflecting from adjacent crystal planes. When this condition is fulfilled, strong reflections of x-rays from the crystal are observed, but even slight deviations from this condition will cause destructive interference from the multitude of crystal planes in any given sample, destroying the reflected intensity.

Strictly speaking, with perfectly monochromatic x-rays incident on a perfect crystal, the Bragg condition necessary to see a reflection would be infinitesimally small, and we would never expect to see x-rays reflected from a crystal, however none of these measurements is perfect. The incident x-rays have a distribution of wavelengths, the goniometer stage containing the x-ray source, detector, and sample is of finite size, as are the actual source and detector, meaning that a distribution of 2θ angles are being polled with each measurement, and most importantly, the crystal planes of the sample are imperfect and exhibit a distribution of widths and tilts. The actual "width" of the Bragg peak in angular space as you sweep the detector through different 2θ values, is a convolution of all three of these uncertainties. High-resolution x-ray diffractometry is based on a highly monochromated source and optimal geometry for angular measurement, so that any measured peak width should be dominated by the crystalline quality of the sample, but the following sections will bring up examples where specific usage or improper setup can result in measuring a peak limited by angular distribution or wavelength distribution instead of sample quality.

Reciprocal Space

Reciprocal space is a convenient geometric construction where diffraction spots in reciprocal space correspond to sets of planes that exist at various spacings and angles in a real crystal. The basis vectors of reciprocal space have units of length^{-1}, and the lattice of "diffraction

spots" which appear in reciprocal space constitute the Fourier transform of a real-space lattice representing a physical crystal structure. An example of this transformation is in Figure 2.13.

Although at first it feels arbitrary, reciprocal space is extremely convenient for X-ray diffraction measurements because it immediately contains all of the relevant information for a diffraction experiment. In order to detect a Bragg reflection from a particular set of crystal planes, you need to know d, the spacing between those planes, and the angle those planes make with another known direction. The reciprocal space point corresponding to those real space planes tells you both of those pieces of information.

If you imagine reciprocal space projected out from the crystal (Figure 2.14), a near-perfect crystal would create a near-perfect reciprocal lattice, with vanishingly sharp $\approx\delta^3$ lattice points, but real crystals contain defects like dislocations, grain boundaries, and stacking faults, which all

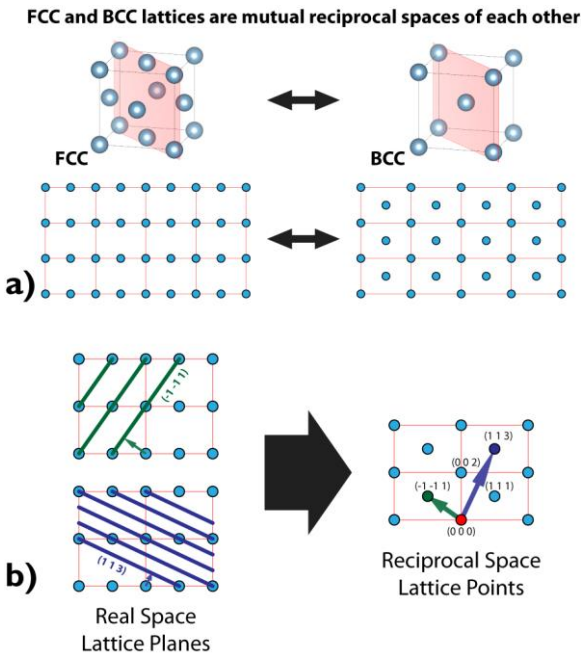

Figure 2.13 – **Reciprocal Space example with FCC and BCC Bravais lattices.** (a) FCC and BCC lattices are reciprocals of one another, meaning if you take the Fourier transform of either one, you get the other. This is convenient for materials scientists because these two highly symmetric lattices appear in many real space crystals and are well-understood. (b) Real space and reciprocal space are graphically linked by the relationship between planes in a crystal. In this example, two sets of planes are indexed in a real-space FCC lattice, and they correspond to points in a BCC lattice. From the origin, the angle perpendicular to the plane is maintained, and the distance from the origin to the reciprocal space point is the inverse of the distance between the relevant real-space planes. Note the close spacing of the purple (113) planes in real space, but the long length of the vector to the (113) point in reciprocal space. Also notice that in this construction, vector addition continues to work in reciprocal space. All indexing remains self-consistent.

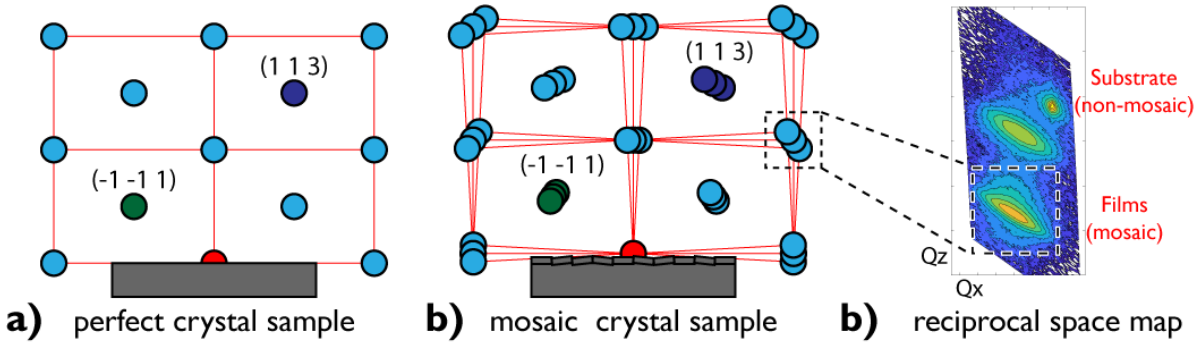

Figure 2.14 – **Reciprocal space and mosaicity.**
Reciprocal space projected from (a), a perfect crystal, and (b), a crystal with mosaicity. (c) shows a reciprocal space map collected using x-ray diffractometry to directly image reciprocal space points of a substrate with two films grown on it. X-rays can penetrate microns into most semiconductors, so it is possible to record data that is not only a spatial average across the surface of a film, but also an average in depth, across multiple layers of material. The top peak in this example is perfectly round and very sharp because it is a Bragg reflection from the substrate, a near-perfect crystal, while the lower two spots are Bragg reflections from mismatched films grown on that substrate, and they contain significant mosaicity, causing a smearing of the reciprocal space points.

induce a slight degree of local misorientation. This "noise" in the crystal structure is frequently depicted as nanoscale grains which are perfect, but mutually tilted, known as "mosaicity". Each localized mosaic element projects its own slightly tilted reciprocal space, and any x-ray measurement with a typical beam spot size on the order of hundreds of microns or even millimeters will necessarily be an average over many mosaic grains, so the once-sharp reciprocal space points will be smeared-out averages of many locally misoriented crystallites, and a strong Bragg reflection can be seen from a wide distribution of angles.

Scanning reciprocal space with x-ray diffraction

It's important to remember that reciprocal spots projected from a defective crystal are irregularly shaped 3-dimensional objects, and x-ray diffraction offers us a number of routes to probe the shapes of these spots and learn about our crystals. One of the most common XRD measurements is known as a 2θ-ω scan, because both the sample tilt ω and the detector angle 2θ

change in unison. Three examples of 2θ-ω scan geometries are depicted in Figure 2.15, a symmetric scan and two asymmetric scans. Notice that the third scan is an example of a forbidden reflection, and will produce no result. A 2θ-ω scan in terms of Bragg's law sweeps through a variety of interplanar spacings without changing the orientation of the sensitive plane – a symmetric scan is effectively taking a 1D sample through reciprocal space, along a straight line pointed away from

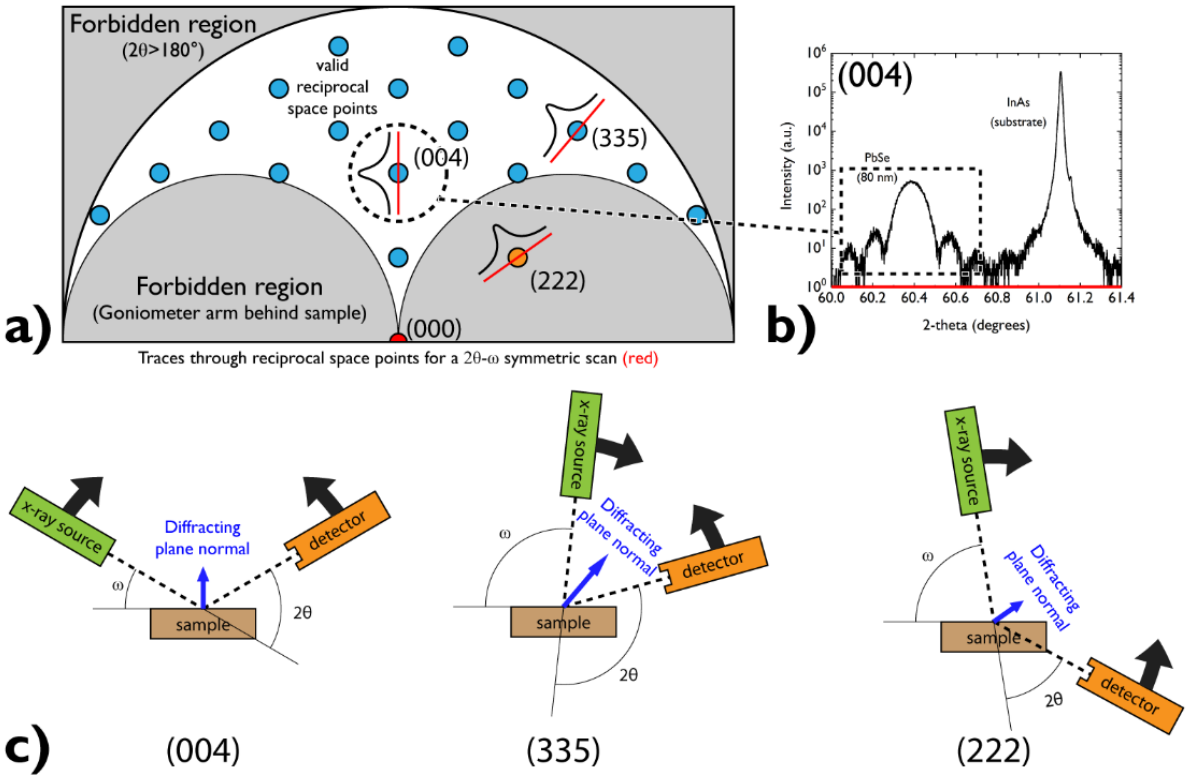

Figure 2.15 – **Probing different reciprocal space points.**
(a) 2D slice of reciprocal space for an (001)-oriented FCC crystal with a lattice parameter of 6.12 Å and an x-ray wavelength of 1.54 Å, with limiting circles shown. Outside the large circle, the relevant diffracting planes are spaced too closely to allow for Bragg diffraction, even with the source and detector normal to the surface. We also cannot access the reciprocal space points that fall inside the smaller circles, as those geometries necessitate one of the goniometer arms falling behind the sample, where the bulk of the sample and the sample stage absorb the diffracted beam. (b) an example of a symmetric 2θ-ω scan is shown (reproduced from Figure 6.10a). (c) Three examples of physical detector geometries are shown, with an on-axis symmetric scan of the (004) point, an off-axis 2θ-ω, and an off-axis 2θ-ω scan through the forbidden region, demonstrating the impossibility of the necessary detector placement.

the origin. These samples of reciprocal space are marked as red lines in Figure 2.15, and the sample geometry necessary to probe each reciprocal space point is shown. The width of this peak indicates a distribution of inconsistent interplanar spacings within a crystal. Rocking curves are XRD scans where the x-ray source and the detector arm remain fixed, selecting a particular interplanar spacing, and the sample is tilted through various conditions until the peak is found. As many samples have mosaic tilt which smears reciprocal space points laterally, rocking curves are a good method for directly measuring this mosaicity. Instead of the sample rotating through multiple tilts, it's also valid to imagine the source and detector arms moving in unison around the sample, looking for the same crystalline plane which may appear at different angles. In Figure 2.16, ω scans trace the magenta lines through reciprocal space, curving about the origin. Such a scan can only measure the tilt of the sample in one direction, but for many films grown on substrates with low rotational symmetry, spinning the entire sample by 60° or 90° and repeating the measurement may yield a

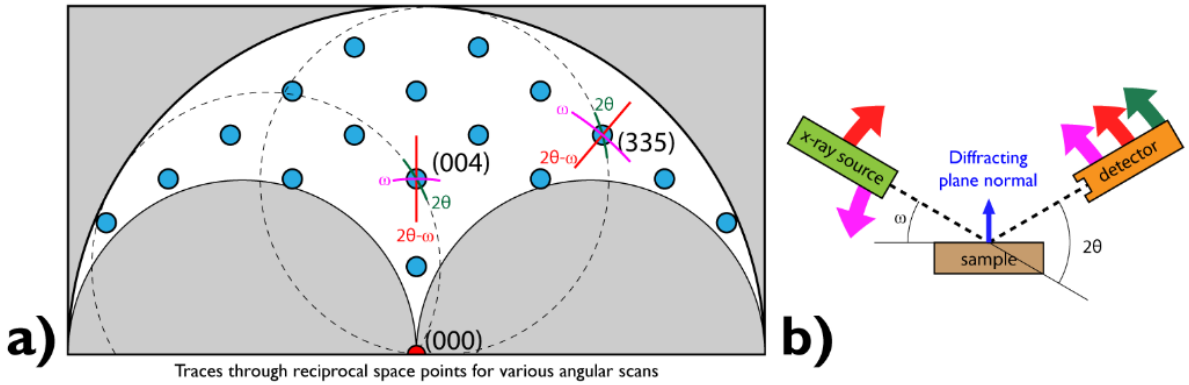

Figure 2.16 – **Scanning through reciprocal space in different directions.** (a) shows a map of reciprocal space, with three different types of scans highlighted through two different reciprocal space points. 2θ-ω scans measure a distribution of interplanar spacings; ω scans measure sample tilt mosaicity at a fixed interplanar spacing; and 2θ scans, take an oblique cut through reciprocal space. (b) shows the detector motion geometry for each scan: 2θ-ω scans require symmetric motion of both detector and x-ray source; ω scans require simultaneous motion of both source and detector with respect to the sample – in practice, the detector arm is fixed and the sample is rotated through the relevant condition; 2θ scans only require motion of the detector arm.

more complete picture of the relevant reciprocal space point. 2θ scans are less common, but sometimes are used for alignment, and are important to consider for reciprocal space mapping with a 1D pixelated detector. In a 2θ scan, the sample and the x-ray source remain fixed while the detector arm moves back and forth, sweeping through reciprocal space diagonal to both the 2θ-ω scan and the ω scan. The exact direction in reciprocal space taken by a 2θ scan is determined by the Ewald Sphere construction, shown as a dotted line in Figure 2.16, with the 2θ scans shown in green. For planes with very narrow interplanar spacing (far from the origin in reciprocal space) 2θ scans closely resemble ω scans, while for very wide planes, close to the origin in reciprocal space, 2θ scans more closely resemble a 2θ-ω scan. Because the 2θ scan does not isolate either angle or interplanar spacing, it is less useful as a lone scan, although the ease of acquisition (ie. only requiring motion of a single arm) lends itself to multi-scan measurements.

Some XRD systems have 1D detectors with a pixel array on the detector arm, effectively allowing for the instantaneous capture of a short 2θ scan by reading the x-ray intensity from each pixel instead of physically moving the arm through space. Such a pixel array typically doesn't have the resolution of a high quality scan with a moving analyzer, but with this speed, many scans can be taken in a short period of time. Specifically, if 2θ scans are taken at a variety of ω tilts, a 2D slice of reciprocal space can be imaged, known as a reciprocal space map (RSM) (Figure 2.17). After the relevant transformations, this technique yields an actual image of reciprocal space, and allows for analysis of a reciprocal space point, detecting irregularities in tilt (ω) and spacing (2θ-ω), and more importantly, visualize the relative positions of reciprocal space points from multiple strained layers in a film.

The RSM pictured in Figure 2.17 was recorded on a sample with three discrete layers, all of which have their own composition, crystal structure, and strain state. In an RSM, a lateral (Qx) offset of a peak from its expected position indicates in-plane strain, and a vertical (Qz) offset

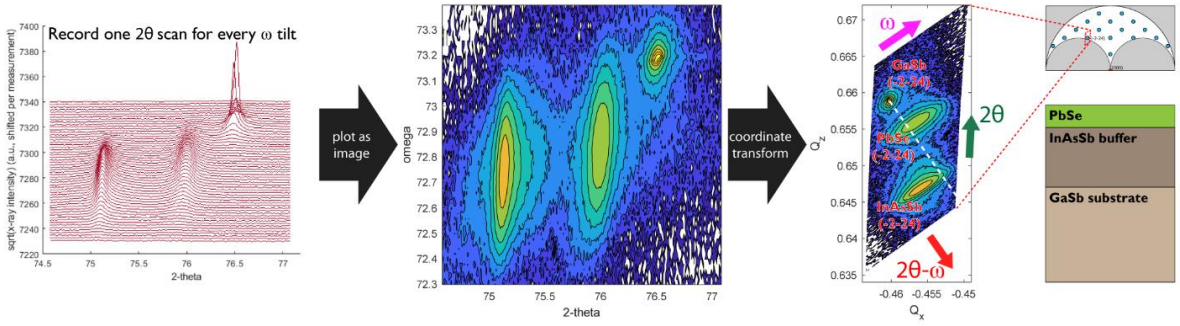

Figure 2.17 – **Reciprocal Space Mapping.**
A series of 2θ scans are recorded using a 1D pixel detector, and in between scans, the sample is tilted by a fraction of a degree, so the 2D dataset spans both 2θ and ω. These traces are combined and transformed into reciprocal space coordinates so that the reciprocal space spots corresponding to the $(\bar{2}\bar{2}4)$ planes in the sample can be fully visualized. In this case, spots from a GaSb substrate and two film layers can be seen (Sample structure on far right). The InAsSb buffer and the PbSe layer have significant mosaicity, and their reciprocal space points are smeared out in the ω direction. A standard 1D ω scan would represent an angled cut through one of these spots along the stretched direction.

indicates out-of-plane strain. For a sample which consists exclusively of fully relaxed cubic layers with different lattice parameters, we would expect all of the $(\bar{2}\bar{2}4)$ reciprocal space points to fall on the same line, tracing back to the origin. This would imply that all the $(\bar{2}\bar{2}4)$ planes are parallel, but exhibit different interplanar spacings. However in this RSM, the dashed line drawn from the substrate towards the origin of reciprocal space does not intersect either of the film peaks, implying both are strained at room temperature. The GaSb peak is extremely intense and narrow, as a wafer of near-perfect single-crystalline GaSb was used as a substrate. A layer of InAsSb, a III-V material with a different lattice parameter, was grown on this substrate. If we draw a line from the center of the GaSb peak to the origin of reciprocal space (in the direction a 2θ-ω scan would sample), the InAsSb peak falls below this line, implying compressive in-plane strain. The PbSe layer grown on top of the InAsSb buffer lies almost directly above the InAsSb peak, indicating almost no in-plane relaxation between these two layers. The PbSe peak also lies above the line of relaxation, indicating in-plane tensile stress in that layer at room temperature. For 1D scans like rocking curves (ω scans)

and 2θ-ω scans, the most important measured parameter is typically the peak width, measured as the full width at half max (FWHM). If you take a rocking curve measurement, you want to know the distribution of tilted mosaic grains in your sample as a function of angle. The FWHM provides a quantitative metric to describe this spread in tilt angle. However, if the detector itself measures angles imperfectly, we could define a FWHM for the detector's sensitivity distribution. Likewise, we can define a distribution of wavelengths emitted from the x-ray source, not assuming the beam is perfectly monochromatic. The actual measurement made by the system is necessarily a convolution of all of these distributions, and if the actual material parameter doesn't have the largest spread, no scan will be able to measure it accurately. Any results will only effectively be measuring the equipment error. Figure 2.18a shows the effective "probe shape" of a typical diffractometer in reciprocal space. Visually, this shape is moved through reciprocal space for any given scan, and convoluted with the shape of the reciprocal space peak being measured. The angle ω is the incident angle of the x-ray radiation from the source. The physical tilt of the sample can be mechanically controlled to high precision, so the limiting factor on ω precision is spread of the incident beam. In both cases depicted, a 4-bounce monochromator is assumed, so the incident beam is extremely narrow and the spread in ω is small. A 4-bounce monochromator is a set of carefully positioned, structurally pristine silicon surfaces that the beam reflects from, only allowing one specific narrow reflection to exit the x-ray source. The angle 2θ is measured as the angle from the source to the sample to the detector, so beam spread after leaving the sample can be a limiting factor. It's possible to run most diffractometers in an "open detector" mode, where a wide range of 2θ values are accepted to increase signal, but this comes at the expense of 2θ precision. The effective probe gets thicker in the 2θ direction if an open detector geometry is used, and is narrow if extra optics before the detector are used to cut down the acceptance angles.

The last angle mentioned in this diagram, ϕ, is rotation about the sample normal (Figure

2.18c). For a sample with mosaic twist, as opposed to mosaic tilt, reciprocal space points could spread out in the ϕ direction. Unfortunately, typical diffractometers have extremely wide acceptance ranges in the ϕ direction, so a simple ϕ scan will only measure mosaic twist in the case of an exceptionally defective sample – the probe is almost always going to be wider than the signal. To address this, and measure mosaic twist with accuracy, the sample can be mounted in the "skew-symmetric" geometry, where the sample is rotated 90° in ϕ and canted sideways in the χ direction until the relevant reciprocal space point can be probed "sideways" with a regular ω scan. The last important example of artificial measurement broadening we will discuss here is glancing-angle measurements. One of the most common off-axis measurements we use for (001)-oriented PbSe films is the (224) peak, which is extremely close to the forbidden region where one probe would be behind the sample. That means that either the source or detector will be nearly parallel to the sample surface. As shown in Figure 2.18b, the physical area of the sample illuminated becomes an important variable. In a glancing exit geometry, a very small area of sample is illuminated, and an even narrower reflected beam is emitted, but in a glancing-incidence geometry, a very large area is

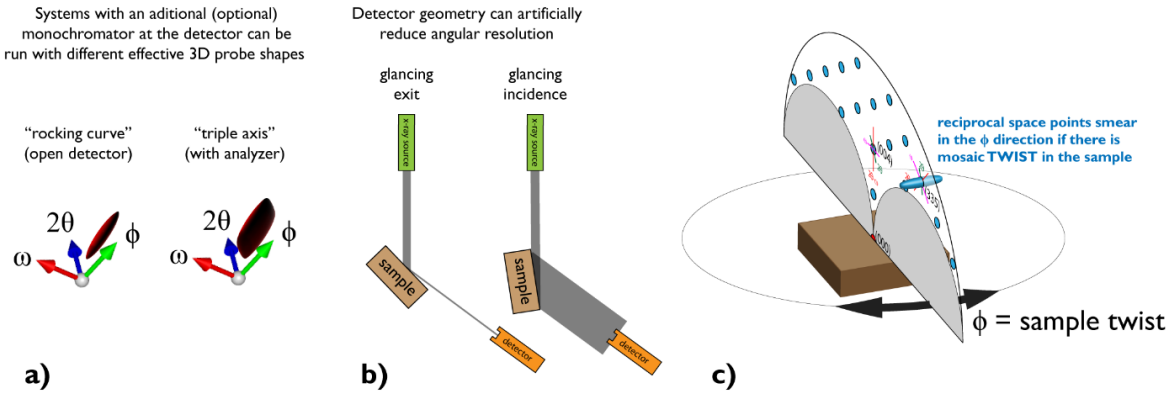

Figure 2.18 – **Probe "shape" in reciprocal space**.
(a) shows the 3d reciprocal space "probe" shape with respect to the ω, 2θ, and ϕ directions. (b) Glancing incidence vs glancing exit geometry, and their effect on beam detection. (c) position of the ϕ axis in 3D reciprocal space, with the effective probe shown in blue. As the probe extends wide horizontally, a simple ϕ scan does not accurately measure sample mosaic rotation.

illuminated, and an extremely wide beam is reflected from the sample. Although this wide beam is strictly parallel, and at very long distances, the spatial extent of the beam shouldn't matter to an angular measurement, diffractometer goniometers are finite in size, and such a wide spread in x-z space is interpreted as a wide distribution of reflection angles in angle-space. It's important to consider all these factors to minimize the probe size in reciprocal space, and scan through a reciprocal space point in the proper way to infer the desired material parameters.

IV. ELECTRON MICROSCOPY

Introduction

Electron microscopy is a very important class of characterization tools, allowing for analysis of surface morphology, chemistry, grain structure, sample thickness, interface atomic structure, and defect structure. In general, electron microscopy can reach higher resolutions than optical microscopy because the wavelength of 10-100 kV electrons is much smaller than the wavelength of optical or even ultraviolet light. However, the capabilities of electromagnetic lenses for electron focusing are relatively primitive when compared to the precision ground optics employed by modern light microscopes, and since electrons are charged, coulombic repulsion can also contribute to defocusing of a beam. Resolution in an electron microscope is currently limited by lens aberration rather than physical diffraction and resolution limits.

In any form of microscopy, it is important to visualize an image as the sum of many sources of contrast. The same way a greyscale image taken by a digital camera may be the element-by-element sum of the red, green, and blue channels, a backscatter scanning electron micrograph may be a single image made from many components. Z-contrast, topographical contrast, and channeling contrast may be convoluted, and separating these "original" channels is impossible. Proper interpretation of electron micrographs comes from identifying important features in the

image and understanding which contrast-forming mechanism is responsible for each. This process becomes challenging as these image-forming mechanisms become more overlapping and complex, so frequently, imaging conditions are designed to amplify only a particular type of contrast, like putting a colored filter over an optical camera.

On the other hand, with scanning techniques, images can be captured using multiple detectors simultaneously, and we find ourselves in the opposite situation. For example, taking an SEM image involves rastering an electron beam over an area and detecting radiation from the sample. If we simultaneously build an image using a backscatter detector and a secondary detector, we effectively have an image with two channels of data, but each of these channels, again, is made from a number of different contrast sources. Granted, with careful setup, each detector can be made to amplify a different contrast-forming mechanism, making critical feature identification easier when comparing data from multiple detectors.

Scanning Electron Microscopy

Scanning electron microscopy (SEM) is the most basic and most common electron microscopy technique. SEM can provide topographical, chemical, and orientational contrast on the surfaces of materials with little to no sample preparation. During scanning electron microscopy, a high-energy (1-30 keV) focused electron beam is incident on the sample. As these electrons interact inelastically with the sample surface, they donate some energy to the crystal, a fraction of which is emitted as so-called secondary electrons, which exit the sample surface with energies less than 50 eV. These secondary electrons can be collected with a positively charged detector, and the rate of secondary electron collection provides an analog of optical "reflectivity" or "brightness" for the exact site on the sample where the electron beam is positioned. By rastering the focused beam across the sample surface, this (now time-varying) secondary electron signal can be used to build up an image of the sample surface. Dwell times on each pixel are on the order of

hundreds of nanoseconds to tens of microseconds, so high resolution images can be assembled quite quickly. Secondary electron emission provides largely topographical contrast based on the geometry of the sample surface and the position of the SE detector. The most common secondary electron detector is an Everheart-Thornley detector (Figure 2.19a), which attracts secondary electrons with a wire mesh held at a low positive voltage (200-300 V), and then accelerating the captured secondary electrons into a scintillator with a much higher potential, in the kilovolt range. Because secondary electrons emitted from a sample surface are relatively low-energy, this initial 300 V potential is sufficient to capture a large fraction of all the secondary electrons detected – even if they leave the sample headed away from the detector. However, concave regions of the sample, and undulating regions where emitted secondary electrons may re-impact the sample surface can affect the signal received. When reconstructed into an image, these effects appear similar to shadows cast over a rough surface by light. However, secondary electrons are only the

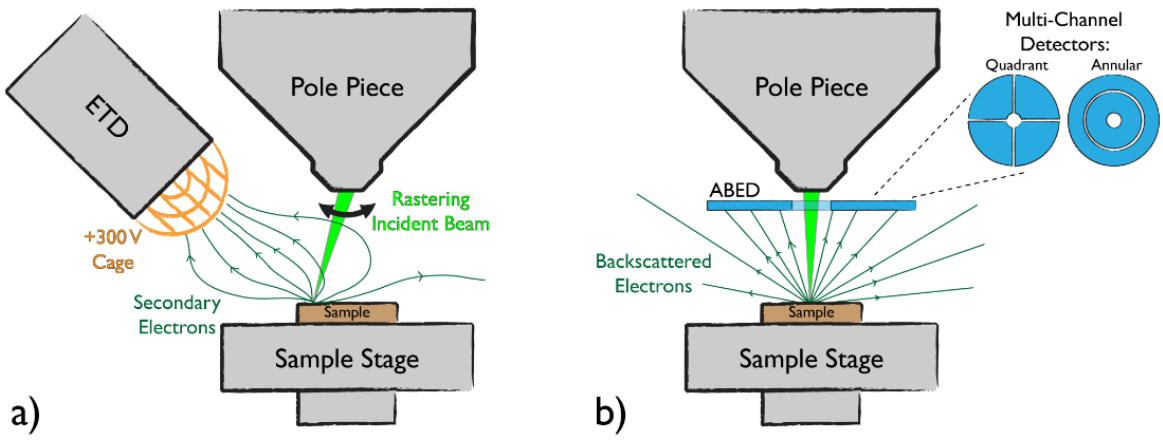

Figure 2.19 – **Scanning electron microscopy: standard detector geometries.** (a) an Everheart Thornley Detector uses a static charge to attract low energy secondary electrons for detection. (b) backscattered electrons are too energetic to be attracted with a small potential, so a solid state annular backscattered electron detector is placed above the sample, in the path of the backscattered electrons. Segmented backscatter detectors can be used to reconstruct images from multiple signals: quadrant detectors, for example, can give extreme topographical contrast if an image is created by subtracting the left quadrants' signal from the right quadrants' signal.

most common source of contrast in an SEM. When a high energy electron beam is incident on a sample, the energy of that beam is reemitted as secondary electrons, backscattered electrons, optical radiation, and x-ray radiation, all of which can be measured with the correct detectors as a source of "contrast", allowing microscopists to map changes in many different material parameters over the width of a raster scan. Even sharper topographical contrast, and chemical Z-contrast on flat surfaces, can be provided by backscattered electrons. When an incident electron is scattered elastically by a nucleus in the sample, it can be re-ejected from the sample surface still with significant energy, in the range of keV. These electrons are moving much too fast to be attracted by the +300 V potential of an ETD, so they are frequently detected by placing a solid state detector in the flight path of the electrons (Figure 2.19b). The intensity of this backscattered signal is proportional to the atomic number of the scattering atoms, making backscattered electrons an important technique for analyzing multi-component microstructures. Backscattered electrons can also provide very high quality topographical contrast with careful detector design. A detector with multiple segments creates multiple time-varying signals as the electron beam rasters over the sample, and these channels can be mixed to highlight regions of the sample with surface tilt towards or away from a particular quadrant of the detector, yielding a more intense version of the "cast shadow" contrast observed with secondary electron imaging.

In the work presented in this document, the most important scanning electron microscopy technique used is an emerging variant of backscattered electron imaging known as ECCI, or electron channeling contrast imaging. ECCI is a diffraction based technique that utilizes sample tilt to provide orientational contrast when imaging crystalline samples[53,54]. This technique enables direct imaging of dislocations, grain structures, and stacking faults, because all of these defects cause local changes in crystalline orientation.

To locate and set up an ECCI condition, the electron beam must be incident on the sample

surface at a variable angle. While state-of-the-art microscopes are now able to rock the beam's incidence angle back and forth without moving the beam across the sample, the simplest alignment entails bringing the sample to a close working distance, defocusing completely to produce a parallel beam, and zooming out to sweep the widest possible angle with the beam (Figure 2.20a). When imaging a crystalline sample, the backscatter yield will drop at specific angles, Bragg conditions. A full discussion of Bragg's law as it relates to x-ray diffraction was in the previous section – the primary difference here is the incident radiation, electrons not photons. For very specific incidence angles, determined by the wavelength of the incident electrons and the spacing of the crystallographic planes within the sample, electrons are able to resonantly travel far into the crystal, a process known as channeling. When they inevitably scatter from deep within the crystal, it is less likely that they escape. In practice, this means that there are particular incidence angles where backscatter yield drops due to crystallography.

By rocking the beam back and forth across the sample, the beam's incidence angle is continuously changing. The Bragg conditions appear as pairs of dark bands (Figure 2.20b) across the sample, creating a gridded star shape known as a Kikuchi pattern. The form of this pattern will depend on the orientation and structure of the material being imaged. The example in Figure 2.20b is (001) oriented GaAs, imaged on an FEI Quanta, a microscope with a very narrow beam convergence angle (highly parallel beam) and a wide maximum beam tilt angle.

These dark bands *do not move* when the sample stage is translated, because they aren't created by a feature on the sample, but rather an interaction between crystal planes in the sample and the electron beam. However, *tilting* the sample *does* appear to move the kikuchi pattern, because a "DC offset" is being mechanically added to the continuous tilting of the electron beam. The sample must be tilted until the desired condition is centered, frequently the A or B sites marked in Figure 2.20b. When the magnification is increased, the area of sample being rastered shrinks, as

does the angular space traced by the beam, so the kikuchi pattern appears to expand proportionally with the sample. By "zooming into a dark channeling line", you converge the beam in a channeling condition and the backscatter yield drops. Any bright spots that appear in the image at this point are formed by defects in the crystal (Figure 2.20c) or surface debris that bears no crystallographic relation to the sample.

Because the ECCI signal depends on channeled electrons *not* escaping from the crystal, where unchanneled electrons are likely to backscatter, we can enhance the ECCI contrast as a

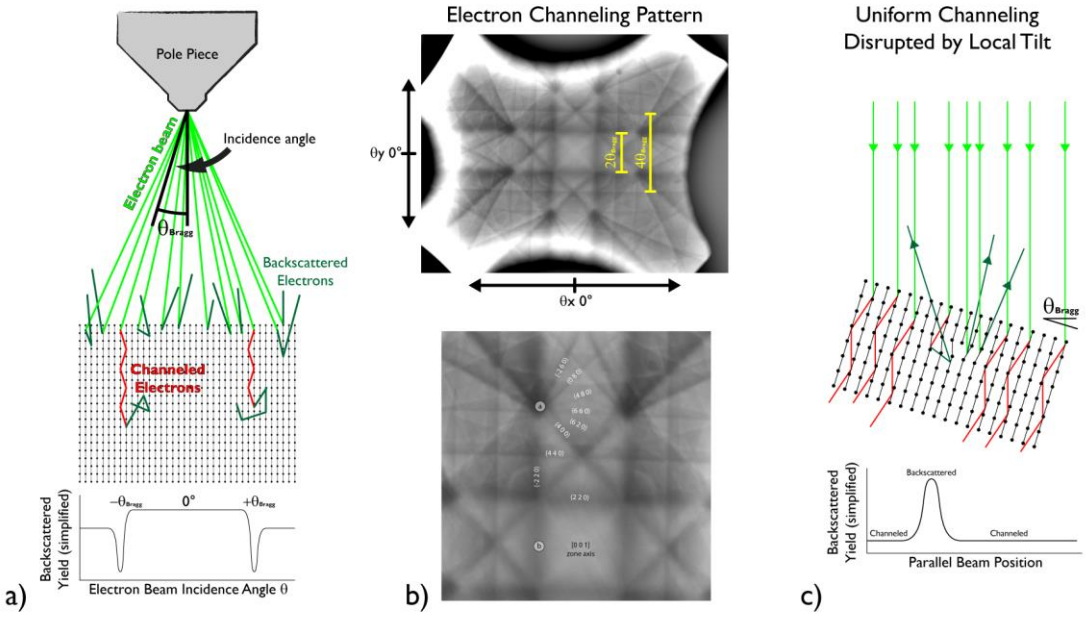

Figure 2.20 – **Electron Channeling and ECCI.**
(a) shows the geometry of Bragg channeling of incident electrons deep into the crystal where they cannot backscatter out of the crystal. When the angle of incidence is not equal to a Bragg angle, the incident electrons are more likely to backscatter near the surface and escape from the surface. (b) Electron channeling patterns made from rastering a 30 kV electron beam across an (001) GaAs surface, sweeping through a very wide angle in two dimensions. Pairs of Bragg conditions appear as dark lines around the zone axis. The bottom pattern is annotated with the Miller indices of the crystallographic planes causing each dark line. (c) When the electron beam is tilted to a Bragg condition, the backscatter yield drops significantly, but where crystalline defects locally tilt the crystalline planes, channeling can cease and backscatter signal can spike. This method can be used to locate crystalline defects in real space using a scanning electron microscope.

fraction of the total signal by only probing the backscattered electrons from lower takeoff angles[55]. For a channeled incident electron deep in the crystal, if it backscatters towards the surface, it's most likely to escape if it goes straight up – if it scatters at a shallow angle to the surface, it has to pass through significantly more material to escape, making escape unlikely. One can imagine that the backscattered electrons emitted from the sample at different angles actually contain different information, and by using a wider ring of an annular detector, for example, one could increase the proportion of ECCI contrast in the recorded signal.

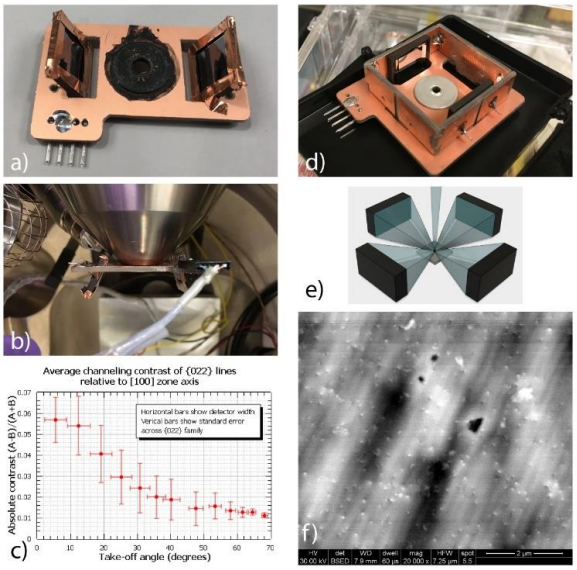

Figure 2.21 – **Custom ECCI Detector developed for high-contrast defect imaging.**
(a) early prototype with two solid state detectors (b) mounted in the microscope with foil covering most of the detector area, allowing for backscattered electron transmission through a narrow slit at a known take-off angle from the sample. (c) Take-off angle vs. ECCI contrast (contrast of a (220) type line compared to the [001] zone axis). (d) final design of the detector with two of the eventual four detectors installed. (e) incident and backscattered electron geometry. (f) early test image with the custom detector, exhibiting dramatically more contrast and signal than the standard annular detector, although slightly more susceptible to electrical interference due to its larger size.

Figure 2.21 shows a progression of custom backscatter detectors to enhance ECCI contrast. First, a detector with two narrow slits was created to restrict acceptance angles. By adjusting the working distance – the height of the sample with respect to the pole piece and detector slits, images could be taken using backscatter signal from a variety of take-off angles. Electron channeling patterns were recorded at each position, and the intensity of the (220) line (position B in Figure 2.20b) was compared to the intensity of the [001] zone axis, producing the plot in Figure 2.21c. At high angles, channeling contrast is only about 1% of the

total backscatter signal, but for low angles in the range of 5-15° takeoff, channeling contrast exceeds 5% of the total signal. A four-panel detector was designed to capture low-takeoff-angle backscattered electrons from all sides of a sample. The detector fits over the microscope pole piece, and the sample is raised into the assembly, so it is surrounded by detectors. In practice, at a working distance of 6-8mm, this maximizes signal and channeling contrast. In the FEI Quanta microscope where this detector was installed, the most important limit to overcome was electrical interference, which appeared to be amplified by the custom detector's larger physical size, and somewhat limited scan rate.

Figure 2.21f shows an example image with many threading dislocations on a GaAs surface. Threading dislocations commonly appear as a spot with dark contrast on one side and bright contrast on the other side. The alternate strain fields around a dislocation can cause the crystal planes on one side to be in a better channeling condition (darker) and the planes on the other side to be farther out of channeling condition (brighter). The misfit dislocation schematically demonstrated in Figure 2.20c assumes a perfect channeling condition where any divergence makes the signal brighter, but in practice this is rare.

Transmission Electron Microscopy

Transmission techniques, TEM, STEM, and TSEM, are most commonly used to observe crystalline defects using diffraction contrast. "transmission" implies that electrons pass completely through the sample before being detected. As opposed to the backscattered and secondary electrons emitted from a sample back towards the electron source, here, forescattered electrons are detected, which have interacted with the entire thickness of the sample. This requires that samples for transmission electron microscopy be exceedingly thin – ie. "electron transparent" (Figure 2.22). This thinning process can be completed by mechanical polishing: wedge polishing, dimple polishing, or flat polishing, with a final broad ion milling/smoothing stage. Alternately, ion

milling can be used for the entire fabrication process using a focused ion beam microscope, which will be detailed in the next section.

Transmission electron microscopy (TEM) utilizes broad parallel illumination. The sample is held between the objective lenses which parallelize the beam as it passes through the sample, then expand the transmitted beam to magnify it, projected onto a phosphor screen or pixelated electronic detector. As the electron beam passes through the sample, it interacts with the periodic nature of the crystalline sample and diffracts. If all of the electrons that pass through the sample are used to assemble an image, the resulting image will contain predominately Z-contrast and thickness contrast. This image is literally a shadow of the semi-transparent sample, showing how many electrons were able to pass through each location on the foil (Figure 2.23, Standard).

Notice that prior to forming an image, the electron beam in Figure 2.23 crosses over. At this point, mathematically speaking, the lower objective lens is focusing diffracted electrons, akin to taking a Fourier transform of the crystal. At the back focal plane, a diffraction spot pattern can

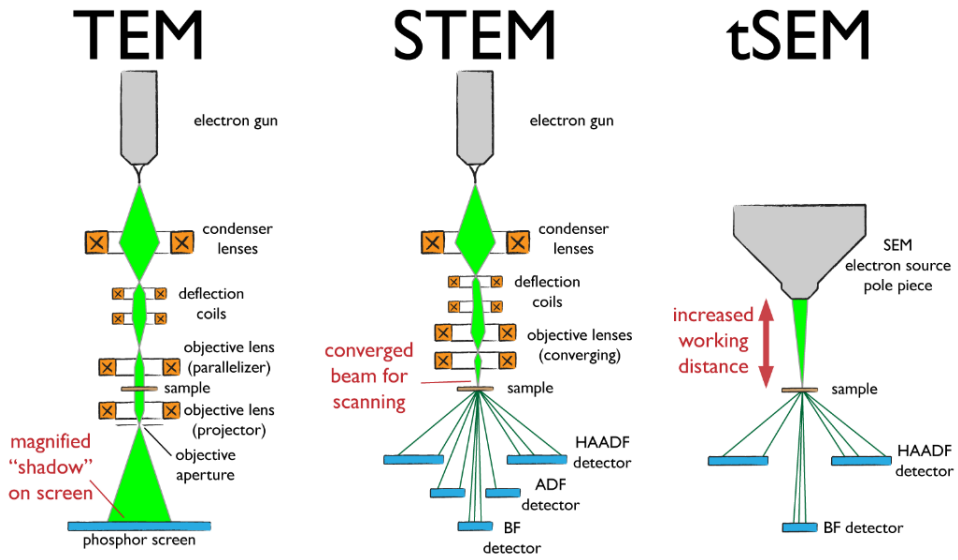

Figure 2.22 – **Three different forms of transmission-based electron microscopy.**
These are simplified layouts demonstrating the difference in sample illumination and data collection.

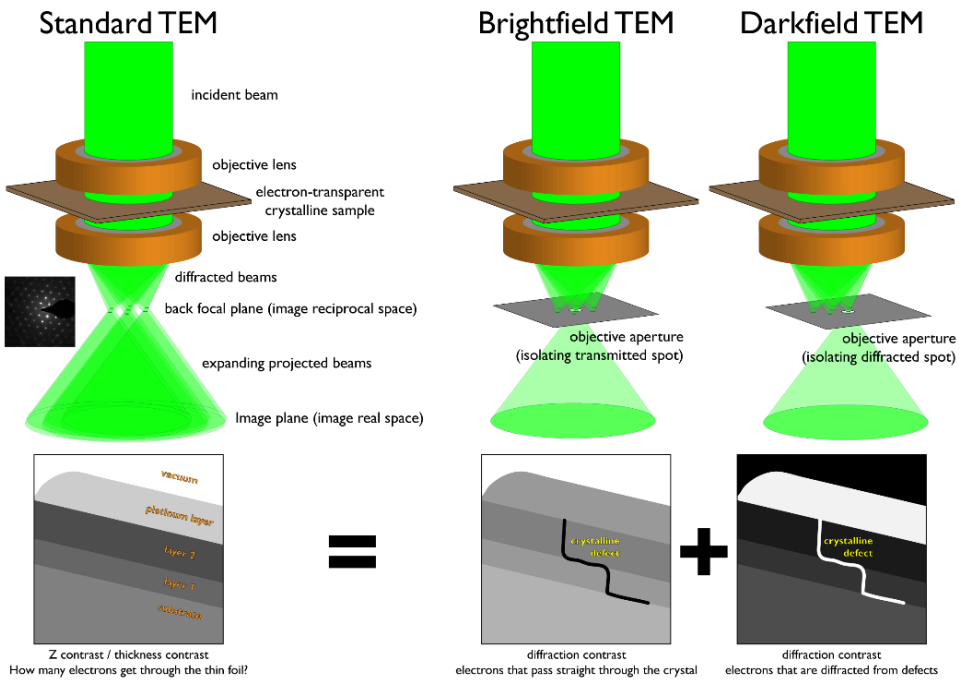

Figure 2.23 – **Image formation in a TEM**.
Using apertures to isolate electrons that contain diffraction information, and projecting images of crystalline defects like dislocations.

be directly imaged, and diffraction spots can be indexed and labeled with their reciprocal space coordinates. Interestingly, the electrons which pass through each of these diffraction spots contain different information, and if electrons from only one spot are used to produce an image, that image will contain diffraction information not present in standard TEM. From an image processing perspective, a standard TEM image is the sum of a variety of channels which can be separated using diffraction.

In Figure 2.23, schematic examples of brightfield and darkfield images are shown. A brightfield image is formed from undiffracted electrons by isolating the transmitted (000) spot, so regions of vacuum and perfect crystal appear bright. Defective regions of the sample, near dislocations, stacking faults, etc., appear dark, because electrons passing through these regions do not pass through uninhibited. Electrons that interact with a crystalline defect are instead deflected to one of the diffracted spots. Notably in the case of dislocations, the contrast of a defect in the

projected image is proportional to $\vec{g} \cdot \vec{b}$, where $\vec{g}$ is the reciprocal space index of the diffracted spot, and $\vec{b}$ is the dislocation's Burgers vector. This additional ability to further segment the contrast from images can provide significant insight into dislocation structure and behavior. In darkfield images, vacuum and perfect crystals appear dim, but defects appear bright. If you were to record an image projected from every diffraction point on the back focal plane and add those images together for a uniform-Z-thickness region of a sample, you would get the exact inverse of the brightfield image.

Scanning transmission electron microscopy (STEM) is a convergent-beam technique, meaning that unlike the parallel beam used for TEM, the probe electron beam is focused to as small a spot as possible, preferably subatomic. As shown in Figure 2.22, a microscope configured for STEM uses the objective lens to achieve this tight focus, and for atomic resolution imaging, great care must be taken to correct the objective focus and astigmatism. Where TEM is essentially a global-shutter technique, and a pixel array is necessary to record images projected onto a screen, STEM is a scanning technique, so images are formed by rastering the focused probe beam to different locations across the sample and building up an image by interpreting a time-varying signal. The electrons that impact detectors in a STEM configuration are all below the sample – only forescattered electrons are detected. Additionally, the microscope runs in diffraction mode, meaning that the back focal plane is extended to be in the range of the detector array. As the probe beam rasters across the sample, each detector is actually keeping track of the brightness of a single diffraction spot, or group of spots, and from this data, images are constructed. Three detectors are depicted in Figure 2.22, each accepting a different angular range of diffracted electrons. The same way isolating the central diffraction spot in TEM yields a brightfield image, building an image using data from the center detector collects information about transmitted electrons, resulting in brightfield contrast. The ADF detector, or annular dark field, is used to produce dark field

diffraction contrast, and generally can detect signal from the first order of diffraction spots around (000). The final detector, high angle annular dark field (HAADF) collects electrons which have been scattered to extreme angles, typically incoherently. Incoherent scattering means that these electrons lose almost all of their crystallographic information, so HAADF images can consist of extremely pure z-contrast. When HAADF images are recorded with a probe beam of subatomic radius, the microscope can directly image atomic columns within a crystal. Many results in this dissertation rely on high resolution STEM to characterize atomic stacking at interfaces and defects.

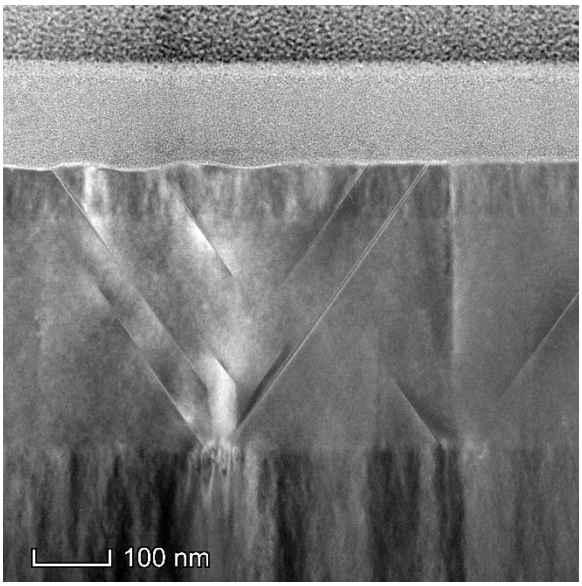

Figure 2.24 – **A STEM micrograph with two sources of contrast.**
Phase separation and stacking faults in a III-V quaternary solar cell structure are imaged using an annular dark field STEM detector. In this image, contrast comes from two significant sources: z-contrast and diffraction contrast. Z contrast (heavy elements appear brighter) allows for the easy differentiation between layers in the structure, and the mottled texture of the quaternary layers indicates phase separation. The sharp lines forming Vs in crystallographic directions are stacking faults, visible due to diffraction contrast.

Every physical sample contains innumerable parameters, and electron microscopy in many cases is a game of finding the correct imaging condition to produce an image that contains as little information as possible – an image that contains only a particular type of defect or feature. Figure 2.24 is an example of a darkfield (ADF) STEM image with two primary mechanisms contributing to image contrast, Z-contrast and diffraction contrast. This sample is a cross section extracted from a III-V stack designed as a radiation-hard solar cell, and this image depicts the ternary GaInP BSF layer sandwiched between two quaternary GaInAsP layers, the contact (top) and the

absorber(bottom). The curtained/mottled texture in these quaternary layers is phase separation, visible as a change in Z as elemental species separate, but also as diffraction contrast, as this phase separation induces strain in the material. During the transition from quaternary to ternary material, some of these phase separated regions give rise to stacking faults which propagate outwards from the heterointerface. These stacking faults are visible as bright lines in highly crystallographic directions. In many cases, the shape of a feature, like lines being straight and parallel, may indicate the identity of the defect, even without first knowing the mechanism of contrast.

The final transmission technique I will discuss here is 2-beam STEM. The same way individual diffraction spots can be targeted in darkfield TEM, 2-beam STEM allows for diffraction contrast sensitive to only a particular dislocation burgers vector. Figure 2.25 shows a series of images of the same set of dislocations, all imaged in different 2-beam conditions. Because STEM is a convergent-beam technique, the diffraction pattern formed at the back focal plane is not made of infinitesimal points, but circles known as CBED disks, or convergent beam electron diffraction disks. For suitably thick samples, these CBED disks will be superimposed on a Kikuchi pattern similar to the channeling patterns from the previous section. The CBED disk shapes are most obvious in Figure 2.25b, where two CBED disks are visible, and the top disk is circled in red. In each of these images, the red circle signifies the area of the brightfield detector, so (a) and (b) are each created using contrast information from a single CBED disk, isolating a particular g-vector projection. (c) is recorded on-axis, so every dislocation in the film should be visible, excepting those with a burgers vector pointing directly into or out of the page, parallel to the imaged zone axis. These 2-beam conditions were achieved by tilting the sample, which, like when aligning a channeling condition, moves the Kikuchi pattern and CBED disks across the detector without necessarily translating the sample.

The particular 2-beam conditions used in Figure 2.25 dictate that any dislocation appearing in (a) but not (b) has an exclusively in-plane Burgers vector. Dislocation segment 3 meets this criterion. Notably, because SnSe is a 2D van der Waals material, this type of defect would be either the edge of a vdW sheet, or a threading hyperdislocation. Any dislocation appearing in (b) but not (a) has a dislocation that projects into the PbSe[001] direction. Dislocation segments 1 and 5 meet this criterion. They could be pure screw dislocations, or mixed dislocations with Burgers vectors inclined in or out of the page. Dislocations which appear in both (a) and (b), like segments 2 and 4, have burgers vectors that project onto this cross section at an oblique angle, for example PbSe[011]. In the case of this assembly of dislocations, it's clear that reactions are occurring between dislocations to alter their burgers vectors, for example the 1-2-3 intersection. At the 3-4 intersection, the burgers vector appears to change abruptly, which is impossible without an additional dislocation, so from this we can infer a third segment exists that overlaps with another dislocation in projection, or has a line direction perpendicular to the cross section.

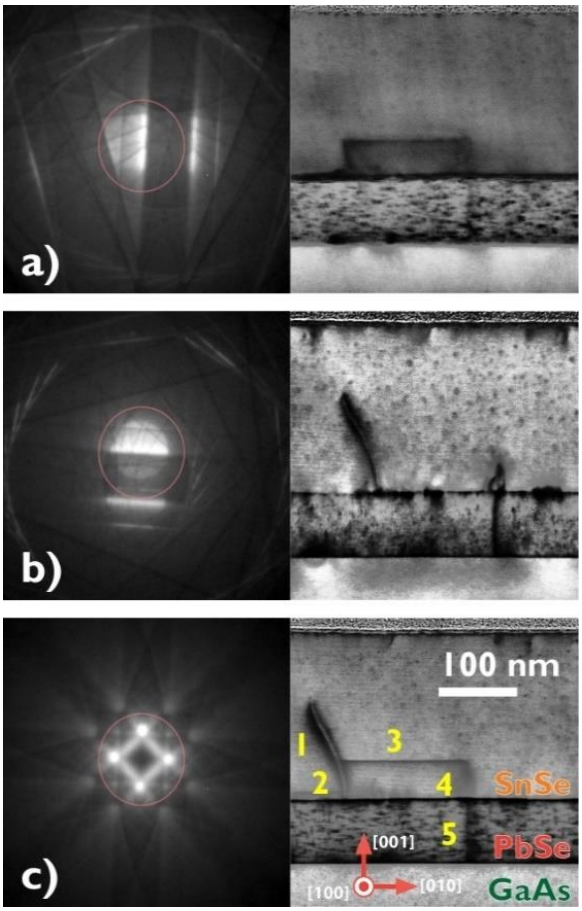

Figure 2.25 – **2-beam STEM.**
Three brightfield images of the same assembly of dislocations in a SnSe film, taken in different diffraction conditions. (a) and (b) are 2-beam conditions, and (c) is on zone-axis. Reproduced from Figure 5.9.

Dislocations are critically important defects to understand in electronic materials and the

ability to directly image them using STEM is an unparalleled tool for characterization of fine detail. It's important to remember, though, that an electron transparent foil prepared for STEM imaging is extremely small. This means that it may not be statistically representative of the entire sample, and the strain state of dislocations within the foil may be entirely different than in a bulk sample (large area thin film).

Focused Ion Beam Microscopy

30 kV electrons do not damage a sample when they impact it. As I will show in the next chapter, 30kV electrons can excite electronically active defects, but no direct mechanical damage is done. On the other hand, a focused beam of 30 kV gallium ions is extremely damaging to a semiconductor crystal, and such a beam can be used as a tool to erode and sculpt semiconductors at the nanoscale. Focused ion beam (FIB) microscopes are designed for exactly this purpose, and are frequently built in a "dual-beam" configuration where the electron beam is used for high resolution imaging and the ion beam is used for milling and polishing. With such a tool, a small cross section or plan view section can be extracted from a semiconductor stack and thinned to electron transparency via high-energy ion bombardment. Figure 2.3.8 shows a complete cross sectional sample prepared on a FIB microscope and ready for transfer to the STEM.

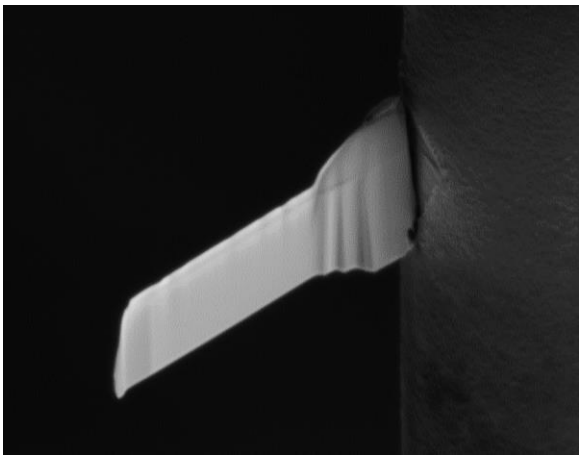

Figure 2.26 – **An electron-transparent sample ready for STEM**
Prepared via focused ion beam milling and liftout, the sample is less than 200nm thick supported on a copper post.

In general such a sample is prepared by first depositing a protective platinum slab, then using high energy gallium ions to erode the film around the desired cross section,

isolating it to the point where it can be transferred via micromanipulator to a copper transfer holder, where it is thinned and polished to final thickness. Specific details of sample preparation vary significantly depending on what material information is sought, and what imaging conditions will be used in TEM/STEM. For high resolution STEM imaging of interfaces, samples must be prepared extremely thin, preferably around 50 nm.

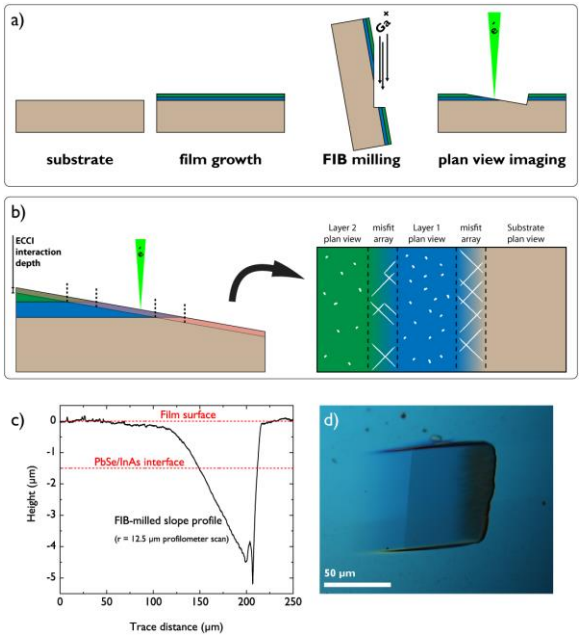

Figure 2.27 – **Exposing buried interfaces with slope-profile ECCI.**
(a) a multilayer film can be grown with multiple interfaces, and when sectioned at a shallow angle using FIB milling, imaged in plan-view using normal ECCI alignment. (b) Defects within different layers and defects trapped interfaces are visible. (c,d) Implementation of this technique showing (d) a Nomarski micrograph of a slope-profile trench at a grade of ≈3.3° alongside the plot in (c), the corresponding profilometer trace.

Slope-profile ECCI

FIB milling can also be used to create a sloped structure allowing for depth-resolved ECCI measurements. In many cases, interfaces can be imaged simply by growing an extremely thin film which ONLY includes interface, but in the case of the IV-VI materials which grow via island nucleation and coalescence, the only way to image a IV-VI/III-V interface in plan view is to grow a film and then extract the interface using FIB liftout and image it separately in TEM/STEM, a labor-intensive and time consuming process. Slope-profile ECCI is a technique that overcomes this limitation and allows for plan-view imaging of every layer within a structure as a gradient across the image with less FIB preparation.

Figure 2.27 shows a schematic of the sample preparation procedure with pictures of an

actual milled trench and its height profile recorded via profilometer. After a film is grown, it is transferred to the FIB. Tilted at a very shallow angle relative to the ion beam, a trench is milled into the film surface at high energy (30 kV) then polished at low energy (2-5 kV) to produce a smooth surface. This sample can be taken to a regular SEM, tilted into a typical ECCI condition, and imaged with diffraction contrast in plan view. Any such images recorded can be "depthed" by locating their position relative to a known-depth feature like an interface and measuring vertical displacement using a profilometer trace. This process of comparing plan view micrographs at different elevations through the *same film*, which can yield very different results compared to growing multiple films of varying thickness.

V. EXPERIMENTAL DETAILS REGARDING THE PRESENT WORK

III-V homoepitaxial films and buffer layers were grown in a Veeco Gen III MBE system utilizing elemental metal sources in standard effusion cells, and group V elements As and Sb in valved cracker sources. Substrates were prepared via thermal desorption and were held in indium-free transfer blocks. Typical growth rates were on the order of 1-10 ML/s, and RHEED was the primary characterization tool. Once RHEED confirmed that a film was uniform and smooth, and had the desired reconstruction, samples were cooled to room temperature under arsenic flux to deposit a thick capping layer for out-of-vacuum transfer. These III-V substrates were cleaved, indium-bonded to new platens, and loaded into the Riber MBE. InAs(111)A substrates were synthesized by collaborators off campus[56], but were prepared using similar methods and arsenic-capping procedures.

For early experiments on GaSb substrates, GaSb homoepitaxial layers could be grown in the Riber IV-VI system using a gallium effusion cell and an antimony valved cracker source, but the Riber MBE rapidly became an exclusive IV-VI deposition system. All PbSe, SnSe, and SnSe

films were grown in this Riber Compact 21T MBE system utilizing compound PbSe and SnSe sources, as well as molecular selenium from a valved cracker source. Typical growth rates were approximately 0.3 ML/s, corresponding to a PbSe flux (measured via ion gauge) of approximately 3×10^{-7} Torr. Cold base pressure in this system was between 10^{-11} and 10^{-9} torr.

As all temperature measurements reported here are merely our internal temperature metrics, measured by pyrometer or converted to the same scale, so it's valuable to provide some additional information for the sake of repeatability. We observed PbSe growth rate to be constant (sticking coefficient = 1) under 340-350 °C, and films did not grow above 360-370 °C (sticking coefficient = 0). The best growths on (001) substrates were nucleated above 325 °C to extinguish misoriented grains, but below 345 °C to avoid PbSe evaporation from the surface and subsequent roughening. This growth window then extends from the onset of PbSe re-evaporation, down about 20 °C. After nucleation and coalescence, the temperature could be dropped 30-40 °C to reduce adatom mobility near defects and grow smoother films free of pits. In the (111) orientation, growth initiation temperature was not as critical, provided the initial surface treatment had succeeded. Most growth temperatures were 280-330 °C, all below the PbSe re-evaporation temperature. The surface treatments discussed in much more detail later take place at approximately 400°C, about 50-60 °C greater than the onset of PbSe re-evaporation.

X-ray diffraction (XRD) experiments were executed on three Panalytical MRD PRO systems. All contained a monochromator for high-resolution coupled scans and rocking curves, and one also possessed a 1D pixel array detector for rapid collection of reciprocal space maps. Alignments alternated between ω, 2θ-ω, and χ scans iteratively. Whenever possible, scans were aligned to known substrate peaks, and collected data was shifted to agree with known substrate peaks before analysis.

Five scanning electron microscopes were used for the imaging work in this dissertation.

An FEI Quanta, FEI Nova Nano 650, FEI Apreo C, and FEI Apreo S, and FEI Helios Dualbeam Nanolab 600. All were used for secondary imaging and backscatter imaging, while the Quanta and Apreo C were primarily used for ECCI measurements. The Quanta column has the largest angular beam deflection, making it the ideal tool for collecting electron channeling patterns over a large region of Kikuchi-space and for aligning ECCI conditions, but suffered in resolution. The custom ECCI backscatter equipment, and custom hot and cold stages, were built for this microscope to facilitate dislocation studies. The Helios Dualbeam system included a gallium FIB, platinum and carbon GIS systems, and a micromanipulator for foil liftout and transfer, and was used to prepare all TEM and STEM samples used in this dissertation.

Transmission experiments were performed on an FEI Technai TEM, FEI Titan TEM/STEM, and an FEI Talos TEM/STEM. The vast majority of the work presented here came from the Talos microscope, operating in STEM mode in a variety of geometries and imaging conditions. Despite not having aberration correction, careful alignment allows for extremely high-resolution imaging of atomic columns and interface structures.

3. *In situ* dislocation characterization and REDG

I. INTRODUCTION

Extended defects and failure of III-V devices

In Chapter 2, I introduced ECCI, a diffraction-based SEM technique. This technique has been foundational to film characterization in our group, and before continuing on to IV-VI growth studies, I wanted to discuss some earlier work on electronically active defects in infrared III-V materials. In this chapter, I present direct observations of dislocation motion in a thermally-strained thin film. Dislocations are imaged using ECCI, and kinetically freed to glide via electron-hole recombination. This chapter is directly adapted from the paper *Direct observation of recombination-enhanced dislocation glide in heteroepitaxial GaAs on silicon* co-first authored by Patrick G. Callahan and myself in 2018[57].

GaAs and AlGaAs, InAs, and InGaAs are widely used for infrared optoelectronics, and recent efforts by the Bowers group at UCSB and others are pushing towards high quality heteroepitaxy of III-V quantum dot devices on cheap Si substrates. Direct growth of GaAs on silicon would enable integration of low-cost computing with datacom optoelectronics, but the 4% difference in lattice constant between GaAs and silicon results in a very high density of dislocations that render devices ineffective. Additionally, a significant mismatch in thermal coefficient of expansion applies significant tensile strain to these films during post-growth cooldown. During operation, dislocations in these materials glide to relax this residual thermal strain, resulting in the creation of misfit segments in the active region of the device[58]. These unfortunately-positioned misfit segments then experience recombination enhanced dislocation climb (REDC)[59], congregate point defects, and cause device failure.

To investigate these effects, we examined dislocations from a combined electromechanical

perspective. While dislocations are the carriers of plastic deformation in all standard crystalline materials, in semiconductors, they take on an extra role, creating additional electronic states due to dangling bonds in the dislocation core reconstruction, or assembly of point defects around the core, a so-called "Cottrell atmosphere". These electronic states trap and recombine carriers and are almost always deleterious to devices, forming a major obstacle to the heterogeneous integration of semiconductors on low-cost substrates. Exploring this dual electronic-mechanical nature of dislocations is an active area of research[60]. In GaAs, this coupling results in a phenomenon unique to semiconductors: carrier recombination via dislocation electronic states enabling dislocation motion. Semiconductors such as GaAs are normally brittle at room temperature and dislocations do not have the energy to move. However, recombination-enhanced dislocation glide and climb (REDG and REDC) occur in many III-V devices at ambient temperatures, leading to rampant dislocation growth and device failure[61–64]. Our understanding of these processes has been inferred largely from post-mortem transmission electron microscopy of failed devices[65] or low-resolution cathodoluminescence microscopy on bulk semiconductor samples[66]. REDG is phenomenologically understood as a momentary lowering of the dislocation-kink nucleation and migration barriers[64,67] which can be induced locally by carrier injection or above-bandgap illumination[64,68,69]. It is important to note that REDG is realized not simply as a heating of the sample surface[66], but as a direct coupling between the recombination of carriers and bonding at the dislocation core[67].

Experimental design

The GaAs samples examined in this study were grown via MBE on on-axis (001) GaP/Si substrates (NAsP III/V GmbH) and GaP substrates (ITME)[70]. The films were 3.1 μm thick, unintentionally doped p-type ($<10^{16}/cm^3$), and are considered fully strain relaxed at growth temperature. Upon cooling to room temperature however, the GaAs layer on silicon is placed in

a significant state of tension (0.2% strain). The array of misfit dislocations at the Si/GaAs interface was nucleated during growth to relieve compressive strain, as GaAs has a larger lattice constant than Si. Therefore, these dislocations have the opposite Burgers vector necessary to relieve the residual tensile strain induced upon cooling. As a result, there exists a significant driving force to *reduce* the total length of interfacial misfit dislocations at room-temperature, on the order of 150–200 MPa. In an electron microscope, as incident high energy electrons from the imaging beam undergo inelastic scattering with the crystal and transfer energy into the semiconductor, electron-hole pairs are generated (along with secondary electrons, x-rays, auger electrons, etc.)[71]. These electron-hole pairs recombine at dislocations and lower kinetic barriers for dislocation glide, facilitating relaxation, and the net removal of existing misfit dislocations, even at room temperature.

II. *In situ* ECCI OF THREADING DISLOCATIONS

Inducing dislocation motion

To resolve individual dislocations in these films, we utilized electron channeling contrast imaging, utilizing a 30 kV electron beam at a current (measured at sample) of 3–5 nA. Under excitation of this imaging electron beam, electron-hole pairs (approximately 10^{17}–10^{18}/cm^3) are generated in the tensile-strained GaAs, which go on to recombine at dislocations. This leads to the observed dislocation glide at room-temperature by REDG. The plan-view ECCI micrographs in Figure 3.1a-b show the extent of these changes in selectively-exposed GaAs layers grown on silicon (large CTE mismatch) and GaP (small CTE mismatch). The CTEs at 300 K for Si, GaP, and GaAs, are 2.6×10^{-6}, 4.65×10^{-6}, and 5.73×10^{-6} °C^{-1}, respectively [72]. The central region indicated in both cases has been exposed to a rastered electron beam for approximately 35 minutes at room-temperature, while the outer regions have not. The most obvious change at this

magnification is the appearance of light and dark lines in the [110] direction. This contrast is due to misfit dislocations, studied experimentally and verified via simulation by Carnevale[73]. In this case, these misfit dislocations originate at the heterointerface and glide via REDG towards the sample surface where they become visible to ECCI. The light and dark contrast arise from their different Burgers vectors with respect to the channeling condition used. In Fig. 1(b), there are many fewer visible misfits, owing to the much lower residual thermal strain driving dislocation motion. Interestingly, this misfit dislocation glide (most visible in Figure 3.1a) extends 2–3 μm outside the central excited region. The region of influence is a convolution of the size of the plume of electron-hole pairs generated by the impinging electron beam (1 μm radius) and the carrier

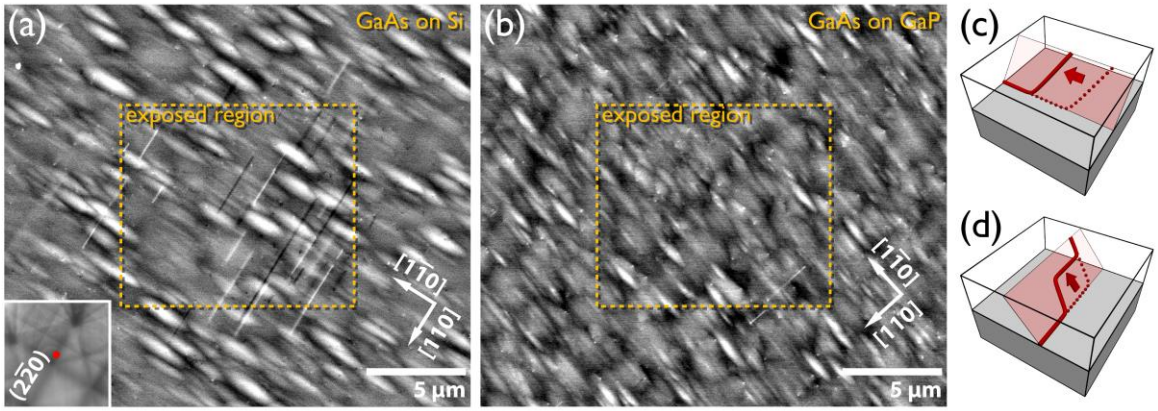

Figure 3.1 – **Electron beam exposure induces dislocation glide.**
(a,b) Plan view ECCI micrographs of a GaAs surface grown on (a) silicon substrate with significant thermal mismatch and (b) GaP substrate with little thermal mismatch. The center (outlined) in each case has received a 35 min exposure to a 30 kV electron beam at an average current density of 2.0 mA/cm^2 (3.4–3.7 nA beam current). A number of β-misfit dislocations running in the [110] direction have risen towards the surface, visible as white and black lines. The oblong shapes in the [1$\bar{1}$0] direction are topographical contrast from surface hillocks. The GaAs/Si sample experiences a higher residual thermal strain, and has more visible glide activity – highlighting the importance of residual strain in predisposing a device to failure. (a, inset) Channeling pattern with one possible (2$\bar{2}$0) alignment indicated. (c,d) Observed mechanisms for recombination-enhanced relaxation of thermal strain: (c) A threading dislocation gliding along the [1$\bar{1}$0] direction, shortening an α-misfit dislocation. (d) A [110] β-misfit dislocation rising from the interface towards the sample surface, shifting a threading segment.

capture radius of the dislocations in question. This capture radius is governed by the carrier diffusion length, approximately 1–3 μm in GaAs[74–76]. It is worth noting that the plume of generated carriers does not extend to the heterointerface, so carrier diffusion is necessary to explain the appearance of misfit dislocations. Overall, within the region affected by the beam, REDG has allowed dislocations to glide and interact with each other, pinning, reacting, or multiplying, with the general result of increasing the complexity of the dislocation network.

The misfit dislocations visible in Fig. 1(a) only appear in one orientation because of the anisotropy in 60° dislocations in the zincblende structure which arises from differences in chemical bonding at their cores.[77,78] α-misfits of the glide-set have a $[\bar{1}10]$ line direction and an As core while β-misfits of the glide-set have a $[110]$ line direction and a Ga core. This disparity lends orthogonal misfit dislocations in compressively-relaxed (001) films significantly different mechanical and electrical behaviors[64,79–82]. We find that residual strain in the $[110]$ direction is relieved exclusively by the lateral glide of threading dislocations to shorten α-misfits at the heterointerface (Figure 3.1c). Vertical glide of α-misfits was not observed to contribute to strain relief in any way. In contrast, residual strain in the $[\bar{1}10]$ direction was primarily relieved by vertical glide of β-misfits (Figure 3.1d). This process occasionally leads to misfit dislocations exiting the sample entirely, but frequently we observed this glide arrested within 100 nm of the surface (see Figure 3.2), resulting in visible light and dark lines as in Figure 3.1a. Lateral glide of threading dislocations was also occasionally observed in the $[\bar{1}10]$ direction, but this motion was difficult to measure, as it was typically interrupted by rising misfit dislocations.

These gliding misfit dislocations exhibited interesting behavior, and can be effectively imaged using ECCI within approximately 200-300 nm of the surface; the contrast from deeper dislocations is frequently too diffuse to measure. One such rising misfit event is shown in Figure

3.2a. As the dislocation glides towards the surface, the associated channeling contrast becomes sharper and shifts in the $[\bar{1}10]$ direction. This shift is due to the dislocation gliding on the inclined $(1\bar{1}1)$ plane, and not straight towards the surface. This known semiconductor glide geometry allows us to couple the lateral and vertical motion of the dislocation, enabling study of dislocation behavior as a function of depth. In Figure 3.2b, a plot showing the dislocation's $[1\bar{1}0]$ position vs. time shows a decay in dislocation speed near the surface. This stagnation is likely the result of a local depletion of carriers due to surface recombination, inhibiting REDG. For very high beam currents (>30 nA), the density of misfit dislocations immobilized at the surface drops dramatically, indicating that increased electron-hole pair generation is sufficient to saturate the surface

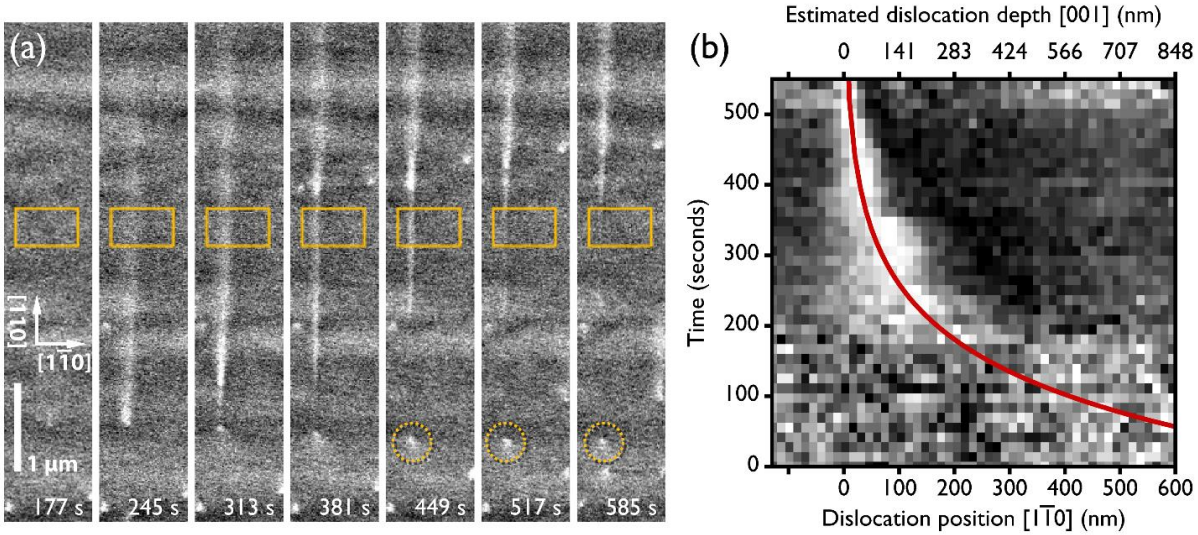

Figure 3.2 – **Detail of the rising β-misfit relaxation mechanism.**
(a) ECCI sequence showing a misfit dislocation (vertical white line) rising towards the surface of the film. In the first frame, the dislocation cannot be identified by the unaided eye, as the contrast from misfit dislocations blurs with dislocation depth. In subsequent frames, the misfit appears as a blurry, then sharp line, before beginning to vanish as it exits the sample. After the bottom edge of the misfit dislocation exits through the surface, a threading dislocation remains (circled in last three frames). (b) shows the integrated contrast from inside the orange box in (a) over the $[1\bar{1}0]$ spatial axis (X) and time (Y), demonstrating an apparent shift in the $[\bar{1}10]$ direction as time goes on. This is actually a projection of motion in the $[\bar{1}12]$ direction as the dislocation glides towards the surface on the $(1\bar{1}1)$ plane. The dislocation slows down as it approaches the surface. The red line is a guide to the eye.

recombination mechanism, allowing carriers to instead contribute to REDG. This enables gliding misfit dislocations to fully exit the crystal.

The unique structure of dislocations in heteroepitaxial thin films makes it difficult to directly apply results from bulk crystal research to this system. In bulk GaAs crystals, dislocations of the glide set are most stable as α-, β- or screw-type, characterized by having As, Ga, or no dangling bonds, respectively, at an ideal unreconstructed core. However, in (001) oriented thin films, the threading dislocations which terminate α- and β-misfits typically have an intermediate line direction[83,84], making them not screw or 60° type. The non-screw threading dislocations terminating α- and β- misfits have α- and β- character to match their associated misfit. Previous research has suggested that in undoped and n-type bulk GaAs, α-dislocations glide orders of magnitude faster than β-dislocations[64,79,85]. However, the asymmetric processes we observed imply that β-misfit dislocations are more mobile here, and act as the primary strain relief mode along $[\bar{1}10]$, while α-misfit dislocations are effectively stationary. There is some evidence in GaAs to show that β-dislocations are more susceptible to REDG, experiencing a larger Peierls barrier lowering under excitation[64,67], and that β-dislocations are much more sensitive to charged dopants [79,85]. These factors may contribute to the results we observed, but more work is necessary to determine if electronic structure, strain state, or other influences prevent dislocations in these thin films from behaving as in a bulk crystal. These differences in dislocation behavior are technologically relevant, as the favored relaxation mechanisms of REDG-prone strained layers have implications for heteroepitaxial device longevity.

Dislocation glide velocities

Individual threading dislocation velocities were studied as a function of temperature using a variable temperature SEM stage between -20 °C and 80 °C, a range typical for semiconductor laser operation in the field. Even within this narrow range, the measured dislocation velocities

varied significantly with temperature. This observation provides further evidence that the observed motion is due to a direct electronic coupling and not localized sample heating. If the sample was being heated to high enough temperatures to enable dislocation motion, a relatively small change in the initial sample temperature would have little impact on dislocation velocity. At the low temperatures in this experiment where GaAs is normally brittle, the measured unpinned dislocation glide velocity is given by $v = v_0 e^{(-E_a/kT)}$[64,67]. Here, E_a is the activation energy for recombination-enhanced glide and v_0 is a beam-current-dependent prefactor. E_a can be expressed as $E_a = E_d(\tau) - \Delta E$, a function of the stress, τ, dependent Peierls barrier $E_d(\tau)$ lowered by an energy ΔE, which is related to the detailed mechanism of REDG such as energy levels of trap

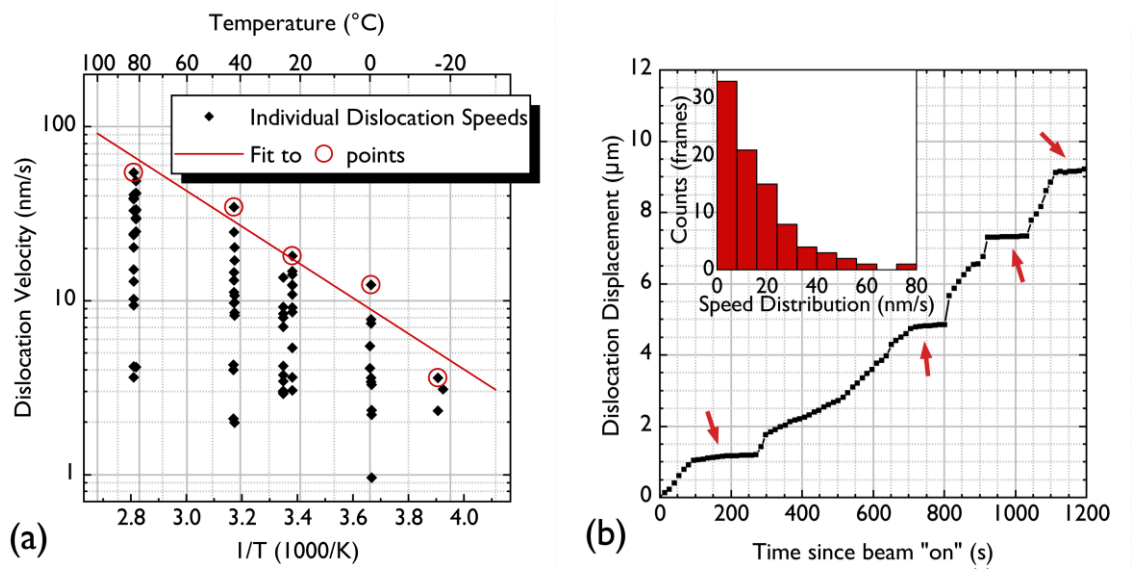

Figure 3.3 – **Threading dislocation motion.**
(a) Threading dislocation velocities in the $[\bar{1}10]$ direction were measured at varying temperatures under a beam current density of approximately 1.9 mA/cm^2. The large spread in measured dislocation speeds at each temperature is due to local dislocation-dislocation interactions. An activation energy for dislocation glide of 0.2 eV was calculated from the fastest dislocations measured at each temperature step, closest to the unpinned case. (b) A single threading dislocation is tracked along the $[\bar{1}10]$ direction for 1200 s, with temporal resolution of 13.5 s, showing repeated dislocation pinning and unpinning. The plateaus indicated by red arrows correspond to separate pinning events, caused by separate adjacent threading dislocations. (b, inset) distribution of instantaneous velocities of the tracked dislocation during observation (three-frame numerical derivative).

states associated with recombination at the dislocation. In our GaAs/Si films, individual threading dislocations moving in the $[\bar{1}10]$ and $[1\bar{1}0]$ directions were tracked for an average of 200 seconds using high-framerate time-lapse sequences; their velocities versus inverse temperature are shown in Figure 3.3a. Dislocation-dislocation interactions such as pinning are known to occur during the growth of lattice-mismatched semiconductor thin films, lowering the overall glide velocity. We directly measure the effect of pinning on REDG in our films with the capability to track individual dislocations as well as their surroundings. An activation energy, E_a, of 0.2 eV for REDG of $[1\bar{1}0]$-bound threading dislocations was calculated from the fastest dislocation at each temperature. Here, it was assumed that these dislocations experienced the minimum number of interactions and would yield a value closest to the unpinned limit. Despite the activation energy being low, it is sufficient to yield a three-fold increase in dislocation velocity when the device temperature is raised from room-temperature to 80 °C, important for modeling failure. Using cathodoluminescence (CL) measurements, Maeda et al.[64,66,67] measured the activation energies for REDG of α-, β-, and screw-type dislocations in bulk GaAs as 0.29 eV, 0.6 eV, and 0.64 eV, respectively. Our results are in reasonable agreement with this report, considering the as-yet unstudied effects of the intermediate line direction of the threading dislocations.

The wide spread in observed dislocation velocities in Figure 3.3a is the result of the dislocation scattering and pinning events occurring repeatedly in these films. ECCI enables the observation of the jerky motion of individual dislocations and provides insight into these processes. Figure 3.3b shows the position of a single threading dislocation tracked over the course of 20 minutes. Its motion is impeded multiple times during observation, resulting in a large spread in the instantaneous velocity (Figure 3.3b, inset). The plateaus highlighted in the figure indicate pinning events, and correspond with interactions between the tracked gliding dislocation and other nearby threading dislocations. The mutual forces between these defects not only impedes the

tracked dislocation, but in some cases visibly shifted the nearby "pinning site" dislocations. We believe the vast majority of pinning events observed in these films to be thread-thread interactions.

For a dislocation to inhibit another dislocation's motion, it must either locally reduce the stress driving glide or remove electron-hole pairs from the system that contribute to REDG. As the limiting factor for energy dissipation at clean, impurity-free dislocations is often the recombination rate[86,87], nearby dislocations are not expected to significantly influence this. Instead, dislocations interact with the strain fields of adjacent dislocations, experiencing a reduction in the driving force for glide. Even with the surface sensitivity of ECCI, its ability to observe thick epitaxial layers with realistic strain states differentiates it from other *in-situ* techniques. Previous work has modeled thread-misfit interactions thought to be typical during semiconductor growth [88,89], and further studies directly observed these interactions using *in-situ* TEM[90,91]. ECCI enables the extension of this research to samples of bulk thickness, where thread-thread interactions might dominate dislocation pinning.

Dislocation reduction via glide reactions

In addition to transient interactions between passing dislocations, we have also directly observed threading dislocations permanently reacting with each other and with free surfaces. Threading dislocations have been observed to fuse and annihilate, and dislocation segments have been observed to exit the sample via glide through the sample surface and edges. This subset of interactions is critical for reducing dislocation density in heteroepitaxial systems. In Fig. 4(a), two threading dislocations on parallel glide planes are drawn towards each other, react, and vanish from view. We believe this is an annihilation reaction, and the two original misfit dislocations are now connected by a short segment of dislocation at the heterointerface. Fig. 4(b) shows the paths taken by these threading dislocations before reacting; the light-contrast dislocation glides in the $[110]$ direction and the dark-contrast dislocation glides in the $[\bar{1}\bar{1}0]$ direction. Romanov et al.

describe a theoretical critical radius of interaction, inside which dislocation annihilation is inevitable [83]. In GaAs, this radius is predicted from growth modeling to be between 50 and 100 nm. The glide planes of the two dislocations we observed are, at minimum, separated by approximately 70 nm. This separation is closed due to either climb (unlikely) or cross slip (likely) in less than one frame at the end of the sequence (≈13.5 seconds). These results provide direct evidence for individual dislocation annihilation processes in semiconductor thin films that have

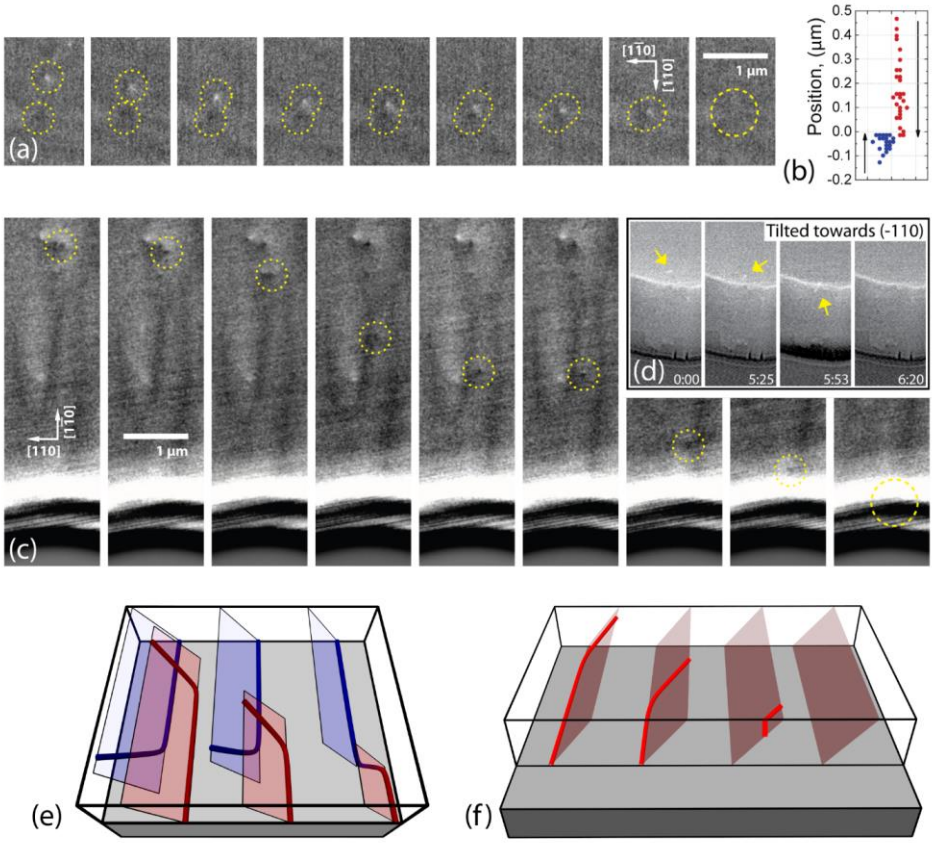

Figure 3.4 – **Two mechanisms for threading dislocation density reduction**. (a, 40.5 seconds per frame) Two dislocations with different Burgers vectors migrate towards each other on parallel glide planes and react. (b) the positions of both dislocations visible in part (a), showing the interaction distance of approximately 70 nm at the time of annihilation. (c, 18 seconds per frame) A threading dislocation exiting the sample, gliding out of a free surface provided by a mesa etch through to the GaAs/Si interface. (d, time marked per frame) A tilted view of a different dislocation on the same mesa exiting the sample. In the third frame, the complete dislocation on the (111) plane is visible as an inclined white line, simultaneously intersecting the sample surface and the mesa edge. (e, f) schematics of possible 3D dislocation shapes during the fusion event and the edge glide event.

previously only been inferred indirectly.

Driving dislocations to the free surface at the edge of a sample is another mechanism often considered for threading dislocation removal. To directly observe this process, mesas were dry etched through the GaAs layer to create vertical free surfaces and REDG was used to drive dislocations out of an area of interest. Figure 3.4c shows a threading dislocation gliding in the $[\bar{1}10]$ direction. After it escapes two pinning sites, it approaches the mesa step and glides completely out of the sample. Multiple threading dislocations were observed to travel to the edge of this mesa, exiting the sample entirely and removing segments of misfit dislocation at the same time. To confirm this, an additional time-lapse sequence (Figure 3.4d) was taken with the same mesa edge tilted at high angle towards the $[\bar{1}10]$ direction while maintaining the channeling condition. In the third frame of Figure 3.4d, the dislocation appears as a diagonal white line bridging the top corner of the mesa step. This is a small dislocation segment (half loop) on the (111) glide plane, the result of an inclined threading dislocation which has already eliminated its associated misfit and is simultaneously intersecting the sample surface and side wall. By the next frame, the dislocation has exited the sample. This dislocation activity is of technological interest because it not only decreases misfit dislocation length, but also decreases the threading dislocation density near a mesa step. It is possible that a similar technique could be used to intentionally remove threading dislocations from low dimensional regions such as nanowires or finFET structures. Additionally, such a treatment would leave the device uniquely prepared to combat REDG-based aging, as it effectively pre-empts the failure mode, filtering out the dislocations most likely to glide due to nonradiative recombination during device operation. Such a filtering step could also be performed on large areas using diffuse low-energy electron flood sources or intense above-bandgap optical illumination, both capable of creating the electron-hole pairs necessary for REDG[64,68,69].

III. CONCLUSION

We have shown that ECCI possesses some fundamental advantages over both CL and TEM for the study of individual dislocation motion in semiconductors. ECCI enables the imaging of large sample areas without requiring sample preparation that alters the material's strain and electronic states. Likewise, while CL is capable of resolving long-range REDG, in general, the technique is limited to light emitting semiconductors and suffers from low spatial resolution, reported as ≈3μm by Maeda et al.[66]. This limits its ability to resolve the finer movement and interactions between dislocations seen in this study, typical of higher defect density devices on silicon. With careful device and contact mask design, we propose that ECCI could even be used to track dislocation evolution *in-operando*. This is a fascinating opportunity to explore the failure mechanisms of semiconductor devices such as GaAs/Si quantum dot lasers[92,93] and GaN[94] and SiC[95] power devices where carrier recombination or electric field-induced dislocation motion is suspected or has been observed post-degradation.

This work on III-V semiconductors has revealed previously inaccessible dislocation dynamics, and although GaAs on silicon is a heteroepitaxial system with near-term application, translation of these observations to other less-understood material systems is important. After the publication of these early results, dislocation glide during cooldown and device operation was found to create misfit dislocation segments in the strained active regions of QD lasers, and by reducing this behavior, the limiting failure mode for GaAs QD lasers on silicon could be significantly improved. Throughout the rest of this dissertation, which will focus on IV-VI semiconductors, this emphasis on dislocation kinetics and behavior is underlying. The IV-VI materials have peculiar glide planes and deformation mechanisms which will be discussed in detail in Chapter 6.

4.Nucleation of PbSe on III-V Substrates

I. INTRODUCTION

Heteroepitaxy of materials involving the growth of dissimilar crystals results in non-trivial interface atomic arrangements, unexpected film-substrate orientation relationships, and overall complex growth mechanisms[96]. Yet, the ability to control such interfaces holds the key to new phenomena and device designs, harnessing features of both materials and potentially leading to emergent properties. Systematic studies in the heteroepitaxy of heterovalent semiconductors with iso-crystal structures (e.g. GaAs/Ge, ZnSe/GaAs, etc.) have yielded control over previously immutable electronic properties like the band-alignment[97]. Likewise, control over isovalent interfaces with different crystal structures such as that in ErAs/GaAs have resulted in advances in the fields of optoelectronics and thermoelectrics[98–100]. This work builds on these pioneering efforts by exploring tools to mediate both heterovalency and heterocrystallinity in semiconductors simultaneously. Epitaxial growth of the mixed-bonded rocksalt IV-VI semiconductor family on covalently-bonded zincblende III-V substrates presents a fascinating set of problems. Parts of this chapter are based on published results from the papers *Nucleation control and interface structure of rocksalt PbSe on (001) zincblende III-V surfaces*[101] and *Interface structure and luminescence properties of epitaxial PbSe films on InAs (111)A*[102].

Heterovalency

One of the most important factors in heteronucleation and growth is heterovalency - differences in polarity and electron transfer among species across a heterointerface can cause charge buildup or other discrepancies. This problem was first articulated by Harrison et al.[103] who posited that perfectly flat Ge/GaAs interfaces would be unstable because of heterovalency, despite matching structure and lattice parameter. Truncating the polar GaAs crystal creates a

trapped layer of charge, and a buildup of potential as the film grows thicker. They propose that some intermixing of atoms can occur across the interface, and mixed-composition monolayers can eliminate the net trapped charge.

In practice, such charge imbalances can cause poor heteronucleation. In the ZnSe/GaAs system (II-VI/III-V heterovalent), Tamargo et al.[104] report layer-by-layer growth of ZnSe on the As-terminated GaAs 2×4 surface, but 3D growth on the Ga-terminated GaAs 4×2 surface. Specific reconstructions contain partial monolayers of atoms as the crystal truncates, and as new species are deposited to effectively fill in the gaps in the reconstruction, regulated amounts of certain species can be trapped at interfaces to create ideally mixed layers[105]. When attempting to grow IV-VI/III-V structures, surface reconstruction, termination, and charge are extremely important variables.

If challenges of nucleation can be overcome, heterovalent interfaces promise unparalleled tunability from the perspective of electronic transport. In growth of III-V/II-VI interfaces, the non-equilibrium growth mode provided by MBE actually allows for deposition of the aforementioned metastable interfaces, and by creating sharp interfaces with varying composition, band-offset between ZnSe and GaAs can be tuned by more than 0.6 eV [97], with heterovalent bonds behaving as acceptors and donors[106]. In a materials system like the IV-VI rocksalts, where novel electronic states are already predicted to exist in thin layers of certain PbSe planes[42], and heterovalent interfaces of two trivial semiconductors (PbTe/CdTe) have demonstrated nontrivial transport[43], the possibility to uncover useful new properties through heterointerface control is significant.

Nucleation orientation and epitaxial arrangements

A full discussion of interfacial atomic arrangements will come in the next chapter – for now, from the perspective of early-growth nucleation, film orientation is a more important

consideration, and more easily measured, than registry with the substrate

Rough film orientation is often predicted via symmetry, looking for coincident site lattices across structures. For a regular epitaxial arrangement to form, the relevant structures need not have the same space group or even Bravais lattice, only a plane within each structure with similar symmetry. MnAs/GaAs (hexagonal on cubic) and $SrTiO_3/DyScO_3$ (cubic on orthorhombic) are two extreme cases, where large rotations are necessary to achieve a coincident site lattice. The square symmetry of the (001) GaAs surface has a short-period coincident site lattice with the m-plane of hexagonal MnAs, so the MnAs is able to nucleate with a $(1\bar{1}00)$ plane parallel to the growth surface, and a c-axis parallel to the GaAs $[1\bar{1}0]$[107]. In the case of $SrTiO_3/DyScO_3$, the $DyScO_3$ (101) face is nearly square, and close enough to the lattice parameter of cubic $SrTiO_3$ that the $SrTiO_3$ can grow on this surface coherently, straining in plane to significant thicknesses[108].

In the case of PbSe deposition on fluorites, silicon, or III-Vs, all structures involved are cubic, but misoriented nuclei obeying coincident site lattices across mismatched planes are still a significant problem. The most common substrate for IV-VI growth is (111)-oriented BaF_2, where nuclei orientation seems to be fairly consistent, where the (111) planes of PbSe or PbTe and BaF_2 align, but interestingly, the 3-fold cubic symmetry rotates 180° through the interface – PbSe$[11\bar{2}]$ direction aligns with the $BaF_2[\bar{1}\bar{1}2]$ direction[109], known as a "Type B" interface. An "unrotated" epitaxial arrangement like that formed by PbTe/Si(111) is known as a "Type A" interface.

Because both crystal structures share identical lattice symmetry on the (111) plane, differences in their atomic basis facilitate a preference for 180° or 0° rotation across the interface. For $PbSe/BaF_2$ Hohnke et al.[109] explain that this rotation is due to nearest- and second-nearest-neighbor effects across the heterointerface, and believe that the Type-B stacking is

thermodynamically favorable. On zincblende CdTe(111), with again the same lattice but a different basis, results are mixed. PbTe typically forms a Type A interface on CdTe, but has been observed to form a Type B interface under certain situations. The authors attribute this phenomenon to a non-equilibrium growth mode, as DFT actually indicates that the Type B interface is more energetically expensive by a slim margin[110].

Unfortunately literature on the early stages of growth of IV-VI materials on III-V substrates is limited[21,22,48,49], although even in these few studies, it's clear that misoriented nuclei are a near-universal challenge. Although PbSe/GaSb heterostructures have been proposed[20] for mid-IR lasers, only one study[21] of PbSe/GaSb growth has been reported, the latter using liquid phase epitaxy (LPE) to synthesize (110)-oriented PbSe quantum dots on GaSb(001). On GaAs(001), PbTe has been observed to grow in mixtures of (001) and (111) orientations[48,49]. On tellurium-treated GaAs[22] there are reports of cube-on-cube (001)-oriented PbSe growth. However on (211) GaAs[22] and (211) ZnTe[111], PbSe does not grow cube-on cube but instead mis-nucleates in the (511) orientations.

Summary

In this chapter, I will detail our efforts to nucleate PbSe on GaSb(001), InAs(001), GaAs(001), and InAs(111)A substrates. All of these surfaces present different combinations of lattice mismatch, surface symmetry, and valency/surface charge to the growing film. In the (001) orientation, we find that PbSe nucleation on bare GaSb, InAs, and GaAs, with 0.5%, 1.1%, and 7.7% mismatch to PbSe at room temperature, respectively, we find no satisfactory growth windows – heteronucleation consistently results in mixed orientation growth due to chemistry-dependent interfacial-energy penalties, irrespective of lattice mismatch. To overcome this, we develop a surface treatment which creates a growth window for cube-on-cube single-orientation

nucleation of PbSe on III-arsenide surfaces: a high-temperature surface treatment with PbSe flux. This pre-treatment creates a good template for subsequent low-temperature growth and leads to sharp interfaces. Our results point towards surface chemistry as the primary factor governing film orientation, and lattice mismatch governing island coalescence behavior in these heterovalent interfaces with dissimilar crystal structures.

In the (111) orientation, we utilize a similar surface treatment to prepare a III-V surface into a good template for ordered growth of rocksalt. The misoriented grains observed in the (111) orientation are primarily in-plane rotations (mutually 180° rotated grains) but also on GaAs(111)B, we have observed significantly symmetry-mismatched (001) grains. Our most consistent results have come from studies on InAs(111)A substrates, and in this work, a high temperature pre-treatment rapidly converts the surface structure and results in a uniform epitaxial arrangement across the sample.

II. MIXED-ORIENTATION PbSe ON BARE III-V SURFACES

PbSe growth on GaSb

In most heteroepitaxy of materials with similar symmetries, lattice mismatch is the most important factor in determining film compatibility and nucleation quality. Considering this, we began our studies with PbSe growth on GaSb substrates, as GaSb is a prototypical III-V bulk material with the lowest lattice-constant mismatch to PbSe. In these nucleation experiments, our primary characterization tool was RHEED, allowing us to assess the orientation and growth mode of PbSe nuclei *in situ*, during and after nucleation.

Figure 4.1a-b shows $[1\bar{1}0]$ RHEED patterns during PbSe growth on 3×1 reconstructed (001) GaSb at high and low growth temperatures. These substrate temperatures correspond to distinct nucleation regimes that we corroborate via scanning electron microscopy (SEM). Figure

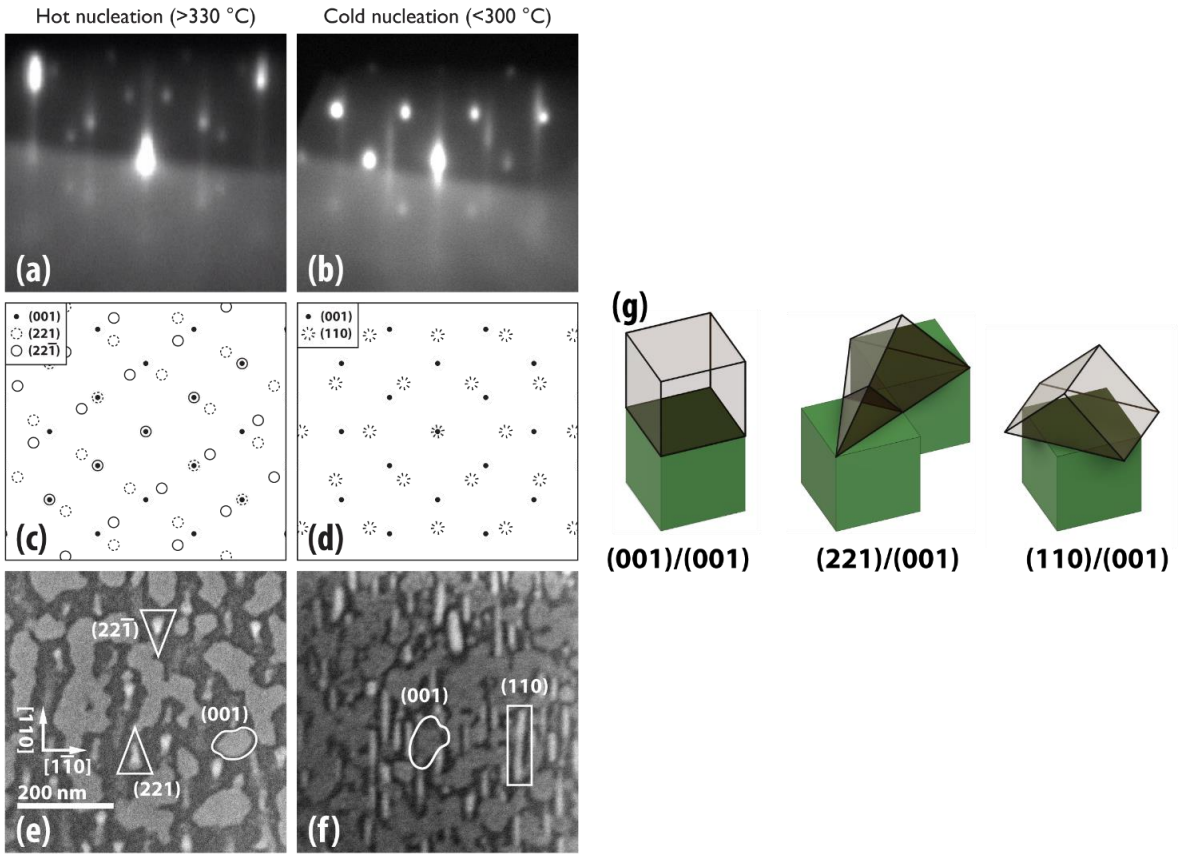

Figure 4.1 – **PbSe nucleation on GaSb**.
(a,b), $[1\bar{1}0]$ RHEED patterns of PbSe nucleated above 330 °C and PbSe nucleated below 300 °C. (b,c) calculated RHEED patterns corresponding to different nuclei orientations. (e,f) SEM micrographs of 90-second (~15 monolayers (ML)) growths of PbSe on GaSb, showing (e) a mix of (001), (221), and $(22\bar{1})$ nuclei, and (f) a mix of (001) and (110) nuclei. The flat tops of the (001) nuclei and the 3D nature of the misoriented nuclei is also reflected in the shape of the observed diffraction spots—the (001) spots appear vertically stretched while the diffraction spots of off-orientation nuclei are sharper points. (g) shows schematics of the relevant (001)-terminated nuclei shapes for a lattice-matched film. The (221) orientation actually provides perfect lattice matching with a short-range coincident site lattice. The (110) nuclei are heavily mismatched and likely strained during deposition.

4.1a shows the case when substrate temperature is high, above ≈340 °C, and the RHEED pattern observed is a superposition of three indexable patterns (Figure 4.1c-d) which correspond to a mix of (001)-, (221)-, and $(22\bar{1})$-oriented PbSe nuclei. The spots corresponding to (001)-oriented nuclei are also slightly more elongated vertically, indicating flatter islands. A different nuclei

orientation prevails at growth temperatures below ≈300 °C. This can be seen in the pattern in Figure 4.1b showing a superposition of two diffraction patterns from a mix of (001)- and (110)-oriented nuclei. At intermediate temperatures, all four orientations of nuclei could be observed in a single growth.

From the corresponding SEM images in Figure 4.1e-f, we can see that the PbSe island shape appears to be governed by the low-energy {100} rocksalt surfaces: (001)-oriented nuclei are large and have flat (001) tops and relatively disordered in-plane shapes; while (221)- and $(22\bar{1})$-oriented nuclei form opposing triangular pyramids. (110)-oriented nuclei observed at lower substrate temperatures form long tent-like structures on the surface (Figure 4.1e-g).

Fortunately, the highly faceted nature of the PbSe islands leads to single-orientation films eventually via overgrowth. With continued deposition (typically 20-40 nm), the (001)-oriented nuclei outgrow the other orientations due to geometric factors—as seen in Figure 4.1e-g, the low-energy (001) surface dominates PbSe growth, and the islands with tilted surfaces grow vertically more slowly. As the misoriented grains are still truncated on {100} planes, their vertical growth rate is limited by the angle these faces make with the growth direction. The

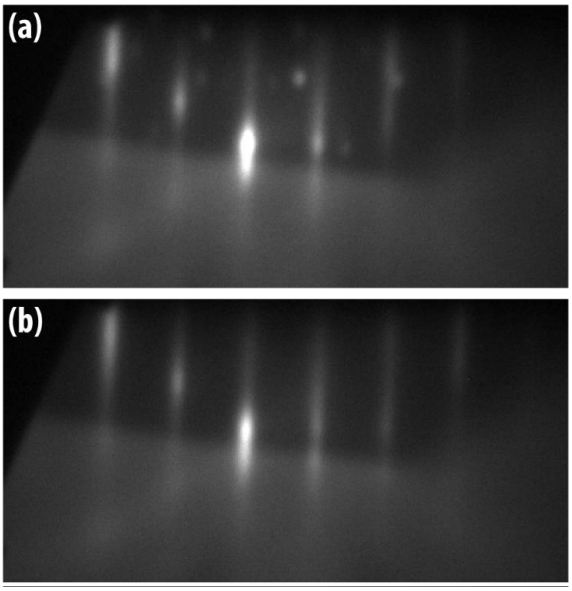

Figure 4.2 – **Overgrowth of misoriented PbSe nuclei**.
Time-resolved RHEED of grain growth in multi-orientation PbSe films. (a) Soon after nucleation. The visible streaks represent flat-topped (001)-oriented islands, while the visible spots are the result of misoriented (110) and {221}-oriented islands. (b) After 80 nm of growth. Due to the highly faceted {100} growth of PbSe islands, non-(001) grains are overgrown but remain buried at the heterointerface.

coalescence and overgrowth times are affected by the size and distribution of nuclei, which vary considerably within a short range of temperatures and can be difficult to control. This overgrowth is shown by the RHEED patterns in Figure 4.2 – immediately after nucleation, diffraction from multiple types of grains is visible: Streaks indicate flat-topped (001) oriented islands while three sets of overlapping spots indicate the existence of distinctly 3D (110) and {221} oriented islands. After continued growth, spots associated with non-(001) grains fade, leaving behind a smooth single-orientation surface. Similar overgrowth of misoriented grains occurs during growth of the IV-VI SnTe on $SrTiO_3$[112] where (001) grains are observed to out-grow (111) grains and eventually produce a single-orientation film.

The orientation of PbSe nuclei appear to depend on bond angles at the interface. Huang et al.[21] grew (110)-oriented PbSe quantum dots on (001) GaSb via liquid phase epitaxy (LPE), and attributed the misorientation to a favorable bonding arrangement around an interfacial selenium atom that resulted in a 90° rotation of the symmetry. They proposed that selenium replaces the top monolayer of antimony, and then with each selenium bonded to two gallium atoms at a wide (but somewhat greater than 90°) angle, the selenium's inclination for octahedral coordination with lead results in 4 lead atoms being bonded to the Se such that the four lead atoms and two gallium atoms form a nearly-uniform octahedron around the selenium. This arrangement, including influence of the gallium atoms in the substrate, produces a 90° rotated crystal.

These results these results agree with our observations in the lower-temperature regime accessible via MBE, where we would normally consider growth to be more kinetically limited, and highly sensitive to bond angles and geometry of individual monolayers. Perplexingly then, LPE is frequently considered an equilibrium growth technique, implying a more thermodynamic process and less dependent on surface kinetics, but it still results in this seemingly unfavorable rotated epitaxy.

The $\{221\}$ nuclei we observe at slightly higher temperatures we believe are effectively (110) nuclei which have canted over $\pm 19.47°$ for better lattice matching. As shown in Figure 4.1g, The $\{221\}$ orientation has a very small coincident site lattice with the (001) orientation, comprising only 1.5 unit cells diagonally. To be specific, when looking at the top face of an (001) surface, the center of one unit cell is $\left(\sqrt{1.5^2 + 1.5^2}\right)a = \left(\sqrt{4.5}\right)a$ away from the corner of the next unit cell. The matching arrangement in the (211) grain is the distance from the bottom of the base of the unit cell to the top corner of the next unit cell: also a distance of $\left(\sqrt{2^2 + 0.5^2 + 0.5^2}\right)a = \left(\sqrt{4.5}\right)a$. If the film and epitaxy had identical lattice parameters, these two nucleation orientations would both match up ideally, but with different interfacial bond angles and changes in symmetry. Unfortunately even after overgrowth, this mixture of $\{221\}$ grains and (001) grains traps a significant area of grain boundary near the interface below the coalesced film.

Alternate surface chemistries and reactions

We also sought to nucleate PbSe on alternate surface reconstructions, in the hope that the altered bond angles, chemistry, and periodicity could produce a template for single-orientation growth. From analogous experiments, we see that PbSe islands also nucleate with multiple orientations on 2×5 Sb-terminated GaSb surfaces, Ga-terminated GaSb surfaces, and 4×2 and 2×4 As-terminated surfaces of InAs and GaAs, respectively. In all cases mixes of (001), (110), and $\{221\}$ nuclei were observed.

With bare III-V surfaces presenting extremely high interfacial energy penalties and prohibiting single-orientation nucleation, surface treatments were necessary to convert III-As surfaces into better templates for PbSe deposition. In particular, we exposed III-V surfaces to group VI elemental flux and IV-VI molecular flux at high substrate temperature in order to alter the chemistry and symmetry of the surface. Altering the properties of the growth surface with a

brief flux treatment is not a new concept in the growth of dissimilar materials. On III-V substrates, group-V species can be replaced near a film's surface; for example, by exposing GaSb to arsenic flux at elevated temperatures, the top monolayers can be converted to GaAs[113]. In MBE growth of heterovalent ZnSe/GaAs interfaces, a brief pre-exposure to either selenium or zinc flux changes the growth mode significantly[114], with zinc pre-exposure possibly supporting charge neutrality during interface formation[115]. Growing PbSe on III-V substrates, Huang et al.[21] hypothesized that selenium could replace antimony near the substrate surface, and Wang et al. [22] exposed their GaAs substrates to Te flux during the GaAs oxide desorb before PbSe growth.

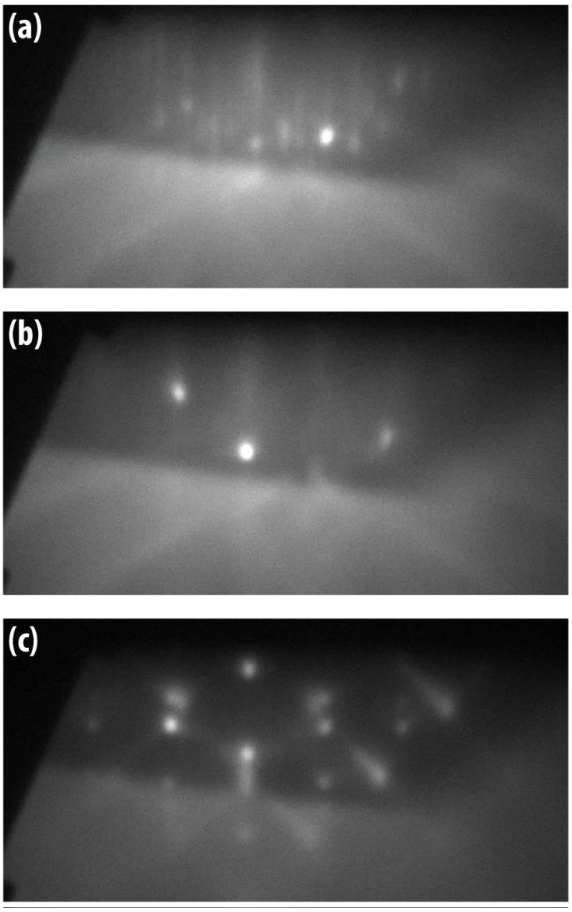

Figure 4.3 – **RHEED of alternative surface reconstructions.**
GaSb surface treated with selenium flux. (a) 5× GaSb reconstruction persistent after antimony flux cutoff. (b) after Se flux treatment at growth temperature – portions of the surface remain extremely flat, but the background appears "fuzzier" indicating a partially damaged surface. (c) After PbSe growth initiation - spotty pattern with chevrons indicates formation of strongly faceted islands or crystallites on the previously smooth surface. Multiple crystal orientations are present.

Figure 4.3 shows a series of RHEED patterns from an early experiment in dosing a GaSb (001) surface with group-IV species: (a) shows a faint GaSb 5× pattern, half of the well-characterized 2×5 reconstruction; (b) shows this same surface after exposure to selenium flux – the arc of bright spots indicates a large fraction of the surface is atomically smooth, but the

background has gotten more diffuse, indicating that the selenium dose has created local spots of damage on the substrate. Prolonged exposure would eventually disorder the entire surface, resulting in no diffractive RHEED pattern, only a diffuse glow. This surface damage is confirmed in (c), where after PbSe deposition, a chevron pattern reveals multiple orientations of highly faceted PbSe nuclei. While many attempted surface treatments failed to eliminate extra grains, there were few that actively degraded the substrate so distinctly.

In the case antimonide surfaces, we believe these treatments largely failed due to species replacement creating subsurface defects in the film. Gallium selenide is a lone stable compound, and with only Se or PbSe flux incident on a III-Sb surface, antimony replacement by selenium is almost unavoidable. Figure 4.4 shows examples of subsurface defects observed in HR-TEM. Figure 4.4a shows a very large defective region in the GaSb homoepitaxy approximately 20 nm

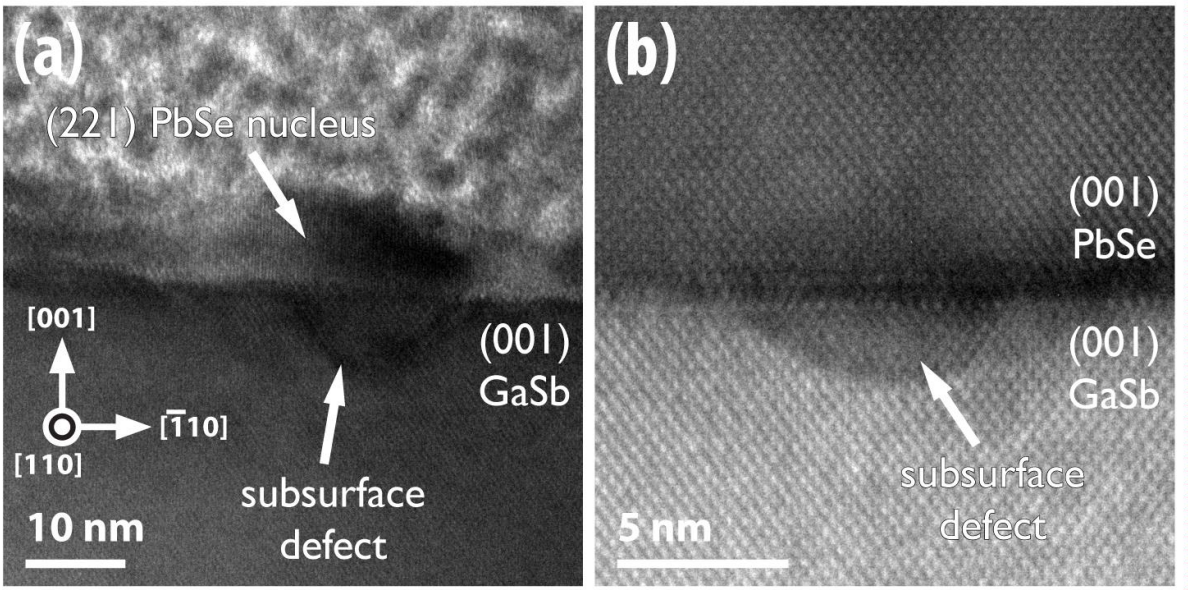

Figure 4.4 – **Subsurface defects at the PbSe/GaSb interface.**
Phase-contrast high resolution transmission electron microscopy. (a) 90-second growth of PbSe (15 ML nominal) shows a (221)-oriented nucleus above a v-shaped defect in the GaSb surface. (b) Phase contrast HR-TEM of the PbSe/GaSb interface in a fully coalesced film. A subsurface defect is visible, but the PbSe film is not misnucleated. Not all interfacial defects necessarily produce misoriented grains.

across, with a (221) oriented PbSe nuclei directly above it. Figure 4.4b shows a much smaller defective region, a notable change in contrast within the GaSb homoepitaxy, but this defect has not nucleated a misoriented grain. It's small enough it was likely overgrown laterally by (001) oriented PbSe which nucleated elsewhere. These types of defects, species replacement and pitting, are likely to blame for the disorder observed in RHEED patterns of treated GaSb surfaces. It is worth noting that antimony and selenium have more disparate electronegativities than arsenic and selenium, and Sb_2Se_3 has a lower formation energy than As_2Se_3[116]. This suggests that Se-Sb interfacial reactions are much more likely, and arsenides may be more resistant to degradation during treatment – I'll explore this in the next section.

III. CONTROLLED PbSe NUCLEATION VIA SURFACE TREATMENTS

Although surface treatments were not able to produce single-orientation PbSe nucleation on GaSb substrates, we were successful in nucleating single-orientation PbSe on III-As substrates. Here, InAs provides a useful contrast to GaSb by presenting a chemically different surface while retaining a relatively small lattice mismatch. These findings highlight the importance of chemical compatibility, not simply lattice mismatch, in heteroepitaxial nucleation and growth.

A recipe for single-orientation PbSe(001) nucleation

A qualitative schematic of the PbSe nucleation procedure (omitting substrate oxide desorption) is shown in Figure 4.5. To modify the surface for PbSe nucleation, the substrate is brought to 400 °C and exposed to 3×10^{-7} Torr PbSe flux for 10–30 seconds. At this flux and temperature, PbSe evaporation is faster than deposition, so we observed no multi-layer accumulation of PbSe on the surface – the growth rate is effectively zero. Even so, in the first 5-10 seconds of PbSe exposure, the 4×2 reconstruction transforms to a well-defined 2×1 reconstruction. If PbSe flux is continued, after 2-4 minutes, the surface disorders along one axis

into an n×1 reconstruction. Both the 2×1 and the n×1 reconstructions appear to be robust below 400 °C – the PbSe flux can be halted and either reconstruction will persist while the substrate is cooled to 330 °C before PbSe flux is reinitiated to begin growth. The 2×1 and n×1 reconstructions can be produced by identical methods from both the InAs 4×2 and the GaAs 2×4 surfaces.

More detailed RHEED patterns of the bare (001) InAs 4×2 reconstruction are shown in Figure 4.6, followed by the stages of surface conversion and film growth. Through this entire dosing/treatment procedure, the surface remains extremely flat, and when growth is reinitiated on either the 2×1 or the n×1 treated surfaces, we see single-orientation nucleation of (001) PbSe at substrate temperatures greater than ≈310 °C. It seems this surface treatment is effective at suppressing all {221}-oriented nuclei that we saw forming on untreated surfaces at elevated nucleation temperature. The growing (001)-oriented nuclei exhibit a typical unreconstructed 1×1 rocksalt (001) surface during and after growth. Despite streaky RHEED patterns immediately after PbSe flux initiation, we find the growth mode remains Volmer-Weber (3D islands and

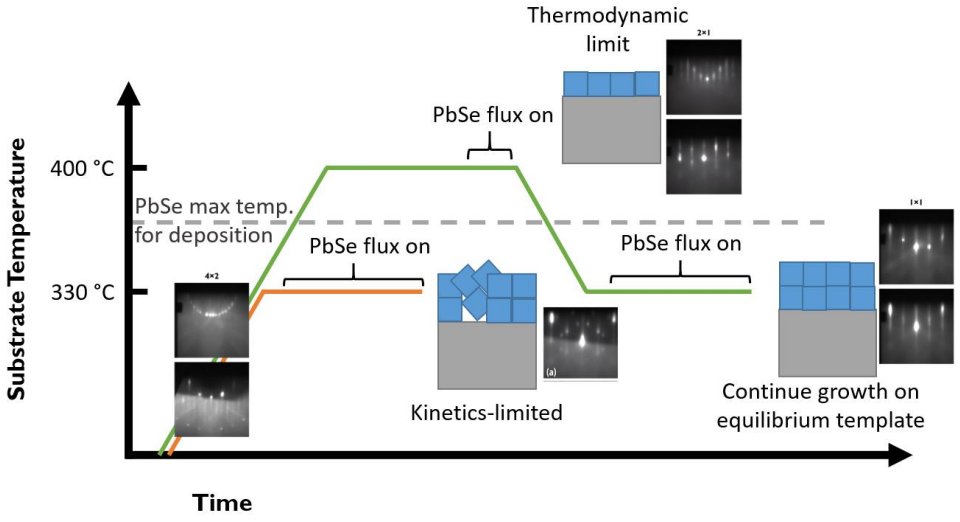

Figure 4.5 – **A surface treatment recipe for single-orientation PbSe growth.** In orange, a simple ramp up to growth temperature is unsuccessful, and results in misoriented grains. In green, the successful treatment, the surface is exposed to PbSe flux above the PbSe re-evaporation temperature. For simplicity, the oxide desorb step is omitted.

coalescence) and not layer-by-layer. Still, this conversion of the arsenide surface is able to control nucleation orientation and create a single-orientation film with a sharp interface.

Chemistry of the surface treatment

The precise structures of the 2×1 and n×1 reconstructions are not known to us, but we believe that both selenium and lead species are present in the most stable case. Others [117,118] have explored a Se-stabilized 2×1 reconstruction on GaAs substrates, but we believe the 2×1 reconstruction we observe on PbSe-treated InAs and GaAs is distinct from this selenized GaAs surface, and involves Pb species as part of the termination. Although we have been able to produce a 2×1 reconstruction on InAs using selenium flux only, the process is not as robust as when using

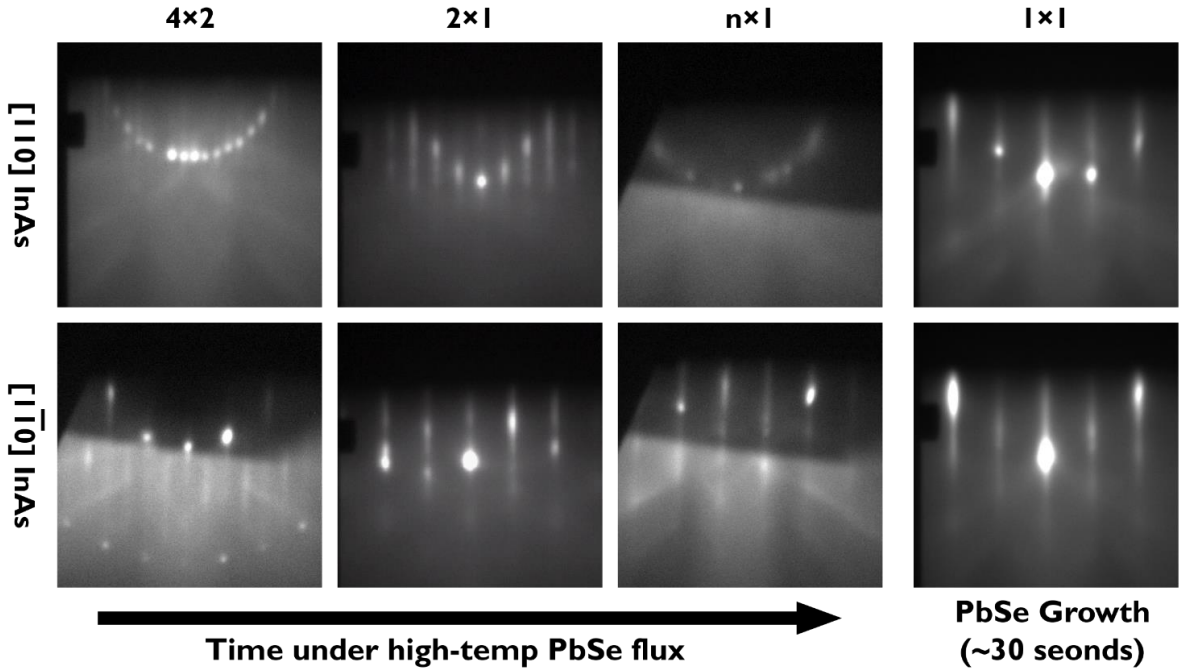

Figure 4.6 – **RHEED patterns showing evolution of a PbSe:InAs surface.** Under PbSe flux at 400 °C, the initial 4×2 surface is replaced with a 2×1 reconstruction after 5-10 seconds, and eventually an n×1 reconstruction after 2-4 minutes. Both the 2×1 reconstruction and the n×1 reconstruction suppress formation of off-orientation PbSe grains at high temperatures, so at the onset of PbSe growth at 330 °C, a streaky 1x1 reconstruction is recovered very quickly. Even when the film has not fully coalesced (see Figure 6.3 below), the only 3D diffraction can come from the step-edges of otherwise smooth islands.

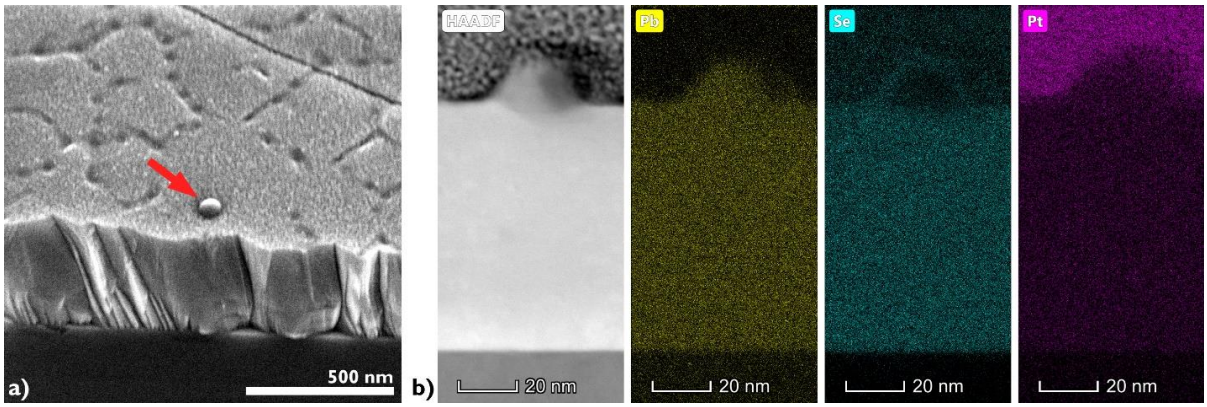

Figure 4.7 – **Lead droplets formed during surface pre-dose.**
(a) shows an SEM micrograph of a thick PbSe film tilted at a 45° angle so the cross section and top surface are visible. Amongst other surface defects, a large round droplet is visible. (b) shows cross-sectional STEM micrographs of a similar droplet on a thinner PbSe film. A typical HAADF image is recorded simultaneously with EDS spectra allowing for chemical mapping of the cross section, showing the droplet consists primarily of lead, with an outer layer of selenium.

PbSe flux, and attempts to control nucleation orientation on InAs using only selenium have been inconsistent. Very high doses of selenium flux on InAs surfaces result in RHEED patterns with chevrons (similar to Figure 4.3), indicating possible surface reactions and roughening to facets. The presence of lead species may serve to stabilize the new surface structure and prevent deeper reactions from occurring.

During a treatment of a GaAs or InAs surface with PbSe flux, exempting limited surface reactions, it appears most unused Pb and Se species readily evaporate. However, for long doses or slightly lower temperatures, a significant density of droplets can be seen on the PbSe surface after growth. We believe that the lower vapor pressure of lead sometimes causes preferential Se evaporation, leaving lead species on the surface to coalesce into metallic droplets. Figure 4.7 shows SEM and STEM micrographs of such a droplet, its apparent morphology on a PbSe surface, and with STEM-EDS, chemical confirmation that the droplet core is Pb. Interestingly, if formed during the dose, these droplets must ride on the surface of the film while it is growing, and in this

STEM cross section, a thin layer of selenium is seen to coat the top of the droplet. Some diffusion or convection of species within the liquid droplet must allow for continued growth, like a miniature implementation of liquid phase epitaxy. These growth mechanics are probably not worth exploring further, but serve as a reminder that overly lead-rich growth can cause defects in these materials.

IV. NUCLEATION OF PbSe(111) ON InAs(111)A

Eliminating rotational twin boundaries with surface treatments

Even between the same pair of materials, forming an interface in a different orientation is an entirely different problem to solve because different crystallographic faces have different symmetry, termination, and surface charge. Every crystallographic plane then presents a unique energetic landscape for the impinging flux species, and new problems need to be solved to achieve single-orientation nucleation. In the case of PbSe deposition on InAs(111)A, we could expect a cube-on-cube nucleation scheme where the 3-fold cubic symmetry persists through the heterointerface, however this is not always the case. Figure 4.8 shows a RHEED pattern of a growing PbSe wafer showing a duplicate pattern: two distinct populations of grains, mutually twinned, but both (111) oriented. Where (001) misorientations tended to tilt about an axis parallel to the growth plane, misorientations of these (111) films are better classified as in-plane rotations. The symmetry of PbSe allows these grains to be considered mirror twins, 60° rotations, or 180° rotations of each other.

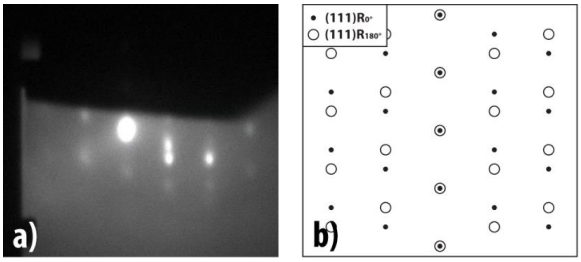

Figure 4.8 – **RHEED indexing of a mixed-domain (111) PbSe surface.** (a) RHEED pattern down a (110)-type zone axis, showing two sets of spots. (b) simulated RHEED pattern, showing that vertical pairs of spots will be present in cases where two orientations exist.

Similar to nucleation on (111) oriented substrates, we find that single crystalline films can be obtained via proper application of the high-temperature surface treatment described above. The films in Figure 4.9a, and Figure 4.9c are both 65nm PbSe films that received different surface treatments. The film in Figure 4.9a has nanoscale rotated/mirrored grains, while the film in Figure 4.9c is single-crystalline, with only threading dislocations visible to ECCI.

The polycrystalline film (Figure 4.9a) was grown on an InAs substrate treated with PbSe flux at 360 °C for 15 minutes, but this substrate temperature was too low and the RHEED pattern became spotty during the dose. When growth was reinitiated at 320 °C, triangular nanoscale grains were observed (Figure 4.9b). We believe that this substrate temperature was not far enough above the evaporation temperature for PbSe, and some PbSe was deposited on the substrate in the form of very small islands, which acted as seeds for later deposition.

The single-crystalline film (Figure 4.9c) was grown on an InAs substrate treated with PbSe flux at 400 °C for 15 minutes. During this dose, the surface reconstruction transitioned smoothly from a 2×2 to a 1×1 and remained streaky, indicating that a smooth surface was maintained while the surface structure was altered. Subsequent growth on this smooth altered surface at 320 °C resulted in single-crystalline films. Later experiments showed a 400 °C surface treatment is effective after only 30 seconds, so at a high temperature, a relatively short surface treatment is sufficient to chemically and structurally prepare the surface for single-orientation growth.

In order to determine the mechanism behind this dosing procedure, we examined these two possible interfaces in more detail. Essentially, the PbSe film shown in Figure 4.9a is the result of uncontrolled competition between two distinct interfacial stackings which are 180° rotated with respect to one another but share the [111] direction with the substrate. One of these orientations shares three-fold rotational symmetry with the substrate (the so-called "Type A" epitaxy), while the other is reversed, effectively making the entire heterointerface a rotational twin ("Type B"

epitaxy). The preferred triangular habit of the coalesced islands, along with the dark/light orientational contrast provided by ECCI, reveal their internal structure (Figure 4.9b). The heterovalent interface between InAs(111)A and PbSe(111) appears to be very high-energy, and consequently, heteroepitaxy occurs in the Volmer Weber growth mode of island nucleation and coalescence. Like-facing grains coalesce evenly, likely forming misfit and threading dislocations during island fusion, but in the more extreme case of oppositely-rotated grains, coalescence results in a twin boundary marked by a shallow trench in the film's surface. For this reason, controlling the nominal orientation of every island with respect to the substrate is essential for high quality crystal growth. Paradoxically, the film in Figure 4.9c, free of grain boundaries, actually has the Type B stacking where the rotational symmetry changes across the interface. The mechanics of this unexpected interface formation are detailed in the next chapter.

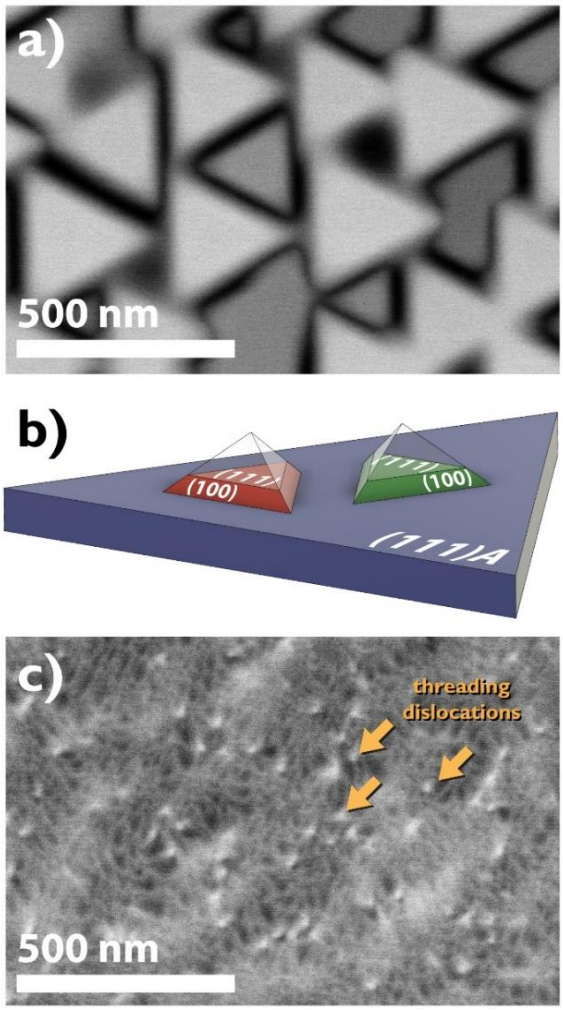

Figure 4.9 – **Surface treatment eliminates twinned grains in (111) oriented PbSe films.**
ECCI micrographs show 65 nm thick films of PbSe grown on InAs at 320 °C with different pre-treatments. (a) A film receives a 15 minute dose at 360 °C and shows two populations of triangular grains with shallow trenches between them marking twin boundaries. (b) Schematic of the rotations in cubic symmetry observed in film (a). (c) A film receives a 15 minute dose at 400 °C and shows a single-orientation structure with some dislocations. Note that (c) is processed with significantly higher contrast than (a).

5.Interfaces and registry

I. INTRODUCTION

In this chapter, I will take a closer look at these interfaces, discussing HR-STEM investigations of four heteroepitaxial combinations involving IV-VI materials, with an emphasis on interface formation mechanisms and heterovalent bonding. The first three examples are heterovalent interfaces between lead selenide and III-arsenides in different crystallographic orientations. These interfaces are between cubic materials with similar symmetry, are sharply defined and relatively well-behaved. The fourth interface I'll discuss is the SnSe/PbSe interface. Both of these materials contain chemically similar species, but form dramatically different equilibrium crystals structures: one 3D cubic, one orthorhombic with 2D van der Waals layers. Parts of this chapter are based on published results from the papers *Nucleation control and interface structure of rocksalt PbSe on (001) zincblende III-V surfaces*[101] and *Interface structure and luminescence properties of epitaxial PbSe films on InAs (111)A*[102], as well as results from a forthcoming paper on SnSe epitaxy.

Heterovalent interfaces, especially heterocrystalline interfaces, present a fascinating problem for materials science. Crystals in their idealized form are infinite, where the same atom in every unit cell has the same charge state, coordination, bond angles, etc., but in the last chapter, we discussed how crystals end, and how important these surface reconstructions are in determining how crystals interact with new impinging species. Once nucleation occurs, a new equilibrium structure forms between the film and substrate, bridging the many discontinuities and incompatibilities that exist between disparate crystalline materials.

Coordination

The most obvious fault at an interface is one of coordination – transitioning from a

tetrahedrally coordinated zincblende substrate to an octahedrally coordinated rocksalt film necessitates at least one layer of atoms with atypical, even asymmetric coordination. Even if the film and substrate share cubic symmetry and orientation in space, the exact structure at the interface can vary significantly. One well-characterized example is the case of rare-earth rocksalts on III-V substrates: eight possible interfacial stackings were enumerated by Tarnow[119], who calculated that between lattice-matched ErAs and AlAs, either the Shadow[As,As] or Chain[Er,As] structures were minimum-energy configurations for As-terminated AlAs, however, he acknowledges that kinetics and particular growth conditions could dramatically alter interface formation. In experiment, two studies [99,120] had observed the arsenic sublattice to persist across the interface between GaAs or InGaAs and ErAs, eliminating some possibilities, and Klenov et al.[121] used HR HAADF STEM to directly image the interface, determining a precise stacking of Chain[As,In/Ga]. This configuration places the burden of coordination compromise on the interfacial arsenic species, each of which is bonded asymmetrically to five erbium atoms in the film and two gallium atoms in the substrate.

Kinetics and interface formation

There can be significant discrepancies between heterointerfaces predicted by equilibrium DFT simulations and interfaces that are actually formed in MBE growth. In the last chapter I explained the tendency for cubic films in the (111) orientation to rotate 180° during nucleation, creating a twin boundary at the heterointerface. This problem is not unique to the IV-VI films – Type B (rotated) interfaces have also been observed in the Ge/CaF_2 system[122], a covalent diamond cubic film on a fluorite substrate, and the $CoSi_2$/Si system[123], a metal fluorite film on a diamond cubic substrate. In the case of Ge/CaF_2, the energy difference between stackings is calculated to be less than 10 meV/atom[122]. This very narrow energy difference results in a slight preference towards the Type B interface that paradoxically increases at higher temperatures. If we

were imagining any configurational space with only 10 meV difference between two minima, at hundreds of °C, we would expect an exactly 50:50 mixture of the two states, but here, one state is clearly favored, even more so at elevated temperatures. The thermodynamics of two slabs of different crystal structures pressed together is very different than the thermodynamic landscape seen by a partial layer of adatoms navigating an existing surface looking for low-energy binding sites.

A similar situation has been observed for PbTe/CdTe, where the Type A and Type B stackings are predicted to differ by only 12.5 meV/atom[110], but clear preferences still exist. On (111) Si substrates, the nucleation orientation of PbSe depends on temperature[13]. While on CaF_2, PbTe orientation is based on step orientation and varies with surface/subsurface defects[124]. In the case of Ge/CaF_2, the authors additionally point to removal of the top fluorine layer of the substrate as critical for forming the Type B stacking[122]. Here, as with the IV-VI examples, it appears placement of the first monolayer of atoms past the heterointerface is critical to set epitaxial symmetry for the rest of the growing film.

Such discrepancies are one of the reasons MBE is widely regarded as a non-equilibrium growth technique – because crystals are formed one layer of atoms at a time, the kinetics of this process need not result in an energetically ideal interface, merely that each layer of atoms deposited finds a deep local minima in its own configuration space. This can be frustrating if films are nucleating into defective high-energy configurations, but the kinetics-limited growth of MBE should be considered a feature, not a bug, for giving materials scientists many extra variables to tune – extra dimensions of parameter space to step through. Substrate temperature over time, the molecular, cracked molecular, or elemental nature of the incident flux, and even the shutter sequencing over time[125] can be used to control surface termination, replacement reactions, and ordered layer formation.

Value in tunable interfaces

Controlling the atypical heterovalent interface atomic arrangement between the IV-VI and III-V semiconductor families will also grant control over the induced interfacial charge, with both electronic and structural implications for thin films. In addition to classical optoelectronics, a subclass of IV-VI materials including PbSnSe and PbSnTe belong to the topological crystalline insulator phase of matter, and these heterointerfaces can host novel electronic states. The ability to grow ordered interfaces between topologically trivial and non-trivial materials would expand the study of the well-known non-trivial surface states to interface states[126] that have the potential to be pristine and controllable.

II. INTERFACE STRUCTURE OF PbSe(001)/InAs(001)

Interfacial reconstruction

HAADF-STEM is sensitive to atomic number, and at high resolution, grants unparalleled ability to map atomic registry between two crystals. Figure 5.1 shows cross sectional STEM micrographs of the epitaxial interface between InAs and PbSe when PbSe is grown on a PbSe flux-treated 2×1 (001) InAs surface. Based on these two orthogonal cross-sectional images, we propose a Chain[Pb,As] structure[119] for the hetero-crystal-structure interface. STEM reveals an As-terminated III-V crystal bonded to a ¼,¼-shifted rocksalt unit cell. Lead atoms take the place of what would be the next layer of indium atoms, apparently bonded to the tetrahedrally-coordinated arsenic termination layer. Selenium fills in between the lead to complete the checkerboard (001) rocksalt surface. Lead species effectively continue the indium sublattice, creating a (nominally) continuous cation sublattice across the interface.

This Chain[Pb,As] structure seems to be unique in the literature. Most studies of rocksalt/zincblende heteroepitaxial systems depend on a continuous sublattice of one species:

(001) ErAs/GaAs has a continuous FCC arsenic sublattice[127], and both (110) and (001) PbTe/CdTe have a continuous tellurium sublattice[128]. The PbSe/InAs system has no common species between the substrate and film. Unlike these examples with a continuous, same-atom cation sublattice, the PbSe/InAs interface has a mixed-species, continuous-anion sublattice across the interface. Ignoring the interfacial spacing change, the FCC indium sublattice in the substrate matches up with the lead FCC sublattice in the film.

Although the valency mismatch is different between this system and our IV-VI/III-V growth, our observation of Chain[Pb,As] is most similar to the Chain[Er,As] model, suggesting that the interface could be a thermodynamically optimal one[119]. Experimentally, this hypothesis is supported by the high substrate temperature during the surface treatment, which likely provides sufficient energy for the surface to exit any local minimum arrangement, however the

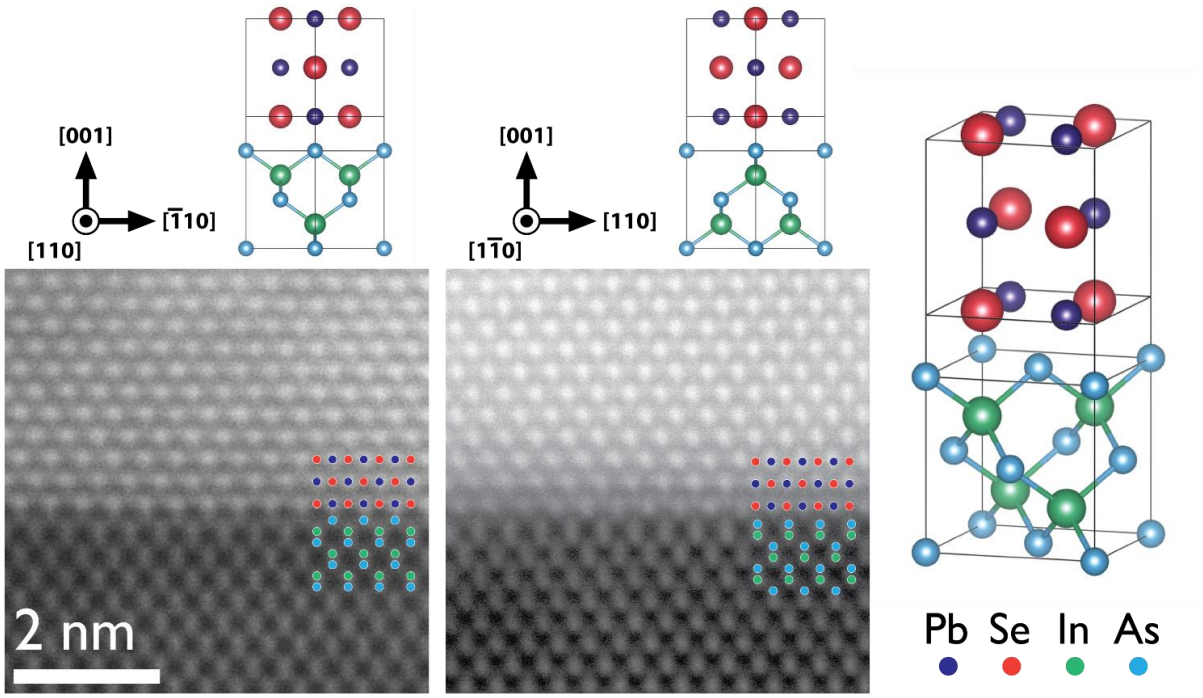

Figure 5.1 – **PbSe/InAs(001) interfacial structure.**
High resolution HAADF STEM reveals a sharp interface with no obvious reactions or atomic exchange across the interface. A proposed atomic column mapping/structure is overlaid and shown graphically to the right.

thermodynamic arrangement achieved is again, not equivalent to the difference between two slabs, merely favorable for one monolayer of adatoms.

The STEM reconstruction indicates that the directional Pb-As bond is critical to the Chain[Pb,As] interface formation, implying that lead is the most important species and is likely present in the most stable 2×1 reconstruction prior to film growth. Surface treatments using only selenium produced inconsistent results – it's possible that a coating of selenium delays lead reaching the group V species and making a strong oriented bond. Alternately, a different chain or shadow structure may form on Se-only reconstructed surfaces, but with a lower energy barrier to misorientation.

Selenium sublattice distortions

Measured via HAADF traces, the $[001]$ spacing between the top layer of arsenic and the bottom layer of lead is 2.5 Å, intermediate between the $d_{PbSe(002)} = 3.06$ Å, and $d_{InAs(004)} = 1.52$ Å. Interestingly, the first few monolayers of PbSe seem slightly distorted, with selenium species slightly displaced away from the interface. The first layer of the selenium sublattice is 0.5 Å displaced from the first layer of the lead sublattice, and this discrepancy fades significantly over the first ~10 monolayers until the lead and selenium sublattices begin to line up. Figure 5.2 shows this distortion with two HAADF-contrast traces across the PbSe/InAs interface.

We hypothesize an interfacial bonding arrangement where the strong covalent bonds from the substrate, a continuation of the tetrahedral bonding from the terminating arsenic layer, extend up to the lead atoms in the first monolayer of IV-VI rocksalt. Obeying more typical IV-VI bonding, the selenium sublattice effectively fills in square interstices in the first monolayer of semi-tetrahedrally bonded lead, and is not directly bonded to the InAs layer. Unlike in bulk rocksalt material, the first layers in the selenium sublattice are compressed (See Figure 5.2 inset). This is a

different distortion than the alternating rumpling previously seen at PbSe interfaces and surfaces[128,129]. We speculate that charge at the heterovalent interface may be responsible for this spatially varying structural distortion, but more study is required to locate the excess charge which will depend on the band offset between PbSe and InAs, which is not yet known.

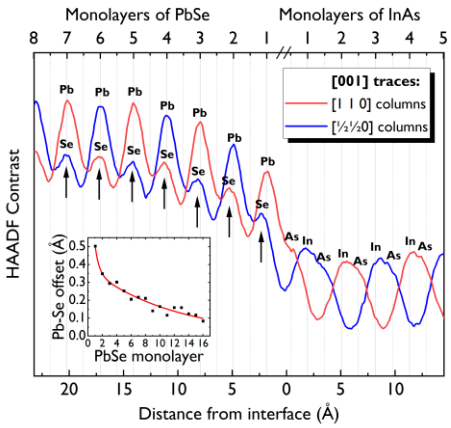

Figure 5.2 – **Sublattice distortion.** [001] contrast traces (averaged without fitting) across the HAADF STEM micrograph from Figure 5.1 (left). The InAs barbells can be seen on the right, and the alternating Pb/Se species on the left. At the interface, the final InAs layers appear slightly stretched, and the first few monolayers of the selenium sublattice are warped away from the interface. The vertical grid lines are at a regular interval.

To speculate that this distortion is exclusively due to electrostatic forces and effective charge buildup at the interface, such a distortion would imply a built-in E-field[130], and graduated potential near the interface. It's possible that measurement of such a distortion is a method of directly measuring interfacial band bending as $V \propto \int E \cdot dx$.

Implications of interface distortions

For certain compositions, IV-VI materials such as SnTe and PbSnSe exhibit a TCI phase with an inverted bandgap[37,38,40,131]. Such a state is linked to crystal mirror symmetries, so tracking symmetry across the heterovalent interface is important for considering future applications. The 2×1 reconstruction appears to leave behind no residual disorder or partial monolayers at the interface so the nominal atomic structure we observe at the IV-VI/III-V interface is a near best-case scenario for preserving symmetry: one crystal structure simply ends and the other begins. That said, there are two structural distortions present near the interface with potentially interesting effects. The asymmetric strain state resulting from island coalescence

imposes a shear in the (001) plane which maintains important mirror symmetries, but still distorts the band structure and has been predicted[132] to shift but not gap topological states on the (001) rocksalt surface. The other significant symmetry-altering perturbation at the interface is the offset between the Pb and Se sublattices very near the III-V termination. Serbyn and Fu[132] show that the rhombohedral ferroelectric distortion ($w = \langle 110 \rangle$) breaks one important mirror symmetry and gaps the topological surface states. If the ($w = [001]$) distortion we observe has similar behavior, it may gap the states immediately at the interface, but because this distortion is isolated close to the hetero-interface, it would displace the topological interface state deeper into the IV-VI film.

III. INTERFACE STRUCTURE OF PbSe(001)/GaAs(001)

Nominal structure and bonding

The PbSe/GaAs interface bears close resemblance to the PbSe/InAs interface. On both substrates, exposure to PbSe flux at elevated temperatures produces a 2×1 reconstruction, and PbSe nucleates with a single orientation in a cube-on-cube epitaxial arrangement. At the moment of nucleation, we assume that PbSe also adopts the Chain[Pb,As] stacking, but once growth begins, it becomes impossible to define one stacking sequence. The bonding across the heterointerface is so weak that dislocation cores become extremely wide, with the core width approaching the dislocation spacing, and the film and substrate continuously shifting in and out of mutual registry.

Figure 5.3 shows a HAADF STEM comparison between two edge dislocations in PbSe: (a) shows a dislocation at the interface between GaAs and PbSe, and (b) shows a dislocation in the center of a PbSe layer. The interfacial dislocation in (a) is undissociated, but has an extremely wide core, nearly equivalent to the equilibrium misfit dislocation spacing of ~5 nm. In contrast, the dislocation in (b) is dissociated over a length of multiple unit cells (2-3 nm), and each partial

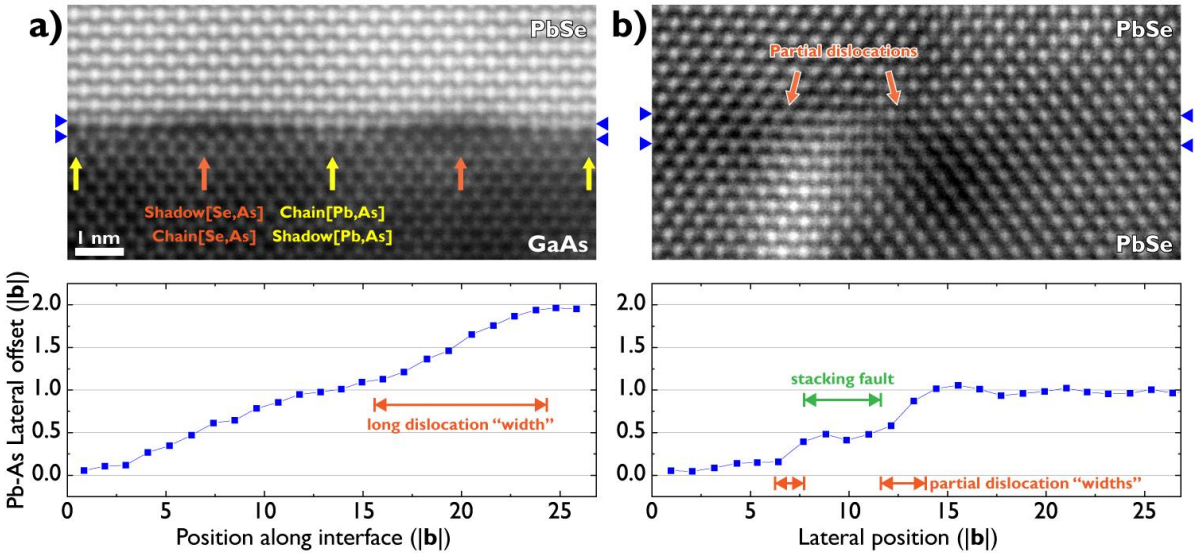

Figure 5.3 – **Interfacial dislocation widths and bond strength.**
(a) HAADF STEM of a PbSe/GaAs interface, with two edge dislocations visible in the image. (b) HAADF STEM of an edge dislocation in PbSe. Also included are plots of (lateral) atomic displacements, generated from HAADF contrast traces along the layers marked with arrows. Distances are in units of burgers vector magnitude.

dislocation is extremely small, less than 1 nm wide. These images indicate a stark difference between the 3D bonding within a PbSe layer and the much weaker heterointerfacial bonding between the PbSe layer and the GaAs substrate.

Moiré heteroepitaxial registry

On first impression, this interface looks almost van der Waals bonding, with effectively zero interaction between the PbSe and the GaAs layers, as if they were free surfaces, but a more careful analysis of the atomic positions in the two interfacial layers reveals a slight preference for lead to align over arsenic, demonstrated by a flattening of the "lateral offset" curve at displacements of 0, 1, and 2 times the burgers vector. These flat regions indicate coherently strained film, while the sloping regions indicate a gradually changing registry, a "vernier scale" where the two lattices fade in and out of alignment.

Figure 5.4 shows the moiré pattern formed by the bonding (001) planes of PbSe and GaAs if there was no preference for a particular registry (a nearly-true approximation). As these lattices combine, there is actually a checkerboard of different interfaces that are formed periodically. The Chain[Pb,As] structure is the structure we observe at the better-matched PbSe/InAs interface, but in this case we also see Shadow[Pb,As], Chain[Se,As], and Shadow[Se,As]. The cross section in Figure 5.3 is looking at this pattern down the axis from "Shadow[Pb,As]" to "Chain[Pb,As]", and from "Chain[Se,As]" to "Shadow[Se,As]", so alternately we observe columns of atoms where lead interacts with arsenic and where selenium interacts with arsenic. Looking closely at the dislocated regions in Figure 5.3a, the PbSe lattice actually appears to bow away from the GaAs surface when selenium and arsenic are placed in close proximity. Not only is this what we would expect from the perspective of charge and polar bonding between species in each material, but it implies that in PbSe films grown on GaAs, the interface will have a 2-fold symmetric periodic array of attractively bonded and repulsive areas depending on local

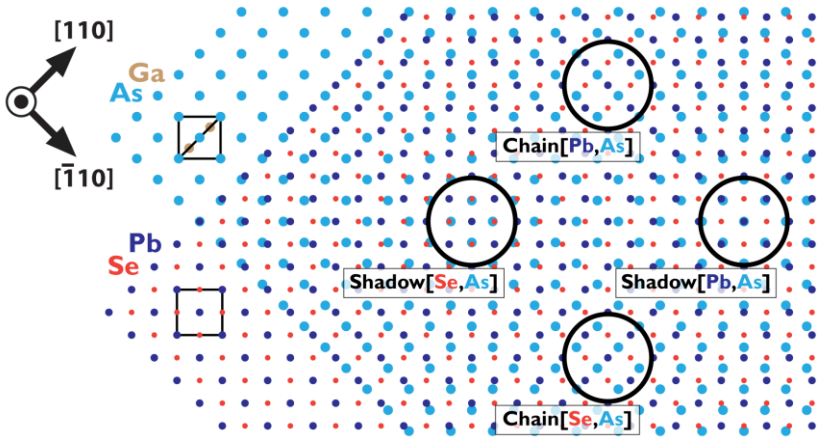

Figure 5.4 – **Moiré of bonding and registry at the PbSe/GaAs interface.** The bonding monolayer from each structure are drawn overlayed, and the lattice mismatch has been rationalized to a 12-atom period. Four options for registry are shown, and at this interface, a repeating grid of these four stackings will exist throughout the plane of interface. This diagram can also be used to determine nominal edge dislocation core structure in better-matched examples like PbSe/InAs.

registry. The electronic and mechanical implications for such a periodic bonding structure are not yet known, but these interfaces are completely unlike mismatched III-V/III-V interfaces, which have condensed dislocations with coherent bonding in between. Chemical incompatibility and large lattice mismatch combine to create these unique structures.

IV. INTERFACE STRUCTURE OF PbSe(111), PbSe(111)R180° /InAs(111)A

For structural reasons that will be explored in detail in the next chapter, most epitaxial IV-VI films are grown in the (111) orientation. As the (001) and (111) surfaces of a zincblende crystal are dramatically different in terms of symmetry, charge, and bond geometry, in many ways it was serendipitous that a similar surface treatment was able to create oriented PbSe nucleation on both the (001) and (111)A surfaces of InAs. Initial measurements utilizing typical diffraction-based techniques like XRD, ECCI, and RHEED actually indicated the surface treatments were unsuccessful because of confounding defects below the heterointerface, and high resolution STEM, with the ability to directly image atomic structures, became a critical tool for evaluating nucleation orientation.

Type A and Type B stackings

As discussed in the last chapter, without an adequate surface treatment, the high-energy heterovalent interface readily produces two populations of PbSe grains that are rotated 180° in-plane with respect to each other, separated by rotational twin boundaries. We have characterized both of these interfacial stackings: unrotated, Type A, and rotated, Type B (Figure 5.5). The primary difference between the A and B stackings is the placement of the first layer of lead atoms: in the Type A interface, these lead atoms are lined up directly above the top layer of arsenic in the substrate, while in the Type B interface, the lead and arsenic are farther apart. In both cases, the bond angles around the first layer of lead atoms define the 3-fold cubic symmetry for the rocksalt

film. We believe that during our high-temperature surface pre-treatment, we are giving this first layer of lead atoms the kinetic freedom to migrate to the energetically favorable A or B site. Interestingly, this equilibrium structure achieved in Figure 4.9c is actually Type B epitaxy—it seems counterintuitive that the creation of a rotational twin across an already expensive heterointerface could be energetically favored.

A more detailed analysis reveals slight distortions at the interface, the most dramatic of which is the spacing of the first PbSe monolayer. Although actual lattice distortions are likely more nuanced, a tentative interpretation of the interplanar spacings near the interface (Figure 5.5c) indicates that the first layer of PbSe in both structures is a nearly zincblende-ordered monolayer

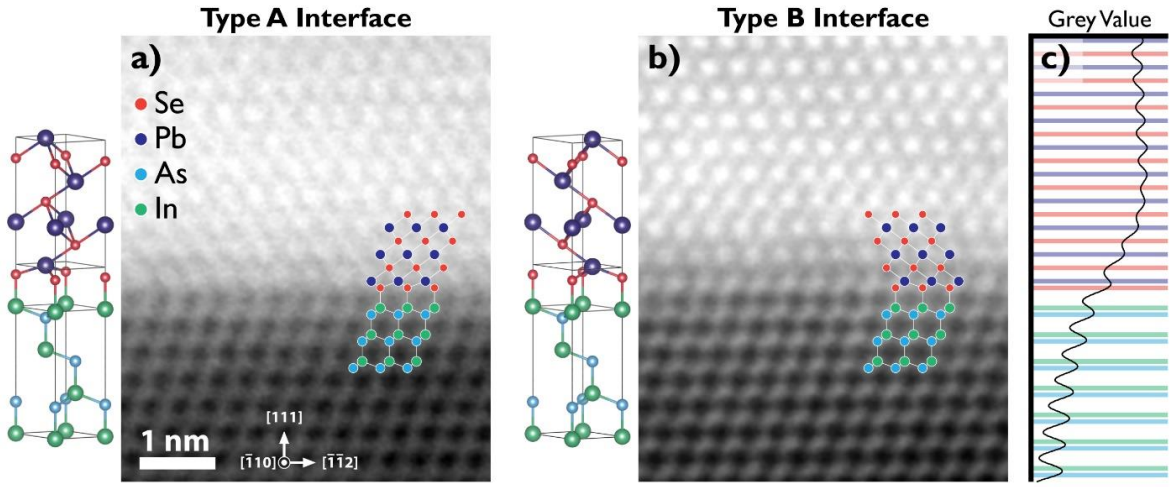

Figure 5.5 – **PbSe/InAs(111)A interfacial structures.**
High-resolution HAADF-STEM cross sections of two PbSe/InAs interfaces with proposed structures. Reconstructed structures assume 3-fold rotational symmetry in the growth plane. (a) The metastable Type A cross section was cut from a stacking-fault-free region of the PbSe/InAs interface from a sample that received an ineffective surface treatment (Figure 1a). (b) The equilibrium Type B cross section was cut from a sample treated with PbSe flux at 400 °C where all PbSe/InAs interfaces include exactly one rotational twin, resulting in a 180° rotated film. A wide integrated line trace (c) of the Type B interface HAADF image is also shown to demonstrate regular interplanar spacings through the interface, with the first layer of PbSe compressed towards zincblende. [STEM Processing details: 20 images, stacked for drift correction, smoothed with α = 200 pm gaussian blur.]

of PbSe. If this interpretation is correct, there is a slight separation between the chemical heterointerface and the structural heterointerface. During the high-temperature dose at 400 °C, the PbSe evaporation rate is high and only a single monolayer can adhere to the substrate. In the absence of more rocksalt layers, the most stable conformation for a *single* PbSe monolayer is to continue the existing tetrahedrally coordinated zincblende lattice. When this pseudo-zincblende monolayer is cooled to ~300 °C and PbSe growth is initiated, the first layer of lead atoms assumes its octahedral rocksalt coordination, and the bond angles of this lead layer set the symmetry for the rest of the PbSe film.

It is important to note, however, that this is an idealized picture of the interface. A single monolayer of zincblende-oriented PbSe would imply a sharp chemical interface and a separate sharp structural interface, but in reality these are probably not perfectly abrupt. Before the PbSe dose, in RHEED we observe a 2×2 reconstruction on the InAs surface, which could indicate an arsenic trimer structure and as much as ¾ of a monolayer of arsenic remaining. During the PbSe dose, it is likely that not all of this residual arsenic is evaporated, resulting in a mixed composition layer. Such a mixed selenium-arsenic layer would have a much stronger bias towards tetrahedral bonding when in the presence of an existing zincblende film. After the PbSe dose we see a 1×1 RHEED pattern, which we believe corresponds to an unreconstructed pseudo-zincblende lead-terminated surface. With this evidence, accepting a slightly blurred chemical interface helps to explain the symmetry reversal between the first "monolayer" and the rest of the film.

With only a single monolayer of material deposited on a substrate during the pre-treatment, we find this procedure essentially 100% effective at regulating stacking. Necessarily then, the selective driving force for Type B stacking must be much higher than k_BT during the treatment to cause such an extreme bias. There may also be a rapid ripening process that results in single-orientation film across the wafer after initial nucleation, but if such a ripening process

does contribute, we know it is limited by the underlying structure – as in Figure 5.6. The PbSe does not form a continuous layer of the majority stacking, instead it conforms closely to the twinned regions that already exist in the buffer. The difference between Type A and Type B slab-on-slab interfacial energies doesn't matter, only the energetics of layer-by-layer growth and the geometry of ultra-thin structures.

Propagation of substrate twins

A PbSe film free of grains would be ideal, but homoepitaxial growth of InAs(111)A is still under development and the InAs buffer layers used in this work contain some twins which are transmitted up to the PbSe films. It is worth clarifying that these boundaries are between twinned grains of PbSe crystal. As PbSe has 3-fold rotational symmetry about the [111] direction, and mirror planes parallel to the [111] direction, the structure on one side of one of these boundaries can accurately be considered either rotated or mirrored with respect to the structure on the other side. Although the vertical boundaries we observe are frequently not in symmetric directions, and so may be largely incoherent. While not perfect substrates for devices, these differing grains present on the same sample surface actually provide an excellent test of robustness for the high-temperature dose mechanism.

Figure 5.6 shows how large twinned grains in the substrate are propagated through the heterointerface to the PbSe film. In Figure 5.6a, we see two twin boundaries in the InAs buffer (with a third below the imaged frame). One of these twin boundaries curves to intersect the heterointerface. On the left, a 0° rotated InAs layer that shares cubic symmetry with the substrate grows 180° rotated PbSe, forming a heteroepitaxial rotational twin. On the right, a 180° rotated InAs layer acts as a substrate for 0° rotated PbSe, similarly forming a rotational twin, but resulting in film that shares 3-fold symmetry with the substrate. The boundary continues vertically between the left and right grains of PbSe, producing a wide moiré pattern in the center of the image.

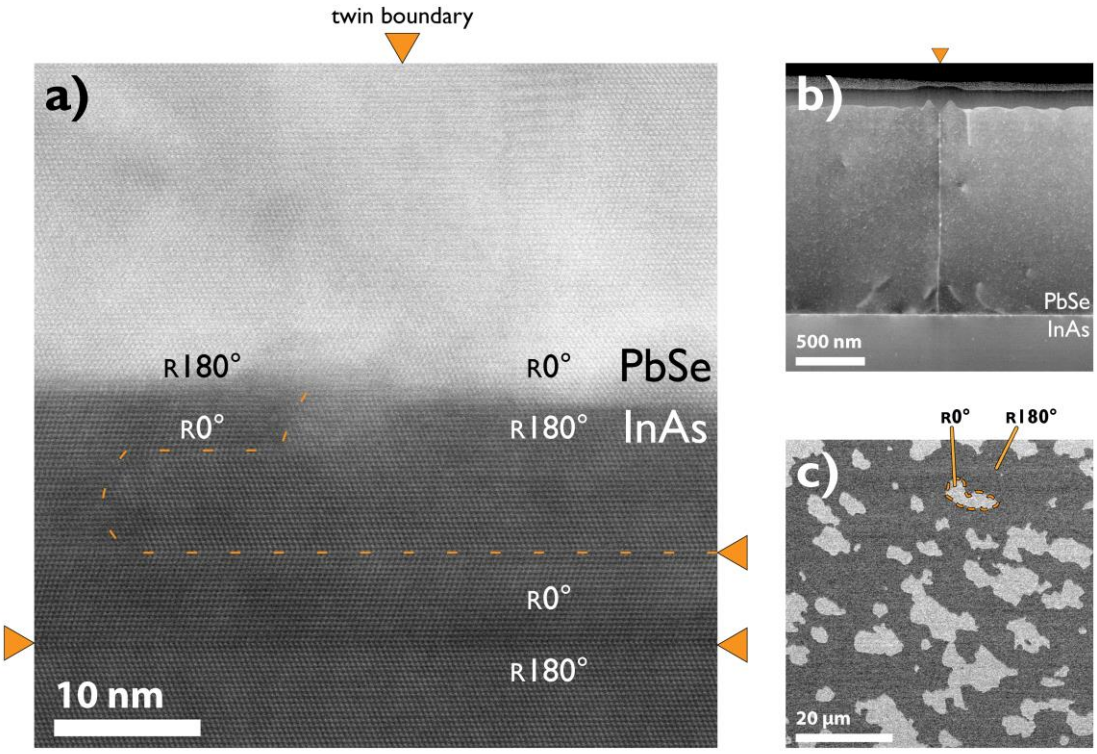

Figure 5.6 – **Subsurface twins in InAs can propagate into the PbSe film**
(a) HR HAADF-STEM of a twin boundary in the InAs buffer intersecting the heteroepitaxial interface and inducing a twin boundary in the 1.5 µm PbSe film. (b) ADF-STEM of a twin boundary in a PbSe film, terminating in a faceted trench at the film surface. (c) Plan-view ECCI micrograph of a 65 nm PbSe film with rotated/mirrored grains originating in the buffer layer. [Processing details: (b) denoised with 2px median filter, (c) smoothed with α = 1 µm gaussian blur.]

Figure 5.6b shows a wider view of one of these boundaries in darkfield STEM. The twinning in the InAs substrate is close enough to the interface that it is nearly invisible at this scale, but the twin boundary in the PbSe is bright, and grows upwards vertically until intersecting the surface, where a shallow trench has formed between the grains. Interestingly, this trench is also highly crystallographic, and opens with faces ~36° to vertical, indicating mirrored {100} surfaces form the internal faces of the trench.

The grain structure in these PbSe films inherited from the InAs substrate is quite large, with typical faulted regions spanning tens of microns. Figure 5.6c shows plan-view ECCI of a 65 nm PbSe film – we believe that the majority of the film (dark contrast) does not have rotational

twins in the buffer, and is then 180° rotated to the substrate, while the pockets of light contrast are grown on rotated/mirrored buffer, and share symmetry with the substrate.

V. INTERFACE STRUCTURE OF SnSe(100)/PbSe(001)

Introduction to 2D/3D interfaces

Unlike the 3D rocksalt IV-VI materials like PbSe, PbTe, and PbSnSe, SnSe is a 2D layered van der Waals (vdW) material with an orthorhombic unit cell and the Pnma structure. Granted this difference, we have used this IV-VI/IV-VI system to explore 2D/3D heterointerfaces, exploring how mixed-dimensional structures can form between chemically compatible and structurally commensurate materials with different crystal structures and symmetries.

Integrating materials with different structural and bonding dimensionality, 0D to 3D, forming mixed-dimensional heterostructures, allows for the harnessing of new physical phenomena in devices – careful work in developing nearly defect-free routes for high quality 0D,1D, and 2D III-V semiconductor quantum dots, wires, and wells in 3D semiconductor matrixes not only enabled new science but also practical electronic and photonic devices. Recently, 2D layered materials with van der Waals (vdW) interlayer bonding and dangling-bond-free interfaces led by transition metal dichalchogenides (TMDCs) have generated excitement in a special class of mixed-dimensional vdW heterostructures with conventionally bonded 3D materials that show promise in a range of electronic devices. Such structures may one day allow for defect-free integration, accommodation of thermal mismatch, and electronically active mixed-dimensional junctions.

These 2D/3D structures present new challenges for heteroepitaxy and require managing even greater disparities in symmetry, bonding, and structure than other systems. One of the most popular routes to 2D/3D integration eliminates the concern of symmetry by relying on the on the

6-fold or 3-fold symmetry shared by many TMDCs and the (111) surfaces of cubic materials[133], but many lower-symmetry layered materials, like SnSe, also show promise[134,135] and warrant investigation. We have worked to integrate SnSe films on GaAs(001) substrates through the use of a PbSe interlayer. Leveraging the work I presented in the last chapter to create a stable heterovalent interface between PbSe and GaAs, we can isolate the problems of symmetry and dimensionality at the interface between PbSe and SnSe.

SnSe(100)/PbSe(001) interface: dimensionality and heterocrystallinity

When grown on chemically and structurally-compatible rocksalt PbSe, SnSe takes on a controllable epitaxial arrangement where SnSe[100] (vdW axis) is parallel to PbSe[001] and SnSe[001] is parallel to either PbSe[110] or PbSe[1$\bar{1}$0], respectively (Figure 5.7). SnSe has a layered structure with two mutually 180° rotated vdW layers per unit cell, each of which consists of two covalently bonded atomic monolayers, and the atomic arrangement of any individual atomic layer bears striking resemblance to the rocksalt (001) plane (Figure 5.7e) - if the SnSe unit cell is strained +4.66% in the [010] direction and -2.53% in the [001] direction, the base of the unit cell is made square and corresponds with the (001) plane of PbSe rotated 45°.

It's also important to note – SnSe has lower rotational symmetry than PbSe, so the epitaxial arrangement shown could be just as easily nucleated in any of four directions. This randomness is an unavoidable side effect of symmetry, and Figure 5.7d shows a plan-view ECCI micrograph revealing two distinct populations of grains: 0°/180° and 90°/270° rotations, with grain boundaries falling preferentially along the SnSe[110] and SnSe[1$\bar{1}$0] directions. Only two populations of grains can be seen, not four, because a 180° rotation of SnSe is equivalent to a vertical displacement of a/2, rendering them indistinguishable to diffraction.

Where an interface between PbSe and InAs (chemically-incompatible 3D) or Bi_2Se_3/SiC

(Chemically incompatible 2D/3D)[136] may be atomically sharp, the chemically-compatible 2D/3D interface we observe is smeared out distinctly over 2-3 vdW bilayers. Notably, the onset of vdW layer formation appears to precede the full SnSe orthorhombic structure by 3 bilayers

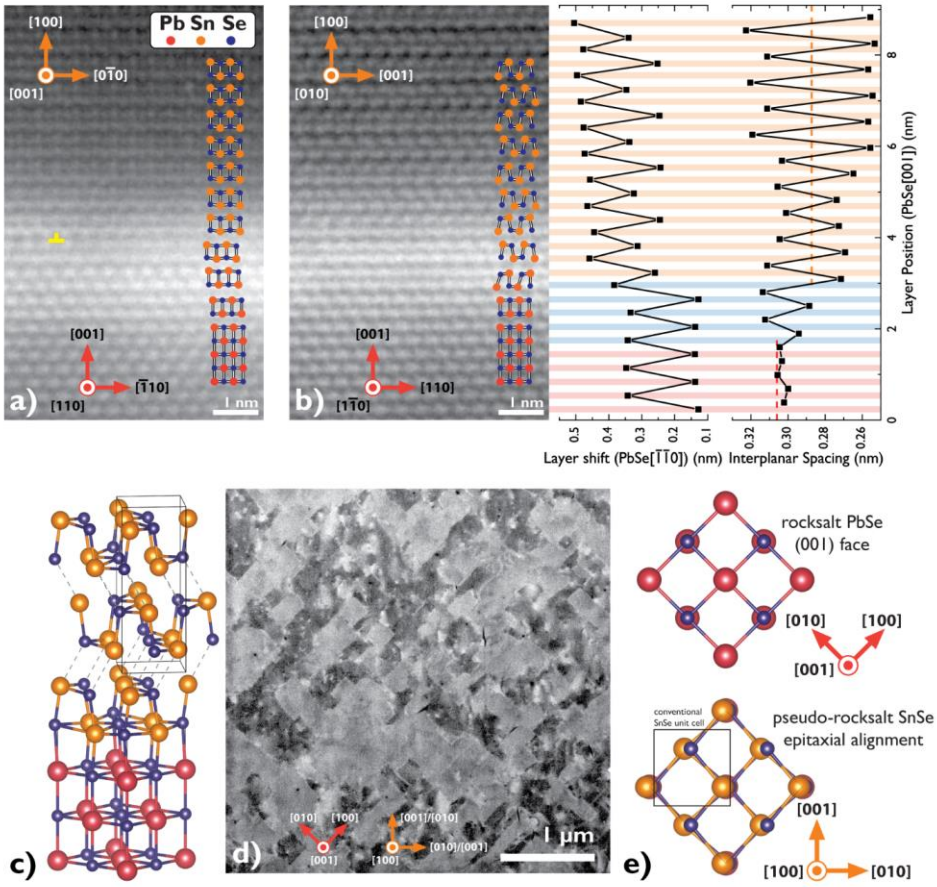

Figure 5.7 – **SnSe/PbSe(001) interfacial structures.**
High resolution HAADF STEM of the SnSe/PbSe interface and plan-view ECCI, showing the heteroepitaxial arrangement. (a) and (b), orthogonal cross-sectional projections of the interface. [HAADF images processed with linear brightness/contrast and α = 0.2 Å gaussian blur.] (b) includes two graphs which, based on averaged HAADF contrast, show the lateral layer shift and interplanar spacing of and between each monolayer of atoms. The blue-marked region is transitionary, and contains a layered structure with rocksalt-like stacking. (c) Isometric projection of a hypothetical sharp interface, conventional SnSe unit cell included. (d) ECCI of a SnSe layer polished by FIB showing two populations of 90° rotated grains with rectangular grain boundaries, and dislocation contrast within one of those populations of grains. (e) the pseudo-rocksalt stacking of SnSe on PbSe, showing the similarity of the PbSe (001) surface and the SnSe (100) surface. The SnSe unit cell shown has been slightly strained to appear square. Notice that even in this symmetrized form, SnSe has lower rotational symmetry than PbSe.

(Figure 5.7b), resulting in an epitaxially constrained transition region which exhibits a layered structure, but the stacking order of rocksalt. Even beyond this transition region, the layer spacing doesn't stabilize for approximately 3 nm into the SnSe layer. As stable alloys of PbSnSe exist in both the rocksalt and Pnma structures, and atom probe tomography suggests that the chemical interface between PbSe and SnSe is approximately 5 nm wide, we do not think it is reasonable to define a specific truncation point for the SnSe unit cell, instead, the unique chemical and structural similarities between these otherwise distinct materials allow for a wide transitionary layer.

Layer stacking and defect transmission between disparate crystal structures

The highly commensurate crystal structures and compatible chemistry between PbSe and SnSe allow for the direct transmission of defects like dislocations from substrate to film, and the lower symmetry of the SnSe epitaxy on the highly symmetric PbSe buffer allows for rotational grains and stacking faults to be formed from previously-innocuous features like steps on the PbSe surface.

Figure 5.8a shows a variety of methods to achieve different stacking sequences in SnSe films, and near the interface, we commonly see a variety of stacking defects, like those highlighted in Figure 5.8b. When first nucleating SnSe on PbSe, (or at least orthorhombic PbSnSe on rocksalt) symmetry considerations allow for the synthesis of defective stacking sequences when different rotations of SnSe nucleate on adjacent PbSe terraces and overgrow each other, resulting in a locally random sequence of four different possible layer rotations. The most common defective stacking sequence in 2D materials seems to be a metastable AA stacking sequence, which has commonly been produced via spiral growth, and has been observed in the 2H layered TMDCs $SnSe_2$, MoS_2, and WSe_2 [137–139], as well as hBN[140]. In MoS_2, this AA stacking was first observed as the "3R" structure [141], and recent first principles calculations suggest that the 2H and 3R structures differ by just 0.06 eV/formula unit[137], highlighting the relative independence of vdW layers in

2D materials.

In Figure 5.8b, where the stacking sequence changes from AA in the bottom left corner to AB stacking in the bottom right, the boundary between these layers only actually creates a defect (a mirror twin) in *every other* vdW layer. Half of the vdW layers are unaffected, and the overall 2D nature of the material is preserved. After the SnSe in Figure 5.8b grew to be 10-15 nm thick, the equilibrium AB stacking has completely dominated, so the step-overgrowth or spiral growth effects which created these irregular stackings do not dominate epitaxy far from the interface. Based on these results, and very smooth surfaces indicated by RHEED, we tentatively assume a layer-by-layer growth mode for thick layers of SnSe via MBE.

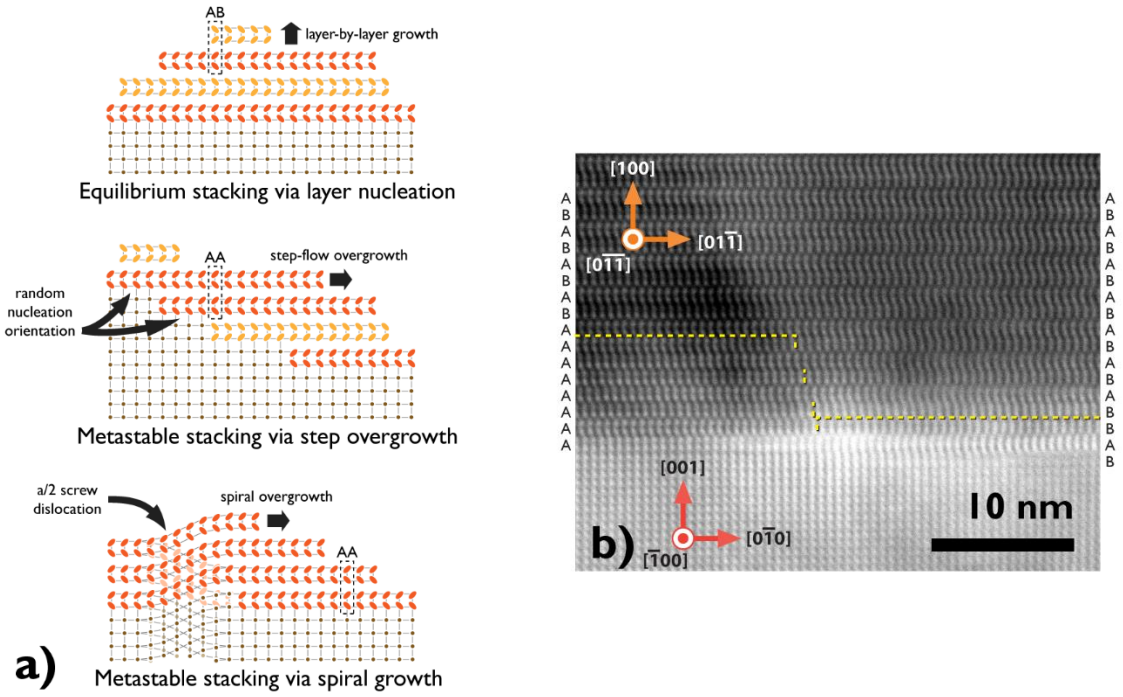

Figure 5.8 – **Stacking irregularities during SnSe nucleation and growth.** (a) three ways to create different stacking sequences in SnSe. (b) PbSe[100] high resolution HAADF STEM cross section showing irregular stacking near the SnSe/PbSe interface. This projection cannot distinguish between the SnSe [011] and [01$\bar{1}$] directions, which look identical, but can distinguish between these directions and their mirrors, [0$\bar{1}\bar{1}$] and [0$\bar{1}$1]. Making the *assumption* that all layers pictured are either 0° or 180° rotated, boundaries between different stacking sequences are marked with a dotted line.

Dislocation structures in SnSe are complicated, made worse by the very tall unit cell and, in this study, the tendency to inherit atypical dislocations from the PbSe substrate. Figure 5.9a-c show a high density of dislocations within the grains. Two different 2-beam conditions, PbSe(040) and PbSe(004), and an on-axis condition PbSe[100] are used here to differentiate between dislocations with burgers vectors which lie exclusively in or out of the growth plane. Dislocations which appear in (a) and not in (b) have burgers vectors that lie in the growth plane, regardless of line direction – so called threading hyperdislocations[142,143] or inter-sheet dislocations like the edge misfit dislocation highlighted in Figure 5.7a would meet this criterion. Dislocations which appear in (b) have a finite burgers vector projection in the SnSe[100] direction, and so mark the edge of a vdW sheet (misfit dislocation) or a helical spiral of vdW sheet (threading dislocation). Figure 5.9a-c shows many dislocations with a variety of burgers vectors,

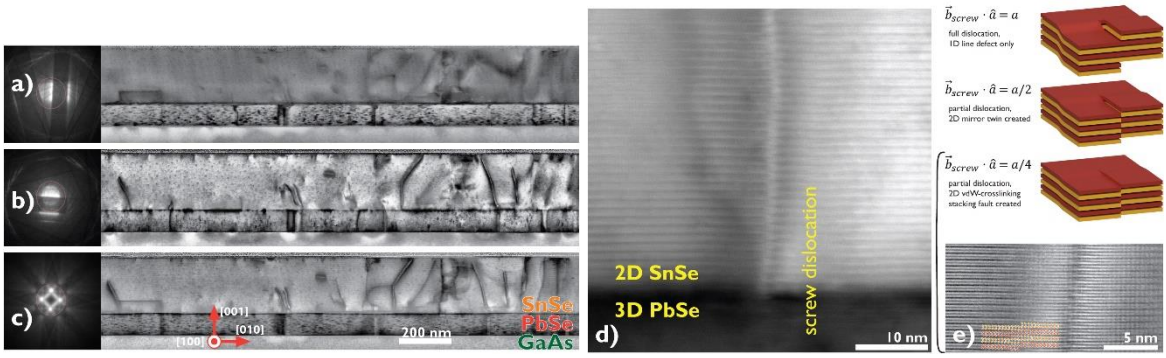

Figure 5.9 – **Novel dislocations and stacking faults in 2D SnSe films.**
(a-c) Cross sectional STEM with different diffraction conditions to highlight that a mixture of burgers vectors and stacking faults exist in these layers. This image is part of a larger analysis: across a 22 μm long STEM cross section, approximately 1/3 of dislocations in the PbSe buffer layer had a matching dislocation directly above in the SnSe layer, and the number of distinguishable defects (dislocations and grain boundaries) at the bottom of the SnSe layer is approximately 25% higher than at the top of the PbSe buffer layer. (b) brightfield STEM of a single dislocation with an a/4 screw component continuing from the PbSe buffer into the SnSe film. (e) full dislocations and partial dislocations with a/2 and a/4 burgers vectors bound different 2D stacking faults. An a/4 stacking fault is pictured with HAADF STEM, demonstrating crosslinking between vdW sheets. [Processing notes: (a) enhanced with local contrast adjustment. (e) image stacked and smoothed with a 0.1Å Gaussian blur]

some of which appear to originate directly from the PbSe buffer.

We believe that unlike in most vdW epitaxy, these SnSe/PbSe interfaces are so gradual as to allow for the direct passage of dislocations from one crystal system to the next. We have previously characterized the burgers vector of misfit dislocations formed during coalescence of PbSe/InAs as $\langle 101 \rangle$ family[101]. If nucleation defects on GaAs substrates behave similarly, then most of the dislocations exiting the top surface of the PbSe buffer will have a burgers vector of $\frac{\sqrt{2}}{2} a\langle 101 \rangle$ type with a magnitude of 4.33 Å. When translated into SnSe with its pseudo-rocksalt epitaxial arrangement, this burgers vector necessarily distorts to match the new structure, but constitutes only a partial dislocation in the SnSe structure, nominally one monolayer, half of a vdW bilayer, or one quarter of a unit cell tall. Instead of a full screw dislocation which creates a line defect but preserves the crystalline structure of SnSe away from the core, or a nominally a/2 dislocation, which would result either in AA stacking, or the creation of a mirror twin *within* each vdW layer, either while preserving the overall 2D structure, a nominally a/4 dislocation creates a stacking fault that binds adjacent vdW layers together with covalent crosslinks (Figure 5.9e, graphic). Figure 5.9d shows a threading dislocation that starts in the PbSe layer and continues into the SnSe layer that we believe has an a/4 screw component, but the existence of the stacking faulted region bordering this dislocation makes the HR images difficult to interpret directly. The HAADF cross section of Figure 5.9e, however, directly images a stacking fault resulting from such a dislocation. Alternate vdW layers are bonded together, locally creating a 3D covalent network within the 2D material.

Even when not grown epitaxially, layered van der Waals materials frequently grow via spiral growth and step-flow mechanisms [138,144–146], implying a significant bias for adhesion at step edges, and a very high adatom mobility on top of a van der Waals sheet. One notable

example of spiral growth in a van der Waals material comes from Liu at al. [144], who grew Bi_2Se_3 on chemically incompatible Graphene/SiC and observed vdW layers peeling up to overgrow surface steps on the substrate, creating new defects and initiating spiral growth with a full screw dislocation. Although Bi_2Se_3 could theoretically incorporate an unfavorable partial screw dislocation, loose bonding to the substrate allows it to avoid this energetically costly outcome. This opportunity is not available at the SnSe/PbSe interface, where a gradual transition in both chemistry and structure forces the epitaxial SnSe to incorporate defects like surface steps and threading dislocations. When transformed into the taller and less symmetric SnSe structure, common rocksalt dislocations can induce large-area defects in a 2D material.

Such large-area defects have significant implications for the deformability of a 2D material. The asymmetry of bonding and subsequently, mechanical properties, in 2D materials are one of the reasons they are so intriguing from a research perspective. Ideal 2D materials can easily be sheared in the basal plane as adjacent layers slide over each other. But by crosslinking adjacent layers and breaking the vdW gap, these unique defects significantly inhibit dislocation motion and "sheet sliding" as mechanisms of shear in 2D SnSe. The next chapter will include discussion of sliding SnSe buffer layers for quasi-vdW epitaxy.

6.Film Coalescence and Relaxation

I. INTRODUCTION

PbSe growth modes

Unsurprisingly with their peculiar bonding, the IV-VI rocksalts are not known to grow layer-by-layer on any non-IV-VI surface. The high interfacial energy of heteronucleation prevents otherwise low-surface-energy rocksalt films from wetting the relatively high-energy surfaces of fluorite [13,46,147], diamond cubic[13,15], cubic perovskite[112], or zincblende[21,22,49] substrates. Poor bonding between ionic PbSe and covalent Si has been known to prevent growth of high quality layers[13], and weak bonding between IV-VI films and BaF_2 substrates has also been observed. Highlighted most notably in section III of the previous chapter, PbSe films can be almost completely non-interacting with their substrate.

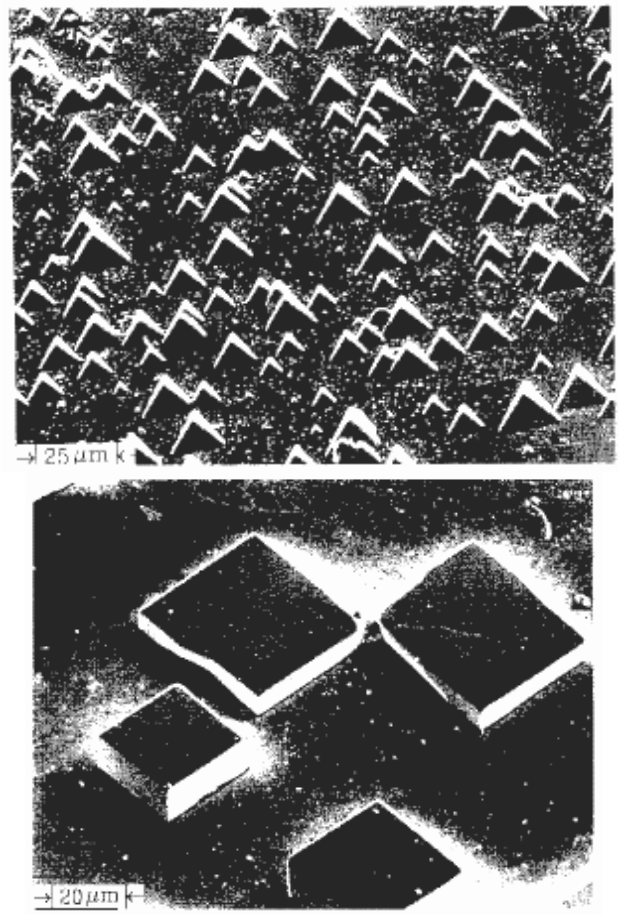

Figure 6.1 – **PbSe nuclei grown on BaF2 substrates via LPE in two orientations.** Top, (111); bottom, (001). Reproduced from [152].

In cases where film is loosely attached to substrate, and allowed to obey its own equilibrium preferences, the IV-VI rocksalts exhibit extreme preferences for surface faceting. Clearly visible {100} terminations on islands (Figure 6.1) highlight the stability of these crystalline surfaces, where (111)-oriented PbSe islands adopt a truncated-cube pyramidal confirmation, and

(001)-oriented PbSe islands form large rectangular prisms. In the present work, we have also never observed a reconstructed PbSe or PbSnSe surface in either the (001) or (111) orientation. RHEED always shows a 1×1 periodicity after the onset of IV-VI growth.

Much of the difficulty in growing high-quality PbSe layers comes in controlling the defects created when these islands fuse and coalesce into a contiguous film. The weaker the bonding between the film and substrate, the more misoriented each independent grain will be, and the more dislocations will be incorporated during coalescence.

Thermal mismatch and dislocation glide in the IV-VI Rocksalts

Unlike most ionic rocksalts[148], the IV-VI rocksalts' primary slip system is $\{001\}\langle\bar{1}10\rangle$, meaning typical dislocation burgers vectors lie in $\langle\bar{1}10\rangle$ directions and dislocations glide on $\{001\}$ planes. Consequently, this slip system feels no resolved shear stress from in-plane strain on an (001)-oriented film[16] and thermally mismatched IV-VI films readily crack upon cooldown[13,15,149,150], even when cooling from low growth temperatures. As the IV-VI rocksalts have extremely high thermal expansion coefficients, only the fluorite substrates (BaF_2, CaF_2) come close to thermal-matching[151], and these substrates are prepared by cleaving on (111) planes, making their similar thermal expansion a moot point (only one study[152] has used polished BaF_2(001)). Growth on more conventional (001) III-V or Si substrates will always have to contend with this problem, and successful attempts to limit or eliminate cracking largely credit climb[150,153,154] or secondary slip systems[13,14,149] like the $\{101\}\langle\bar{1}01\rangle$ that do feel resolved shear for (001) in-plane strain. Using LPE, Strecker et al.[150] grow PbSe from an off-stoichiometry melt, resulting in a high concentration of selenium vacancies which they claim facilitates relaxation via climb. Li et al.[149], using LPE to grow PbSnSe, observe fewer cracks at high temperatures, which they attribute to activation of secondary slip by climb-nucleating

secondary-glissile dislocations during growth. They clarify that the selenium vacancy concentration necessary to achieve such a result is not attainable via MBE.

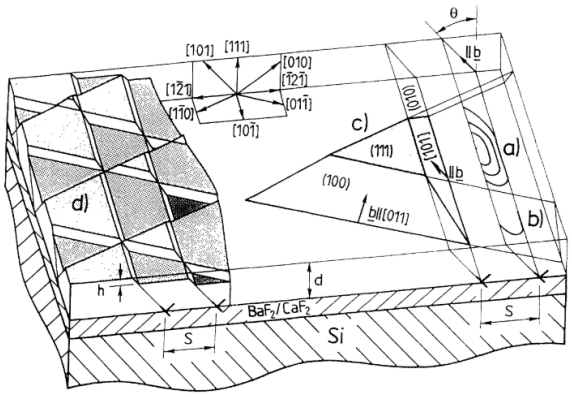

Figure 6.2 – **Active {001}⟨110⟩ slip system of PbSe.**
This schematic shows relaxation of in-plane strain in a (111)-oriented film grown on a BaF_2/Si buffer. This process results in a triangular grid of misfit dislocations, and a corresponding triangular grid of surface steps. Reproduced from [151].

The handicap of the PbSe slip system becomes an asset when growing IV-VI films oriented in the (111) direction. With this geometry, in-plane strain exerts significant resolved shear stress on three slip planes of PbSe (Figure 6.2). This slip system has extremely low barriers to dislocation glide[148], amazingly enabling glide even at cryogenic temperatures, permitting full relaxation[151], and allowing for annihilation of dislocations during growth with high efficiency[16]. The ability to access this slip system enables (111)-oriented IV-VI structures to be grown thicker without cracking, to be improved via thermal cycling, and to be temperature-tunable without inducing strain into a device. With these considerations in mind, the vast majority of MBE growth of IV-VI rocksalts has been in the (111) orientation, on fluorite substrates or silicon(111) substrates, often with a fluorite buffer layer to facilitate epitaxial nucleation. One of the primary goals of my work was to explore the relaxation behavior of PbSe when strongly-interacting with an (001)-oriented substrate.

Parts of this chapter are based on published results from the papers *Nucleation control and interface structure of rocksalt PbSe on (001) zincblende III-V surfaces*[101] and *Interface structure and luminescence properties of epitaxial PbSe films on InAs (111)A*[102], as well as results from a forthcoming paper on SnSe epitaxy.

II. COALESCENCE DEFECTS IN (001) PbSe

PbSe island coalescence on InAs(001)

In order to examine the growth behavior of single-orientation PbSe towards usable thin films, we truncated growth at different stages of island coalescence and characterized the structure with standard secondary electron imaging as well as electron channeling contrast imaging (ECCI) in SEM. SEM of partially coalesced samples grown at 330 °C (Figure 6.3) reveals the single-

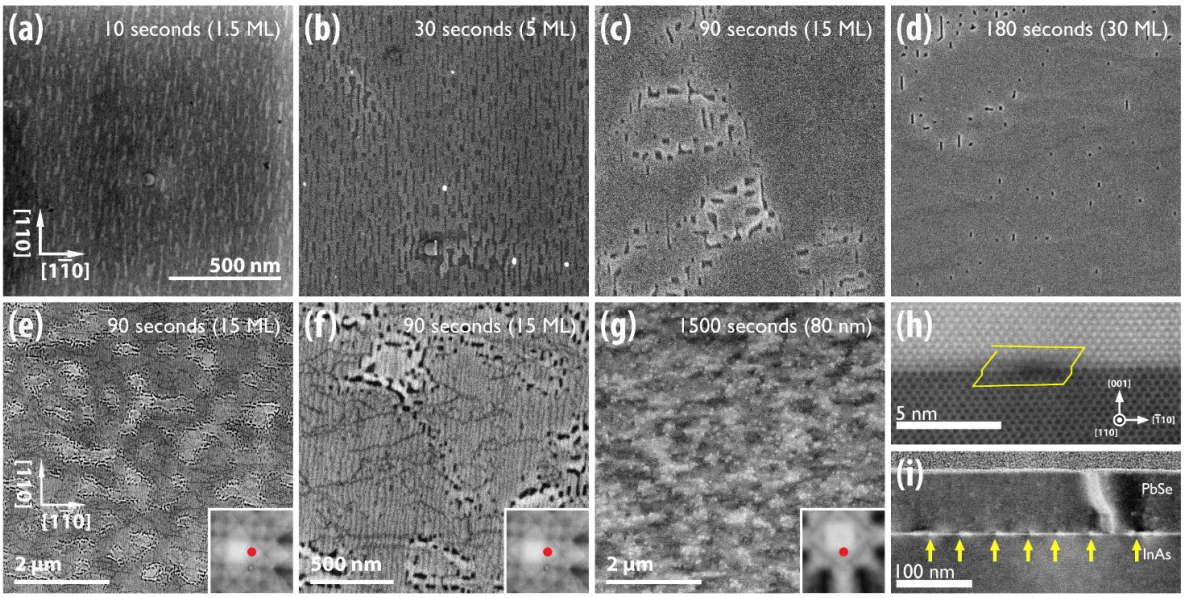

Figure 6.3 – **Coalescence of PbSe islands on InAs.**
(a-d) SEM micrographs of PbSe coalescence geometry: After nucleation on the 2×1 InAs surface, initial elongated islands come together to form a dense network. As this is "filled in" by continued PbSe flux, some gaps remain, decorating the edges of low-angle grain boundaries. Eventually the film fully coalesces, resulting in a moderately smooth, hole-free surface. (e-i) Origin and persistence of coalescence defects: (e,f) ECCI micrographs ({220} conditions) of a coalescing 90 second growth with orientation contrast highlighting low angle grain boundaries bordered by holes in the film. (g) ECCI micrograph of a fully coalesced film highlighting the persistence of these slight misorientations, now decorated by threading dislocations. (h,i) HR-HAADF STEM and DFSTEM of the PbSe/InAs interface, looking down the [110] zone axis. In ECCI (f), dark lines within grains form a grid of dislocations highly ordered across [1$\bar{1}$0] but inconsistent across [110]; these misfits are also observed in STEM; and a single misfit from the PbSe/InAs interface is traced with an incomplete Burgers circuit. We also believe the prominent planar defect in the DFSTEM micrograph is a low-angle grain boundary like those visible in ECCI

orientation (001) PbSe islands that form on the treated 2×1 (001) InAs surface are significantly longer in the [110] direction and very shallow in the [001] (growth) direction. Although they rapidly form an interconnected network, they are slow to coalesce into a smooth pinhole-free film. At these growth temperatures, the sticking coefficient of PbSe on the treated InAs surface is near unity, with rapid PbSe migration across the surface enabling the formation of few-monolayer-tall islands (Figure 6.4). Figure 6.3a-d shows the coalescence progression of PbSe films on InAs. After only ≈1.5 monolayers (ML) of PbSe flux, (001)-oriented islands begin to elongate in the [110] direction. After 5 ML of deposition, these islands are fully interconnected, and after 15 ML, there are large regions of flat coalesced film developing. The remaining gaps in the film coalesce slowly, forming defects which decorate low-angle grain boundaries in the coalesced film.

After 5 minutes (~15 nm) of growth at 330 °C nucleation temperature, the films are generally fully coalesced, but the best results were obtained by subsequently dropping the temperature by 30-60 °C and continuing growth colder. These two-temperature growths produced the highest quality fringing in XRD, and produced 80 nm films with an AFM-measured RMS roughness of 1.8 nm over a 2×2 μm area.

The elongation of the initial nuclei shapes is likely inherited from the dimerized 2×1 PbSe:InAs surface. As adjacent islands grow together, they create a grid of dislocations, very closely spaced in the $[1\bar{1}0]$ direction, but more irregular and spread-out

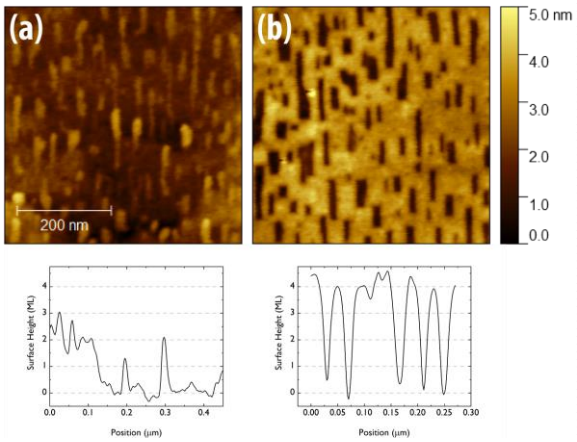

Figure 6.4 – **AFM micrographs of PbSe nuclei on the 2×1 treated InAs surface.** (a) a 10 second growth, and (b) a 30 second growth. Representative height traces from each image are depicted below. Initially, the uncoalesced islands are only 1-3 ML tall, and island interconnection occurs after less than 4 ML. Some of these pinholes persist well into growth due to strain effects.

in the [110] direction. Figure 6.3e-f shows orientation-sensitive ECCI micrographs of the grain structure of these films during and after coalescence. The resultant grains are slightly elongated in the $[1\bar{1}0]$ direction, and the dislocation density necessary to define these small grains is very high.

Figure 6.3h-i show a more detailed view of one these boundaries and an array of misfit dislocations. Low-angle grain boundaries appear inconsistently every few hundred nanometers, while the misfit dislocations are evenly spread along the interface, remnants of island coalescence. The Burgers circuit traced in Figure 5h indicates a Burgers vector of $\frac{1}{2}[101]$ or $\frac{1}{2}[0\bar{1}1]$; with a line direction of [110], these dislocations must be sessile, unable to rearrange at the interface to form an even grid as has been observed at PbTe/PbSe interfaces[154]. The less-regular $[1\bar{1}0]$-oriented dislocations observed in Figure 6.3f are likely similar and also locked-in immediately after island coalescence. Although the primary $\{100\}\langle 110\rangle$ slip system in PbSe is active even at low temperatures, dislocations in this system experience no resolved shear stress from in-plane biaxial strain for (001)-oriented growth[16], preventing glide of any dislocations to alleviate film-substrate mismatch.

Modifying island shape with chemistry and mismatch

In an effort to reduce misfit formation during island fusion, we investigated the use of excess selenium flux to control the shape of the islands pre-coalescence. By enforcing selenium termination of the PbSe film, theoretically, islands could be made to truncate preferentially on {111}-type planes, creating shallower islands with negatively sloped walls. As these islands would meet only at their vanishingly thin edges, we hoped it would suppress formation of [101]-type dislocations and coalesce a perfectly coherent layer below critical thickness. While experiments show excess selenium produces markedly different island shapes (Figure 6.5b), fusion of these modified islands does not create coherent films (Figure 6.5c).

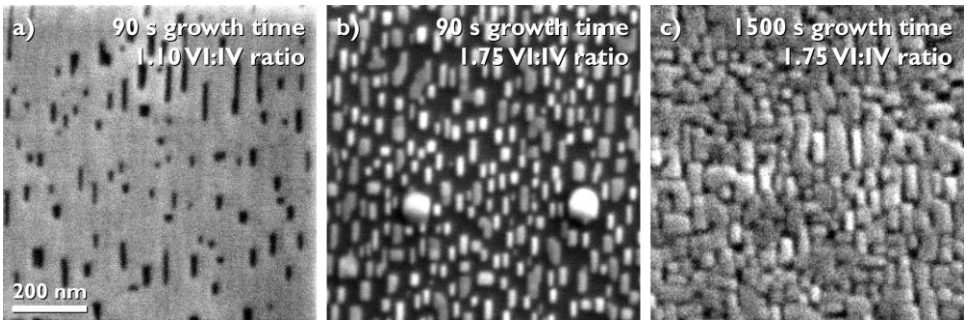

Figure 6.5 – **Modifying PbSe island shape with excess selenium flux.**
By adding selenium flux in addition to molecular PbSe flux, islands get narrower and taller before coalescence, leaving lasting trenches in the coalesced film. (Flux ratios calculated assuming elemental Se at the ion gauge)

It is clear that at these scales, with islands tens of nanometers across and units of nanometers tall, selenium overpressure does not create pyramidal islands. For larger surfaces it may alter the relative surface energies of (110) and (111) facets of PbSe, but at these scales, surface tension seems dominant. In fact, selenium overpressure appears to make PbSe islands grow taller and narrower, indicating that a selenium adlayer significantly increases cohesive surface tension or significantly alters adatom mobility.

Lattice mismatch, as well as surface chemistry, can produce qualitatively distinct island shapes and film grain structure, but via lattice mismatch, not chemistry. (001) PbSe islands on treated (001) GaAs surfaces favor termination on {100}-type planes – the low-energy-rocksalt planes (Figure 6.6a) – rather than elongating in the [110] direction as on treated InAs (Figure 6.3a) or having little lateral order as on GaSb (Figure 4.1e-f).

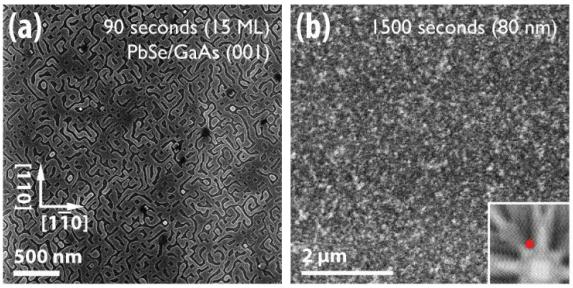

Figure 6.6 – **Coalescence of PbSe islands on GaAs.**
(a) SEM micrograph of a coalescing PbSe layer on GaAs. The islands have formed an interconnected network but have not fully coalesced into a smooth film. The islands preferentially truncate on {100} planes. (b) ECCI micrograph of a fully-coalesced film. Orientation contrast highlights the high density and uniformity of low-angle grain boundaries.

It appears that connected PbSe islands on GaAs grow laterally to a characteristic width of 40-50 nm then grow vertically, leaving a notable fraction of exposed substrate even after significant material deposition. Compared to an equivalent growth on InAs (Figure 6.3c), the coalescence on GaAs (Figure 6.6) is extremely slow, suggesting PbSe adatoms may have higher mobility around highly strained (or mismatched) crystals. On InAs, we hypothesized that the holes visible early in PbSe film growth could be the result of local strain between islands, where holes encapsulated non-zero Burgers circuits. On GaAs, a chemically similar but lattice-mismatched substrate, we observe this lack of adhesion across the entire surface – apparently the macroscopic ramifications of the weak bonding discussed in the last chapter (Figure 5.3). The low adhesion of PbSe near strained regions highlights a peculiarly specific preference for lattice-matched substrates - a small amount of local strain can affect resonantly-coupled bonds for long distances.

Strain induced pitting and PbSe growth on ErAs(001) buffer layers

When we grow PbSe in such a configuration to induce significant amounts of strain or limit the relaxation capability of the film, we find pits and cracks in films. The holes in the PbSe film on InAs(001) in Figure 6.3 we believe are open-core dislocations – ie. we believe they encircle non-zero burgers circuits, but the most extreme pitting we have observed occurred during experiments with rocksalt ErAs buffer layers.

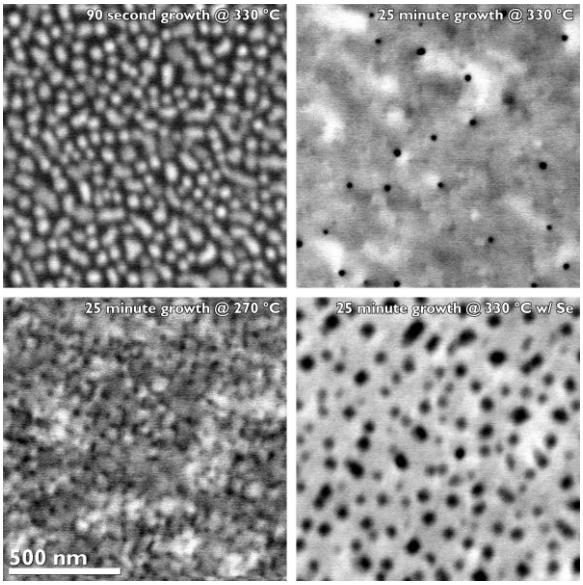

Figure 6.7 – **Slow coalescence of PbSe on ErAs.**
ECCI micrographs of PbSe/ErAs/GaAs grown under varying conditions. (nucleation only, nominally 80nm film low-temperature growth, and growth with a selenium surfactant layer.)

ErAs is a rare-earth rocksalt nearly lattice matched to GaAs, indeed it is known to wet GaAs, and can be grown layer-by-layer[155–157] with monolayer resolution[158]. We grew 3 ML of ErAs on GaAs(001) substrates to achieve a rocksalt termination with "vertical" dangling bonds in an effort to produce a better nucleation template for PbSe. By isolating the symmetry and surface charge shifts at the ErAs/GaAs interface, we hoped to make the next PbSe/ErAs interface simpler, only dealing with heterovalency and lattice mismatch. ECCI micrographs of these films are shown in Figure 6.7.

PbSe nucleation on these templates was extremely uniform, with no indication of off-orientation grains via RHEED, implying a strong favorable interaction between the substrate and film. Unfortunately, this strong film-substrate bonding contributed to extremely small grains, likely coherently strained prior to coalescence. We believe that local strain near the edges of the islands prevented adatoms from sticking, slowing coalescence. Once these highly strained islands finally collided, many misfit and threading dislocations were created, and threading segments again became pits, or open-core dislocations. Attempts to grow the PbSe film colder or under a surfactant layer of excess selenium flux only made this problem worse, resulting in a higher density of pits. In the ECCI micrographs of Figure 6.7, the regions between pits also has a mottled texture, the extreme mosaicity that results from nanoscale grain fusion.

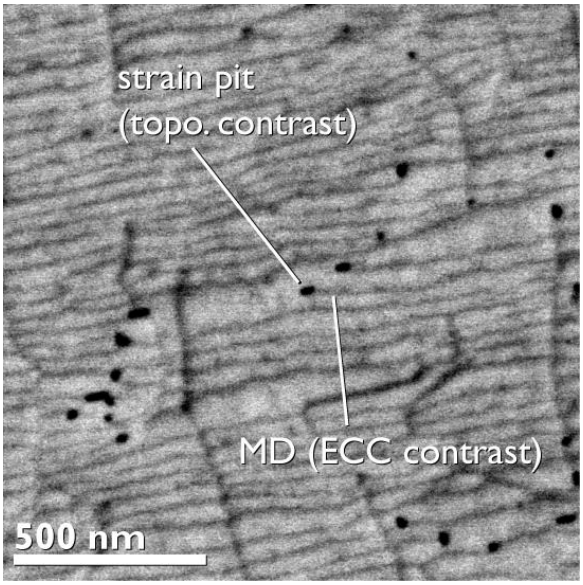

Figure 6.8 – **Strain pits in a PbSe film.** ECCI micrograph of a PbSe film grown on a PbSe/GaAs buffer layer. A misfit dislocation (distortion visible to ECCI) terminates at a pit (topography visible to BSE). [stacked image]

A close-up example of a strain pit in

PbSe on a III-V substrate is shown in Figure 6.8. A misfit clearly terminates at a pit, and since a dislocation cannot end within the crystal, it must effectively bend into a threading segment, but in this case the pit, not a closed dislocation core, transmits the necessary Burgers character to the surface of the film. These pits can frequently be eliminated by growing at a lower temperature, so these pits may simply be thermal etch pits, where adatoms are easy to remove near strained features like dislocations. This effect may be amplified by the "resonant" bonding in PbSe, where stretching or breaking of one bond may weaken those around it. Considering that nucleation needs to occur at higher temperatures to eliminate misoriented grains, this surface instability makes strained PbSe very difficult to grow smoothly. Our best results at fighting this effect on any substrate have been achieved by dropping the growth temperature immediately after coalescence to increase the sticking coefficient near defective regions.

Cracking in alloy PbSnSe

Alloy hardening in the IV-VI family appears to be a significant problem, at least when depending on climb and secondary slip to relax films. Figure 6.9 shows an alloy PbSnSe film with cracks every 3-2 μm along the surface. In pure PbSe, films, thermal cracking does not occur for films thinner than 200-300 nm, however this alloyed film is less than 80nm thick and cracked readily. It also seems to have more internal strain near dislocation cores, as the surfaces between cracks contain many strain pits.

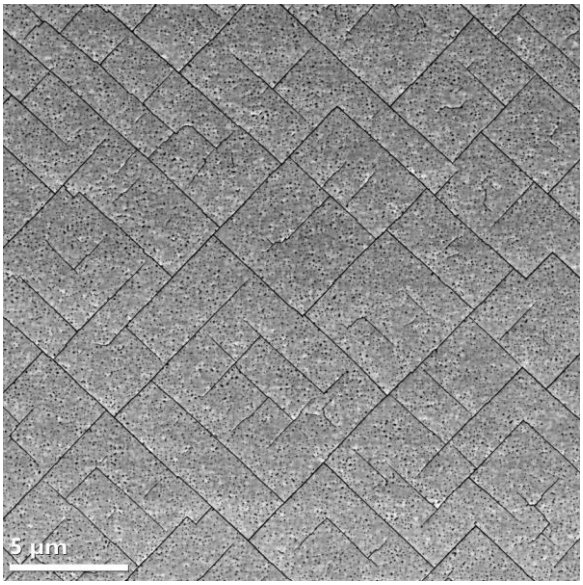

Figure 6.9 – **Alloy hardening: cracks in a thin film of $Pb_{0.6}Sn_{0.4}Se$.**
ECCI micrographs of a PbSnSe film grown on a PbSe/GaAs buffer layer. The film is covered with small strain-induced pits, and has cracked during cooldown. This film is less than 80nm thick, far below the critical thickness for cracking of pure PbSe films.

Alloy hardening is typically a term relegated for structural materials, but it is becoming more important in semiconductor growth as the limits of heteroepitaxy are pushed farther[58]. For the IV-VI rocksalts, especially in the(001) growth orientation, alloy hardening could become a very severe limiter of device design, as alloyed layers necessary for bandgap engineering could become embrittled, either directly, or via dislocation pipe-diffusion easily mixing lead and tin species across layers.

Structural quality of PbSe/InAs(001)

Successfully-coalesced PbSe films grown on InAs substrates are of relatively high crystalline quality with sharp interfaces, good rocking curve widths, and good registry to the substrate (Figure 6.10). The 2θ-ω full width at half maximum (FWHM) of the PbSe (004) peak is 410 arcseconds for an 80 nm film, and for a thicker ~320 nm film, a 2θ-ω FWHM of just 181 arcseconds was measured. For the 80 nm film, mosaic twist about the [001] direction was measured via a {224} ω rocking curve in skew-symmetric geometry, with an observed FWHM of 457 arcseconds. Mosaic tilt in the 80 nm film was measured with orthogonal (004) ω rocking curves. FWHMs of 185 and 369 arcseconds were observed about the [110] and $[1\bar{1}0]$ directions, respectively. This result is on par with microns-thick layers of PbSe on (001) GaAs, with a rocking curve FWHM of 266 arcseconds reported by Wang et al.[22]. Figure 6.10 also includes a pole figure, a 360° ϕ-scan of the {224} peaks of PbSe and InAs, showing excellent epitaxial registry with no apparent population of significantly twisted grains. Analysis of ECCI micrographs (eg. Figure 6.3g) yields a threading dislocation density in the mid 10^9 cm^{-2}.

Coalesced films of PbSe on InAs contain residual strain resulting from asymmetric relaxation that slightly distorts the cubic lattice. This residual strain is a combination of lattice mismatch during growth and thermal mismatch during cooldown. Measurements of the {224}

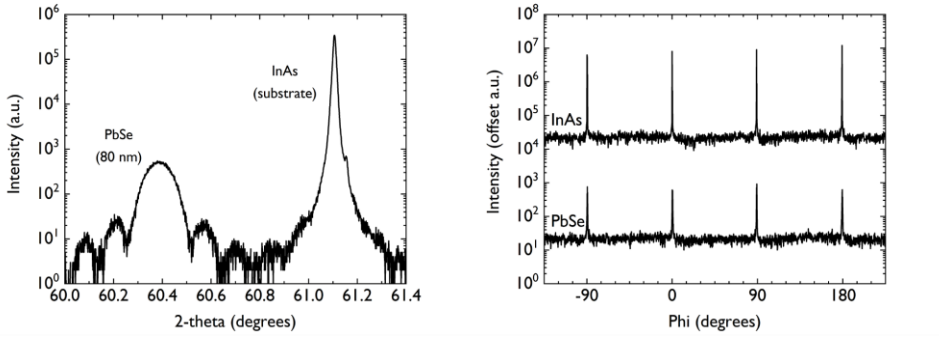

Figure 6.10 – **Crystallinity of PbSe films on InAs.**
(a) 2θ-ω coupled scan of the (004) peak showing a high-quality interface with distinct thickness fringes. (b) A 360° ϕ-scan of the {224} peaks in PbSe and InAs, showing that the nominal epitaxial registration between the film and substrate is (001) cube-on-cube.

plane spacing reveals that the PbSe unit cell at room temperature is 0.02% compressed along the $[1\bar{1}0]$ direction and 0.2% stretched along the [110] direction. We believe this asymmetric relaxation is due to the asymmetric distribution of dislocations observed in ECCI during the early stages of growth (Figure 6.3f), affecting relaxation both at growth temperature and during cooldown. Even with a significant difference in the misfit density in orthogonal directions, the relaxation of in-plane strain is hindered by the immobility of PbSe's primary slip system in the (001) orientation.

III. PbSe GROWTH ON LATTICE MATCHED III-V SUBSTRATES

Lattice mismatch and coalescence defects

As previous experiments growing PbSe on III-V substrates with different lattice parameters (GaAs, InAs, and GaSb: Figure 6.6, Figure 6.3, and Figure 4.1) produced dramatically different island/nuclei morphology, we understood that strain was linked intimately with coalescence behavior and film relaxation during island fusion. To explore this further, we grew PbSe on metamorphic InAsSb buffer layers with varying in-plane lattice parameter, both tensile

and compressively strained to PbSe. Fascinatingly, we see that many different relaxation mechanisms are active in these films, and many variables are involved in governing film behavior.

Figure 6.11 contains overlayed reciprocal space maps of many of these experiments, showing relaxation within each PbSe film. X-ray from each buffer-grown PbSe film contains a substrate peak, GaSb, a partially relaxed buffer layer peak (below) and the PbSe film peak (center). Figure 6.11b-c also include a PbSe film grown directly on InAs as reference, as InAs is more than 1% mismatched to PbSe at growth temperature. In the [110] direction, we see that nearly-lattice-matched compressively-strained PbSe films grow coherently. PbSe films R262, R276, and R279 appear to share an in-plane lattice parameter and approximate FWHM with their buffer layers E037, E045 and E043. In comparison to our results on InAs, sample R111 in the plot, these results are startling, as they imply PbSe islands with low mismatch to a III-V substrate can coalesce *without* creating defects at the interface. Unfortunately, this result does not extend to the tensile-strained

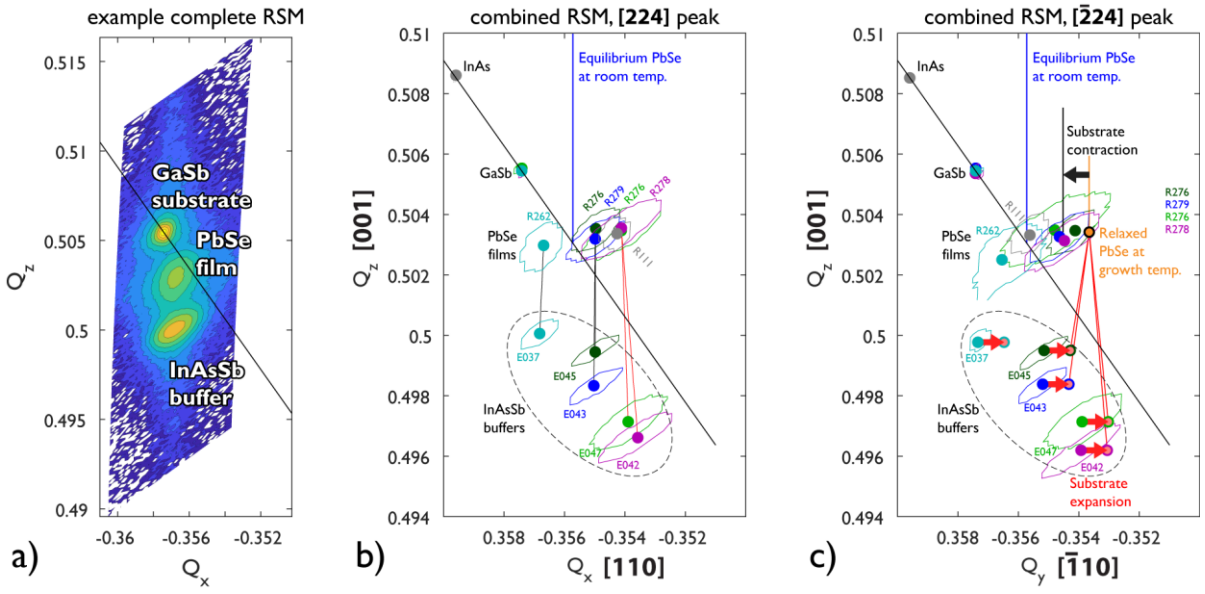

Figure 6.11 – **RSM study of PbSe growth on varying lattice parameter substrates.**
(a) Example RSM with color-scaled data projected into reciprocal space. (b,c) Condensed RSMs showing only the peak positions and half-max contours of the substrate, buffer, and film. For comparison, a PbSe film grown on InAs is also included: the sample analyzed further in Figure 6.10.

PbSe films R276 and R278, or any of the films in the $[\bar{1}10]$ direction. In this orthogonal direction we see the PbSe films under slight tensile and compressive stress relax fully during growth, then contract with the substrate during cooldown, not relaxing to relieve thermal mismatch strain. R262/E037 is an outlier here, failing to fully relax during growth.

We observe that PbSe/InAs, PbSe(compressive)/InAsSb, PbSe(tensile)/InAsSb, and PbSe/InAsSb(low dislocation) relax via entirely different mechanisms. Figure 6.12 shows ECCI of these films where FIB milling has been used to bring the interfacial misfit structure within the ECCI interaction depth and ensure a smooth surface. When PbSe is grown under slight compressive strain on a substrate with high TDD (Figure 6.12c), secondary and tertiary slip systems seem to activate, allowing for some dislocation glide in the $\langle 100 \rangle$ directions (likely the $\{101\}\langle\bar{1}01\rangle$ slip system) and significant (asymmetric) glide in the $[110]$ direction, possibly the $\{111\}\langle\bar{1}01\rangle$ slip system. PbSe most commonly slips on the $\{100\}$ planes, and slip on the $\{101\}$ planes is considered secondary. Slip on the $\{111\}$ planes is much more rare, but has been previously observed in PbS[159].

In the case of slight tensile strain (Figure 6.12d), distinctly different relaxation behavior is

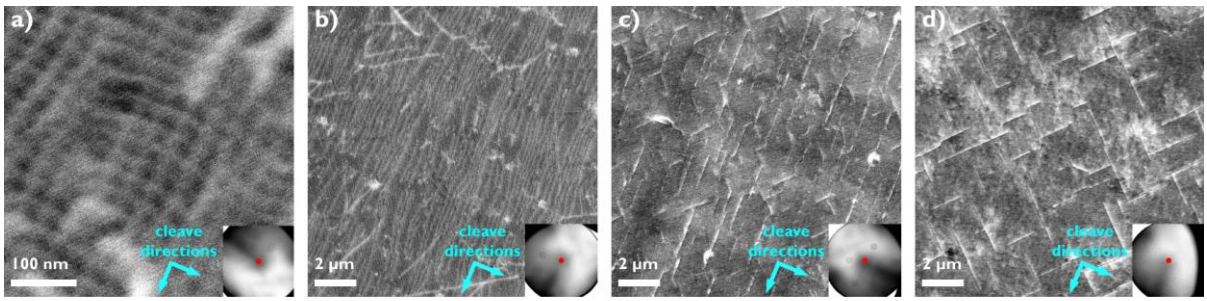

Figure 6.12 – **ECCI of PbSe on varying lattice parameter substrates.** ECCI micrographs recorded from FIB-polished samples showing moiré and varying dislocation structures (and differing relaxation mechanisms) in PbSe films nucleated on different substrates in different strain states: compressive, tensile; varying substrate TDD.

observed. Misfit dislocations have almost exclusive preference for ⟨100⟩ line directions. As these dislocation cores are equivalent in terms of the interfacial symmetry, there is no preference for glide in one direction or the other. It appears the $\{101\}\langle\bar{1}01\rangle$ slip system acts on pre-existing dislocations to uniformly relax these samples, resulting in the bidirectional relaxation observed in X-ray.

Earlier studies in LPE-grown PbSe have claimed secondary slip systems could be activated if dislocations were initially nucleated by climb[150]. This implies that the ability for PbSe(001) to relax is limited primarily by the existence of dislocations, because although secondary and tertiary slip can allow for glide, they are alone insufficient to allow for glide-based half-loop nucleation. In this case, a significant number of dislocations are injected from the metamorphic buffer, and these dislocations are allowed to glide, interestingly with strong preference for ⟨100⟩ line directions in tension, and a [110] line direction in compression. Indeed the elongated PbSe islands we observe on InAs substrates also extend in the [110] direction, and upon coalescence form misfit dislocations with a [110] line direction. So this preference is a consistent behavior during early nucleation. Based on these results, we tentatively attribute this preference to the 2-fold symmetry of the IV-VI/III-V interface which assigns a different core chemistry to misfit dislocations with [110] and $[1\bar{1}0]$ line directions (see Figure 5.4). At III-V/III-V interfaces and in bulk III-V samples[160], there is a significant preference for glide of dislocations with opposite core composition (α vs. β dislocations), but we don't know the energetics of the equivalently orthogonal dislocations found at the IV-VI/III-V interface.

Climb-nucleated dislocations

The most promising result came from sample R262, which appeared to coalesce without creating interfacial defects. R262 was grown on an InAsSb buffer that barely relaxed, resulting in

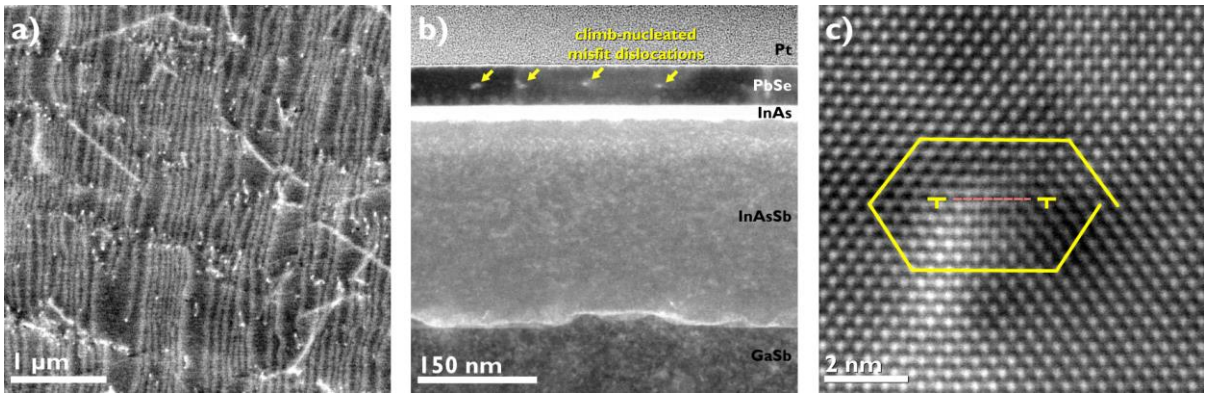

Figure 6.13 – **Climb-nucleated dislocations in PbSe/InAsSb.**
(a) ECCI micrograph of R262 with no FIB polishing, indicating these misfit dislocations are close to the surface. (b) dark field STEM of the buffer stack and PbSe layer, showing the mid-layer misfit dislocations. (c) HR-STEM of one of these slightly dissociated dislocations with a burgers circuit trace, showing it is a pure edge dislocation.

an asymmetrically strained, relatively low-TDD substrate. The surface is very flat, and although the film is thicker than typical ECCI interaction depth, we observe a 1D array of misfit dislocations (Figure 6.13a). These dislocations are visible because they do not lie deep at the heterointerface, but halfway through the PbSe film, and they can be easily observed in cross-sectional STEM (Figure 6.13b-c).

Unlike the dislocations we observed at the PbSe/InAs interface (Figure 6.3h), these dislocations appear to have a burgers vector of $\frac{1}{2}[1\bar{1}0]$ with a line direction of $[110]$, making them pure edge dislocations. Pure edge misfit dislocations at PbSe/PbTe interfaces have been studied by Springholz and Wiesauer[154], who found that PbTe under significant (5.2%) compressive stress readily relaxes using these dislocations beyond a critical thickness of only 1-2 monolayers. In our case, PbSe is under compressive stress of less than a percent at growth temperature, so the critical thickness is much larger.

As these climb-nucleated dislocations only appeared in one direction, we have to realize that PbSe is a 4-fold symmetric material so unlike dislocations which originate at the IV-VI/III-

V interface, half-loops nucleated from the IV-VI surface should be uniformly nucleated to relieve strain in all directions. However we also have to remember that the InAsSb substrate in this instance was itself asymmetrically strained because of asymmetric α/β nucleation and glide at the InAsSb/GaSb interface, so the initially-coherent PbSe was experiencing much more strain in the $[1\bar{1}0]$ direction. After nucleating these defects, the PbSe film on this substrate is nearly equally in-plane strained, with the climb-nucleated dislocations relieving the more-strained direction – this actually allows us to place bounds on the critical thickness for nucleation. For a PbSe film at 300 °C under 0.8% compressive stress in the $[1\bar{1}0]$ direction, the critical thickness for climb-nucleating dislocations is less than 50 nm. Alternately, for a film under just 0.65% compressive strain, the critical thickness is greater than 50 nm.

These results are very exciting as they point towards a route for defect-free PbSe films on III-V substrates. A sufficiently lattice-matched III-V substrate (less than 0.5% at growth temperature) with low pre-existing TDD should be an excellent template for growth of coherent PbSe, enabling extremely high-quality interfaces, maybe even electrically-active heterointerfaces which could play host to novel electronic states. In practice, to achieve such a precise buffer layer, use of a metamorphic mixed-III (InGaSb) layer instead of a mixed-V (InAsSb) layer would be easier to control, but necessitates careful capping with a strained InAs layer to achieve the arsenic termination necessary for IV-VI pre-treatment and nucleation.

IV. RELAXATION OF (111) ORIENTED PbSe FILMS

For growth of (111)-oriented PbSe films, we have very different objectives. Coalescence defects aren't locked in the way they are for (001) oriented films because dislocation glide can enable reactions and annihilation, so our primary focus has been on understanding how dislocations move within (111) layers, and how we may be able to leverage this behavior. Our

highest quality (111) oriented PbSe has been grown on InAs(111)A substrates that contained some fraction of twinned grains, so our structural results involve characterizing both dislocations and inherited twin boundaries.

Structural quality of PbSe layers on InAs(111)A

In 65 nm thick PbSe layers on InAs(111)A substrates, via ECCI, we observe a threading dislocation density (TDD) of 7×10^{9} cm^{-2}. In the thicker 1.5 μm film, this defect density drops precipitously: we measure a TDD of 1.6×10^{8} cm^{-2} via plan-view TEM a couple hundred nanometers below the surface, and approximately 1×10^{8} cm^{-2} just below the top surface via ECCI, across both populations of grains. With thermal cycling, etch pit density (EPD) in 4 μm thick PbSe(111) on silicon has been previously reported as low as 10^{6} cm^{-2} [16]. The reported lower TDD in these earlier works are partly explained by the thicker film and higher thermal expansion mismatch between PbSe and Si (leading to more efficient dislocation filtering during cyclic annealing), but our observation of dislocation clustering via ECCI and STEM suggests that EPD may also underrepresent TDD. TDDs of 10^{7}-10^{8} cm^{-2} have been measured for 4 μm films of PbTe(111)/BaF_2 via scanning tunneling microscopy[52], aligning closely with our results. We further characterize the structural relaxation of these materials via XRD and PL.

At room temperature, XRD measurements of the (444) peak of PbSe show that a 1.5 μm PbSe(111) film is fully relaxed within the measurement limits of the high-resolution diffractometer used (Figure 6.14a). Calibrating to a predicted InAs (444) spacing of 0.8744 Å, we observe a PbSe (444) spacing of 0.8837 Å, corresponding to a cubic lattice parameter of about 6.123 Å that is matched to the bulk[161]. The 2θ-ω full width at half maximum (FWHM) measured 442 arcseconds, corresponding to approximately ±0.06% variability in (444) layer spacing. Rocking curve width was measured at 197 arcseconds. These x-ray measurements are comparable

to our previous work[101], PbSe/InAs(001) with an asymmetric (004) rocking curve width of 185 arcseconds and 369 arcseconds along the [110] and [1$\bar{1}$0] azimuths, respectively. Other recent PbSe/III-V work from Wang et al.[22] measured rocking curve widths of 266 arcseconds and 1700 arcseconds for PbSe/GaAs(001) and PbSe(511)/GaAs(211)B, respectively. High quality PbSe(111) on well-established fluorite buffer layers can reach rocking curve widths around 150 arcseconds[151], but 500-1500 arcseconds is not uncommon[13,149]. Extremely high quality PbTe has been grown on BaF_2 substrates with rocking curve width of only 30 arcseconds[162].

The lattice mismatch between PbSe and InAs is accommodated by a dense triangular grid of misfit dislocations at the heterointerface. We have observed these misfits directly using plan-view ECCI on a sloped, ion-polished sample of PbSe, where the misfit network is briefly shallow enough to generate channeling contrast (Figure 6.14b). Figure 6.14c shows HAADF STEM of the

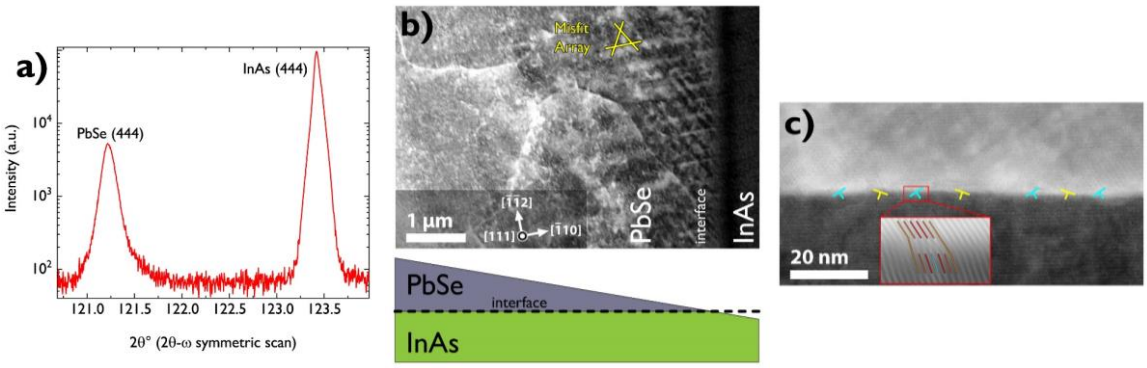

Figure 6.14 – **Structural quality of a fully relaxed 1.5 μm thick PbSe(111) film.** (a) Symmetric 2θ-ω XRD scan showing good structural quality, with a film FWHM of 442 arcseconds. Rocking curve FWHM was 197 arcseconds. (b) plan-view ECCI micrograph of FIB-polished sloped PbSe film, showing threading dislocations and twin boundaries in the thicker PbSe to the left, and a triangular array of misfit dislocations to the right where the film thickness approaches the ECCI interaction depth. The resolution of ECCI does not resolve every misfit dislocation. (c) shows the grid of misfit dislocations at the heterointerface, with approximate dislocation core positions determined through inverse fast Fourier transform analysis (c, inset). The cyan and yellow dislocation symbols indicate the two visible populations of dislocations, half perpendicular to the imaging plane, half inclined ±60° to the imaging plane.

PbSe/InAs interface with approximate positions of misfit dislocations marked. Across this 95 nm section, seven misfit dislocations are observed, resulting in an average spacing of ~14 nm. Misfit dislocations in these materials are expected to have burgers vectors in ⟨110⟩ directions and glide on {100} planes. In a (111)-oriented film, this means that a triangular grid of misfit dislocations will lie at the heterointerface[16]—each set with an equilibrium spacing of 30–40 nm. Because three discrete sets of dislocations exist, we would expect to see a dislocation intersect a [110] cross section every 17 nm, but in practice direct observation and burgers circuit analysis is made difficult by the inclination of the dislocations to the imaging plane. Only half of the visible dislocations will be perpendicular to the imaging plane, and the rest are inclined at ±60°, causing distortion and blurring at the interface in a foil of finite thickness. However, via masking and inverse fast Fourier transform analysis (Figure 6.14c inset) approximate positions for dislocation cores can be determined.

As (111) is not the low-energy plane of these rocksalt materials, we noticed slightly rougher surfaces on these films than similar films grown on (001) substrates. Interestingly, pits in thin films of (001) PbSe[101] seem to terminate on {111} planes, but pits in thin films of (111) PbSe seem to preferentially terminate on {001} planes. Additionally, pits on (001) films seem to form around dislocations early in growth and later close to form a smooth surface, but in the (111) orientation, the opposite occurs. PbSe films can be very smooth immediately after coalescence, and only develop shallow surface pits with very long growth. The density of these surface imperfections exceeds the density of threading dislocations at the film surface, so if these pits are indeed forming due to dislocations, this implies that dislocation glide in the relaxing film allows the same dislocation to nucleate multiple pits that persist.

Cryogenic relaxation in PbSe(111)

Figure 6.15a shows high excitation spontaneous emission PL spectra from the 1.5 μm PbSe/InAs film collected from 83–300 K. Where conventional semiconductors increase in bandgap at low temperatures, PbSe is well-known to do the opposite[6,30]. We also note in Fig. 5a that the emission intensity around room temperature is greater than that at cryogenic temperatures. We do not have a clear explanation for this at this time—there could be non-monotonicity from competing temperature-dependent recombination lifetimes (discussed subsequently) or this may be an artifact of the PbSe/InAs interface. Regarding this latter point, none of the thinner samples (65 nm) of PbSe/InAs (111)A emit light that is characteristic of PbSe. It may be tempting to suggest that the network of misfit dislocations at the interface is responsible for the lack of photoluminescence from the thin PbSe films, but we do not think this is the case. When carriers in PbSe are contained by

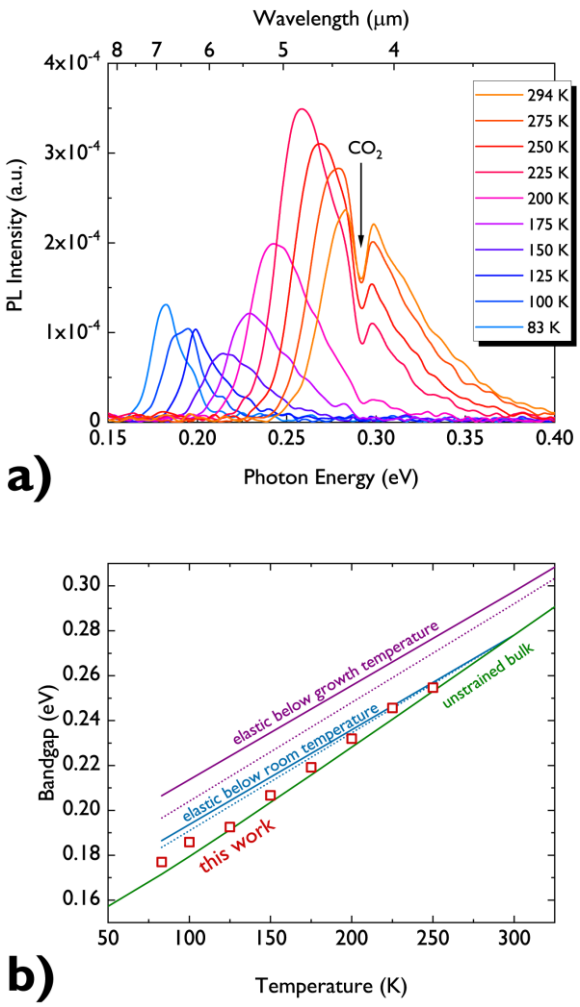

Figure 6.15 – **Temperature-dependent bandgap derived from PL.** (a) Photoluminescence spectra of 1.5 μm PbSe/InAs between room temperature and 83 K, showing the decrease in bandgap and peak broadness with temperature. The room-temperature spectrum is interrupted by absorption from atmospheric CO_2. (b) bandgap is plotted against temperature, showing a near-linear decrease in bandgap with temperature, in rough agreement with anticipated bulk PbSe[6]. For point of comparison, the blue and purple lines show hypothetical bandgaps from strained PbSe films calculated from deformation potentials[165]. The solid lines represent the [111] L-valley gaps, and the dotted lines represent the oblique L-valley gaps.

a larger bandgap substrate (i.e. a PbSe/GaAs structure), we have seen both (111) and (001) oriented PbSe emit light even for 50 nm thick films, in spite of an 8% lattice mismatch and a very dense network of misfit dislocations. InAs has a similar narrow bandgap to PbSe at room temperature, and while the band alignment between PbSe and InAs(111)A across this Type B epitaxial interface is not known, we anticipate a type-III alignment as in the case of PbTe/InSb[23]. This suggests that in the thinner samples, photo-generated carriers may diffuse into the InAs substrate before radiatively recombining. More work is needed to understand if the luminescence intensity in the 1.5 μm film is characteristic of bulk behavior or is influenced by the heterostructure, especially at cryogenic temperatures where photo-generated carriers may be highly mobile.

Figure 6.15b shows the PL-calculated bandgap as the sample temperature is changed. Due to thermal mismatch with the InAs substrate (α_{InAs}=5.4×10^{-6} K^{-1}, α_{PbSe}=19.4×10^{-6} K^{-1}) [161,163], the PbSe layer should be significantly biaxially compressively strained (0.7%) while cooling from 573 K growth temperature to 83 K. Yet, a closer inspection of the temperature dependence of the thin film band gap as derived from PL spectra highlights the remarkable ability of these films to stay relaxed due to dislocation glide even at cryogenic temperatures. In contrast, III-V/Si(001) films do not experience thermal dislocation glide below 200–300 °C and routinely crack upon cool down, even with substantially smaller thermal mismatch[164]. The bandgap of the PbSe film reduces approximately linearly with temperature (~0.48 meV/K), in excellent agreement with the unstrained bulk PbSe band gap[6]. Hypothetically, if dislocation glide did not take place, the elastic (111) biaxial strain would break the star-degeneracy of the normal and oblique ⟨111⟩ direct L-valley gaps, shifting them dissimilarly (strictly leading to an indirect semiconductor) as well as shrinking them, the [111] L-valley (normal) forming the smallest direct

gap[165–167]. Figure 5b shows this splitting and decrease in bandgap for two hypothetical elastically strained PbSe films, one all the way down from the growth temperature and the other only from room temperature and below.

Threading dislocation reduction with PbSe(111) thickness

As I explored in Chapter 3 for GaAs, dislocation-dislocation interactions are critical to consider when growing lattice- or thermally-mismatched films. This section presents preliminary work to understand dislocation interactions in PbSe(111) (Figure 6.16). In the case of PbSe(111), we have seen that dislocations are extremely free to move within layers of the material, implying that the thicker a sample is grown, the larger the total mutual force between any two dislocations, and the more opportunity any two dislocations will have to collide and react or annihilate.

As simply growing a film thicker is a very common way to decrease dislocation density, this is not a new concept. In GaAs/Si, threading dislocation density (TDD) has been observed to scale inversely with sample thickness for thin samples and exponentially with sample thickness for extremely thick samples[168]. These observations are mathematically explained by calculating the probabilities of interaction between two dislocations as they grow longer. This result was obtained using a combination of etch-pit density on multiple thick samples and cross-sectional TEM of thin samples with very high TDDs.

In PbSe, a relationship of $TDD \propto t^2$ has been proposed[16] by etching a PbSe sample grown on Si(111) down to different thicknesses and annealing before counting dislocations via etch-pit density. These authors explain this very fast decrease in TDD with the second anneal step, claiming that additional motion of the dislocations allows for increased reaction and annihilation, and the PbSe slip system is more than capable of supporting long-distance glide of threading dislocations. However, the use of post-etch anneals and the use of etch-pit density to count

dislocations make this data difficult to interpret.

Both of these studies seem to conflate "grown-in" dislocations, the surface-TDD after growth, and the surface-TDD during growth. Although the TDD during growth at growth temperature is impossible to measure, all three of these metrics need not coincide. As a film grows thicker, dislocations will occasionally fuse, reducing the apparent surface-TDD, but under the surface, it's likely that in systems with very high dislocation mobility that line tension will pinch these threading dislocations together, eliminating a dislocation not only at the surface, but through a significant thickness of the film, retroactively (Figure 6.16e). Note that this process cannot occur if the film wasn't grown thick enough for the dislocation tips to fuse in the first place, so examining the dislocation density at the surface of a 1 μm thick film is not the same as measuring the dislocation density 1 μm deep in a 2 μm thick film.

In Figure 6.16, a sample of PbSe(111) has been milled into a slope profile for depth-resolved ECCI. This PbSe(111) sample is 1.5 μm thick, and it has been thermally cycled incidentally as the result of indium bonding/debonding and cooling for cryogenic PL measurements after growth. In Figure 6.16a-c, we see plan-view ECCI micrographs at different depths in the sample. Where the PbSe layer is extremely thin the defect density is extraordinarily high, making quantification of TDD difficult, and subject to large errors. Where the PbSe is thicker, threading dislocations are much sparser. Although quantification in this particular sample is difficult, this technique should be able to provide an instantaneous snapshot of the TDD within a sample because the milling, polishing, and imaging occur at room temperature with no treatments in between.

Dislocation reduction in PbSe can occur via glide and climb, and is theoretically unlimited. The fastest recombinations will be between two glissile dislocations on intersecting glide planes. Favorable combinations of glissile dislocations fuse to form a sessile dislocation with a burgers

vector in the growth plane. Any favorable collision between a glissile dislocation and a sessile dislocation with an in-plane burgers vector will produce a new glissile dislocation, but this process is limited by the interaction cross section of both dislocations trying to meet each other on a 2D plane with 1D of free motion. Fusion of opposing burgers vectors via glide requires dislocations to exist on the exact same glide plane, so is an effectively climb-limited process.

Following these rules, a film will statistically never run out of glissile dislocations, although these dislocations may become too far apart for mutual attraction, even with thermal cycling. Because thicker films will have longer dislocation line length, they have stronger inter-dislocation

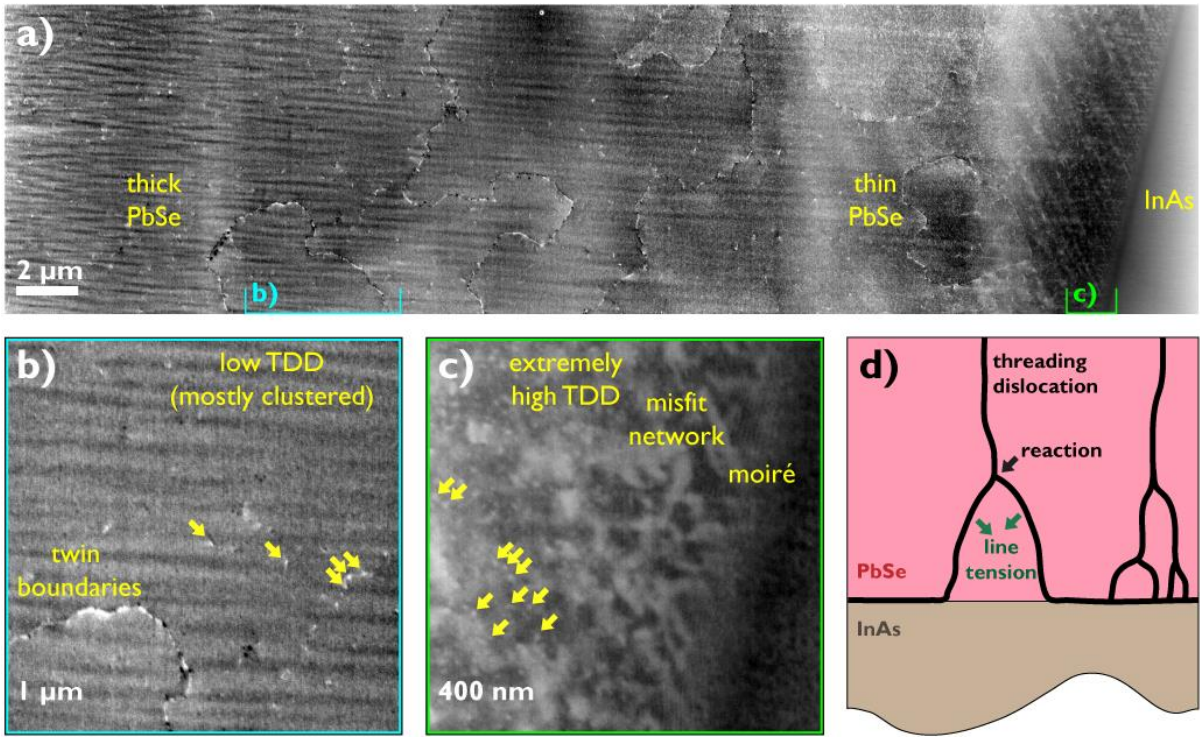

Figure 6.16 – **Slope-profile ECCI of thermally-cycled PbSe/InAs(111)A.** (a) Mosaic of ECCI micrographs along a FIB-milled slope through a PbSe layer (See Figure 2.27 for more on this structure). (b) and (c) show higher-magnification of selected regions showing different features visible through the PbSe thickness. At the very base of the film, a triangular grid of misfit dislocations and moire with the substrate is visible, while in thicker parts of the film, contrast is dominated by threading dislocations, appearing as bright spots. (d) illustrates the proposed tendency for reacted dislocations to fuse together, concentrating defects near the interface and leaving a nearly-uniform TDD distribution in the bulk of the film.

forces. As these dislocations also exist on inclined glide planes, their effective cross section also increases. The combination of these two effects causes dislocation density to drop with film thickness until all dislocations become too sparse to react or become locally pinned (Figure 3.3). Indeed in PbSe(111) films, many of the threading dislocations observed near the surface appeared clustered into groups, likely mutually preventing glide, and blocking further reactions. This clustering may also help to explain the distribution of dislocations in a film - one may expect that upon reaction, line tension would immediately contract the fused threading dislocations down to their respective misfit segments, resulting in an extremely high density of dislocation near the interface, and then almost no change in TDD through the rest of the thickness of the film, but if the final stages of dislocation fusion are frequently climb-mediated, not glide, then there may be residual kinks in the threading dislocations that prevent this line-tension contraction and leave forked dislocations in the middle of a layer. These structures require more investigation to understand such effects.

V. THERMAL STRAIN RELAXATION VIA vdW EPITAXY

Introduction

The ease with which van der Waals materials can slide over each other (effectively glide of edge dislocations between the sheets, Figure 6.17a) has historically made them attractive as mechanical lubricants, and has inspired the technique of "van der Waals epitaxy" for integrating a significantly mismatched film and substrate[169]. Most vdW epitaxy is done with weakly-interacting 2D and 3D materials, so the PbSe/SnSe/PbSe system, so strongly bonded that defects can pass from one crystal structure to the next, presents an intriguing contrast.

In previous sections, I explored the growth of PbSe directly on III-As(001) substrates – during cooldown, these PbSe(001) films regularly crack if grown thicker than a few hundred

nanometers. In order to grow thicker layers of PbSe(001), new mechanisms of strain relief need to be leveraged, either climb, secondary slip, or the more exotic solution, vdW epitaxy.

PbSe/SnSe/PbSe experiment

We grew two 250 nm thick PbSe films on InAs substrates, just barely below the critical thickness for cracking, and supported one film on a 40 nm SnSe strain relief layer. Unexpectedly, the PbSe layer grown on SnSe cracked while the other did not (Figure 6.17c-d) – The SnSe did not act as a strain relief layer, and in fact hastened the cracking process, both transmitting thermal stresses efficiently despite being a 2D material, and reducing the critical thickness for cracking in PbSe. We tentatively attribute this embrittlement to alloy hardening of a secondary slip system, facilitated by pipe diffusion of Sn through threading dislocations in the PbSe layer, but the existence of any thermal strain at all in the PbSe/SnSe layer is surprising. If vdW epitaxy was able to relieve thermal strain via a sliding-sheet deformation mechanism, we should find a dramatically different strain state in these two PbSe films, but XRD measurements of both are nearly identical (Figure 6.17e).

The mismatch-strain relief facilitated by vdW epitaxy relies on easy sliding of vdW sheets. With perfect 2D sheets, or better yet, superlubricious sheets which contain many hyperdislocations and poor sheet-to-sheet registry[143], adjacent layers can slide past each other with almost no resistance. Unfortunately in our materials, many defects disrupt this 2D layered structure, closing the vdW gap and inhibiting sliding. In order for an edge misfit dislocation to glide through a full screw dislocation in SnSe, it must create a kink – a misfit dislocation segment, structurally appearing as a pair of extra half-planes terminating in the film, similar to the structures investigated by Medlin et al. in Bi_2Se_3[170]. A similar process occurs when an in-plane edge dislocation glides through an a/2 screw dislocation: an energetically expensive mirror twin is created, but the 2D

vdW structure is still not broken over large areas, only at the dislocation core. However, a/4 screw dislocations, and rotational boundaries which may include an a/4 shift, induce cross-linking between the vdW layers continuously over a large area, resulting in a "mixed dimensional" structure which no longer behaves mechanically like a 2D material. A stacking fault like the one imaged in Figure 5.9e and schematically pictured in Figure 6.17b (created by an a/4 screw dislocation) would be a significant hurdle for a dislocation to cross: an edge misfit dislocation with its core between vdW bilayers would glide through this stacking fault and find itself inside a bilayer rather than between them. This dislocation would be forced to break covalent bonds to glide, or rely on climb to move into a new vdW channel; both of these options are dramatically slower than simply shuffling vdW bonds to glide between 2D sheets.

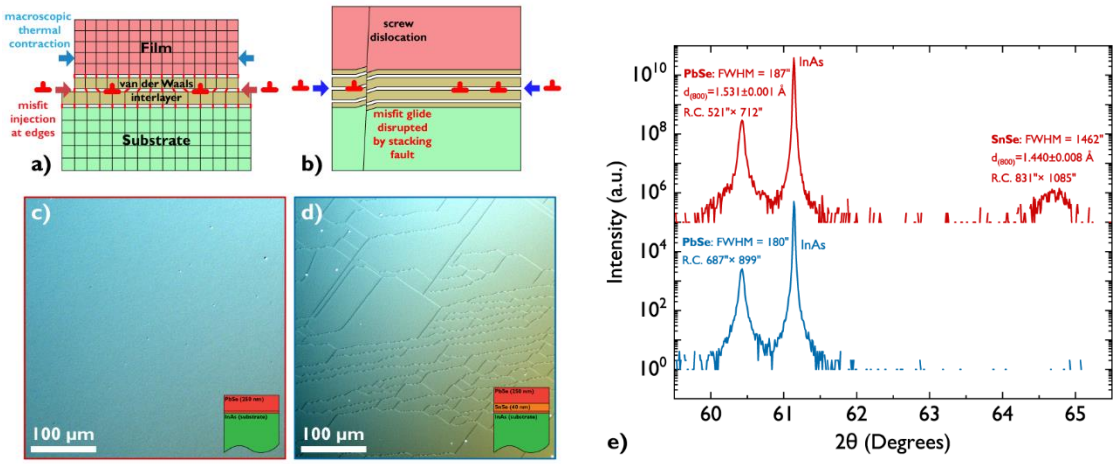

Figure 6.17 – **"Sliding Sheet" strain relief and mixed-dimensional SnSe defects.**
(a) Schematic of proposed "sliding sheet" relaxation of thermal cooldown stress. An ideal "floating film" is able to contract independent of the substrate, facilitated by edge dislocation injection from the sample or mesa edge. (b) this process is significantly inhibited by a/4 grain boundaries and stacking faults, which cause covalent cross-linking between van der Waals layers. (c) A thick PbSe layer on an InAs substrate. (d) the same thick layer, with 40 nm of SnSe interlayer between the PbSe nucleation/coalescence layer and the 250 nm slab. The sample with the SnSe interlayer exhibits surface cracking. (e) x-ray diffraction of the PbSe films from (c) and (d). Both PbSe films are of comparable quality, but the 40 nm SnSe buffer layer has significant tilt and variation in layer spacing.

In order to realize sliding sheet relaxation in vdW epitaxy, a 2D material interlayer should be chosen with very weak bonding to the substrate so that defects are limited to energetically favorable threading dislocations within the 2D material (ie. integer-layer screw components). Ideally then, a van der Waals 2D interlayer should be highly symmetric to eliminate stacking faults wherever possible, weakly interacting with the substrate, and strongly interacting with the desired epitaxial material to promote layer-by layer nucleation of the 3D crystal.

7. Luminescence

I. INTRODUCTION

Photoluminescence

Photoluminescence (PL) is a technique for probing the optical and electronic properties of a semiconductor sample. As an experimental method, it was not discussed in Chapter 2 because these measurements were made by our collaborators in Dan Wassermann's group at UT Austin, but I'll summarize here. When a semiconductor is illuminated with above-bandgap radiation, electrons are excited directly from the valence band to the conduction band. At high excitation, this creates what amounts to a very temporary intrinsic semiconductor, with very high equal populations of both carriers. For low excitation in an already-doped semiconductor, both electrons and holes are still created, but the change in minority carrier density is by far the most important factor in governing what happens next. In either case, as soon as this excess of carriers is generated, they attempt to recombine. Any radiative carrier recombination, ie. when carriers recombine and generate a photon, can be detected by a spectrometer outside the sample. At UT Austin, to probe these extremely long wavelengths, they use a HgCdTe detector in a Fourier Transform Infrared Spectroscopy (FTIR) setup. This detector, importantly, has an extremely fast response time.

Especially for narrow-bandgap materials with historically poor quantum efficiencies, the vast majority of recombining carriers do *not* emit a photon, so we must use the signals we observe (radiative recombination) to infer information about other recombination mechanisms, Shockley Reed Hall (SRH) and Auger. SRH recombination relies on trap states within the bandgap, and scales with the defect density. Auger recombination is a multi-carrier process that is unfortunately a material parameter – dependent on the particular electronic band structure, notably the shape of the bands near the minimum. Parts of this chapter are based on published results from the paper

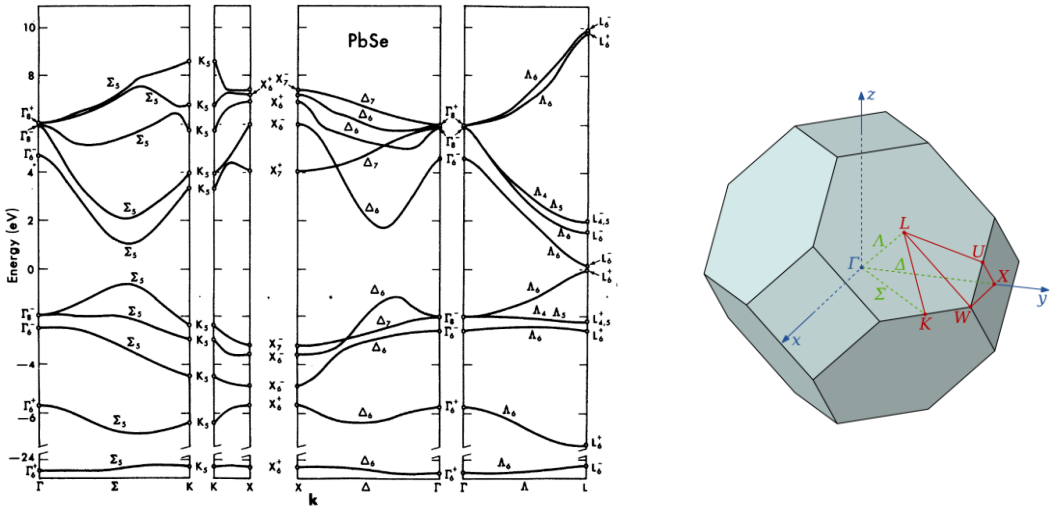

Figure 7.1 – **Electronic band structure of PbSe.**
PbSe is an L-valley direct-gap semiconductor. (left) is the calculated band structure of PbSe (empirical pseudopotential method), illustrating the allowed energies of electrons with varying crystal momenta, on a trace through reciprocal space through the symmetry points Γ, Σ, K, X, Δ, Γ, Λ, and L. For reference, these symmetry points are shown depicted in the Wigner Seitz cell of an FCC lattice (right). The L-valleys lie at the cell boundary in the ⟨111⟩ directions. Band structure reproduced from [196].

Interface structure and luminescence properties of epitaxial PbSe films on InAs (111)A[102].

Electronic/optical structure of PbSe

PbSe is an L-valley direct bandgap material. That means both the conduction band minimum and the valence band maximum occur at the L-point in reciprocal space, not the more typical Γ point. This means that upon exposure to a pump beam during a photoluminescence experiment, photogenerated electrons and holes will migrate to the L points in reciprocal space, congregating at the valence band maximum and conduction band minimum before recombining. The L valleys exist on the edge of the Wigner Seitz cell in the eight ⟨111⟩ directions. As nominally half of each valley is inside the cell, there are four distinct L valleys in any semiconductor that can be altered uniquely by strain that breaks crystal symmetry. In the previous chapter, PL data was used to illustrate that a (111)-oriented PbSe film was unstrained, and there were two possible lines for "strained" PbSe, marking possible splitting of the emission peak wavelength, because in

the (111) orientation, in-plane strain will affect the valley perpendicular to the film surface differently than the three valleys that point at oblique angles to the film surface.

II. STRONG LUMINESCENCE FROM IV-VI FILMS

Apparent improvement with surface treatment/substrate

Our earliest photoluminescence results explored the difference between PbSe grown with different techniques on different III-V substrates. Figure 7.2 shows photoluminescence spectra of three PbSe(001) samples, all 60-80 nm thick on III-V substrates: R057 was grown on a GaSb substrate and contained a significant population of off-orientation grains. As shown in Figure 4.2, many of these misoriented grains could be overgrown, but in a film only 80 nm thick, these residual interfacial defects may still be very important to overall film performance. R069 was grown on a GaAs substrate prepared under selenium overpressure, and while we didn't fully understand the effectiveness of the pre-dose procedure at this point, RHEED indicates this sample had dramatically fewer misoriented grains at the interface. R289 was PbSe grown on a regrown InAs substrate at 330 °C with a controlled nucleation and no defective grains at the interface. Paradoxically, this structurally superior sample produces almost no photoluminescence emission.

Despite the 8% lattice mismatch between PbSe and GaAs, the PbSe layer has very strong emission in the 5-6 μm wavelength regime, an order of magnitude

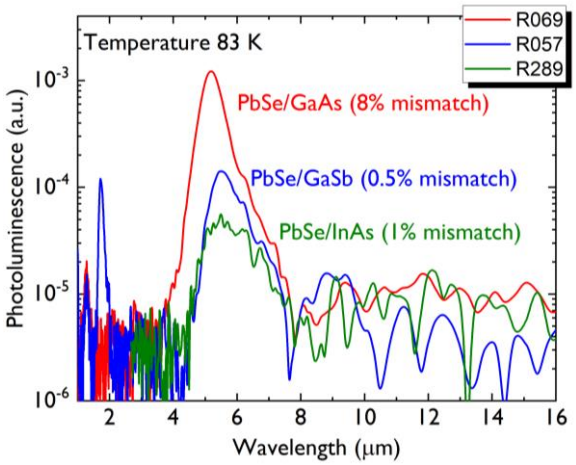

Figure 7.2 – **PL spectra of three thin PbSe films on different substrates.** Despite the 8% lattice mismatch, photoluminescence response of PbSe/GaAs is an order of magnitude stronger than PbSe grown on GaSb or InAs.

stronger than emission from the nearly-lattice-matched PbSe grown on GaSb. Initially we attributed these results to interfacial defects, but as confirmed single-orientation samples like R289 also produce almost no light, we now believe this lack of performance is due to a Type II or III band offset between PbSe and the narrower-gap III-V substrates. Unfortunately, band offsets between the IV-VI rocksalts and the III-V materials are not yet known. GaAs has a bandgap of 1.424 eV but GaSb and InAs have much smaller bandgaps of only 0.726 eV and 0.354 eV, respectively. When aligned to PbSe's extremely narrow bandgap of 0.27 eV, GaAs is most likely to find a favorable Type I band alignment. If PbSe assumes a Type II or Type III band alignment with its substrate, it's possible that photogenerated carriers simply leak out of the 80 nm thick PbSe layer into the substrate before recombining. For PbSe layers on InAs substrates, no light is emitted for thin samples, but strong PL can be observed for thick samples, hinting at a Type III alignment. Future photoluminescence investigation will need to consider these offsets, and more research on band alignments is needed to make any progress on heteroepitaxial device design.

Evidence for defect-tolerance vs. III-V materials

A significant amount of modern mid-infrared research focuses on the narrow-gap III-V materials InAs, InSb, and InAsSb. These materials are easier to integrate on III-V substrates (InAs is available *as* a high-quality substrate), and a lot of work has been done to understand the principles of their

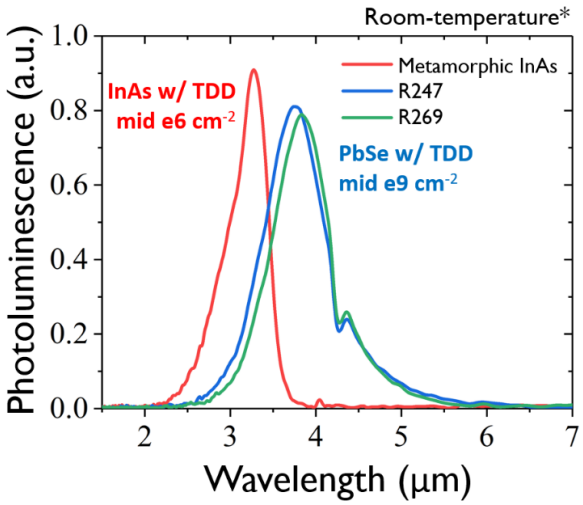

Figure 7.3 – **PL spectra of PbSe/GaAs compared to defective III-V layers** Two samples of PbSe/GaAs emit strong PL at room temperature at approximately 4 μm. These intensities are on par with emission from metamorphic InAs films emitting at just over 3 μm with three orders of magnitude fewer threading dislocations.

growth, but unfortunately they reach physical limits and nonradiative recombination dominates. At low temperatures, they are largely Auger limited, but at room temperature, defects become quite important, and SRH recombination at dislocations and point defects prevents efficient light emission.

Figure 7.3 shows photoluminescence spectra from two samples of PbSe/GaAs compared to a sample of metamorphic InAs with many dislocations. The InAs sample was provided by our collaborators in Larry Lee's group at UIUC, and was intentionally grown to be dislocation rich; 5×10^{6} cm^{-2} is very high for these III-V materials. The PbSe samples were grown using our surface-dose treatment on arsenide surfaces, and therefore should be free of rotated grains, however they contain *extremely* high dislocation densities on the order of 5×10^{9} cm^{-2}. These threading dislocation densities would render most III-V materials optically dead, but we still see strong emission, equivalent to the dislocated III-V analog, and at a higher wavelength.

III. RECOMBINATION MECHANISMS

Time-resolved photoluminescence

Despite thin films of PbSe on InAs emitting no light (possibly due to an unfavorable band alignment), we observe significant PL emission from a 1.5 μm thick film, with a minority carrier lifetime of 20 ns at low-excitation conditions, even with threading dislocation densities exceeding 10^{8} cm^{-2}. Complementary to continuous-wave PL measurements, time-resolved photoluminescence (TRPL) (Figure 7.4) allows for the probing of minority carrier recombination in the 1.5 μm PbSe film. In the low-injection regime at room temperature; the TRPL intensity is seen to decay (single) exponentially over nearly two orders of magnitude after photoexcitation. From this, we calculate a recombination lifetime of 20 ns. A faster pump-power dependent recombination pathway is apparent in the early stages of decay, when the excitation becomes

comparable to the background doping in the sample. Making the bold assumption that the luminescence from PbSe/InAs is characteristic of bulk-behavior, the low-injection minority carrier lifetime τ_{eff} can be ascribed to radiative and nonradiative recombination occurring in parallel, $\tau_{eff} = \frac{1}{\tau_{SRH}} + \frac{1}{\tau_{Rad}} + \frac{1}{\tau_{Auger}}$ where τ_{SRH} is the nonradiative Shockley-Read-Hall (SRH) lifetime, τ_{Rad} is the radiative lifetime, and τ_{Auger} is nonradiative bulk Auger recombination lifetime[171].

Typically, recombination in room-temperature PbSe is reported to be Auger-dominated[172,173], so we first consider the contribution of e-e-h τ_{Auger} recombination, calculated as $\tau_{Auger} = \frac{1}{Cn_0^2}$ where C is the Auger recombination coefficient, and n_0 is the doping density[171]. We are not able to measure actual carrier concentration in these films via Hall due to the conductive InAs substrates, but nonstoichiometry induced n-type doping of 1–5×10^{17} cm^{-3} is typically expected in films evaporated from a compound PbSe cell without excess Se-flux [11]. Indeed, exceeding this electron concentration would result in lead droplets in the film that we did not observe. Recent first principles calculations by Zhang et al. place the Auger recombination coefficient C for PbSe with 5×10^{17} cm^{-3} carriers at approximately 4 × 10^{-29} cm^6 s^{-1}, just slightly lower than that

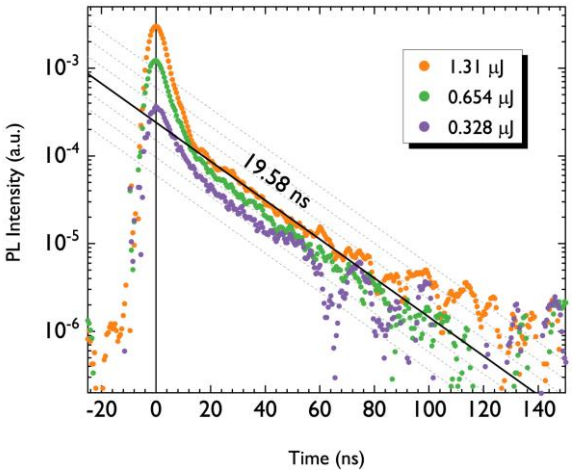

Figure 7.4 – **Recombination characteristics from PL at room temperature.**
TRPL: Three different pumping intensities (all more than an order of magnitude below the PL above) produce photoexcited carriers which recombine over the span of about 100 ns. By fitting to the single exponential region of this data, a minority carrier lifetime of approximately 20 ns can be calculated, given by the slope of the black line.

measured experimentally by Klann et al. and Findlay et al. [174–176] This yields a bulk Auger lifetime of ~ 100 ns, barely within an order of magnitude of the effective lifetime of 20 ns we observe. Radiative recombination appears similarly unlikely, as τ_{Rad} in PbSe has been calculated to be approximately 150 ns at $n_0 = 5 \times 10^{17}$ cm^{-3} at room temperature[173] – also far too slow to explain the measured τ_{eff}.

SRH-limited solution

Despite being able to control island orientation, the process of island coalescence still produces many threading dislocations. In III-V and II-VI infrared-active semiconductors, an average TDD of ~1×10^8 would severely compromise the luminescence properties via SRH recombination. We can obtain an upper bound for the dislocation recombination activity by *assuming* that the measured lifetime is SRH limited and comparing to a simple model where dislocations are infinitely strong recombination sinks for minority carriers. Yamaguchi et al. use this model to calculate the effect of threading dislocations on the SRH lifetime in GaAs[177,178], $\frac{1}{\tau_{SRH}} = \frac{\pi^3 D_p N_d}{4}$ where D_p is the minority carrier (hole) diffusion coefficient and N_d is the TDD. This model works satisfactorily for III-V semiconductors[179–181]. The hole mobility in bulk PbSe at 300 K has been measured to be roughly 300 cm^2/V-s[182], which yields a D_p of 7.8 cm^2/s. Even for a best-case surface TDD of 1×10^8 cm^{-2}, this simple model suggests $\tau_{SRH} = 170\ ps$. Considering the measured total effective lifetime in these samples is 120× longer, the recombination activity of dislocations (and the surface) in PbSe appears to be low compared to III-V materials, a conservative estimate. Detailed verification of this will require the ability to tune the TDD in the film as has been done for III-V/Si samples. For a point of comparison to other IR material systems, MBE-grown $Hg_{0.22}Cd_{0.78}Te$ with EPD of 10^8/cm^2 is reported to have a dislocation-limited minority carrier lifetime of about 15 ns at 78 K [183], similar to our results at

room temperature.

Considering compounding factors like photon recycling[184], and more unconventional Auger-limited cases[185–187], including trap-assisted Auger[188,189], we believe recombination in these materials is SRH-limited, but that SRH recombination in these films is extremely low relative to other materials. More study of luminescence data, preferably experiments that could compare luminescence from samples with different defect concentrations, will help elucidate these differences.

This outstanding dislocation-tolerant behavior in PbSe, perhaps, should not be surprising given accounts of greatly reduced surface recombination velocities in the IV-VIs[20,190] and very early demonstrations of lasing[3,4]. The lack of SRH recombination has often been attributed to high static dielectric constants, allowing for the screening of charged defects[30]. More recent work has also pointed to the character of covalency in PbSe to explain defect tolerant behavior, governing both the material polarizability and the absolute position of defect states and relevant bands[29], drawing some parallels to the methylammonium lead halide material system. We hope that studies on carrier capture coefficients at simple defects in PbSe may shed light on this issue[34]. At the same time, we should not discount the more mundane mechanisms of impurity passivation of surfaces and defects[191].

8.Summary

I. HIGHLIGHTED RESULTS

PbSe is a semiconductor material that has been studied for almost a century, and we are still learning about new features of this fascinating material family. The unique bonding, advantageous band structure, and tolerance for charged defects make PbSe and its related materials good candidates for infrared optoelectronics, and more modern studies are even exploring quantum applications of this semiconductor family. Prior to the present work, very little published research addressed IV-VI growth on III-V surfaces, and this research was spread across multiple combinations of materials and crystalline orientations. Here, I have systematically studied PbSe nucleation and growth on (001) and (111) oriented III-V substrates, developed techniques for ordered nucleation, and examined the resulting films using modern techniques to understand defect behavior in these materials, building towards defect removal and high-quality epitaxy.

Development of new techniques for defect characterization

In the process of this research, we have pushed the characterization technique of electron channeling contrast imaging forward, creating new techniques that give unique perspectives on defect structures in semiconductor films. First and foremost, we published the first report of *in situ* ECCI, using an electron beam to enable dislocation glide at room temperature in-microscope to observe thermal strain relaxation in mismatched semiconductor layers. With this technique, I directly observed dislocation-dislocation pinning, a threading dislocation annihilation event in a GaAs film, and dislocations interacting with both the film surface and mesa walls.

Additionally, I have made use of a new technique, slope-profile ECCI, to explore the relaxation mechanisms of PbSe films. By carefully etching and polishing an inclined profile using FIB milling, interfaces previously only accessible to time-intensive plan-view TEM/STEM can be

imaged over large areas at varying depths using a single minimally intensive milling procedure. This method has allowed re-analysis of samples from earlier in my work to uncover new structures and identify active slip systems and defect formation mechanisms.

Achieving PbSe nucleation control via interfacial chemistry

The first milestone we achieved in PbSe growth was orientation control on (001) III-V substrates. At such a high-energy heterovalent interface, chemistry and dangling bond angles are critical to determining nuclei orientation. On chemically-incompatible substrates like GaSb, we observe interfacial reactions and interfacial energies so high as to make the nucleation orientationally ambivalent. By terminating the III-V surface with arsenic to prevent replacement reactions with selenium species and exposing this surface to PbSe flux at high temperature, we generate a 2×1 surface reconstruction that acts as a high-quality template for PbSe(001) nucleation and growth. This dosing procedure appears robust on GaAs, InAs, and InAs/InAsSb surfaces, and is now a standard technique in our growth of (001) oriented films.

When we expanded the scope of our study to (111) substrates, we found that a similar dosing procedure was effective at controlling twinning at a IV-VI/III-V interface – high temperature treatment again generated a successful growth template. The kinetics of growth are fascinating and difficult to model, because the energetic landscape involved in layer-by layer growth of a material need not reflect the bulk interfacial formation energy – most notably in heteroepitaxy when two different crystal structures are involved with different equilibrium coordination and polarity about each elemental species. MBE is a non-equilibrium technique, and this gives materials scientists great power over the structures formed, granted these mechanisms can be understood.

Using atomic resolution STEM, I explored the interfaces formed between these disparate materials, and the distortions necessary to convert one crystal structure to the next. These

observations informed our explanations of the surface treatment procedure and lead to hypotheses of interface formation. Specific problems, like coordination and surface charge discrepancies, leave observable traces in the resulting films. On (111) oriented substrates, the chemical and structural interfaces seem slightly displaced, resulting in a narrow layer of deformed PbSe, nearly forming a zincblende structure before a preference for octahedral coordination converts the material completely to rocksalt. In the (001) orientation, interfacial charge trapped between the polar InAs(001) and the nonpolar PbSe(001) causes a novel distortion of the selenium sublattice, breaking a mirror symmetry of the PbSe structure near the heterovalent interface.

Exploring PbSe coalescence and relaxation behavior

As PbSe films in all of our experiments grew via a 3D island nucleation and coalescence growth mode, understanding coalescence behavior and coalescence defect formation was critical. On InAs, GaAs, and GaSb(001) substrates, island morphology was qualitatively distinct. On significantly mismatched GaAs substrates, PbSe islands terminated in ⟨100⟩ directions, the equilibrium low-energy planes of rocksalt. On less-mismatched InAs substrates, islands elongated in the [110] direction, and formed misfit dislocations between these long islands upon coalescence. On the nearly-matched, although chemically incompatible GaSb substrates, (001) nuclei formed irregular rounded shapes with flat tops that covered larger areas than the islands on GaAs or InAs.

In pursuit of coalescence which did not create defects, I grew III-V metamorphic buffer layers terminated with strained InAs to create nearly-lattice-matched templates for growth. In cases where these buffer layers themselves had high threading dislocation densities, these threading dislocations would glide in the PbSe layers via secondary or tertiary glide, with a preference to first glide along the [110] direction. Interestingly, this matches the dislocations we

observed forming between InAs islands. This asymmetry is peculiar in PbSe, a 4-fold symmetric material, however the IV-VI/III-V interface is not 4-fold symmetric, and dislocations that lie at this interface may have different core reconstructions in different line directions, causing a bias to PbSe relaxation. On the more mismatched GaAs, where the PbSe film barely interacts with the substrate, this variance in "dislocation" chemistry manifests as a repeating grid of interfacial registries, some of which are more energetically favorable than others.

For nearly-lattice-matched substrates without a high density of preexisting threading dislocations, we observe what may be coherent nucleation and coalescence, with defects subsequently formed beyond a critical thickness via climb. Pure edge misfit dislocations are nucleated as half-loops from the PbSe surface to relax the film due to the lack of available slip systems. While these results of coherent coalescence are extremely promising, controlling climb relaxation in samples greater than critical thickness will be a challenge. Exploring embrittlement of PbSe layers and the effect of pre-existing dislocations in these layers is important.

One very unexpected facet of PbSe coalescence was the material's tendency to form pits around dislocations and stacking faults. It appears that mobile adatoms have a significant aversion to binding to strained positions in the crystal, and with locally-mediated sticking coefficients come roughened films. We believe this phenomenon is linked to the resonant aspect of PbSe bonding, where breaking or straining one bond weakens those around it. This same effect may also help govern the elongated shape of islands on InAs surfaces – asymmetric strain caused by shifting registry and dislocations of differing chemical character.

II. FUTURE WORK AND EXTENSIONS

Coherent growth

With recent analysis of PbSe samples grown on metamorphic buffers, it appears an avenue

towards coherent heteronucleation of PbSe/III-V substrates exists. To pursue such a film, manufacturing a buffer layer with easily controllable species (ie. mixed-III) would be ideal. The TDD should be kept low, so a graded buffer may be effective, but the surface must be arsenic terminated for the pre-dose to be successful. Ideally too, the film would be thick enough to fully relax, making composition (and lattice parameter) tuning more symmetric and consistent.

If a thick relaxed InAs/InGaSb(graded)/GaSb structure could be synthesized with an in-plane lattice parameter at or just below the lattice parameter of PbSe at nucleation temperature, IV-VI growth should be able to proceed as usual, with a high-temperature pre-dose and nucleation at 330 °C to produce a coherently strained film below a critical thickness >25 nm. After this nucleation, Alloy PbSnSe could be used to strain match and prevent nucleation of defects post-coalescence.

In situ relaxation experiments

In the (111) orientation, PbSe relaxes readily in-plane, and given the thermal mismatch between III-V substrates and IV-VI layers, cyclic annealing could provide an excellent mechanism for defect reduction. Experiments to explore this effect include variable-temperature XRD, cathodoluminescence, surface ECCI, slope-profile ECCI, or plan view STEM. Our collaborators have also recently attempted microscale mechanical straining of these samples during *in situ* tSEM experiments. All of these projects could yield valuable information towards defect reduction in IV-VI(111) films, the historical orientation for IV-VI devices, now on a III-V platform.

Electronic measurements and device fabrication

The present work has placed very little focus on electronic and optical measurements because the primary goals were to control structure, however with the ability to grow consistent, albeit still defective PbSe films, properties for application must be investigated. We have had difficulty measuring reliable Hall carrier concentrations and mobilities, but it is currently unclear

if these problems are the result of bad indium contacts or changes in film stoichiometry from the heat of soldering and indium bonding. There may also be multiple interfacial conduction mechanisms confounding bulk results. A sequence of PbSe growths of varying thickness on GaAs (grown adjacent and non-consecutively) have been prepared for a systematic study of Hall in these materials, but this growth sequence will likely need to be repeated immediately before characterization, and varying contact metal stacks should be tested for sample-to-sample consistency before such a series is analyzed.

Alloys of PbSnSe also merit similar investigation, especially samples with inverted bandgaps. Generating an accurate map of composition vs bandgap and learning the properties of an electronic material with an inverted bandgap would be very interesting results.

Exploration of nonpolar substrates

Finally, new substrates should continue to be explored. This work was able to consistently create single-orientation PbSe growths on III-As substrates by emphasizing the importance of surface chemistry control over lattice parameter mismatch. PbSe has previously been grown directly on silicon substrates, but the quality was reported to be substandard to PbSe grown on a fluorite buffer. Exploring the effectiveness of our pre-dosing procedure, or similar techniques, on nonpolar substrates like silicon and germanium, in the (001) or (111) orientations could be useful not just from a substrate development perspective, but to learn about the dosing procedure in an environment with different charge considerations.

Funding

I am extremely grateful for my primary support from the National Science Foundation (NSF) Graduate Research Fellowship under Grant No. 1650114. This work was also supported by the National Science Foundation through the MRSEC Program of the National Science Foundation through Grant No. DMR-1720256 (Seed Program), and the Materials department at UC Santa Barbara.

References

[1] B. Lange, Photoeffects in Semi-Conductors, Trans. Electrochem. Soc. 63 (1933) 51. doi:10.1149/1.3493833.

[2] E.H. Putley, J.B. Arthur, Lead Sulphide - An Intrinsic Semiconductor, Proc. Phys. Soc. Sect. B. 64 (1951) 616–618. doi:10.1088/0370-1301/64/7/110.

[3] J.F. Butler, A.R. Calawa, R.J. Phelan, T.C. Harman, A.J. Strauss, R.H. Rediker, PbTe DIODE LASER, Appl. Phys. Lett. 5 (1964) 75–77. doi:10.1063/1.1754062.

[4] J.F. Butler, A.R. Calawa, R.J. Phelan, A.J. Strauss, R.H. Rediker, PbSe diode laser, Solid State Commun. 2 (1964) 303–304. doi:10.1016/0038-1098(64)90530-7.

[5] J.F. Butler, Diffused Junction Diodes of PbSe and PbTe, J. Electrochem. Soc. 111 (1964) 1150. doi:10.1149/1.2425939.

[6] H. Preier, Recent advances in lead-chalcogenide diode lasers, Appl. Phys. 20 (1979) 189–206. doi:10.1007/BF00886018.

[7] G. Springholz, G. Bauer, Molecular beam epitaxy of strained PbTe/EuTe superlattices, Appl. Phys. Lett. 62 (1993) 2399–2401. doi:10.1063/1.109377.

[8] T. Schwarzl, W. Heiß, G. Springholz, Ultra-high-finesse IV-VI microcavities for the midinfrared, Appl. Phys. Lett. 75 (1999) 1246–1248. doi:10.1063/1.124656.

[9] G. Springholz, T. Schwarzl, W. Heiss, G. Bauer, M. Aigle, H. Pascher, I. Vavra, Midinfrared surface-emitting PbSe/PbEuTe quantum-dot lasers, Appl. Phys. Lett. 79 (2001) 1225–1227. doi:10.1063/1.1389517.

[10] W. Heiss, T. Schwarzl, G. Springholz, K. Biermann, K. Reimann, Above-room-temperature mid-infrared lasing from vertical-cavity surface-emitting PbTe quantum-well lasers, Appl. Phys. Lett. 78 (2001) 862–864. doi:10.1063/1.1347404.

[11] D.K. Hohnke, S.W. Kaiser, Epitaxial PbSe and Pb 1− x Sn x Se: Growth and electrical properties, J. Appl. Phys. 45 (1974) 892–897. doi:10.1063/1.1663334.

[12] H. Zogg, M. Hüppi, Growth of high quality epitaxial PbSe onto Si using a (Ca,Ba)F2 buffer layer, Appl. Phys. Lett. 47 (1985) 133–135. doi:10.1063/1.96239.

[13] P. Müller, A. Fach, J. John, A.N. Tiwari, H. Zogg, G. Kostorz, Structure of epitaxial PbSe grown on Si(111) and Si(100) without a fluoride buffer layer, J. Appl. Phys. 79 (1996) 1911–1916. doi:10.1063/1.361076.

[14] H. Zogg, C. Maissen, S. Blunier, S. Teodoropol, R.M. Overney, T. Richmond, J.W. Tomm, Thermal-mismatch strain relaxation mechanisms in heteroepitaxial lead chalcogenide layers on Si substrates, Semicond. Sci. Technol. 8 (1993) S337–S341. doi:10.1088/0268-1242/8/1S/075.

[15] H. Zogg, P. Mueller, A. Fach, J. John, C. Paglino, a N. Tiwari, Epitaxy of narrow gap IV-VI materials on Si(111) and Si(100) substrates: growth, properties, and thermal mismatch strain accommodation, in: R.E. Longshore, J.W. Baars, A. Kepten, J.M. Trombetta (Eds.), SPIE's 1995 Int. Symp. Opt. Sci. Eng. Instrum., 1995: pp. 35–42. doi:10.1117/12.218196.

[16] P. Müller, H. Zogg, A. Fach, J. John, C. Paglino, A.N. Tiwari, M. Krejci, G. Kostorz, Reduction of Threading Dislocation Densities in Heavily Lattice Mismatched PbSe on Si(111) by Glide, Phys. Rev. Lett. 78 (1997) 3007–3010. doi:10.1103/PhysRevLett.78.3007.

[17] J. Masek, T.J. Hoshino, C. Maissen, H. Zogg, S. Blunier, J.P. Vermeiren, C.L. Claeys, Monolithic lead-chalcogenide IR-diode arrays on silicon: fabrication and use in thermal imaging applications, Soc. Photo-Optical Instrum. Eng. Conf. Ser. 1735 (1992) 54–61. doi:10.1117/12.138640.

[18] H. Zogg, A. Fach, C. Maissen, J. Masek, S. Blunier, Photovoltaic lead-chalcogenide on silicon infrared sensor arrays, Opt. Eng. 33 (1994) 1440. doi:10.1117/12.165808.
[19] A. Muñoz, J. Meléndez, M.C. Torquemada, M.T. Rodrigo, J. Cebrián, A.J. de Castro, J. Meneses, M. Ugarte, F. López, G. Vergara, J.L. Hernández, J.M. Martín, L. Adell, M.T. Montojo, PbSe photodetector arrays for IR sensors, Thin Solid Films. 317 (1998) 425–428. doi:10.1016/S0040-6090(97)00576-2.
[20] Z. Shi, GaSb–PbSe–GaSb double heterostructure midinfrared lasers, Appl. Phys. Lett. 72 (1998) 1272–1274. doi:10.1063/1.121048.
[21] X.L. Huang, Z. Labadi, A. Hammiche, A. Krier, Growth of self-assembled PbSe quantum-dots on GaSb(100) by liquid phase epitaxy, J. Phys. D. Appl. Phys. 35 (2002) 3091–3095. doi:10.1088/0022-3727/35/23/309.
[22] X.J. Wang, Y.B. Hou, Y. Chang, C.R. Becker, R.F. Klie, T.W. Kang, R. Sporken, S. Sivananthan, Heteroepitaxy of PbSe on GaAs(100) and GaAs(211)B by molecular beam epitaxy, J. Cryst. Growth. 311 (2009) 2359–2362. doi:10.1016/j.jcrysgro.2009.01.140.
[23] K.-K. Lee, W. Priyantha, T.H. Myers, Growth and valence band offset measurement of PbTe/InSb heterojunctions, Appl. Phys. Lett. 100 (2012) 052108. doi:10.1063/1.3681161.
[24] G. Lucovsky, R.M. White, Effects of Resonance Bonding on the Properties of Crystalline and Amorphous Semiconductors, Phys. Rev. B. 8 (1973) 660–667. doi:10.1103/PhysRevB.8.660.
[25] M. Wuttig, V.L. Deringer, X. Gonze, C. Bichara, J.-Y. Raty, Incipient Metals: Functional Materials with a Unique Bonding Mechanism, Adv. Mater. 30 (2018) 1803777. doi:10.1002/adma.201803777.
[26] M. Zhu, O. Cojocaru-Mirédin, A.M. Mio, J. Keutgen, M. Küpers, Y. Yu, J.-Y. Cho, R. Dronskowski, M. Wuttig, Unique Bond Breaking in Crystalline Phase Change Materials and the Quest for Metavalent Bonding, Adv. Mater. 30 (2018) 1706735. doi:10.1002/adma.201706735.
[27] J. Raty, M. Schumacher, P. Golub, V.L. Deringer, C. Gatti, M. Wuttig, A Quantum-Mechanical Map for Bonding and Properties in Solids, Adv. Mater. 31 (2019) 1806280. doi:10.1002/adma.201806280.
[28] S. Maier, S. Steinberg, Y. Cheng, C. Schön, M. Schumacher, R. Mazzarello, P. Golub, R. Nelson, O. Cojocaru-Mirédin, J. Raty, M. Wuttig, Discovering Electron-Transfer-Driven Changes in Chemical Bonding in Lead Chalcogenides (PbX, where X = Te, Se, S, O), Adv. Mater. 32 (2020) 2005533. doi:10.1002/adma.202005533.
[29] Y. Rakita, T. Kirchartz, G. Hodes, D. Cahen, Type and Degree of Covalence: Empirical Derivation and Implications, (2019) 1–45. http://arxiv.org/abs/1907.03971.
[30] G. Springholz, G. Bauer, Semiconductors, IV-VI, in: Wiley Encycl. Electr. Electron. Eng., John Wiley & Sons, Inc., Hoboken, NJ, USA, 2014: pp. 1–16. doi:10.1002/047134608X.W3214.pub2.
[31] T. Chattopadhyay, A. Werner, H.G. von Schnering, J. Pannetier, Temperature and pressure induced phase transition in IV-VI compounds, Rev. Phys. Appliquée. 19 (1984) 807–813. doi:10.1051/rphysap:01984001909080700.
[32] A.Y. Ueta, G. Springholz, F. Schinagl, G. Marschner, G. Bauer, Doping studies for molecular beam epitaxy of PbTe and Pb1 − xEuxTe, Thin Solid Films. 306 (1997) 320–325. doi:10.1016/S0040-6090(97)00239-3.
[33] X. Zhang, J. Shen, C.G. Van de Walle, First-Principles Simulation of Carrier Recombination Mechanisms in Halide Perovskites, Adv. Energy Mater. 10 (2020) 1902830. doi:10.1002/aenm.201902830.

[34] X. Zhang, M.E. Turiansky, C.G. Van de Walle, Correctly Assessing Defect Tolerance in Halide Perovskites, J. Phys. Chem. C. 124 (2020) 6022–6027. doi:10.1021/acs.jpcc.0c01324.
[35] T.H. Hsieh, H. Lin, J. Liu, W. Duan, A. Bansil, L. Fu, Topological crystalline insulators in the SnTe material class, Nat. Commun. 3 (2012) 982. doi:10.1038/ncomms1969.
[36] Y. Sun, Z. Zhong, T. Shirakawa, C. Franchini, D. Li, Y. Li, S. Yunoki, X.Q. Chen, Rocksalt SnS and SnSe: Native topological crystalline insulators, Phys. Rev. B - Condens. Matter Mater. Phys. 88 (2013) 1–6. doi:10.1103/PhysRevB.88.235122.
[37] P. Barone, T. Rauch, D. Di Sante, J. Henk, I. Mertig, S. Picozzi, Pressure-induced topological phase transitions in rocksalt chalcogenides, Phys. Rev. B - Condens. Matter Mater. Phys. 88 (2013) 1–5. doi:10.1103/PhysRevB.88.045207.
[38] P. Dziawa, B.J. Kowalski, K. Dybko, R. Buczko, A. Szczerbakow, M. Szot, E. Łusakowska, T. Balasubramanian, B.M. Wojek, M.H. Berntsen, O. Tjernberg, T. Story, Topological crystalline insulator states in Pb1−xSnxSe, Nat. Mater. 11 (2012) 1023–1027. doi:10.1038/nmat3449.
[39] J. Liu, W. Duan, L. Fu, Two types of surface states in topological crystalline insulators, Phys. Rev. B. 88 (2013) 241303. doi:10.1103/PhysRevB.88.241303.
[40] Y. Tanaka, Z. Ren, T. Sato, K. Nakayama, S. Souma, T. Takahashi, K. Segawa, Y. Ando, Experimental realization of a topological crystalline insulator in SnTe, Nat. Phys. 8 (2012) 800–803. doi:10.1038/nphys2442.
[41] Z. Wang, Q. Liu, J.-W. Luo, A. Zunger, Digging for topological property in disordered alloys: the emergence of Weyl semimetal phase and sequential band inversions in PbSe–SnSe alloys, Mater. Horizons. 6 (2019) 2124–2134. doi:10.1039/C9MH00574A.
[42] E.O. Wrasse, T.M. Schmidt, Prediction of Two-Dimensional Topological Crystalline Insulator in PbSe Monolayer, Nano Lett. 14 (2014) 5717–5720. doi:10.1021/nl502481f.
[43] B. Zhang, P. Lu, H. Liu, L. Jiao, Z. Ye, M. Jaime, F.F. Balakirev, H. Yuan, H. Wu, W. Pan, Y. Zhang, Quantum Oscillations in a Two-Dimensional Electron Gas at the Rocksalt/Zincblende Interface of PbTe/CdTe (111) Heterostructures, Nano Lett. 15 (2015) 4381–4386. doi:10.1021/acs.nanolett.5b01605.
[44] S. G., Molecular Beam Epitaxy of IV-VI Heterostructures and Superlattices, in: K. D (Ed.), Lead Chalcogenides Phys. Appl., Taylor and Francis, NewYork, 2002: pp. 123–207.
[45] H. Holloway, E.M. Logothetis, E. Wilkes, Epitaxial Growth of Lead Tin Telluride, J. Appl. Phys. 41 (1970) 3543–3545. doi:10.1063/1.1659456.
[46] J. Stoemenos, N.N. Zheleva, M.H. Koparanova, Structural study of PbTe films grown on BaF2 by hot wall epitaxy, J. Cryst. Growth. 97 (1989) 443–452. doi:10.1016/0022-0248(89)90225-X.
[47] P.J. McCann, I. Chao, H. Sachar, D. McAlister, C. Li, X. Fang, H. Wu, K. Namjou, IV–VI Semiconductor growth on silicon substrates and new mid-infrared laser fabrication methods, Spectrochim. Acta Part A Mol. Biomol. Spectrosc. 55 (1999) 1999–2005. doi:10.1016/S1386-1425(99)00071-2.
[48] J. Yoshino, H. Munekata, L.L. Chang, Growth of PbTe/CdTe on GaAs (100), J. Vac. Sci. Technol. B Microelectron. Nanom. Struct. 5 (1987) 683. doi:10.1116/1.583804.
[49] H. Clemens, H. Krenn, B. Tranta, P. Ofner, G. Bauer, Epitaxial growth of PbTe on (111)BaF2 and (100)GaAs, Superlattices Microstruct. 4 (1988) 591–596. doi:10.1016/0749-6036(88)90244-3.
[50] M.B. Lassise, T.T. McCarthy, B.D. Tracy, D.J. Smith, Y.-H. Zhang, Molecular beam epitaxial growth and structural properties of hetero-crystalline and heterovalent

PbTe/CdTe/InSb structures, J. Appl. Phys. 126 (2019) 045708. doi:10.1063/1.5097276.
[51] G. Springholz, G. Bauer, Low temperature growth of PbTe and of PbTe/Pb1-xEuxTe multi-quantum wells by molecular beam epitaxy, J. Cryst. Growth. 144 (1994) 157–172. doi:10.1016/0022-0248(94)90451-0.
[52] G. Springholz, G. Bauer, Systematic study of PbTe (111) molecular-beam epitaxy using reflection high-energy electron-diffraction intensity oscillations, J. Appl. Phys. 77 (1995) 540–552. doi:10.1063/1.359038.
[53] Y.N. Picard, J.D. Caldwell, M.E. Twigg, C.R. Eddy, M.A. Mastro, R.L. Henry, R.T. Holm, P.G. Neudeck, A.J. Trunek, J.A. Powell, Nondestructive analysis of threading dislocations in GaN by electron channeling contrast imaging, Appl. Phys. Lett. 91 (2007) 094106. doi:10.1063/1.2777151.
[54] B.. Simkin, M.. Crimp, An experimentally convenient configuration for electron channeling contrast imaging, Ultramicroscopy. 77 (1999) 65–75. doi:10.1016/S0304-3991(99)00009-1.
[55] T. Aoyama, M. Nagoshi, K. Sato, Quantitative analysis of angle-selective backscattering electron image of iron oxide and steel, Microscopy. 64 (2015) 319–325. doi:10.1093/jmicro/dfv026.
[56] K.D. Vallejo, T.A. Garrett, K.E. Sautter, K. Saythavy, B. Liang, P.J. Simmonds, InAs(111)A homoepitaxy with molecular beam epitaxy, J. Vac. Sci. Technol. B. 37 (2019) 061810. doi:10.1116/1.5127857.
[57] P.G. Callahan, B.B. Haidet, D. Jung, G.G.E. Seward, K. Mukherjee, Direct observation of recombination-enhanced dislocation glide in heteroepitaxial GaAs on silicon, Phys. Rev. Mater. 2 (2018). doi:10.1103/PhysRevMaterials.2.081601.
[58] J. Selvidge, J. Norman, E.T. Hughes, C. Shang, D. Jung, A.A. Taylor, M.J. Kennedy, R. Herrick, J.E. Bowers, K. Mukherjee, Defect filtering for thermal expansion induced dislocations in III–V lasers on silicon, Appl. Phys. Lett. 117 (2020) 122101. doi:10.1063/5.0023378.
[59] K. Mukherjee, J. Selvidge, D. Jung, J. Norman, A.A. Taylor, M. Salmon, A.Y. Liu, J.E. Bowers, R.W. Herrick, Recombination-enhanced dislocation climb in InAs quantum dot lasers on silicon, J. Appl. Phys. 128 (2020) 025703. doi:10.1063/1.5143606.
[60] Y. Oshima, A. Nakamura, K. Matsunaga, Extraordinary plasticity of an inorganic semiconductor in darkness, Science (80-.). 360 (2018) 772–774. doi:10.1126/science.aar6035.
[61] L.C. Kimerling, Recombination enhanced defect reactions, Solid State Electron. 21 (1978) 1391–1401. doi:10.1016/0038-1101(78)90215-0.
[62] K. Ishida, T. Kamejima, J. Matsui, Nature of 〈110〉 dark-line defects in degraded (GaAl)As-GaAs double-heterostructure lasers, Appl. Phys. Lett. 31 (1977) 397–399. doi:10.1063/1.89705.
[63] B.D. Schwartz, Dark line defect growth in optically pumped AlxGa−xAs laser material, J. Appl. Phys. 58 (1985) 677–682. doi:10.1063/1.336181.
[64] K. Maeda, S. Takeuchi, Recombination enhanced mobility of dislocations in III-N compounds, Le J. Phys. Colloq. 44 (1983) C4-375-C4-385. doi:10.1051/jphyscol:1983445.
[65] P. Petroff, R.L. Hartman, Rapid degradation phenomenon in heterojunction GaAlAs–GaAs lasers, J. Appl. Phys. 45 (1974) 3899–3903. doi:10.1063/1.1663883.
[66] K. Maeda, S. Takeuchi, Enhanced Glide of Dislocations in GaAs Single Crystals by Electron Beam Irradiation, Jpn. J. Appl. Phys. 20 (1981) L165–L168. doi:10.1143/JJAP.20.L165.
[67] K. Maeda, M. Sato, A. Kubo, S. Takeuchi, Quantitative measurements of recombination

enhanced dislocation glide in gallium arsenide, J. Appl. Phys. 54 (1983) 161–168. doi:10.1063/1.331725.
[68] A. Galeckas, J. Linnros, P. Pirouz, Recombination-Induced Stacking Faults: Evidence for a General Mechanism in Hexagonal SiC, Phys. Rev. Lett. 96 (2006) 025502. doi:10.1103/PhysRevLett.96.025502.
[69] Y. Ohno, Photoinduced stress in a ZnSe/GaAs epilayer containing 90°α partial dislocations, Appl. Phys. Lett. 87 (2005) 181909. doi:10.1063/1.2123392.
[70] D. Jung, P.G. Callahan, B. Shin, K. Mukherjee, A.C. Gossard, J.E. Bowers, Low threading dislocation density GaAs growth on on-axis GaP/Si (001), J. Appl. Phys. 122 (2017) 225703. doi:10.1063/1.5001360.
[71] L. Reimer, Scanning Electron Microscopy, Springer Berlin Heidelberg, Berlin, Heidelberg, 1998. doi:10.1007/978-3-540-38967-5.
[72] P. Rudolph, ed., Handbook of Crystal Growth, Elsevier, 2015. doi:10.1016/C2013-0-09791-5.
[73] S.D. Carnevale, J.I. Deitz, J.A. Carlin, Y.N. Picard, M. De Graef, S.A. Ringel, T.J. Grassman, Rapid misfit dislocation characterization in heteroepitaxial III-V/Si thin films by electron channeling contrast imaging, Appl. Phys. Lett. 104 (2014) 232111. doi:10.1063/1.4883371.
[74] H.A. Zarem, P.C. Sercel, J.A. Lebens, L.E. Eng, A. Yariv, K.J. Vahala, Direct determination of the ambipolar diffusion length in GaAs/AlGaAs heterostructures by cathodoluminescence, Appl. Phys. Lett. 55 (1989) 1647–1649. doi:10.1063/1.102226.
[75] D.R. Luber, F.M. Bradley, N.M. Haegel, M.C. Talmadge, M.P. Coleman, T.D. Boone, Imaging transport for the determination of minority carrier diffusion length, Appl. Phys. Lett. 88 (2006) 163509. doi:10.1063/1.2196236.
[76] B. Sieber, P. Carton, EBIC characterization of bulk GaAs. Temperature dependence of the diffusion length and of the space-charge region width, Phys. Status Solidi. 127 (1991) 423–431. doi:10.1002/pssa.2211270217.
[77] P. Haasen, On the Plasticity of Germanium and Indium Antimonide, Acta Metall. 5 (1957) 598–599. doi:10.1016/0001-6160(57)90129-3.
[78] M.S. Abrahams, J. Blanc, C.J. Buiocchi, Like-sign asymmetric dislocations in zinc-blende structure, Appl. Phys. Lett. 21 (1972) 185–186. doi:10.1063/1.1654336.
[79] I. Yonenaga, K. Sumino, Behaviour of dislocations in GaAs revealed by etch pit technique and X-ray topography, J. Cryst. Growth. 126 (1993) 19–29. doi:10.1016/0022-0248(93)90223-J.
[80] T. Wosinski, A. Zozime, A. Rivière, C. Vermeulin, EBIC investigation of α and β dislocations in GaAs, Phys. Status Solidi. 142 (1994) 347–355. doi:10.1002/pssa.2211420207.
[81] O. Yastrubchak, T. Wosi ski, J.Z. Domaga a, E. Usakowska, T. Figielski, B. Pécz, A.L. Tóth, Misfit strain anisotropy in partially relaxed lattice-mismatched InGaAs/GaAs heterostructures, J. Phys. Condens. Matter. 16 (2004) S1–S8. doi:10.1088/0953-8984/16/2/001.
[82] A.L. Esquivel, S. Sen, W.N. Lin, Cathodoluminescence and electrical anisotropy from α and β dislocations in plastically deformed gallium arsenide, J. Appl. Phys. 47 (1976) 2588–2603. doi:10.1063/1.322978.
[83] A.E. Romanov, W. Pompe, G. Beltz, J.S. Speck, Modeling of Threading Dislocation Density Reduction in Heteroepitaxial Layers, Phys. Status Solidi. 199 (1997) 33–49. doi:10.1002/1521-3951(199701)199:1<33::AID-PSSB33>3.0.CO;2-U.

[84] J.S. Speck, M.A. Brewer, G. Beltz, A.E. Romanov, W. Pompe, Scaling laws for the reduction of threading dislocation densities in homogeneous buffer layers, J. Appl. Phys. 80 (1996) 3808–3816. doi:10.1063/1.363334.
[85] S.K. Choi, M. Mihara, T. Ninomiya, Dislocation Velocities in GaAs, Jpn. J. Appl. Phys. 16 (1977) 737–745.
[86] J.-L. Farvacque, Theoretical aspects of the minority carrier recombination at dislocations in semiconductors, Mater. Sci. Eng. B. 42 (1996) 110–121. doi:10.1016/S0921-5107(96)01691-1.
[87] K. Mukherjee, C.H. Reilly, P.G. Callahan, G.G.E. Seward, Recombination activity of threading dislocations in GaInP influenced by growth temperature, J. Appl. Phys. 123 (2018) 165701. doi:10.1063/1.5018849.
[88] L.B. Freund, A criterion for arrest of a threading dislocation in a strained epitaxial layer due to an interface misfit dislocation in its path, J. Appl. Phys. 68 (1990) 2073–2080. doi:10.1063/1.346560.
[89] L.B. Freund, Dislocation Mechanisms of Relaxation in Strained Epitaxial Films, MRS Bull. 17 (1992) 52–60. doi:10.1557/S088376940004166X.
[90] R. Hull, E.A. Stach, R. Tromp, F. Ross, M. Reuter, Interactions of Moving Dislocations in Semiconductors with Point, Line and Planar Defects, Phys. Status Solidi. 171 (1999) 133–146. doi:10.1002/(SICI)1521-396X(199901)171:1<133::AID-PSSA133>3.0.CO;2-D.
[91] E.A. Stach, R. Hull, R.M. Tromp, F.M. Ross, M.C. Reuter, J.C. Bean, In-situ transmission electron microscopy studies of the interaction between dislocations in strained SiGe/Si (001) heterostructures, Philos. Mag. A. 80 (2000) 2159–2200. doi:10.1080/01418610008212156.
[92] A.Y. Liu, S. Srinivasan, J. Norman, A.C. Gossard, J.E. Bowers, Quantum dot lasers for silicon photonics [Invited], Photonics Res. 3 (2015) B1. doi:10.1364/PRJ.3.0000B1.
[93] D. Jung, R. Herrick, J. Norman, K. Turnlund, C. Jan, K. Feng, A.C. Gossard, J.E. Bowers, Impact of threading dislocation density on the lifetime of InAs quantum dot lasers on Si, Appl. Phys. Lett. 112 (2018) 153507. doi:10.1063/1.5026147.
[94] W.A. Sasangka, G.J. Syaranamual, R.I. Made, C. V. Thompson, C.L. Gan, Threading dislocation movement in AlGaN/GaN-on-Si high electron mobility transistors under high temperature reverse bias stressing, AIP Adv. 6 (2016) 095102. doi:10.1063/1.4962544.
[95] A. Tanaka, H. Matsuhata, N. Kawabata, D. Mori, K. Inoue, M. Ryo, T. Fujimoto, T. Tawara, M. Miyazato, M. Miyajima, K. Fukuda, A. Ohtsuki, T. Kato, H. Tsuchida, Y. Yonezawa, T. Kimoto, Growth of Shockley type stacking faults upon forward degradation in 4H-SiC p-i-n diodes, J. Appl. Phys. 119 (2016) 095711. doi:10.1063/1.4943165.
[96] C.J. Palmstrom, Epitaxy of Dissimilar Materials, Annu. Rev. Mater. Sci. 25 (1995) 389–415. doi:10.1146/annurev.ms.25.080195.002133.
[97] R. Nicolini, L. Vanzetti, G. Mula, G. Bratina, L. Sorba, A. Franciosi, M. Peressi, S. Baroni, R. Resta, A. Baldereschi, J.E. Angelo, W.W. Gerberich, Local interface composition and band discontinuities in heterovalent heterostructures, Phys. Rev. Lett. 72 (1994) 294–297. doi:10.1103/PhysRevLett.72.294.
[98] M. Sukhotin, E.R. Brown, A.C. Gossard, D. Driscoll, M. Hanson, P. Maker, R. Muller, Photomixing and photoconductor measurements on ErAs/InGaAs at 1.55 μm, Appl. Phys. Lett. 82 (2003) 3116–3118. doi:10.1063/1.1567459.
[99] J.M. Zide, D.O. Klenov, S. Stemmer, A.C. Gossard, G. Zeng, J.E. Bowers, D. Vashaee, A. Shakouri, Thermoelectric power factor in semiconductors with buried epitaxial semimetallic nanoparticles, Appl. Phys. Lett. 87 (2005) 112102. doi:10.1063/1.2043241.

[100] W. Kim, J. Zide, A. Gossard, D. Klenov, S. Stemmer, A. Shakouri, A. Majumdar, Thermal Conductivity Reduction and Thermoelectric Figure of Merit Increase by Embedding Nanoparticles in Crystalline Semiconductors, Phys. Rev. Lett. 96 (2006) 045901. doi:10.1103/PhysRevLett.96.045901.
[101] B.B. Haidet, E.T. Hughes, K. Mukherjee, Nucleation control and interface structure of rocksalt PbSe on (001) zincblende III-V surfaces, Phys. Rev. Mater. 4 (2020) 033402. doi:10.1103/PhysRevMaterials.4.033402.
[102] B.B. Haidet, L. Nordin, A. Muhowski, K.D. Vallejo, E.T. Hughes, J. Meyer, P.J. Simmonds, D. Wasserman, K. Mukherjee, Interface structure and luminescence properties of epitaxial PbSe films on InAs(111)A, J. Vac. Sci. Technol. A. In Review (2020). doi:10.1116/6.0000774.
[103] W.A. Harrison, E.A. Kraut, J.R. Waldrop, R.W. Grant, Polar heterojunction interfaces, Phys. Rev. B. 18 (1978) 4402–4410. doi:10.1103/PhysRevB.18.4402.
[104] M.C. Tamargo, Structural characterization of GaAs/ZnSe interfaces, J. Vac. Sci. Technol. B Microelectron. Nanom. Struct. 6 (1988) 784. doi:10.1116/1.584331.
[105] H.H. Farrell, M.C. Tamargo, J.L. de Miguel, Optimal GaAs(100) substrate terminations for heteroepitaxy, Appl. Phys. Lett. 58 (1991) 355–357. doi:10.1063/1.104632.
[106] F. Lu, Z.Q. Zhu, K. Kimura, T. Yao, Acceptor- and donor-like interfacial states at ZnSe/GaAs heterovalent interfaces, Appl. Surf. Sci. 190 (2002) 302–306. doi:10.1016/S0169-4332(01)00895-9.
[107] A. Trampert, F. Schippan, L. Däweritz, K.H. Ploog, Phase-transition-induced residual strain in ferromagnetic MnAs films epitaxially grown on GaAs(001), Appl. Phys. Lett. 78 (2001) 2461–2463. doi:10.1063/1.1367302.
[108] M.D. Biegalski, D.D. Fong, J.A. Eastman, P.H. Fuoss, S.K. Streiffer, T. Heeg, J. Schubert, W. Tian, C.T. Nelson, X.Q. Pan, M.E. Hawley, M. Bernhagen, P. Reiche, R. Uecker, S. Trolier-Mckinstry, D.G. Schlom, Critical thickness of high structural quality SrTiO3 films grown on orthorhombic (101) DyScO3, J. Appl. Phys. 104 (2008) 114109. doi:10.1063/1.3037216.
[109] D.K. Hohnke, H. Holloway, M.D. Hurley, Epitaxial lead chalcogenide films: Orientation on substrates with the fluoride structure, Thin Solid Films. 38 (1976) 49–55. doi:10.1016/0040-6090(76)90277-7.
[110] S. Jin, C. Cai, B. Zhang, H. Wu, G. Bi, J. Si, Y. Zhang, Twisted ZB–CdTe/RS–PbTe (111) heterojunction as a metastable interface structure, New J. Phys. 14 (2012) 113021. doi:10.1088/1367-2630/14/11/113021.
[111] W. Wang, G. Lee, M. Huang, R.M. Wallace, K. Cho, First-principles study of GaAs(001)-β2(2×4) surface oxidation and passivation with H, Cl, S, F, and GaO, J. Appl. Phys. 107 (2010) 103720. doi:10.1063/1.3369540.
[112] O.E. Dagdeviren, C. Zhou, K. Zou, G.H. Simon, S.D. Albright, S. Mandal, M.D. Morales-Acosta, X. Zhu, S. Ismail-Beigi, F.J. Walker, C.H. Ahn, U.D. Schwarz, E.I. Altman, Length Scale and Dimensionality of Defects in Epitaxial SnTe Topological Crystalline Insulator Films, Adv. Mater. Interfaces. 4 (2017) 1601011. doi:10.1002/admi.201601011.
[113] R. Kaspi, J. Steinshnider, M. Weimer, C. Moeller, A. Ongstad, As-soak control of the InAs-on-GaSb interface, J. Cryst. Growth. 225 (2001) 544–549. doi:10.1016/S0022-0248(01)00950-2.
[114] S. Guha, H. Munekata, L.L. Chang, Structural quality and the growth mode in epitaxial ZnSe/GaAs(100), J. Appl. Phys. 73 (1993) 2294–2300. doi:10.1063/1.354079.
[115] S. Miwa, L.H. Kuo, K. Kimura, T. Yasuda, A. Ohtake, C.G. Jin, T. Yao, The role of zinc

pre-exposure in low-defect ZnSe growth on As-stabilized GaAs (001), Appl. Phys. Lett. 73 (1998) 939–941. doi:10.1063/1.122045.
[116] A. Jain, S.P. Ong, G. Hautier, W. Chen, W.D. Richards, S. Dacek, S. Cholia, D. Gunter, D. Skinner, G. Ceder, K.A. Persson, Commentary: The Materials Project: A materials genome approach to accelerating materials innovation, APL Mater. 1 (2013) 011002. doi:10.1063/1.4812323.
[117] S. Takatani, T. Kikawa, M. Nakazawa, Reflection high-energy electron-diffraction and photoemission spectroscopy study of GaAs(001) surface modified by Se adsorption, Phys. Rev. B. 45 (1992) 8498–8505. doi:10.1103/PhysRevB.45.8498.
[118] D. Li, M.D. Pashley, ZnSe nucleation on the GaAs(001):Se-(2×1) surface observed by scanning tunneling microscopy, J. Vac. Sci. Technol. B Microelectron. Nanom. Struct. 12 (1994) 2547. doi:10.1116/1.587799.
[119] E. Tarnow, Structure of the interface between ErAs, a cubic semimetal and AlAs, a tetrahedral semiconductor, J. Appl. Phys. 77 (1995) 6317–6326. doi:10.1063/1.359101.
[120] N.G. Stoffel, C.J. Palmstrøm, B.J. Wilkens, Ion channeling measurement of the lattice registry of ultrathin ErAs layers in GaAs/ErAs/GaAs (001) heterostructures, Nucl. Instruments Methods Phys. Res. Sect. B Beam Interact. with Mater. Atoms. 56–57 (1991) 792–794. doi:10.1016/0168-583X(91)95029-D.
[121] D.O. Klenov, J.M. Zide, J.D. Zimmerman, A.C. Gossard, S. Stemmer, Interface atomic structure of epitaxial ErAs layers on (001)In 0.53Ga 0.47As and GaAs, Appl. Phys. Lett. 86 (2005) 1–3. doi:10.1063/1.1947910.
[122] T.-L. Chan, C. Gaire, T.-M. Lu, G.-C. Wang, S.B. Zhang, Type B epitaxy of Ge on CaF2(111) surface, Surf. Sci. 604 (2010) 1645–1648. doi:10.1016/j.susc.2010.06.008.
[123] J.M. Gibson, R.T. Tung, J.M. Phillips, J.M. Poate, Crystallography and Interfaces of Epitaxial Fluorite Metals and Insulators on Semiconductors, MRS Proc. 25 (1983) 405. doi:10.1557/PROC-25-405.
[124] M.R. Jordan, D.J. Stirland, Changes in epitaxy produced by electron bombardment, Thin Solid Films. 8 (1971) 221–235. doi:10.1016/0040-6090(71)90111-8.
[125] J.B. Rodriguez, P. Christol, L. Cerutti, F. Chevrier, A. Joullié, MBE growth and characterization of type-II InAs/GaSb superlattices for mid-infrared detection, J. Cryst. Growth. 274 (2005) 6–13. doi:10.1016/j.jcrysgro.2004.09.088.
[126] R. Yoshimi, A. Tsukazaki, K. Kikutake, J.G. Checkelsky, K.S. Takahashi, M. Kawasaki, Y. Tokura, Dirac electron states formed at the heterointerface between a topological insulator and a conventional semiconductor, Nat. Mater. 13 (2014) 253–257. doi:10.1038/nmat3885.
[127] D.O. Klenov, J.M. Zide, J.D. Zimmerman, A.C. Gossard, S. Stemmer, Interface atomic structure of epitaxial ErAs layers on (001) In0.53Ga0.47As and GaAs, Appl. Phys. Lett. 86 (2005) 241901. doi:10.1063/1.1947910.
[128] R. Leitsmann, L.E. Ramos, F. Bechstedt, H. Groiss, F. Schäffler, W. Heiss, K. Koike, H. Harada, M. Yano, Rebonding at coherent interfaces between rocksalt-PbTe/zinc-blende-CdTe, New J. Phys. 8 (2006) 317–317. doi:10.1088/1367-2630/8/12/317.
[129] J. Ma, Y. Jia, Y. Song, E. Liang, L. Wu, F. Wang, X. Wang, X. Hu, The geometric and electronic properties of the PbS, PbSe and PbTe (001) surfaces, Surf. Sci. 551 (2004) 91–98. doi:10.1016/j.susc.2003.12.003.
[130] M.G. Han, M.S.J. Marshall, L. Wu, M.A. Schofield, T. Aoki, R. Twesten, J. Hoffman, F.J. Walker, C.H. Ahn, Y. Zhu, Interface-induced nonswitchable domains in ferroelectric thin films, Nat. Commun. 5 (2014) 1–9. doi:10.1038/ncomms5693.
[131] Z. Wang, J. Wang, Y. Zang, Q. Zhang, J.-A. Shi, T. Jiang, Y. Gong, C.-L. Song, S.-H. Ji, L.-

L. Wang, L. Gu, K. He, W. Duan, X. Ma, X. Chen, Q.-K. Xue, Molecular Beam Epitaxy-Grown SnSe in the Rock-Salt Structure: An Artificial Topological Crystalline Insulator Material, Adv. Mater. 27 (2015) 4150–4154. doi:10.1002/adma.201501676.

[132] M. Serbyn, L. Fu, Symmetry breaking and Landau quantization in topological crystalline insulators, Phys. Rev. B. 90 (2014) 035402. doi:10.1103/PhysRevB.90.035402.

[133] W. Mortelmans, S. De Gendt, M. Heyns, C. Merckling, Epitaxy of new layered materials: 2D chalcogenides and challenges of weak van der Waals interactions, ArXiv. (2020) 1–53. http://arxiv.org/abs/2010.04657.

[134] W. Shi, M. Gao, J. Wei, J. Gao, C. Fan, E. Ashalley, H. Li, Z. Wang, Tin Selenide (SnSe): Growth, Properties, and Applications, Adv. Sci. 5 (2018). doi:10.1002/advs.201700602.

[135] L.-D. Zhao, S.-H. Lo, Y. Zhang, H. Sun, G. Tan, C. Uher, C. Wolverton, V.P. Dravid, M.G. Kanatzidis, Ultralow thermal conductivity and high thermoelectric figure of merit in SnSe crystals, Nature. 508 (2014) 373–377. doi:10.1038/nature13184.

[136] D.M. Kepaptsoglou, D. Gilks, L. Lari, Q.M. Ramasse, P. Galindo, M. Weinert, L. Li, G. Nicotra, V.K. Lazarov, STEM and EELS study of the Graphene/Bi2Se3 Interface, Microsc. Microanal. 21 (2015) 1151–1152. doi:10.1017/S1431927615006546.

[137] Y. Cheng, K. Yao, Y. Yang, L. Li, Y. Yao, Q. Wang, X. Zhang, Y. Han, U. Schwingenschlögl, Van der Waals epitaxial growth of MoS2 on SiO2/Si by chemical vapor deposition, RSC Adv. 3 (2013) 17287–17293. doi:10.1039/c3ra42171f.

[138] Y. Nie, A.T. Barton, R. Addou, Y. Zheng, L.A. Walsh, S.M. Eichfeld, R. Yue, C.R. Cormier, C. Zhang, Q. Wang, C. Liang, J.A. Robinson, M. Kim, W. Vandenberghe, L. Colombo, P.-R. Cha, R.M. Wallace, C.L. Hinkle, K. Cho, Dislocation driven spiral and non-spiral growth in layered chalcogenides, Nanoscale. 10 (2018) 15023–15034. doi:10.1039/C8NR02280A.

[139] R. Yue, Y. Nie, L.A. Walsh, R. Addou, C. Liang, N. Lu, A.T. Barton, H. Zhu, Z. Che, D. Barrera, L. Cheng, P.-R. Cha, Y.J. Chabal, J.W.P. Hsu, J. Kim, M.J. Kim, L. Colombo, R.M. Wallace, K. Cho, C.L. Hinkle, Nucleation and growth of WSe 2 : enabling large grain transition metal dichalcogenides, 2D Mater. 4 (2017) 045019. doi:10.1088/2053-1583/aa8ab5.

[140] Y. Ji, B. Calderon, Y. Han, P. Cueva, N.R. Jungwirth, H.A. Alsalman, J. Hwang, G.D. Fuchs, D.A. Muller, M.G. Spencer, Chemical Vapor Deposition Growth of Large Single-Crystal Mono-, Bi-, Tri-Layer Hexagonal Boron Nitride and Their Interlayer Stacking, ACS Nano. 11 (2017) 12057–12066. doi:10.1021/acsnano.7b04841.

[141] R.E. Bell, R.E. Herfert, Preparation and Characterization of a New Crystalline Form of Molybdenum Disulfide, J. Am. Chem. Soc. 79 (1957) 3351–3354. doi:10.1021/ja01570a012.

[142] I.A. Ovid ko, A.G. Sheinerman, Hyperdislocations in misfit dislocation networks in solid films, J. Phys. Condens. Matter. 15 (2003) 2127–2135. doi:10.1088/0953-8984/15/12/329.

[143] T.H. Ly, J. Zhao, D.H. Keum, Q. Deng, Z. Yu, Y.H. Lee, Hyperdislocations in van der Waals Layered Materials, Nano Lett. 16 (2016) 7807–7813. doi:10.1021/acs.nanolett.6b04002.

[144] Y. Liu, M. Weinert, L. Li, Spiral growth without dislocations: Molecular beam epitaxy of the topological insulator Bi 2Se 3 on epitaxial graphene/SiC(0001), Phys. Rev. Lett. 108 (2012) 1–5. doi:10.1103/PhysRevLett.108.115501.

[145] J. Liu, Q. Huang, Y. Qian, Z. Huang, F. Lai, L. Lin, M. Guo, W. Zheng, Y. Qu, Screw Dislocation-Driven Growth of the Layered Spiral-type SnSe Nanoplates, Cryst. Growth Des. 16 (2016) 2052–2056. doi:10.1021/acs.cgd.5b01708.

[146] X. Liu, Y.P. Chen, D.J. Smith, Y.-H. Zhang, C. Liu, M.Z. Hasan, M. Dobrowolska, J.K.

Furdyna, J. Fan, H. Cao, T.-L. Wu, R.E. Pimpinella, MBE Growth of Thin Hexagonal Films Bi 2 Te 3 , Bi 2 Se 3 , and Their Alloys on Cubic GaAs (001) Substrates, in: H. Li, Z.M. Wang (Eds.), Bismuth-Containing Compd., Springer, New York, 2013: pp. 263–279.
[147] P. Pongratz, H. Sitter, TEM analysis of lead telluride films grown by hot-wall epitaxy on KCI and BaF2, J. Cryst. Growth. 80 (1987) 73–78. doi:10.1016/0022-0248(87)90525-2.
[148] Y. Kamimura, K. Edagawa, S. Takeuchi, Experimental evaluation of the Peierls stresses in a variety of crystals and their relation to the crystal structure, Acta Mater. 61 (2013) 294–309. doi:10.1016/j.actamat.2012.09.059.
[149] C.P. Li, P.J. McCann, X.M. Fang, Strain relaxation in PbSnSe and PbSe/PbSnSe layers grown by liquid-phase epitaxy on (100)-oriented silicon, J. Cryst. Growth. 208 (2000) 423–430. doi:10.1016/S0022-0248(99)00431-5.
[150] B.N. Strecker, P.J. McCann, X.M. Fang, R.J. Hauenstein, M. O'steen, M.B. Johnson, LPE growth of crack-free PbSe layers on Si(100) using MBE-Grown PbSe/BaF2CaF2 buffer layers, J. Electron. Mater. 26 (1997) 444–448. doi:10.1007/s11664-997-0117-5.
[151] H. Zogg, S. Blunier, A. Fach, C. Maissen, P. Müller, S. Teodoropol, V. Meyer, G. Kostorz, A. Dommann, T. Richmond, Thermal-mismatch-strain relaxation in epitaxial CaF2, BaF2/CaF2, and PbSe/BaF2, /CaF2 layers on Si(111)after many temperature cycles, Phys. Rev. B. 50 (1994) 10801–10810. doi:10.1103/PhysRevB.50.10801.
[152] P.J. McCann, C.G. Fonstad, Liquid phase epitaxial growth of PbSe on (111) and (100) BaF2, J. Cryst. Growth. 114 (1991) 687–692. doi:10.1016/0022-0248(91)90417-4.
[153] K. Takayanagi, K. Kobayashi, K. Yagi, G. Honjo, Heteroepitaxy of chalcogenite compounds I. Misfit dislocation formation in monolayer overgrowths, Thin Solid Films. 21 (1974) 325–339. doi:10.1016/0040-6090(74)90119-9.
[154] G. Springholz, K. Wiesauer, Nanoscale Dislocation Patterning in PbTe/PbSe(001) Lattice-Mismatched Heteroepitaxy, Phys. Rev. Lett. 88 (2001) 015507. doi:10.1103/PhysRevLett.88.015507.
[155] C.J. Palmstrøm, N. Tabatabaie, S.J. Allen, Epitaxial growth of ErAs on (100)GaAs, Appl. Phys. Lett. 53 (1988) 2608–2610. doi:10.1063/1.100173.
[156] J.G. Zhu, C.B. Carter, C.J. Palmstrom, S. Mounier, Microstructure of epitactically grown GaAs/ErAs/GaAs, Appl. Phys. Lett. 56 (1990) 1323–1325. doi:10.1063/1.102506.
[157] J.G. Zhu, C.J. Palmstrøm, C.B. Carter, Misfit dislocations at ErAs/GaAs heterojunctions, Acta Metall. Mater. 43 (1995) 4171–4177. doi:10.1016/0956-7151(95)00109-9.
[158] H. Yamaguchi, Y. Horikoshi, Growth of GaAs/ErAs/GaAs structures by migration-enhanced epitaxy, Appl. Phys. Lett. 60 (1992) 2341–2343. doi:10.1063/1.107020.
[159] A. Foitzik, W. Skrotzki, P. Haasen, Slip on {111} planes in lead sulphide, Mater. Sci. Eng. A. 132 (1991) 77–82. doi:10.1016/0921-5093(91)90363-R.
[160] I. Yonenaga, Dynamic behavior of dislocations in InAs: In comparison with III–V compounds and other semiconductors, J. Appl. Phys. 84 (1998) 4209–4213. doi:10.1063/1.368638.
[161] O. Madelung, U. Rössler, M. Schulz, eds., Lead selenide (PbSe) crystal structure, lattice parameters, thermal expansion, in: Non-Tetrahedrally Bond. Elem. Bin. Compd. I, Springer-Verlag, Berlin/Heidelberg, n.d.: pp. 1–4. doi:10.1007/10681727_903.
[162] G. Springholz, G. Bauer, G. Ihninger, MBE of high mobility PbTe films and PbTe / Pb1-x Eu x Te heterostructures, J. Cryst. Growth. 127 (1993) 302.
[163] O. Madelung, U. Rössler, M. Schulz, eds., Indium arsenide (InAs) lattice parameters, thermal expansion, in: Gr. IV Elem. IV-IV III-V Compd. Part a - Lattice Prop., Springer-Verlag, Berlin/Heidelberg, n.d.: pp. 1–6. doi:10.1007/10551045_146.

[164] V.K. Yang, M. Groenert, C.W. Leitz, A.J. Pitera, M.T. Currie, E.A. Fitzgerald, Crack formation in GaAs heteroepitaxial films on Si and SiGe virtual substrates, J. Appl. Phys. 93 (2003) 3859–3865. doi:10.1063/1.1558963.
[165] I.I. Zasavitskii, E.A. de Andrada e Silva, E. Abramof, P.J. McCann, Optical deformation potentials for PbSe and PbTe, Phys. Rev. B. 70 (2004) 115302. doi:10.1103/PhysRevB.70.115302.
[166] J.R. Burke, G.P. Carver, Magnetophonon and Shubnikov-de Haas oscillations in n-type PbTe epitaxial films, Phys. Rev. B. 17 (1978) 2719–2727. doi:10.1103/PhysRevB.17.2719.
[167] D. Genzow, M. Mocker, E. Normantas, The influence of uniaxial strain on the band to band recombination in Pb1-xSnxTe, Phys. Status Solidi. 135 (1986) 261–270. doi:10.1002/pssb.2221350127.
[168] M. Tachikawa, M. Yamaguchi, Film thickness dependence of dislocation density reduction in GaAs-on-Si substrates, Appl. Phys. Lett. 56 (1990) 484–486. doi:10.1063/1.102773.
[169] A. Koma, Van der Waals epitaxy—a new epitaxial growth method for a highly lattice-mismatched system, Thin Solid Films. 216 (1992) 72–76. doi:10.1016/0040-6090(92)90872-9.
[170] D.L. Medlin, K.J. Erickson, S.J. Limmer, W.G. Yelton, M.P. Siegal, Dissociated $$ \frac{1}{3}\langle 0\bar{1}11\rangle $$ 1 3 ⟨ 0 1 ¯ 11 ⟩ dislocations in Bi2Te3 and their relationship to seven-layer Bi3Te4 defects, J. Mater. Sci. 49 (2014) 3970–3979. doi:10.1007/s10853-014-8035-4.
[171] M. Grundmann, The Physics of Semiconductors, Springer Berlin Heidelberg, Berlin, Heidelberg, 2010. doi:10.1007/978-3-642-13884-3.
[172] O. Ziep, D. Genzow, M. Mocker, K.H. Herrmann, Nonradiative and Radiative Recombination in Lead Chalcogenides, Phys. Status Solidi. 99 (1980) 129–138. doi:10.1002/pssb.2220990111.
[173] H. Zogg, W. Vogt, W. Baumgartner, Carrier recombination in single crystal PbSe, Solid. State. Electron. 25 (1982) 1147–1155. doi:10.1016/0038-1101(82)90072-7.
[174] X. Zhang, J.-X. Shen, C.G. Van de Walle, Anomalous Auger Recombination in PbSe, Phys. Rev. Lett. 125 (2020) 037401. doi:10.1103/PhysRevLett.125.037401.
[175] R. Klann, T. Hofer, R. Buhleier, T. Elsaesser, A. Lambrecht, Ultrafast recombination processes in lead chalcogenide semiconductors studied via picosecond optical nonlinearities, Semicond. Sci. Technol. 8 (1993) S305–S308. doi:10.1088/0268-1242/8/1S/067.
[176] P.C. Findlay, C.R. Pidgeon, R. Kotitschke, A. Hollingworth, B.N. Murdin, C.J.G.M. Langerak, A.F.G. van der Meer, C.M. Ciesla, J. Oswald, A. Homer, G. Springholz, G. Bauer, Auger recombination dynamics of lead salts under picosecond free-electron-laser excitation, Phys. Rev. B. 58 (1998) 12908–12915. doi:10.1103/PhysRevB.58.12908.
[177] M. Yamaguchi, C. Amano, Efficiency calculations of thin-film GaAs solar cells on Si substrates, J. Appl. Phys. 58 (1985) 3601–3606. doi:10.1063/1.335737.
[178] M. Yamaguchi, A. Yamamoto, Y. Itoh, Effect of dislocations on the efficiency of thin-film GaAs solar cells on Si substrates, J. Appl. Phys. 59 (1986) 1751–1753. doi:10.1063/1.336439.
[179] C.L. Andre, J.J. Boeckl, D.M. Wilt, A.J. Pitera, M.L. Lee, E.A. Fitzgerald, B.M. Keyes, S.A. Ringel, Impact of dislocations on minority carrier electron and hole lifetimes in GaAs grown on metamorphic SiGe substrates, Appl. Phys. Lett. 84 (2004) 3447–3449. doi:10.1063/1.1736318.
[180] R.K. Ahrenkiel, M.M. Al-Jassim, D.J. Dunlavy, K.M. Jones, S.M. Vernon, S.P. Tobin, V.E.

Haven, Minority carrier lifetime of GaAs on silicon, Conf. Rec. Twent. IEEE Photovolt. Spec. Conf. 1 (1988) 684–688 vol.1. doi:10.1109/PVSC.1988.105790.
[181] R.K. Ahrenkiel, T. Wangensteen, M.M. Al-Jassim, M. Wanlass, T. Coutts, Recombination lifetime of InxGa1−xAs ternary alloys, in: AIP Conf. Proc., AIP, 1995: pp. 412–424. doi:10.1063/1.47050.
[182] J. Si, H. Wu, T. Xu, C. Cao, Hole transport and phonon scattering in epitaxial PbSe films, J. Zhejiang Univ. A. 9 (2008) 137–142. doi:10.1631/jzus.A071350.
[183] S.H. Shin, J.M. Arias, M. Zandian, J.G. Pasko, R.E. DeWames, Effect of the dislocation density on minority-carrier lifetime in molecular beam epitaxial HgCdTe, Appl. Phys. Lett. 59 (1991) 2718–2720. doi:10.1063/1.105895.
[184] R.K. Ahrenkiel, D.J. Dunlavy, B. Keyes, S.M. Vernon, T.M. Dixon, S.P. Tobin, K.L. Miller, R.E. Hayes, Ultralong minority-carrier lifetime epitaxial GaAs by photon recycling, Appl. Phys. Lett. 55 (1989) 1088–1090. doi:10.1063/1.101713.
[185] M. Mocker, O. Ziep, Intrinsic recombination in dependence on doping concentration and excitation level application to lead chalcogenides, Phys. Status Solidi. 115 (1983) 415–425. doi:10.1002/pssb.2221150211.
[186] J. Hader, J. V. Moloney, S.W. Koch, Supression of carrier recombination in semiconductor lasers by phase-space filling, Appl. Phys. Lett. 87 (2005) 201112. doi:10.1063/1.2132524.
[187] A. McAllister, D. Bayerl, E. Kioupakis, Radiative and Auger recombination processes in indium nitride, Appl. Phys. Lett. 112 (2018) 251108. doi:10.1063/1.5038106.
[188] J. Vaitkus, M. Petrauskas, R. Tomašiūnas, R. Masteika, Photoconductivity of highly excited A IV B VI thin films, Appl. Phys. A Solids Surfaces. 54 (1992) 553–555. doi:10.1007/BF00324338.
[189] D.J. Myers, A.C. Espenlaub, K. Gelzinyte, E.C. Young, L. Martinelli, J. Peretti, C. Weisbuch, J.S. Speck, Evidence for trap-assisted Auger recombination in MBE grown InGaN quantum wells by electron emission spectroscopy, Appl. Phys. Lett. 116 (2020) 091102. doi:10.1063/1.5125605.
[190] A. Pinto Neto, H. Vargas, N.F. Leite, L.C.M. Miranda, Photoacoustic investigation of semiconductors: Influence of carrier diffusion and recombination in PbTe and Si, Phys. Rev. B. 40 (1989) 3924–3930. doi:10.1103/PhysRevB.40.3924.
[191] F. Zhao, S. Mukherjee, J. Ma, D. Li, S.L. Elizondo, Z. Shi, Influence of oxygen passivation on optical properties of PbSe thin films, Appl. Phys. Lett. 92 (2008) 1–4. doi:10.1063/1.2938417.
[192] L. Däweritz, R. Hey, Reconstruction and defect structure of vicinal GaAs(001) and AlxGa1−xAs(001) surfaces during MBE growth, Surf. Sci. 236 (1990) 15–22. doi:10.1016/0039-6028(90)90756-X.
[193] H.H. Farrell, C.J. Palmstrom, Reflection high energy electron diffraction characteristic absences in GaAs(100) (2×4)–As: A tool for determining the surface stoichiometry, J. Vac. Sci. Technol. B Microelectron. Nanom. Struct. 8 (1990) 903. doi:10.1116/1.584940.
[194] Q. Xue, Scanning tunneling microscopy of III-V compound semiconductor (001) surfaces, Prog. Surf. Sci. 56 (1997) 1–131. doi:10.1016/S0079-6816(97)00033-6.
[195] N.J.C. Ingle, A. Yuskauskas, R. Wicks, M. Paul, S. Leung, The structural analysis possibilities of reflection high energy electron diffraction, J. Phys. D. Appl. Phys. 43 (2010) 133001. doi:10.1088/0022-3727/43/13/133001.
[196] S.E. Kohn, P.Y. Yu, Y. Petroff, Y.R. Shen, Y. Tsang, M.L. Cohen, Electronic band structure and optical properties of PbTe, PbSe, and PbS, Phys. Rev. B. 8 (1973) 1477–1488. doi:10.1103/PhysRevB.8.1477.